Radio and X-ray studies of Coronal Mass Ejections and their relevance for Space Weather

Carolina Salas Matamoros

THÈSE DE DOCTORAT

de l'Université de recherche Paris Sciences et Lettres
PSL Research University

Préparée à l'Observatoire de Paris

Radio and X-ray Studies of Coronal Mass Ejections and their relevance for Space Weather

Ecole doctorale n°127

ECOLE DOCTORALE D'ASTRONOMIE ET ASTROPHYSIQUE D'ILE-DE-FRANCE

Spécialité Astrophysique

COMPOSITION DU JURY :

Mme. POHJOLAINEN Silja
Université, Rapporteur

M. LAVRAUD Benoît
Institut de Recherche en Astrophysique et Planétologie, Rapporteur

M. SAUTY Christophe
Observatoire de Paris, Président du jury

M. KLEIN Karl-Ludwig
Observatoire de Paris, Membre du jury

Mme. BOCCHIALINI Karine
Université Paris Sud, Orsay, Membre du jury

Mme. TALIASHVILI Lela
Université du Costa Rica, Membre du jury

Soutenue par Carolina **SALAS MATAMOROS**
le 20 octobre 2016

Dirigée par **Ludwig KLEIN**

l'Observatoire de Paris

PSL RESEARCH UNIVERSITY PARIS

Declaration of Authorship

I, Carolina SALAS MATAMOROS, declare that this thesis titled 'Radio and X-ray studies of Coronal Mass Ejections and their Relevance for Space Weather' and the work presented in it are my own. I confirm that:

- This work was done wholly or mainly while in candidature for a research degree at this University.
- Where any part of this thesis has previously been submitted for a degree or any other qualification at this University or any other institution, this has been clearly stated.
- Where I have consulted the published work of others, this is always clearly attributed.
- Where I have quoted from the work of others, the source is always given. With the exception of such quotations, this thesis is entirely my own work.
- I have acknowledged all main sources of help.
- Where the thesis is based on work done by myself jointly with others, I have made clear exactly what was done by others and what I have contributed myself.

Signed: _____

Date: _____

Résumé

La couronne solaire est un milieu très dynamique: instabilités du champ magnétique, qui structure le plasma, conduit à l'accélération et le chauffage des particules chargées et à l'éjection de grandes structures dans l'héliosphère, les émissions de masse coronale (CME, selon ces sigles en anglais). Ces structures magnétiques éjectées peuvent interagir avec le champ magnétique de la Terre et affecter le plasma de l'environnement. Ces structures conduisent également à l'induction des courants électriques dans le sol à des latitudes élevées. L'étude de l'origine et de la propagation de ces émissions est d'intérêt pour l'astrophysique dans l'encadre de les applications générales et pour la meteorology de l'espace. La compréhension des processus de base est une condition importante pour l'élaboration des méthodes de prévision des arrivées de ces perturbations en utilisant des observations de la couronne solaire.

Les CMEs sont observées et étudiées à travers des images coronographiques. La limitation fondamentale du coronographe est qu'il montre la couronne seulement dans le plan du ciel, donc il bloque, forcément, la vue sur le disque solaire. Mais le geo-efficacité d'une CME dépend essentiellement de la proximité à la ligne Soleil- Terre et de l'évolution dans la basse couronne que ne sont pas visibles a travers des observations coronographiques. Un des problèmes est la difficulté d'estimer l'arrivée d'une CME à la Terre, parce que les mesures avec coronographes directes de la vitesse de propagation des CMEs qui est dirigée vers la Terre ne sont pas possibles dans la ligne Soleil-Terre.

Cette thèse présente l'étude des CMEs en trois étapes: (1) une étude de cas de l'évolution CME dans la basse couronne et son rôle dans l'accélération des particules, (2) la relation entre la polarisation de l'émission de sursauts radio de type IV associées à CMEs dans la couronne et l'orientation du champ magnétique observé quand les CMEs arrivent à la Terre, et (3) des estimations radiatives de la vitesse des CMEs pour les prévisions des temps d'arrivée des CMEs à la Terre.

Imagerie en utilisant des émissions radio dans la basse couronna peut montrer les signatures des CMEs sur le disque solaire. Des études précédentes avec le Radiohéliographe de Nançay (NRH) suggèrent, en fait, que les images de radio aux longueurs d'onde métriques peuvent suivre l'évolution des CMEs bien avant qu'ils deviennent visibles dans la couronne. Le diagnostic de l'évolution CME dans la basse couronne développée dans ce travail a été illustrée par l'étude de l'événement éruptif du 26 Avril 2008, qui a offert une occasion unique d'étudier le lien physique entre une seule CME bien identifiée, l'accélération des électrons tracé par émission radio, ainsi que la production des particules énergétiques solaires (SEP, selon ces sigles en anglais) observées dans l'espace. Nous effectuons une analyse détaillée en combinant les observations radio (NRH et DAM, Wind / WAVES spectrographe) et les observations de la couronne avec des satellites dans EUV et lumière blanche, ainsi que des mesures 'in situ' des particules énergétiques près de 1UA (satellites SoHO et STEREO). En combinant des images prises à partir de plusieurs points de vue, nous avons pu déduire l'évolution 3D en fonction du temps du front de l'éjection de mass qui s'a développée autour de l'éruption de la CME. Enfin, nous avons identifié, à partir des observations radio et SEP, trois régions différentes d'accélération des particules associées à l'évolution de la même CME, séparés en longitude environ 140º.

Abstract

The solar corona is a highly dynamical medium: instabilities of the magnetic field, which structure the plasma, lead to the acceleration and heating of charged particles and to the ejection of large structures into the heliosphere, the Coronal Mass Ejections (CMEs). These ejected magnetic structures can interact with the Earth's magnetic field and thereby affect the plasma environment and the high atmosphere of the Earth. Studying the origin and propagation of CMEs is of interest for both astrophysics in general and space weather applications. The understanding of the basic processes is indeed a pre-requisite for developing prediction methods of potentially geo-effective disturbances based on observations of the solar corona.

The CMEs are observed and studied primarily through coronographic images. The basic limitation of the coronagraph is that it shows the corona only in the plane of the sky, and blocks by necessity the view on the solar disk. But the geoeffectiveness of a CME depends crucially on the proximity to the Sun-Earth line and the measurements of the propagation speed, onset and early evolution of CMEs in the low corona are not accessible to coronographic observations.

This thesis presents the study of CMEs in three different stages: (1) a case study of the CME evolution in the low corona and of its role in particle acceleration, (2) the relationship between the polarisation of the type IV radio emission associated with Earth-directed CMEs in the corona and the orientation of the magnetic field observed as the CMEs arrive at the Earth, and (3) the estimation of the travel times of CMEs to the Earth.

Radio imaging with the Nancay Radioheliograph (NRH) suggest that radio images at metric wavelengths track the early evolution of CMEs well before they become visible in the corona. The examination of the CME evolution in the low corona developed in this work was illustrated through the study of the eruptive event on 26 April 2008, which offered a unique opportunity to investigate the physical link between a single well-identified CME, electron acceleration as traced by radio emission, and the production of solar energetic particles (SEPs) observed in space. We conduct a detailed analysis combining radio observations (NRH and Decameter Array, Wind/WAVES spectrograph) with remote-sensing observations of the corona in extreme ultraviolet (EUV) and white light as well as in-situ measurements of energetic particles near 1AU (SoHO and STEREO spacecraft). By combining images taken from multiple vantage points we were able to derive the time-dependent evolution of the 3D pressure front developing around the erupting CME. Finally, we identified, from the radio and SEP observations, three different particle acceleration regions associated to the evolution of the same CME, separated in longitude by about 140°. The observations for this event showed that it is misleading to interpret multi-spacecraft SEP measurements in terms of one acceleration region in the corona (Salas-Matamoros, et al, A A, Vol 590, id.A135, 15 pp).

Les observations de cet événement a montré qu'il est trompeur d'interpréter les mesures des SEP avec multi-satellites en termes d'une seule région d'accélération dans la couronne. Un article (Salas-Matamoros, Klein et Rouillard) a été soumis à la revue Astronomy & Astrophysics.
Nous voulons explorer aussi s'il existe une relation entre l'orientation de la polarisation des sursauts radio de type IV et de l'orientation du champ magnétique observé à la Terre basée sur l'étude des CMEs dirigées vers la Terre dans la basse couronne. L'idée de base est que le sens de polarisation de l'émission de radio est liée à l'orientation du champ magnétique dans la structure solaire en l'éruption. Ce travail est en cours qui sera inclus dans le manuscrit de la thèse, mais il n'a pas encore totalement développé.

Une autre question à ce-que la météorologie de l'espace est confronté est la détermination d'arrivée des CMEs à la Terre en fonction de leur vitesse de propagation. Il est connu que l'outil fondamental pour mesurer la vitesse des CMEs dans la couronne est coronographie, mais la vitesse d'une CME dirigée vers la Terre ne peut pas être mesurée par un coronographe situé dans la ligne Soleil-Terre. Différentes estimations ont été conçues, en fonction des mesures à partir des coronographes. Comme alternative, nous explorons les estimations radiatives. Tant l'observation comme la théorie montrent que la dynamique d'une CME dans la basse couronne est liée à l'évolution de la libération de l'énergie dans le 'flare' tracée par le rayon X mou et l'émission microondes. Nous présentons une réévaluation des relations statistiques entre les vitesses des CME au bord et les paramètres radiatifs, en utilisant le catalogue SOHO / LASCO, GOES et les observations microondes (Norp et RSTN). Ensuite, nous utilisons les fluences radiatives comme estimations de la vitesse des CMEs dirigés vers la Terre, ainsi que le modèle empirique de propagation interplanétaire développé par Gopalswamy et al. (2001), pour faire des prévisions de temps d'arrivée des CME à la Terre. Ces prévisions sont comparées avec les temps d'arrivée observées et avec les prévisions basées sur les mesures coronographiques. Un premier article a été publié (Salas-Matamoros et Klein, 2015. solaire Physique, sous presse arXiv: 1503,08613) et le deuxième a été soumis.

Besides, we want to explore if there is a relationship between the orientation of the polarity of type IV radio bursts and the orientation of the magnetic field observed at the Earth based on the study of Earth-directed CMEs in the low corona. The basic idea is that the sense of polarisation of the radio emission reflects the orientation of the magnetic field in the erupting solar structure. This is work in progress that will be included in the manuscript of the thesis but it is not totally developed yet.

Another issue Space Weather faces is the determination of CME arrival time at Earth based on their propagation speed. We explore radiative proxies as an alternative for coronographic proxies. Both observation and theory reveal that the dynamics of a CME in the low corona are closely related to the evolution of the energy release in the associated flare as traced by the soft X-ray and microwave emission. We present a reassessment of the statistical relationships between limb-CME velocities and radiative parameters, using the SOHO/LASCO catalog, GOES and microwave (NoRP and RSTN) observations. Then we use the radiative fluences as proxies of CME speed of Earth-directed CMEs, together with the empirical interplanetary acceleration model devised by Gopalswamy et al. (2001), to predict the CME arrival time at Earth. These predictions are compared with observed arrival times and with the predictions based on coronographic measurements. A first article has been published (Salas-Matamoros Klein, 2015. Sol Phys, Volume 290, Issue 5, pp.1337-1353, in press arXiv:1503.08613). The second one has been accepted for publication in the Space Weather and Space Climate journal.

Mots Clés
Météorologie de l'espace, Émission radio, CME, X-mou

Keywords
Space weather, CME, radio emission, X-ray

Acknowledgements

At the end of this stage of my life, I want to thank God for my academic passion, for guiding my professional career, my life and every step I have taken to be here. He gave me the strength to fight and achieve this dream, without Him by my side, I would have not accomplished this doctorate.

To Dr. Ludwig, my mentor, who helped me with his wisdom to direct this research always seeking for excellence. His fraternal correction made the mistakes become learning. Thanks for opening the doors of your family to me and making me feel welcome in this country. Thank you for all the talks, the good times, the scientific discussions and the crepes at *notre creperie prèfèrè*. My gratitude to Yveline, his wife, for welcoming me in her home and family, teaching me about the wonders of France and showing me Normandy.

I am deeply grateful to Dr. Silja Pohjolainen and Dr. Benoit Lavraud for being the readers of my thesis, and Dr. Karine Bocchialini, Dr. Christophe Sauty and Dr. Lela Taliashvili for being part of the jury. To Dr. Alexis Roulliard and Dr. Gerard Trottet, thank you for all that I learned from you during our work together.

I would also like to thank the members of the solar group with whom I worked during my stay, the researchers: Sophie Musset, Kevin Dalmasse, Rui Pinto, Pietro Zucca, Eion Carley, Rositsa Miteva, Nicole Vilmer, Alain Kerdraonn, Brigette Schmieder, Guillaume Aulanier, Pascal Démoulin, Monique Pick, Gerard Trottet, Francesco Zucarello, Chloé Guennou, Lidia Vandriel, Sophie Masson, Etienne Pariat, Stuart Gilchrist. Having shared all this time with all of you made me feel like not only that I was part of a very professional group from whom I learned so much, but also part of a group of friends that I always can count on. Especially I want to thank Pietro who has been a great friend and office mate, with whom I could share my passion for radio astronomy and taught me a lot in this field. My gratitude to Sophie, who has been a big support during all our doctoral studies, thanks for everything. Also, big thanks to all the professionals in the field with whom I had the opportunity to share knowledge at different conferences and from whom I have learned a lot.

To the people in the Observatory that I had the honor to meet, thank you all for your patience, sincere love and good times. Special thanks to Isabelle Buale, for being so kind to me. Likewise, thanks to Constance Imad, Claudine Colon and Geraldine Gaillant for your patience and support, to Goran Greblo for all the technical assistance, to Ymane Taoufiq for the moments spent together, to Sylvain Cnudde for the wonderful photos and to Alain Docclo for always having a smile for me.

I also want to give special thanks to Dominique and Déborah for welcoming me with open arms and making me a part of their lives. You made me feel the warmth of a home all the time we spent together. Thanks also to all the friends I have met because of you: Bénédicte, Eduardo, Amed, Felix and Françoise, the 'LIEN'... Thanks to all of you for making my stay in France so welcoming.

Similarly, I want to express my gratitude to Dr. Lela Taliashvili and Dr. Jorge Páez, who prompted me to follow this dream since the first steps of my career, for believing in me and encouraging me to continue and fight for my goals. Thanks to my friends in the 'Plane' for supporting me at the distance. I would also like to thank the University of Costa Rica (UCR) and the Ministry of Science, Technology and Telecommunications (MICITT) for making this dream possible.

To Nan, our friendship has been unconditional despite the distance and difficulties we have faced. She has been a great support and great listener whenever I needed someone to practice my talks and presentations or just talk about life. To the *ticos* here that made me feel a little closer to my country and all the moments that we spent together will always remain in my memory and in my heart. We'll always have Paris, don't we Sole?.

To all my friends who in one way or another have been present in this adventure and have prayed for me. I also thank my family that encouraged me during all this time. Especially my cousins Erick and Adri and to those friends who are like family: Jesús and Patricia.

Finally, my greatest gratitude is to my mom María Elena and my sister Andrea, who have been fighting all my life by my side. They have shown me that not having a perfect family is the best perfection that one can dream of. With them I have lived the worst and best moments of my life and they have been the greatest blessing that God gave me. Although we were these last years apart, we were so close that I felt like I was there with you girls. I would not have been strong enough if you two have not been by my side.

Contents

List of Figures

Abbreviations

SEP	**S**olar **E**nergetic **P**article
Dst	**D**isturbance **s**torm **t**ime
CME	**C**oronal **M**ass **E**jection
ICME	**I**nterplanetary **C**oronal**M**ass **E**jection
MHD	**M**agneto **H**ydro **D**ynamics
EUV	**E**xtreme **U**ltra **V**iolet
SXR	**S**oft **X** **R**ay
HXR	**H**ard **X** **R**ay
SDO	**S**olar **D**ynamic **O**bservatory
NRH	**N**ançay **R**adio **H**eliograph
NDA	**N**ançay **D**ecametric **A**rray
NoRP	**No**beyama **R**adio **P**olarimeters
RSTN	**R**adio **S**olar **T**elescope **N**etwork
RSTO	**R**osse **S**olar **T**errestrial **O**bservatory
STEREO	**S**olar **T**errestrial **RE**lations **O**bservatory
SoHO	**So**lar and **H**eliospheric **O**bservatory
LASCO	**L**arge **A**ngle and **S**pectrometric **C**oronograph **E**xperiment

To my mom and my sister

Chapter 1

Introduction

The environment of the Solar System is a medium of complex conditions governed by the solar activity. This activity modifies the conditions in the solar wind which is an extension of the solar corona out into the interplanetary space. Solar wind transports mass, momentum and energy from the Sun through the interplanetary medium and as a consequence, affects the magnetospheric and ionospheric conditions which implies a direct impact on different technologies at the Earth as well as at other planets and spacecraft throughout the heliosphere.

At present, we know that strong solar flares can generate a degradation of radio communication (Radio Blackout Storms) and that Solar Energetic Particles (SEPs) can penetrate spacecraft affecting the electronics and can also block communications at high latitudes through ionisation of the Earth's atmosphere. But the type of interplanetary structures that mostly affect the geomagnetic field is the Coronal Mass Ejection [e.g. Gonzalez and Tsurutani, 1987, Gosling, 1993, Tsurutani and Gonzalez, 1998, Zhang *et al.*, 2004, 2007]. These expulsions of huge mass of plasma and magnetic field into the heliosphere can cause the known Geomagnetic Storms.

geomagnetic storm are the major disturbances of the Earth's magnetosphere that result from variations in the solar wind conditions, such as high-speed, remaining for several hours and a southward directed solar wind magnetic field (opposite to the direction of Earth's field) at the day side of the magnetosphere. The intensity of a geomagnetic storm is determined by the Disturbance Storm Time (D_{st}) index. D_{st} is an index of magnetic activity derived from a network of near-equatorial geomagnetic observatories that measures the intensity of the ring current around the Earth. This ring current produces a magnetic field that is directly opposite Earth's magnetic field (e.g. review by Gonzalez *et al.* [1994]). Then, during a geomagnetic storm the ring current is enhanced leading to the weakening of the magnetic field evidenced by a negative D_{st} value ($D_{st} \leq$

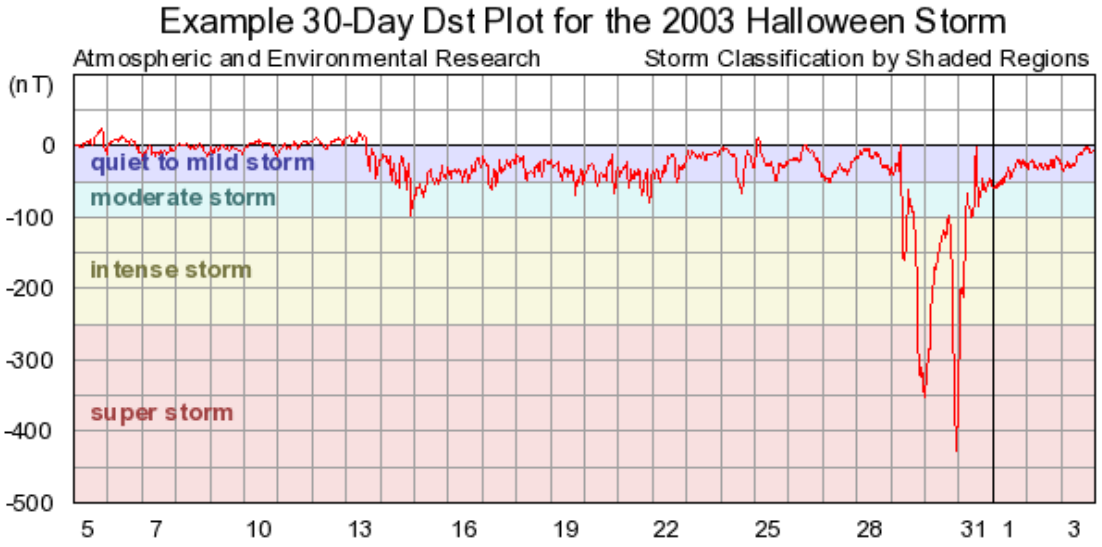

FIGURE 1.1: Data plot for the 2003 Halloween geomagnetic storm. The range of activity levels indicated by the shaded regions. Courtesy of Atmospheric and Environmental Research (AER)[1].

-50 nanotesla (nT)) [e.g. Loewe and Prölss, 1997]. Figure 1.1 shows a plot which contains data for the 2003 Halloween geomagnetic storm with a range of activity levels indicated by the shaded regions. We can compare the quiet-time behaviour on the left side of the plot that shows no geomagnetic storm with the strong negative D_{st} index on the right which is identified as a super storm.

The study of the time variation of these conditions is called *Space Weather* and is focus on fundamental research and practical applications. The capability to predict space weather phenomena is important for many applications and the analysis of the development of the solar activity is fundamental to develop new predicting techniques.

1.1 Coronal Mass Ejections (CMEs)

The first definition of CMEs was given by Hundhausen *et al.* [1984] who describe it as a considerable change in the coronal structure observed in the coronograph field of view. Before coronographs, only interplanetary transients were identified from interplanetary fluctuations in the intensity of radio waves [Hewish, Scott, and Wills, 1964, Vlasov, 1981]. Nowadays it is known that the CME phenomenon involves more than a description of the coronal structure in white-light images, it is an entire physical phenomenon which produces large-scale ejections of mass and magnetic field from the lower corona into the interplanetary space [e.g. Forbes, 2000].

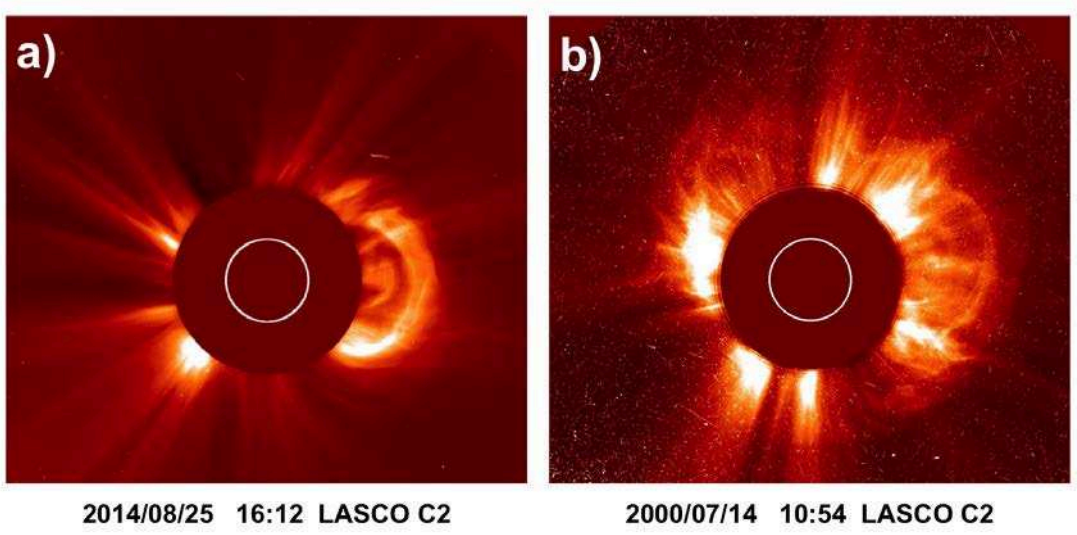

FIGURE 1.2: Snapshot images by LASCO C2 showing a) a partial halo CME and b) a halo CME. Images from SoHO LASCO CME catalog[2].

Measurements by coronographs (such as *OSO-7, Skylab, Solwind, SMM* and *LASCO*) show that CMEs inject on average a few times 10^{15} g of mass (observational compilation in Table 1 from Webb and Howard [2012]). Observations also reveal CME speeds range from a few hundred of km s^{-1} until about 3000 km s^{-1} (e.g. Harrison [1986], Schwenn *et al.* [2006], St. Cyr *et al.* [2000]). Besides, CMEs with an apparent width of 360° in coronographic images are called 'halo' CMEs while the 'partial halo' refers to CMEs with a width between 120° and 300° (review by Webb and Howard [2012]). Examples of partial halo and halo CMEs are presented in Figures 1.2.a and 1.2.b, respectively.

Since halo CMEs surround completely the occulting disk of the coronograph as is shown in Figure 1.2.b, observations of their origin on the solar disc are done in order to distinguish if they were launched from the front or backside of the Sun. The activities associated with the origin of halo CMEs are generally located within a few tens of degrees from the central median with respect of the Sun-observer line of sight (e.g. Cane, Richardson, and St. Cyr [2000], Gopalswamy [2010]). Some studies (e.g Gopalswamy, Yashiro, and Akiyama [2007]) reveal that halo CMEs observed at the Sun-Earth line (by spacecraft such as SoHO) are usually associated with major geomagnetic storms.

On the other hand, CMEs whose origin was located beyond ±45° are known as limb CMEs [e.g. Gopalswamy, 2009] and can exhibit different shapes observed by coronagraphs that cannot be observed for halo CMEs because of projection effects. They can show the classical 'three-part' structure described by Illing and Hundhausen [1985] as is presented in Figure 1.3. The bright front is followed by a dark cavity which is associated with a magnetic flux rope while the bright core is usually identified as a filament. The three-part structure is not always observed in coronographic observations of CMEs. The

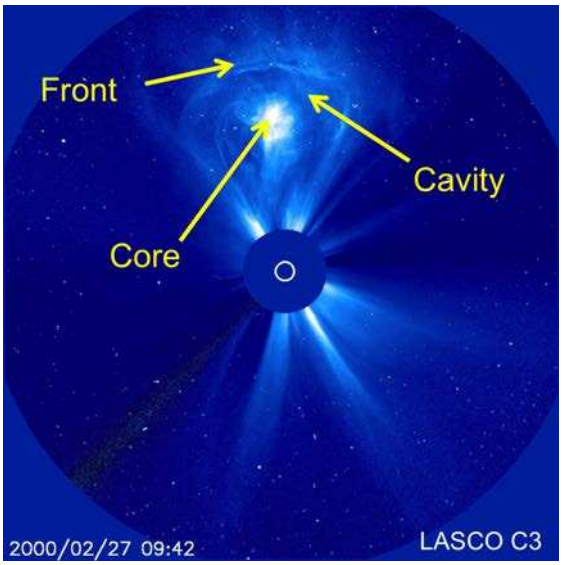

FIGURE 1.3: Typically three-part CME observed by *LASCO/C2* on 2000 February 27. The three CME components are identified by yellow arrows in this image taken from SoHO LASCO CME catalog

reason of this variation of CME structure is still unclear, if this is because of projection effects due to the optically thin nature of the emission is an open question. Even though the debate continues, the common point is that the erupting structure is always a flux rope [e.g. Chen, 2011] since there is not a physical mechanism that can produce a large-scale fast eruption from the corona without ejecting a flux rope.

The eruption of the flux rope that drives the CME is associated with some instability in the magnetic field configuration. Initially, with the first observations of CMEs, it was thought that solar flares were the cause of the CMEs. Solar flares are sudden flashes of brightness observed at the Sun and the associated electromagnetic radiation is emitted from radio to X-ray wavelengths. They occur when the magnetic energy builds up in the solar atmosphere is suddenly released [e.g. Tandberg-Hanssen and Emslie, 1988]. However, observational studies reveal that there is no one-to-one relationship between flares and CMEs and we cannot generalise the flares as the origin of CMEs.

The comparison of coronographic images and observations of filament eruptions provides also evidence of a relationship between filament/prominence eruption and the bright core of the 'three-part' CME (in Figure 1.3) observed by coronographs. Then, the filaments/prominences are thought to be originated by the formation of a flux rope low in the magnetic structure which can eventually erupt as a CME.

It is now generally accepted that CMEs and flares are part of a single driven process [e.g. Webb and Howard, 2012] and the filaments/prominences can be present or can be formed in the models of CME triggering without being a requirement. So, it is more

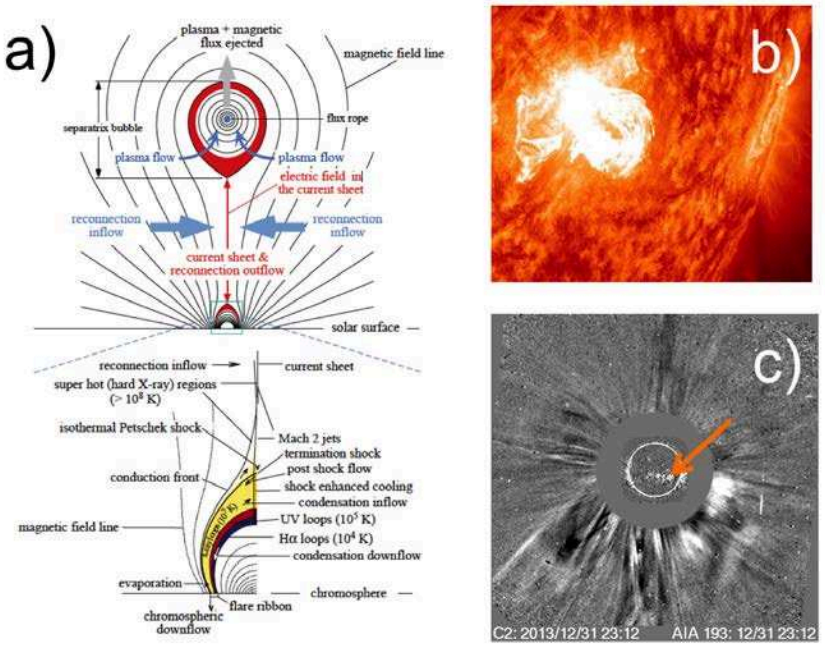

FIGURE 1.4: Compilation of a) Schematic diagram of a disrupted magnetic field that forms in an eruptive process [Lin, 2004], b) 304 Angstrom wavelength image by NASA' s Solar Dynamics Observatory (SDO) showing the eruption of a solar flare observed on 31^{st} December 2013 and c) the consequent CME observed in the difference image by LASCO/C2 associated with the flare.

appropriate to describe the triggering of CMEs in a scenario that includes both flares and filaments/prominences.

The most basic flare/CME scenario is called 'CSHKP model' because of the authors who first developed the model, Carmichael [1964], Hirayama [1974], Kopp and Pneuman [1976], Sturrock [1966]. This model explains the observable features of flares on the basis of magnetic reconnection. This flare/CME scenario has been refined and now is called 'Flux cancelation model' or the 'Catastrophe model' [e.g. Lin, 2004, Lin and Forbes, 2000, Svestka and Cliver, 1992]. Figure 1.4.a shows the schematic diagram of this unified model. As is described in Lin [2004], this diagram was created by incorporating the traditional two-ribbon flare model [Forbes and Acton, 1996] with the CME model by Lin and Forbes [2000].

In this model, coronal loops, which may contain a magnetic flux rope, rise from regions of intense magnetic fields (active regions). The magnetic field starts to stretch and a current sheet develops below the flux rope as the external pressure causes oppositely directed magnetic field lines to converge. When these magnetic lines reconnect, electrons, protons, and heavier ions are accelerated and the liberated energy that is directed downward can heat the reconnected loops (observed as post-flare loops) producing the

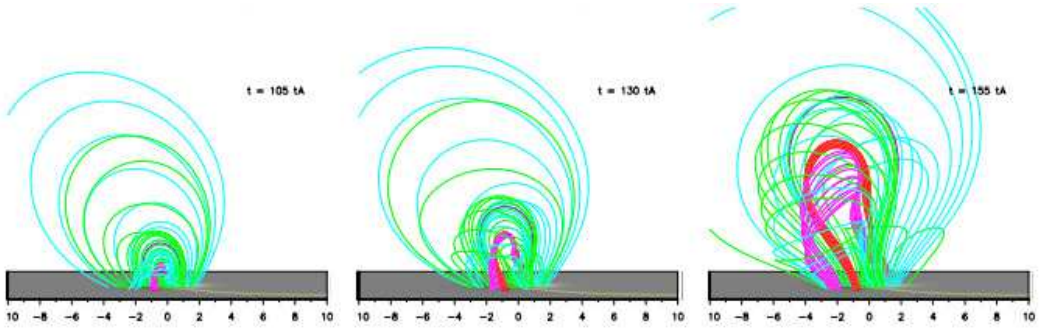

FIGURE 1.5: Numerical MHD simulation of the magnetic field evolution of the shearing and diffusing bipole, before and during the eruption in a nearly 2D projection view along the flux rope axis (i.e., y-direction). Pink/red field lines belong to a forming and erupting weakly twisted flux rope while the cyan/green field lines to moderately sheared overlying arcades. Figure adapted from Aulanier *et al.* [2010]

observed brightening (Fig. 1.4.b). In general, the energy is released during a period which is called impulsive phase and it is gradually dissipated during the decay phase [Antonucci *et al.*, 1982, Sturrock, 1980].

The hot plasma in the loops produces the soft X-ray (SXR) emission while the hard X-ray (HRX) radiation is produced when energetic electrons traveling downward reach the chromosphere and emit via bremsstrahlung mechanism. Non-thermal microwave emission is caused by accelerated electrons that turn around the magnetic fields of the loops while the dm-m radio emission observed at the site of flares is produced by electrons trapped in the magnetic loops.

On the other hand, the magnetic structure (flux rope and filament/prominence) separates from the reconnection site, is pushed away from the Sun and is observed as a CME by coronographs as the example in Figure 1.4.c. If the prominence separates slowly there is not much energy deposited in the post-flare loops to produce a detectable flare. But also there are flares that remain confined because they do not have enough energy to produce an eruption [Chen *et al.*, 2015, Thalmann *et al.*, 2015, Török and Kliem, 2005].

Numerical simulations of CMEs have been developed to understand in more detail the role of filaments/prominences and flares in the CME triggering. These initiation models are classified in 1) *storage and release* and 2) *directly driven* models [e.g. Chen, 2011, Forbes, 2010]. The *storage and release* model refers to the eruption of the magnetic field due to a perturbation of the magnetic energy slowly stored in the coronal magnetic field while the magnetic energy is pumped into the corona during the eruption itself in *directly driven* models [e.g. Zuccarello *et al.*, 2013]. The *storage and release* models can be subdivided into:

Models that do not require magnetic reconnection for the triggering even when it can occur during the process. In this way, the eruption occurs as a consequence of: a loss of equilibrium (mass loading/off-loading [e.g. Wolfson and Dlamini, 1997]) or an MHD instability (kink instability, [e.g Rachmeler, DeForest, and Kankelborg, 2009, Török, Kliem, and Titov, 2004] or torus instability, [e.g Aulanier *et al.*, 2010])

Models that require magnetic reconnection for triggering the eruption. The models include: flux cancelation model [e.g Zuccarello, Meliani, and Poedts, 2012] and the breakout model [Antiochos, DeVore, and Klimchuk, 1999, Zuccarello *et al.*, 2008].

Figure 1.5 shows an example of the build-up and eruption of a flux rope from MHD simulations. Observations combined with these models show that the mechanical energy release to CMEs and thermal and non-thermal energy release should be closely related [e.g Chen, 2011, Pinto, Vilmer, and Brun, 2015, Reeves and Moats, 2010, Schmieder, Démoulin, and Aulanier, 2013, Zuccarello *et al.*, 2014].

This energy release not only produces the huge ejections of mass and magnetic field but also solar energetic particles (SEP). Because SEPs can affect not only electronics at the environment of the Earth but also the human life in the Space, the understanding of how and where these SEPs are produced and how they propagate concerns space weather as well. SEPs are protons, electrons and ions whose energy ranges from a few tens of keV to GeV. In general, they are produced in the reconnection sites during flares [e.g. Aschwanden, 2012, Kahler, Reames, and Sheeley, 2001] or by shock waves driven by CMEs [e.g. Zank, Rice, and Wu, 2000] in the corona or in the interplanetary space. So, CME development in the low corona and its propagation into the interplanetary space are directly linked with SEP events observed at different spacecraft.

1.2 Outline of the thesis: CMEs, Radio and X-ray emissions and Space Weather

As was discussed in the previous section, CMEs are observed and studied through coronographic images. The basic limitation of the coronograph is that it shows the corona only in the plane of the sky, and blocks by necessity the view on the solar disk. But the ability of CMEs to cause geomagnetic storms (known as geo-effectiveness) depends crucially on the proximity to the Sun-Earth line (halo CMEs are more geo-effective Gopalswamy, Yashiro, and Akiyama [2007]) and the onset and early evolution of CMEs in the low corona are not accessible to coronographic observations from Space.

Radio imaging of the low-coronal manifestations of CMEs is able to show the signatures on the solar disk. Previous studies with the NRH, such as Pick and Vilmer [2008], suggest indeed that radio images at metric wavelengths track the early evolution of CMEs well before they become visible in the corona. A characterisation of the radio emission mechanisms as well as the relations with the CME evolution is presented in Chapter 2. The determination of SEP acceleration sites associated with the CME evolution in the corona is illustrated through the study of the eruptive event on 2008 April 26. This event offered an unique opportunity to investigate the physical link between a single well-identified CME, electron acceleration as traced by radio emission, and the production of SEPs observed in the Space. We conduct a detailed analysis combining radio observations (NRH and Decameter Array, Wind/WAVES spectrograph) with remote-sensing observations of the corona in extreme ultraviolet (EUV) and white light as well as in-situ measurements of energetic particles near 1AU (SoHO and STEREO spacecraft). We demonstrate that is misleading to interpret the multi-spacecraft measurements of SEPs in terms of one acceleration region in the corona. Even though the understanding about how and where particles are accelerated is still an open question, radio emission can provide an important diagnostic of particle acceleration sites as we discuss in next chapters.

We also want to explore if there is a relationship between the polarisation of type IV radio bursts associated with Earth-directed CMEs and the orientation of the interplanetary magnetic field observed at the ICME arrival. In Chapter 3 we present an initial characterisation of the polarisation of three type IV bursts in order to establish the basis for a future work in this subject.

Finally, the other issue related to space weather effects of Earth-directed CMEs is the difficulty to estimate their arrival time because direct coronographic measurements of the propagation speed are not possible from the Sun-Earth line. Thus, various proxies have been devised, based on coronographic measurements to estimate this speed. As an alternative, we explore radiative proxies to estimate this speed based on the signatures on the solar disc. Both observation and theory reveal that the dynamics of a CME in the low corona is closely related to the evolution of the energy release in the associated flare as traced by the soft X-ray and microwave emission. We present in Chapter 4 a reassessment of the statistical relationships between limb-CME velocities and radiative parameters. Then the radiative fluences (SXR and microwave) are used to obtain CME speeds of Earth-directed CMEs.

A description of the CME propagation in the interplanetary space is also presented in Chapter 4 where we use the speed obtained from radiative proxies as an input in one empirical model to predict the arrival time of CMEs at the Earth. The predictions

are compared with observed arrival times *in situ* and with the predictions based on coronographic measurements, as well as with techniques using heliographic imaging and MHD modelling.

The main aim of this thesis is to explore complementary diagnostics of CMEs based on radio emission that potentially can be considered in space weather applications.

Chapter 2

Radio Diagnostics of the CME Evolution in the low Corona

2.1 Basics of Radio Emission

Radio waves have wavelengths longer than infrared light (frequencies $\leq$ 3 THz). The radio emission from the Sun can be used as a diagnostic to study fundamental processes in the solar atmosphere and also help us to understand the Sun-Earth connection and, as a consequence, the space weather.

If the solar radiation is considered as 'black body' radiation, the emission would vary with the frequency and the temperature according to Plank's radiation law

$$I_\nu(T) = \frac{1}{e^{\frac{h\nu}{kT}} - 1} \frac{2h\nu^3}{c^2} \ . \tag{2.1}$$

But in radio regime we have that $\frac{h\nu}{kT} \ll 1$ and then we can approximate the Eq. 2.1 by

$$I_\nu(T) = \frac{2kT\ \nu^2}{c^2} \ . \tag{2.2}$$

This equation is known as the *Raileigh-Jeans approximation*. If the kinetic temperature of a maxwellian distribution in Eq. 2.2 is replaced by a *Brightness temperature* (T_B), this approximation can be used to describe all radio regime. This T_B is defined as the needed temperature of a blackbody to produce the observed radiance at the specified frequency. If the intensity (I_ν) is integrated over the source, we obtain the flux density (S):

$$S = \int I_\nu(\nu) d\Omega \ \ [\mathrm{Wm^{-2}Hz^{-1}}] \, . \tag{2.3}$$

Usually, the spectral flux density is measured in Solar Flux Units (sfu) that is often used in solar radio observations and is defined as

$$1 \text{ sfu} = 10^4 \text{ Jy} = 10^{-22} \text{ W m}^{-2} \text{ Hz}^{-1} = 10^{-19} \text{ erg s}^{-1} \text{ cm}^{-2} \text{ Hz}^{-1}. \tag{2.4}$$

Knowing that along the emission path, photons generated in one volume element can also be absorbed, the variation of intensity in a volume element can be expressed as

$$\mathrm{d}I = h_n \ \mathrm{d}l - k_n \ I \ \mathrm{d}l, \tag{2.5}$$

where h_n and k_n are the volume emissivity and the absorption coefficient respectively and $\mathrm{d}l$ is a longitude element along the raypath. Considering a medium in thermodynamic equilibrium we have that emission and absorption occur at the same rate. Thus, $\mathrm{d}I = 0$ and Equation 2.5 becomes

$$0 = h_n \ \mathrm{d}l - k_n \ I \ \mathrm{d}l \ \Rightarrow \ I = \frac{h_n}{k_n}, \tag{2.6}$$

which equals the Planck function in thermodynamic equilibrium and is called *source function*. Now, considering that a hot source radiation can be absorbed on passing through a cool cloud, we have negligible emissivity ($h_n \ \mathrm{d}l = 0$) from the cloud and Equation 2.5 becomes

$$\mathrm{d}I = -k_n \ I \ \mathrm{d}l, \tag{2.7}$$

whose solution is

$$I = I_0 \ e^{-\tau_n}, \tag{2.8}$$

where $\tau_n = \int_0^L k_n \ \mathrm{d}l$ is the optical depth. Then, a cloud with $\tau_n \gg 1$ is optically thick while a cloud with $\tau_n \ll 1$ is optically thin.

We now can rearrange Equation 2.5 to obtain the equation of radiative transfer

$$\frac{\mathrm{d}I}{\mathrm{d}l} + k_n \; I = h_n. \tag{2.9}$$

We want to consider now both the emissivity and the absorption of the radiation in one volume element. For a homogeneous source, from the radiative transfer equation we can derive the total intensity emitted and absorbed along the raypath as

$$I = I_0 \; e^{-\tau_n} \; + \; \frac{h_n}{k_n} \; (1 - e^{-\tau_n}), \tag{2.10}$$

where the first term is the contribution of an external source along the line of sight and the second term is the contribution of the internal emission and absorption of the cloud. Using Equation 2.6 for the *Raileigh-Jeans* limit we obtain

$$T_B = T_0 \; e^{-\tau_n} \; + \; T_{eff} \; (1 - e^{-\tau_n}), \tag{2.11}$$

where the effective temperature, T_{eff}, is the expected temperature of the source obtained by $I_\nu(T_{eff})$ in Equation 2.2. Then,

optically thick: $\tau_n \; \gg 1 \quad \Rightarrow \quad T_B = T_{eff}$

optically thin: $\tau_n \; \ll 1 \quad \Rightarrow \quad T_B = T_0 \; + \; T_{eff} \; \tau_n$

2.2 Radio Observations

Observations of solar phenomena at frequencies between a few of GHz and about 20 MHz are made on ground because this radiation together with the optical radiation are the unique ones not absorbed by the terrestrial atmosphere and it is very convenient in terms of instrument development. Frequencies beyond 20 MHz are observed from the space with the *WAVES* instrument on board the WIND and STEREO spacecraft which provides a comprehensive coverage of radio phenomena in the frequency range from a fraction of a Hertz up to about 14 MHz.

2.2.1 Radio Telescope Basics

Radio telescopes look and operate very differently from the optical instrumentation. Since the range of radio frequencies is so broad compared with the optical range, the

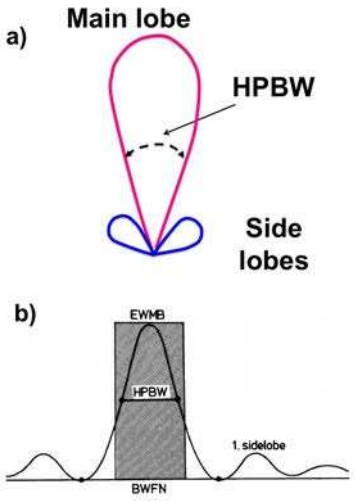

FIGURE 2.1: Power pattern of an antenna and the Half Power Beamwidth (HPBW). a) Schematic of main and side lobes. b) Schematic of telescope beam and beam size for a one-dimensional power pattern. Adapted from Wilson, Rohlfs, and Hüttemeister [2009]

instruments at the lower radio frequencies look very different from those at higher frequencies.

In solar radio astronomy, the quantity measured by radio telescopes is the total flux density in sfu units. The total flux density can be obtained by the *antenna temperature* (T_A) definition [Wilson, Rohlfs, and Hüttemeister, 2009]

$$T_A = \frac{1}{2k} A_{ef} \int\int B_\nu(\theta,\phi) P_n(\theta,\phi) d\Omega, \tag{2.12}$$

which relates the output power of the antenna with a normalized power pattern, $P_n(\theta,\phi)$, pointed at a brightness temperature (in the Rayleigh-Jeans limit) distribution, $B_\nu(\theta,\phi)$, in the sky. The power pattern is equal 1 in the direction of maximum response of the antenna, then the observed flux density from Equation 2.12 is

$$S_{obs} = \frac{2kT_A}{A_{ef}}, \tag{2.13}$$

where the *effective apperture* of the antenna, A_{ef}, can be obtained as $A_{ef} = e_a \cdot A_g$. The *geometric area* of the antenna and the *aperture efficiency factor* are A_g and e_a (typically $\approx 0.55 - 0.65$) respectively.

The primary maximum of the power pattern is called main lobe and the side lobes are the subsidiary maxima (see Fig. 2.1.a). The angular distance between points at which

FIGURE 2.2: North-south antenna array of the *Nancay Radioheliograph*.

the main lobe falls to half its central value is called the Half Power Beamwidth (HPBW). This value is also the spatial resolution of the telescope and is given by

$$\theta_{\mathrm{HPBW}} \approx \frac{\lambda}{D}, \tag{2.14}$$

where D is the dimension of the antenna and λ is the wavelength of the radiation and should be expressed in the same units. The resulting θ_{HPBW} is given in radians.

2.2.2 Interferometry Basics

The interferometry technique is the combination of single elements which work together to form a single telescope. Such arrays are called 'interferometers' and one of the few solar dedicated interferometers is the *Nançay Radioheliograph* whose north-south antenna array is shown in Figure 2.2.

The spatial resolution of an interferometer is determined by the maximum separation between elements. The baseline (B) is the distance between two antennas. If B is considered as the maximum distance of antennas of the array, the spatial resolution is determined by $\theta_{\mathrm{HPBW}} = \frac{\lambda}{B}$.

To explain the basics of interferometry, we consider a simple two dishes interferometer, as the one shown in Figure 2.3, that observes a point source. The radio signal arrives at different antennae at different times, which means that the signal is observed with

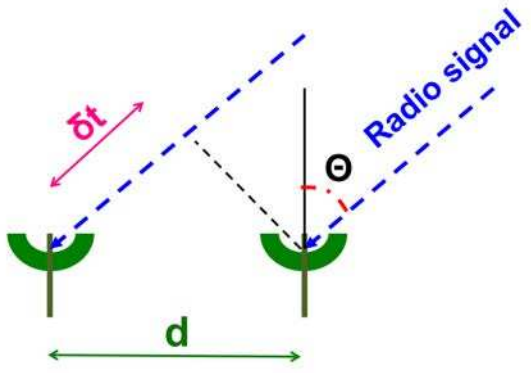

FIGURE 2.3: Schematic configuration of a simple two-dishes interferometer.

a phase difference of $\phi = \omega t = \frac{2\pi d}{\lambda}\sin\theta$. This phase difference is one of the principal issues in interferometry, which can be solved by correlating the different signals.

The correlation function (S) of the signals in terms of the delay time t can be described as

$$S = E_0^2 \int_0^T \cos(\omega t')\cos(\omega(t'+t))\mathrm{d}t', \tag{2.15}$$

where E_0 and T are the amplitude of the monochromatic plane wave and the integration period (longer than $\frac{2\pi}{\omega}$) respectively.

However, for an extended source, the flux density depends on the pointing direction (u, v) of the antennae. So, the interferometer measures the visibility of the extended source ($V(u, v)$) which gives information about the structure of the source (imaging). Since the visibility of the source can be related to the brightness distribution by

$$V(u,v) = \int\int B(\alpha,\beta)e^{i2\pi(\alpha u+\beta v)}\mathrm{d}\alpha\mathrm{d}\beta \ , \text{ with } u = \frac{d_x}{\lambda} \text{ and } v = \frac{d_y}{\lambda} \tag{2.16}$$

where d_x and d_y are the two spatial components of the radio signal arrival, the correlation function is

$$S = e^{i\phi(u_0)}V(u,v), \tag{2.17}$$

where $\phi(u_0)$ is the phase of the reference point of the source (the Sun centre, for instance) and $V(u, v)$ is the result of the imaging.

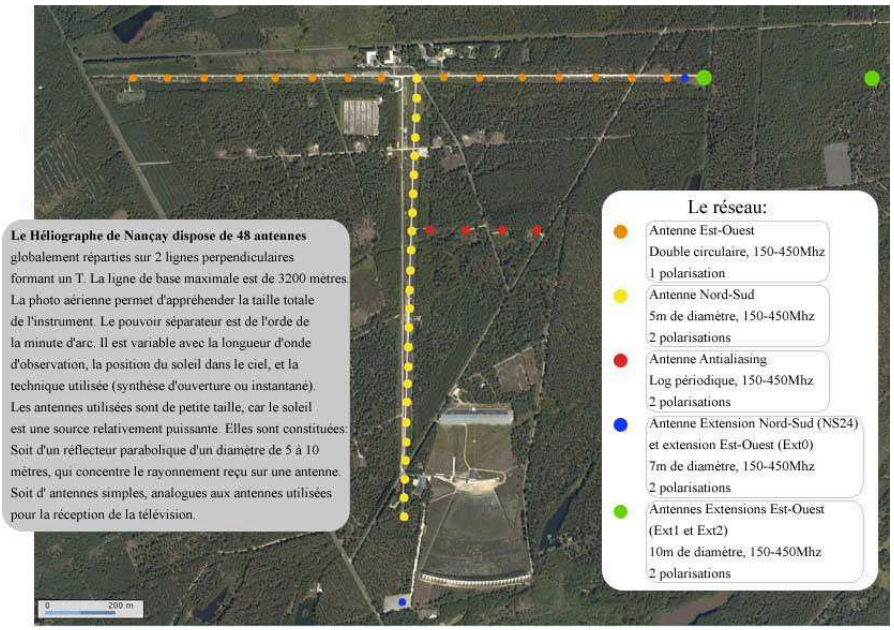

FIGURE 2.4: Schematic antennae configuration of NRH. Image from the web site of Station of Nançay[1]

2.2.3 Solar Radio Instrumentation at Nançay Station

2.2.3.1 Nançay Decametric Array

The *Nançay Decametric Array* (NDA, Lecacheux [2014]) operates in the 10-80 MHz frequency range and consists in two phased antenna arrays in opposite senses of circular polarisation with 4000 m^2 of effective aperture each. The set of receivers of wide band allow to obtain a high resolution and sensitive spectroscopy of Jovian and solar radio emissions with a resolution of 1 sec.

The obtained data is a dynamic spectrum: the intensity received is shown as a function of time and frequency (as the dynamic spectra in Fig. 2.10).

2.2.3.2 Nançay Radioheliograph (NRH)

The *Nançay Radioheliograph* (NRH, Kerdraon and Delouis [1997]) is an instrument dedicated to solar observations at long decimetre and metre wavelengths and was designed to observe the total and circularly polarised radiation (complex visibilities in Stokes I and V) from the Sun. The instrument is a T shaped interferometer of 48 antennas spread over two arrays (EW and NS) as is shown in Figure 2.4. In this figure, the position of the antennas in the array are marked by the yellow, green and blue points. Red points are antennas which are not part of the T-shaped array. Observations of the visibilities

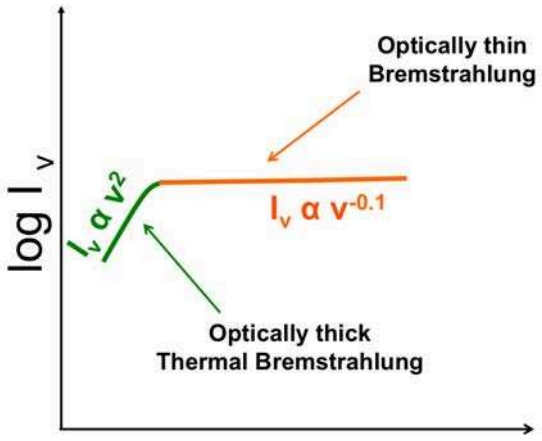

FIGURE 2.5: Expected *thermal bremstrahlung* spectrum. The optically thick and thin parts are represented by green and orange lines respectively.

are done during 7 hours per day in a frequency band of 700 kHz with a selected band between 150 and 450 MHz with sub-second time resolution.

2.3 Solar Radio Emission

The radio emission from the Sun at dm-m wavelengths can be classified according to the dynamic spectrum as: **Quiet-Sun**, **Noise Storms** and **Burst Emission** [Kundu, 1965].

2.3.1 Quiet-Sun Emission

This emission results from the *thermal bremsstrahlung* process in the solar atmosphere and it is distributed over all solar disk. *Bremsstrahlung* emission is produced as a consequence of Coulomb collisions between electrons (test particles) and ions (field particles). *Bremsstrahlung* is *thermal* if the test particles have the same thermal distribution that the field particle, while it is called *non-thermal Bremsstrahlung* when the test particles have a non-thermal distribution. *Thermal Bremsstrahlung* is observed at soft X-ray (SXR) and microwave and dm-m wavelengths, while *Bremsstrahlung* produced by non-thermal particles is observable at hard X-ray (HXR) wavelengths [e.g., Aschwanden, 2004].

The shape of the expected spectrum shown in Figure 2.5 is set then by the balance between the emission process in the optically thin medium and the self-absorption process

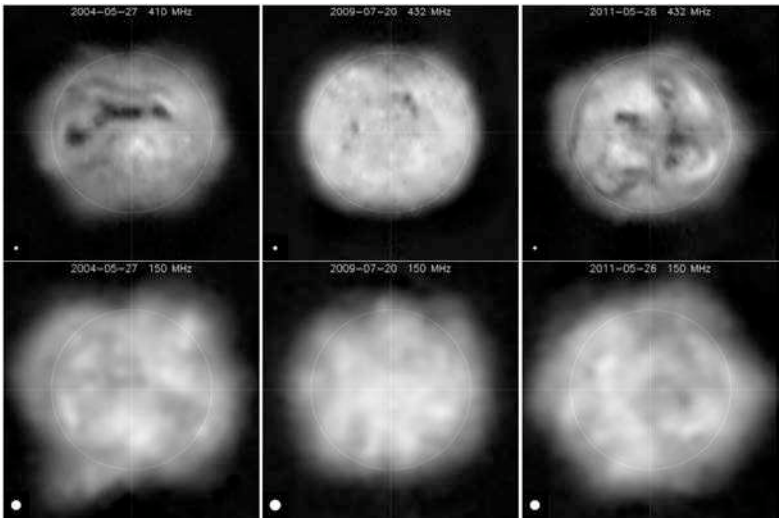

FIGURE 2.6: Images from NRH at 164 and 432 MHz show the quiet Sun morphology. Differences in the solar morphology are observed between both frequencies. Figure adapted from Mercier and Chambe [2015]

in the optically thick medium. In the optically thick region, the spectrum is a blackbody while in the optically thin regime the spectrum is flatter as shown in Figure 2.5.

In images the Quiet-Sun appears like a broad emission covering the whole solar disk. Figure 2.6 shows the emission of the Quiet-Sun at 164 and 432 MHz at three different dates observed by NRH. Coronal holes observed at 432 MHz (top panels) are not observed at 150 MHz because of the refraction of the radiation at lower frequencies.

Because of their thermal origin, the electrons are always in thermodynamic equilibrium, then it is possible to assume the source function as equal to the Planck function. In this way, radio observations of Quiet-Sun can be used to characterise the physical conditions of the solar atmosphere.

Since radio waves at a certain frequency can only be observed from regions where the radio frequency are greater than the local electron plasma frequency and knowing that the electron density decreases with height, coronal density models can be developed based on radio observations. Mercier and Chambe [2015] study the variations of the quiet corona in brightness and size and derive a density model based on radio observations. They find that the electron temperature is less than the scale-height temperature which implies the electron temperature is lower than the ion temperature, contrary of what was found in previous studies.

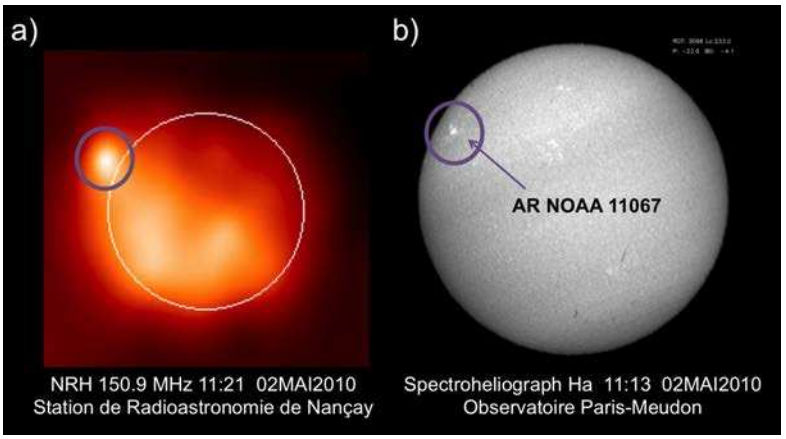

FIGURE 2.7: Solar noise storm. a) Snapshot map by NRH at 150.9 MHz that shows a noise storm at the eastern limb enclosed in the purple circle. b) The associated active region NOAA 11067 is shown enclosed in the purple circle in the H_α image of the solar disc by *Observatoire de Paris*

2.3.2 Noise Storms

The noise storms from the Sun are emissions lasting up hours or days. This emission presents two components: type I bursts or discrete emission (0.1-1 sec) and continuum emission. Both components have high circularly polarisation (e.g Mercier *et al.* [1984]) and are associated with active regions. Also, it was observed that the degree of polarisation of both components decreases as the source is close to the limb [e.g., Kai, 1962] because of the propagation of the radiation in the solar atmosphere.

Even though the link between noise storms and active regions is well known, the emission mechanism is an open subject of study. However, it is accepted that this emission is due to plasma emission of suprathermal electrons trapped in closed flux tubes [e.g., Del Zanna *et al.*, 2011]. This is consistent with the observed high brightness temperatures associated to noise storms [Kerdraon and Mercier, 1983]. Figure 2.7.a shows a 2D image at 150.9 MHz where a noise storm is observed at the eastern limb. This emission is associated with the active region NOAA 11067 observed in Figure 2.7.b.

The onset and enhancement of noise storms has been related to sunspot spatial evolution [Bentley *et al.*, 2000, Malik and Mercier, 1996].

2.3.3 Radio Bursts

The transient emissions from the Sun are called radio bursts and were one of the first phenomena of interest of radio astronomy. Since these emissions originate from different layers in the solar atmosphere, from the low to the outer corona and even the interplanetary space, they allow us to study the energy release, electron acceleration, electron

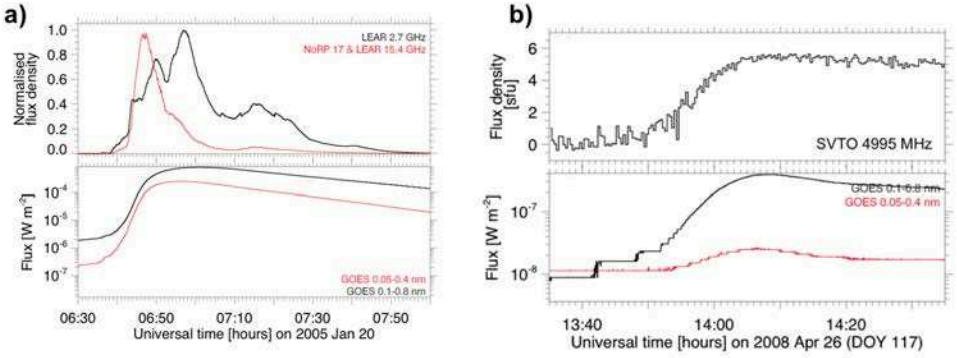

FIGURE 2.8: Examples of microwave bursts. The bottom panels show the time-profile of the SXR burst related to two different flares on a) 2005 January 20 and b) 2008 April 26. The top panels present the time profile of the microwave bursts with b) non-thermal origin and b) thermal origin.

propagation and CME launch. These bursts are mostly related to solar flares through the flare/CME scenario described in Chapter 1. In general, radio bursts can be subdivided into two groups: **microwave bursts** (whose non-thermal emission is produced by gyrosynchrotron mechanism) and **dm-km bursts** (produced by plasma emission). However, occasionally gyrosynchrotron emission can be also observed at m-wavelengths and plasma emission in the microwave domain.

In the following description of radio bursts, the event on 2008 April 26 is used as an example of the analysis of all radio emissions at dm-km λ involved in the CME evolution process. This event has been studied in detail in Salas-Matamoros, Klein, and Rouillard [2016].

2.3.3.1 Microwave Bursts

This kind of bursts are related to mildly relativistic electrons (energies of $\approx$ 100 keV-10 MeV) emitting via the *gyrosynchroton* mechanism. Commonly, this emission is observed in the range from 1 to some tens of GHz during the impulsive phase of flares [Nindos *et al.*, 2008] where the high energy electrons are accelerated and gyrate around the loop magnetic field. Figure 2.8 shows the time profiles of SXR and microwave bursts of two different events. The usual *gyrosynchrotron* emission profile revealing mildly relativistic electrons in the low corona is shown in Figure 2.8.a. This profile presents a pronounced rise and decay phase during a short time with a maximum of about 8400 and 8500 sfu at 2.7 and 15.4 GHz respectively. This figure also shows that microwave emission can be also observed after the impulsive phase of the flare. On the other hand, Figure 2.8.b shows a smooth microwave profile at 5 GHz, similar to the SXR profile and presents a maximum flux density of only 5 sfu. The usual *gyrosynchrotron* emission profile observed

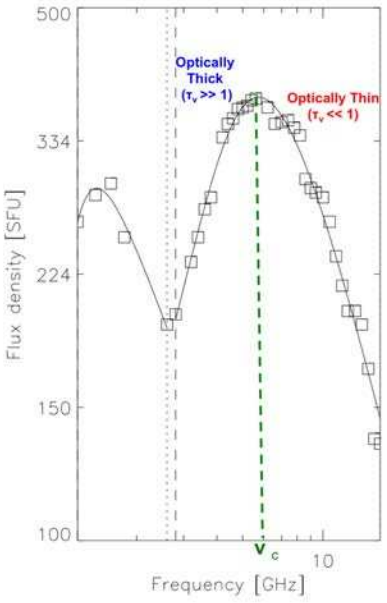

FIGURE 2.9: Example of microwave spectrum of a radio burst adapted from Figure 1 in Nita, Gary, and Lee [2004].

in Figure 2.8.a is lacking, suggesting that there was no substantial electron acceleration to energies above 100 keV in the flaring active region.

The *gyrosynchrotron* emission is the mildly relativistic limit of the *gyromagnetic* emission mechanism. The helicoidal motion of a particle of rest mass m_0, charge Ze and Lorentz factor $\gamma = (1 - \frac{v^2}{c^2})^{-1}$ in an uniform static magnetic field B is described by

$$\frac{d}{dt}(\gamma m_0 \vec{v}) = Ze(\vec{v} \times \vec{B}) \ . \tag{2.18}$$

The acceleration $(\frac{\mathrm{d}\vec{v}}{\mathrm{dt}})$ is always perpendicular to the velocity vector $(\vec{v})$ and magnetic field vector $(\vec{B})$. Considering that the motion has a constant speed in the magnetic field direction, the electrons would describe helicoidal paths with a constant pitch angle α (angle between the magnetic field and the speed vectors).

In general, the number of times per second that the particle rotates about the magnetic field direction ν_g is known as the *gyro-frequency* or *cyclotron frequency* and is given by

$$\nu_g = \frac{ZeB}{2\pi\gamma m_0} \ . \tag{2.19}$$

It is known that for every emission process there is an associated absorption process. For a source of *gyrosynchrotron* radiation at low enough frequencies, the brightness temperature of the source may approach the kinetic temperature of the radiating electrons. When

this occurs, self-absorption becomes important since thermodynamically the source cannot emit radiation of brightness temperature greater than its kinetic temperature in the optically thin part of the spectrum.

Figure 2.9 shows an example of the *gyrosynchrotron* spectrum at frequencies between about 3-18 GHz. The spectrum of the radiation of non-thermal electrons typically shows positive slopes until the maximum frequency, usually $\nu_{\max} = 5 - 10$ GHz (e.g. Nindos *et al.* [2008], Stahli, Gary, and Hurford [1989]), that corresponds to the critical frequency marked by the discontinuous green line in the figure. For frequencies $\nu \leq \nu_{\max}$ the emission is optically thick while at higher frequencies, $\nu \geq \nu_{\max}$, the emission is optically thin. The emission at frequencies lower than 3 GHz does not correspond to gyrosynchrotron emission but probably plasma emission.

2.3.3.2 Radio bursts at dm-km wavelengths

The bursts observed in the frequency range ≤ 1000 MHz are generally associated with non-thermal emission generated by plasma waves via plasma emission [Melrose, 1980]. However, some emission by gyrosynchrotron can be also present. Since the 60's these radio bursts were classified in five groups [e.g., Wild, Smerd, and Weiss, 1963] based on their spectra. At the present, it is known that for space weather considerations, three types of radio bursts are relevant: type II, type III and type IV bursts. Figure 2.10 shows the dynamic spectrum between 70 MHz and 10 kHz in the two top panels. Radio bursts can be also observed in the interplanetary space (frequencies ≤ 10 MHz) and are called *Interplanetary* (IP) bursts as the IP type III bursts in Figure 2.10.

On the other hand, the bottom panels in Figure 2.10 present the two-dimensional scans of the emission at 150 and 327 MHz scaled to show both weak and strong emissions. They are stacked and plotted as 1D images with the time on the abscissa and the position on the solar north-south or east-west, on the ordinate. The one-dimensional positions can be inferred by associating sources with identical temporal evolution in the east-west and north-south images. These radio imaging observations by NRH is a powerful tool for the study of the evolution (location and angular opening) of flare/CME events in the low corona, especially for CMEs whose development on the disk cannot be studied by using white light coronographic observations.

In order to generate coherent plasma emission, an anisotropic electron distribution is required. These electrons can be produced by **magnetic reconnection** during flares [e.g., Benz, 1987, Gonzalez and Parker, 2016, Klein *et al.*, 1999] or by **shock waves** through a shock drift process where the electrons, that encounter once the shock front, are reflected and gain energy [e.g., Holman and Pesses, 1983, Mann, Classen, and Motschmann, 2001].

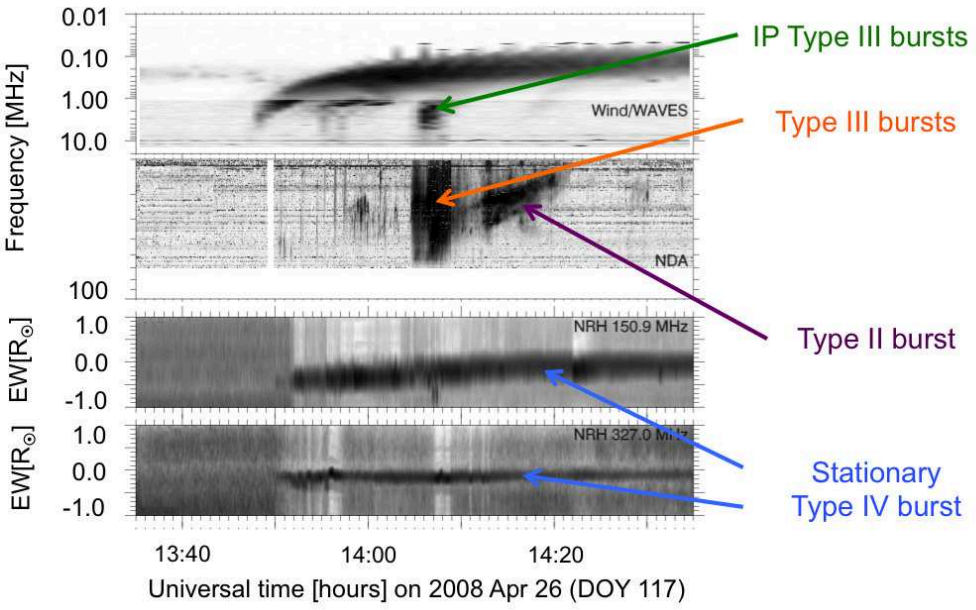

FIGURE 2.10: Dynamic spectra and 1D images of the event on 2008 April 26 showing the three types of radio bursts more relevant in space weather. Two bottom panels are 1D images projected onto the solar east-west direction at 150 and 327 MHz (y axis graded in solar radii from the eastern to the western limb). Two top panels show the dynamic spectra between 70 MHz and 10 kHz.

The second order of Fermi acceleration or **diffusive shock acceleration**, is also another manner to accelerate electrons through multiple encounters with the shock front (e.g. Melrose [1994]). However, a high turbulence is needed (e.g. flare loops or complex field structures) for this model because an effective scattering is required.

Once the electrons have been accelerated, the process to generate plasma emission due to an anisotropic electron distribution covers several stages [McLean and Labrum, 1985]:

1. **Excitation of plasma waves because of an instability.** When the electrons are accelerated via magnetic reconnection process in flares or at the shock fronts propagate in the plasma density medium, the higher energy electrons race ahead of the lower energy electrons which produces **beams** in the forward direction of the particle distribution function. These beams are unstable to the *bump-in-tail* instability and generate plasma oscillations or *Langmuir waves*. Plasma oscillations can be also generated by a loss cone distribution of electrons trapped in closed magnetic configurations like loops. In the case of generation of *Langmuir oscillation*, this high frequency phenomenon involves mainly electrons because the ions are heavier and slower than electrons to follow this movement. The solution of the equation of motion for ambient electrons including the kinetic pressure is the Bohm-Gross dispersion relation

$$\omega^2 = \omega_p^2 + \frac{3}{2}k^2 V_{th}^2 \ , \tag{2.20}$$

where $V_{th}^2 = \frac{2kT}{m_e}$ and $\omega_p = 2\pi\nu_{pe}$ (with $\nu_{pe} \approx 9000\ n_e^{1/2}[\mathrm{cm}^{-3}]$) is the plasma frequency. The resulting waves are known as *Langmuir waves* and they are one of the most fundamental types of plasma waves.

2. **Partial conversion into fundamental radiation.** Plasma waves can interact with other waves through different processes and be converted in electromagnetic radiation (*transverse oscillations* are perpendicular to the direction of energy transfer). The resulting *transverse waves* have frequencies near the fundamental or the harmonic of the local electron plasma frequency (ν_{pe}). For every wave-wave interaction, either decay or coalescence, the corresponding conservation of momentum and energy must be fulfilled

$$\vec{p}_1 \pm \vec{p}_2 = \vec{p}_3 \quad \rightarrow \quad \omega_1(k) \pm \omega_2(k) = \omega_3(k), \tag{2.21}$$

where the subscripts 1 and 2 refer to the primary electrostatic waves and subscript 3 stands for the electromagnetic wave. Accordingly, for the fundamental plasma radiation two three-wave interactions (Among *Langmuir waves* (L), *ion acoustic waves* (S) and *transverse waves* (T)) have been considered [Melrose, 1987] by

$$\omega_{\mathrm{L}} + \omega_{\mathrm{S}} = \omega_{\mathrm{T}} \quad \rightarrow \text{coalescence} \tag{2.22}$$

$$\omega_{\mathrm{L}} = \omega_{\mathrm{S}} + \omega_{\mathrm{T}} \quad \rightarrow \text{decay} \tag{2.23}$$

4. **Generation of second-harmonic radiation.** It is well accepted that the origin of the second harmonic is the result of the coalescence of two *Langmuir waves* whose conservation laws give

$$\omega_{\mathrm{L}_1} + \omega_{\mathrm{L}_2} = \omega_{\mathrm{T}}, \tag{2.24}$$

$$\text{with} \ \ \omega_{\mathrm{L}_1} \approx \omega_{\mathrm{L}_2} \approx \omega_{\mathrm{L}} \quad \rightarrow \quad \omega_{\mathrm{T}} = 2\,\omega_{\mathrm{L}} \tag{2.25}$$

Figure 2.11 shows an example of a type II burst with the two slow drifting components: the fundamental and the harmonic emission. However, the presence of both components is not always observable. In some cases, electromagnetic waves could be absorbed in the solar corona by free-free absorption and do not reach the observer [Aschwanden,

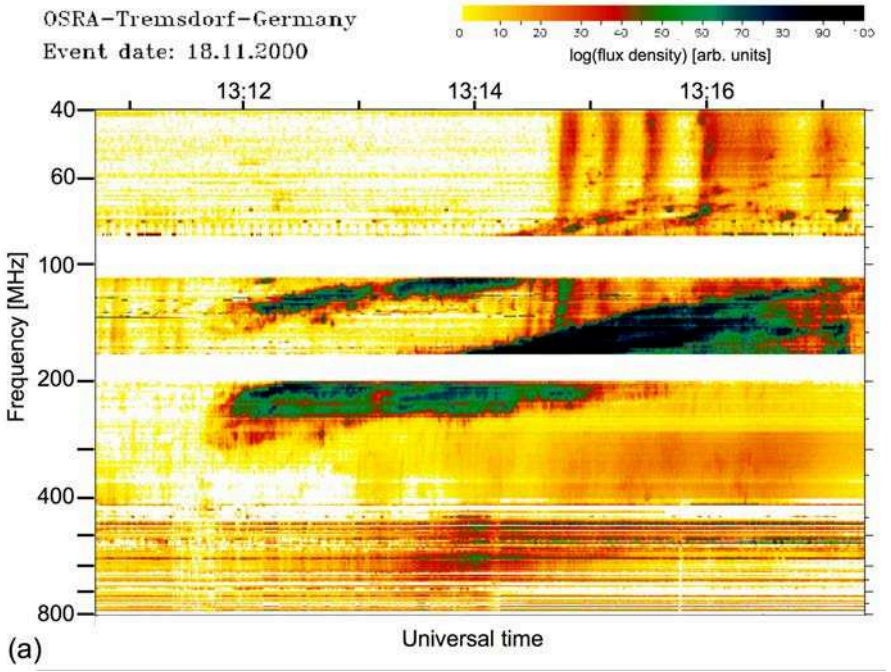

FIGURE 2.11: Typical type II burst spectrum showing two slow drifting bands, the fundamental and the harmonic. Adapted from Mann *et al.* [2003].

2004]. The fundamental can be absorbed more easily than the harmonic because the absorption is higher at the plasma frequency. Then, when only one band is observed in the dynamic spectrum, it is more probable to be the harmonic emission as the case in the spectrum studied for the event on 2008 April 26 in Figure 2.10.

Since the process of radio emission have been discussed, the spectral characteristics of type II, type III and type IV radio bursts are coming up next.

Type II Bursts

Coronal type II bursts are produced by shock waves travelling outward from high density regions [Wild, Smerd, and Weiss, 1963] which accelerate electrons in the corona. They are characterised by slowly drifting bands in the dynamic spectrum as observed in Figure 2.11, which appear often in pairs and are related to the fundamental and the harmonic plasma radiation. These bands differ in frequency by a factor of ≈ 2 (e.g. Cairns *et al.* [2003]) and are called *backbones*.

Additionally, in some cases type II bursts can exhibit a fine structure known as *herringbones* which are short bursts observed as having bidirectional fast frequency drifts from a common band (e.g. Carley *et al.* [2015], Roberts [1959]). Figure 2.13 shows both positive and negative signs of the drifts typical of herringbone emission.

Benz and Thejappa [1988] propose that *herringbone* bursts can arise from a loss-cone distribution of electrons confined below tangential field lines compressed by

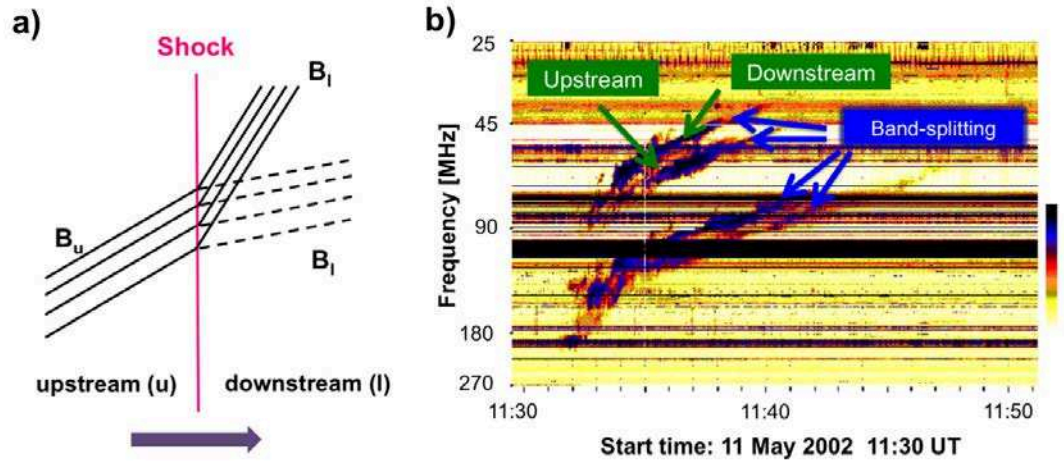

FIGURE 2.12: a) Sketch of a shock front (pink line). Both sides of the discontinuity, the upstream and downstream regions, are denoted by the subscripts u and l respectively. Magnetic field in both regions is represented by the black lines. The dashed and continuous lines in the downstream region represent the magnetic field associated with a fast shock and a slow shock respectively. b) Dynamic spectrum of a type II radio burst showing band-splitting structure in both fundamental and harmonic bands (blue arrows) associated to plasma emission from upstream and downstream shock regions (green arrows).

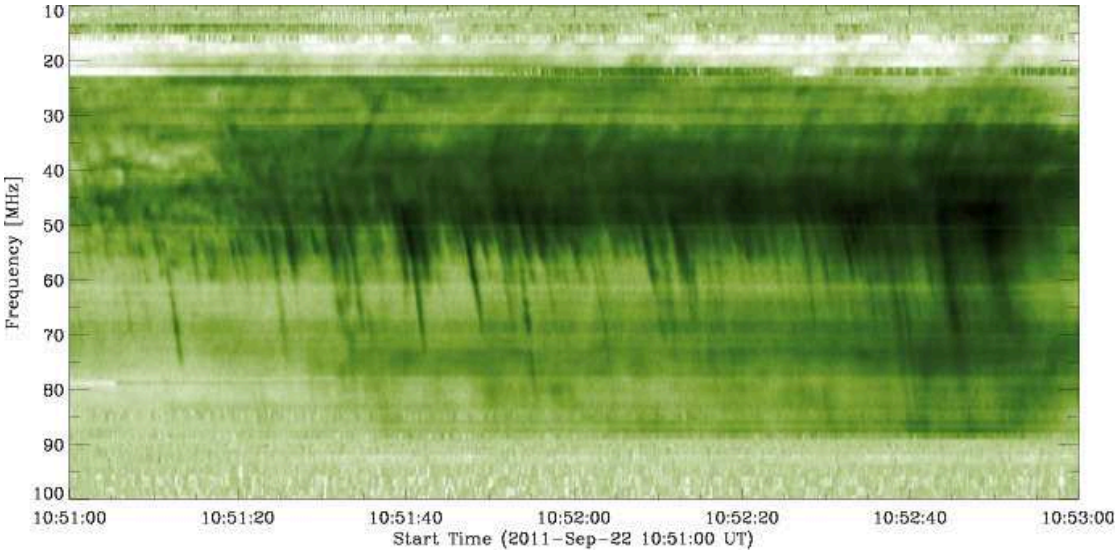

FIGURE 2.13: Dynamic spectrum of herringbones following a Type II radio burst. Spectrum by the Rosse Solar-Terrestrial Observatory (RSTO). Figure adapted from Zuccarello, Meliani, and Poedts [2012]

the shock front. Since both upward and downward drifts have a common start frequency, a common acceleration region can be identified. In this way, *herringbones* can be considered as a direct indicator of particle acceleration at the shock front [Cairns and Robinson, 1987, Cane and White, 1989, Carley *et al.*, 2015].

Another fine structure that can be observed associated to the *backbones* is the *band-splitting*. This is the splitting phenomenon of fundamental and harmonic bands of type II bursts into a pair of ridges [Roberts, 1959] as is shown in Figure 2.12.b. The band-splitting is mostly interpreted as revealing simultaneous emission from the upstream and downstream plasma [Smerd, Sheridan, and Stewart, 1974, Vršnak *et al.*, 2001]. The interpretation of band splitting in terms of simultaneous emission upstream and downstream of the shock was challenged on theoretical grounds [Cairns, 2011], and alternative ideas were developed [McLean, 1967, Sakai and Karlický, 2008, Treumann and LaBelle, 1992]. Schmidt and Cairns [2014] explain the band splitting in terms of different locations at the shock front. However, the fact that band-spliting is always observed in pairs and at the same time are arguments against this statement. On the other hand, Zimovets *et al.* [2012] and Zucca *et al.* [2014] presented two case studies where multi-frequency imaging showed the high-frequency split band to be slightly, but systematically, displaced inward with respect to the low-frequency split band, in agreement with the hypothesis of simultaneous emissions from the upstream and downstream region. Another major support of this interpretation is the finding that in type II bursts where the feature was observed in interplanetary space, the *in situ* density measurements upstream and downstream of the shock wave near 1 AU were indeed consistent with the Earthward extrapolation of the type II split bands [Vršnak, 2001]. Numerical simulations also show that shock-accelerated electrons may penetrate into the downstream region [Savoini *et al.*, 2005].

Type III Bursts

Type III bursts are observed in the dynamic spectrum as emissions with a fast drift of about 20 MHz s^{-1} [Kundu, 1965] produced by electrons streaming from the solar corona to the interplanetary space along open magnetic field lines. The type III bursts have been observed from frequencies of $\approx$ 1 GHz at the bottom of the corona to 30 kHz in the interplanetary medium at $\approx$ 1 AU. Information (such as density and height) of the background ambient plasma conditions where they are traveling through can be obtained from their signatures in the dynamic spectrum as the one shown in Figure 2.10. The detailed analysis of dynamic spectra is presented in Section 2.4.

Adopting a coronal (or interplanetary) density model, the speed of the excited electrons can be obtained by assuming they are traveling along the magnetic field

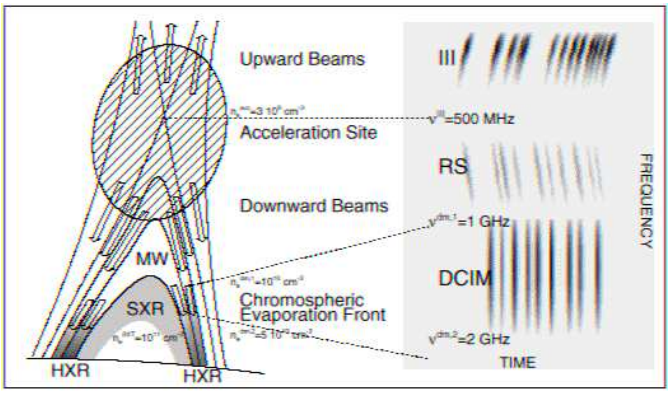

FIGURE 2.14: Diagram of magnetic topology in a basic flare model. The signatures of radio bursts associated to simultaneously detected upward and downward electron beams are illustrated on the right. Figure adapted from Aschwanden [2002]

lines. Generally, the electron beams which produce the type III bursts propagate with speeds from $\approx c/3$ in the solar corona to $\approx c/10$ [Poquérusse *et al.*, 1996]. Saint-Hilaire, Vilmer, and Kerdraon [2013] study solar radio bursts observed by NRH during 1998-2008 and find that the size of the source increases with decreasing frequency. They argue that this observational result could reflect the magnetic field opening as a function of heigh.

The electrons associated with type III bursts are usually accelerated via magnetic reconnection. However, Dulk *et al.* [2000] show that the electrons accelerated by shock drift (revealed by the type II bursts) can also propagate into the interplanetary space when they connect to open magnetic field lines, and are observed as type III bursts. Figure 2.11 shows an example of type III bursts observed coming from the *backbones* of the type II burst.

Magnetic reconnection mostly takes place in active regions and is related to the energy release during flares [e.g., Aschwanden, 2002]. In this scenario, the observation of pairs of oppositely drifting bursts (type III and reverse slope (RS)) are expected [Aschwanden, 2002]. These pairs of bursts that start simultaneously and at the same frequency reveal electrons accelerated upwards and downwards from the reconnection region as is shown in the diagram of Figure 2.14.

Even though type III bursts are often observed during the impulsive phase of flares, this is not always the case. Electrons accelerated via magnetic reconnection during flare process are expected not only be injected onto open magnetic field lines but also to be trapped in close magnetic configuration. If reconnection with the surroundings occurs, the accelerated electrons trapped can have access to open magnetic field lines (as is shown in Figure 2.15) which can also produce type III bursts. This scenario was envisaged by Schatten and Mullan [1977] and modeled by Masson, Antiochos, and DeVore [2013]. A clear distinction between the type

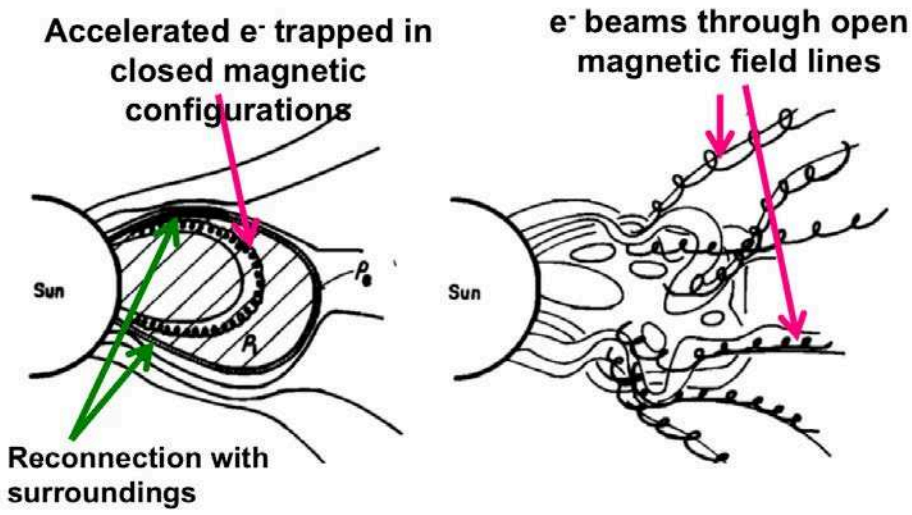

FIGURE 2.15: Cartoon showing the scenario for escaping electrons accelerated by reconnection during flares. The electors can escape trough open magnetic field lines (right panel) but the electrons trapped in closed magnetic structures (left panel) can escape only when they have access to open magnetic field lines when the loops expand and interact with surroundings. Figure adapted from Schatten and Mullan [1977]

III bursts produced by electrons from flares sites and the type III burst by the electrons that escape from a magnetic trap may not be possible.

Magnetic reconnection with the surroundings can also accelerate electrons at this reconnection site and not only as a way to give the access to escape. The type III burst in the event on 2008 April 26 was observed at an unusual time compared with the onset of the associated flare and also was located in isolation far from the flaring active region. From our study, we conclude that it could be related to the reconnection of the expanding magnetic structure of the CME with the surrounding field lines [Dasso *et al.*, 2006]. This observational result shows that type III bursts can also be produced by electrons accelerated elsewhere.

Type IV Bursts

These radio bursts are broadband (i.e. instantaneous band is comparable with the central frequency) emissions observed in the dynamic spectrum at metric and decimetric wavelengths as is shown in Figure 2.16. The first type IV burst was characterised by Boischot [1957] by using the Nançay interferometer observations at 167 MHz. These bursts generally are observed some minutes after the onset of a flare and since the flares are also related with type II bursts, some of type IV bursts can also be observed preceded by type II bursts [Weiss, 1963].

Type IV bursts are produced by electrons that emit via synchrotron radiation [e.g., Aurass *et al.*, 2003] or by electrons radiating via plasma emission [e.g., Gary *et al.*, 1985]. The distinction between both mechanisms is made by the characterisation

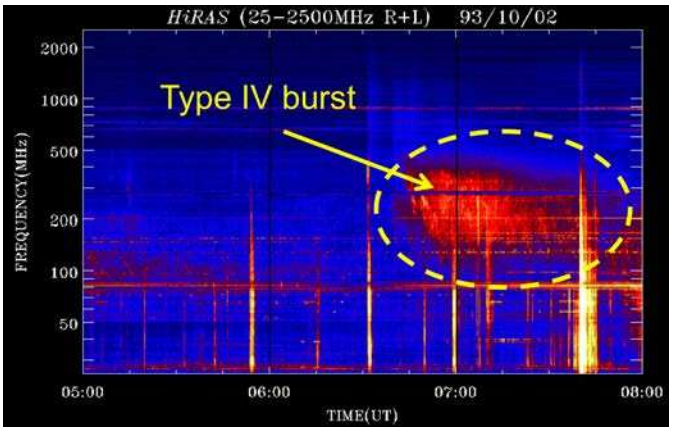

FIGURE 2.16: Dynamic spectrum by Hiraiso Radio Spectrograph showing a type IV burst in the broadband of 500-150 MHz.

of the polarisation and the brightness temperature of the source [e.g., Trottet *et al.*, 1981]. The detailed description of type IV bursts polarisation will be presented in Chapter 3.

The type IV bursts can be separated into *stationary* and *moving* type IV bursts according to their characteristics of height and movement of the source [Klein and Mouradian, 2002, McLean and Labrum, 1985, Pick, 1986, Stepanov, 1974, Weiss, 1963].

Stationary type IV bursts: These bursts are usually located close to active regions (e.g. post-flare loops). Figure 2.17 shows the *stationary* type IV burst observed on 2008 April 26. Radio imaging at 150 and 327 MHz by NRH (Fig. 2.17.b) shows little or no source movement at the location of the post-flare loops shown in the image at 150 MHz in Fig. 2.17.a.

Moving type IV bursts: These bursts are characterised by a short-duration, compared with the *stationary* type IV bursts, and an outward movement through the corona with velocities between 200 and 1500 km s^{-1} [Robinson, 1978]. *Moving* type IV bursts are observed at wavelengths $\geq$ m-λ and are often seen in association with CMEs. An example of *moving* type IV burst is shown in Figure 2.18. An outward moving source is observed in NRH images in Figure 2.18.a. This movement is also observed in the 1D NRH images (two bottom panels in Figure 2.18.b). Initially the source is located at a certain position and it moves eastwards as the time passes. The type IV burst is also observed in the dynamic spectra in the top panels as a continuum emission. This emission also shows a drift at low frequencies (20-80 MHz) which can be associated to the expansion of the magnetic structure that results either in a decrease of the density (if is plasma emission) or a decrease of the magnetic field strength (if is gyrosynchrotron emission).

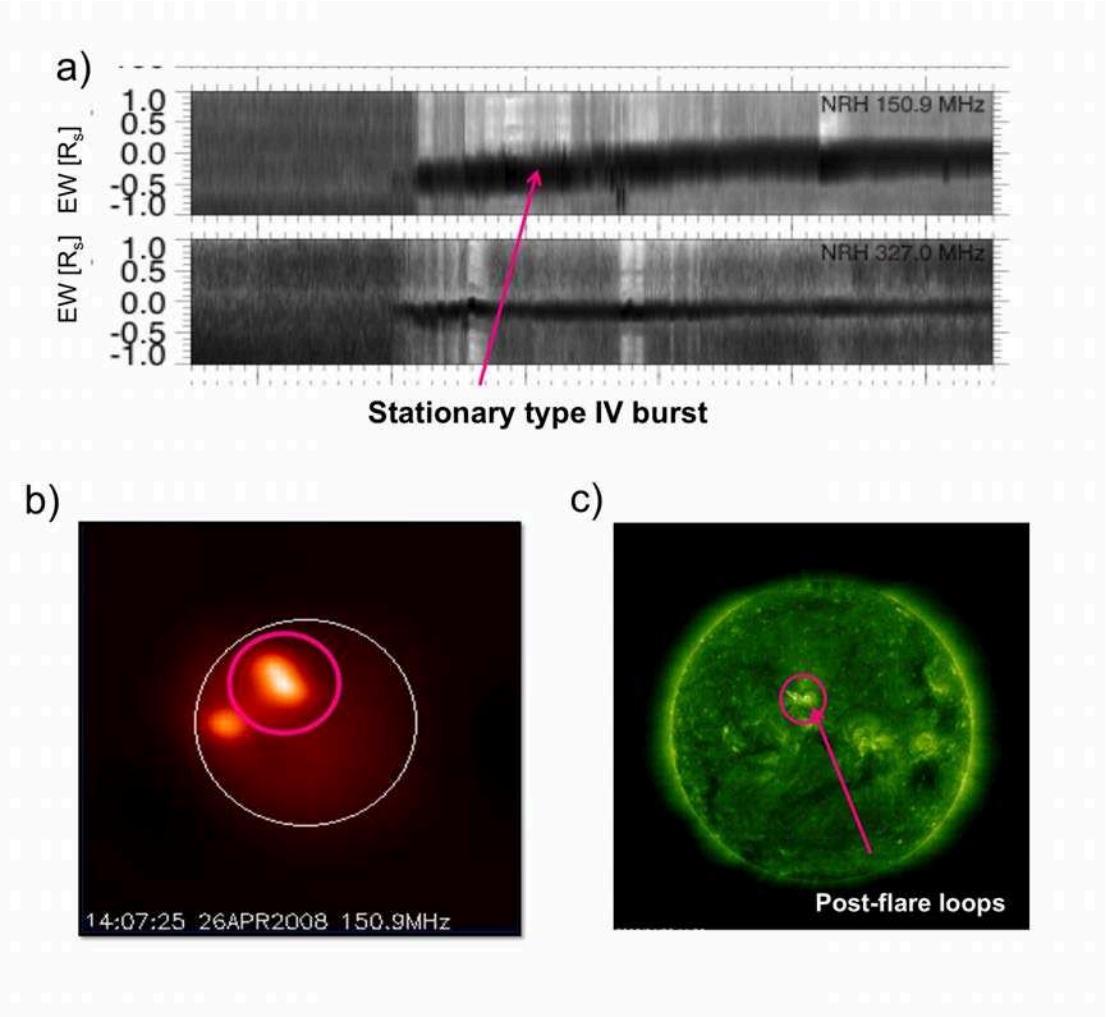

FIGURE 2.17: *Stationary* type IV burst on 208 April 26. a) 1D images projected onto the solar east-west direction at 150 and 327 MHz (y axis graded in solar radii from the eastern to the western limb). b) 2D image of the type IV burst at 150.9 MHz at the place where the post-flare loops are observed in the EIT image (c).

In summary, it is well known that type IV bursts together with all radio bursts described above are associated frequently with the release of coronal mass ejections. The understanding of these processes is an important tool for the study of the development of CMEs in the low corona because radio emission is the unique remote signature of non-thermal electrons in the corona and can be also compared with electrons detected in situ.

2.4 Density model, drift rates and shock parameters from the dynamic spectrum

In this section we focus on the estimation of parameters of the exciter of the type II and type III bursts from the dynamic spectrum.

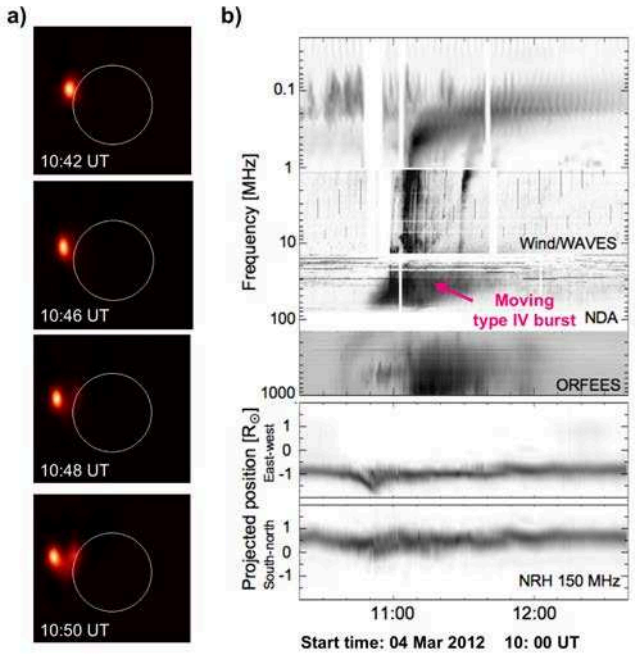

FIGURE 2.18: *Moving* type IV burst on 2012 March 04. a) Compilation of NRH images at 150 MHz showing a moving source. b) Multifrequency plot where the two bottom panels show 1D images projected onto the solar east-west and south-north directions at 150 MHz. The dynamic spectra shown in the four top panel present the signature of the *moving* type IV burst.

2.4.1 Density model

Since the emission mechanism is plasma emission, the plasma frequency ($\nu_{\rm pe}$) at the fundamental is directly associated with the electron density ($n_{\rm e}$) and the parameters of the exciter such as heights and speeds can be obtained by assuming a coronal density model. A coronal density model is basically a hydrostatic model which describes how the electron density of the coronal gas changes as a function of the altitude assuming a constant gravity throughout the corona.

The equation of hydrostatic equilibrium describes how the pressure (P) changes as a function of the distance (r)

$$\frac{{\rm d}P}{{\rm d}r} = -g(r)\rho, \tag{2.26}$$

where $g(r)$ and ρ are the gravity and the volume density respectively at certain r where the temperature (T) is assumed constant. Considering the fluid as an ideal gas, the equation of state relates T, ρ *and* P as

$$P = \frac{\rho}{\mu m_p}{\rm K}T. \tag{2.27}$$

We rewrite Equation 2.26 as

$$\frac{1}{\rho}\frac{\mathrm{d}\rho}{\mathrm{d}r} = \frac{\mathrm{d}(\ln\rho)}{\mathrm{d}r} = \frac{-g(r)\mu m_p}{\mathrm{K}T}, \tag{2.28}$$

whose solution is

$$\ln(\rho) = \frac{1}{H(r)}\ r\ +\ C, \tag{2.29}$$

where the scale height is defined by $H(r) = \frac{\mathrm{K}T}{g(r)\mu m_p}$. To find the integration constant C, we assume a known value for the density (ρ_0) at a reference height r_0 in the explicit form of Eq. 2.29

$$\ln\rho_0 = \frac{GM\mu m_p}{KT}\frac{1}{r_0} + C. \tag{2.30}$$

So, Equation 2.29 becomes

$$\ln(\frac{\rho}{\rho_0}) = \frac{GM\mu m_p}{KT}(\frac{1}{r} - \frac{1}{r_0}). \tag{2.31}$$

Expanding Equation 2.31 as Taylor series around a reference height r_0 we obtain

$$\ln(\frac{\rho}{\rho_0}) = \frac{-GM\mu m_p}{KT}(\frac{r-r_0}{r_0^2}) = \frac{-g_0\mu m_p}{KT}(r-r_0). \tag{2.32}$$

Thus, Equation 2.32 for the electron density (n_e) in the solar atmosphere becomes

$$n_e = n_e(r_0)\ \exp(\frac{-(r-r_0)}{H(r_0)}), \tag{2.33}$$

where $n_e(r_0)$ is the density at r_0 and $H(r_0)$ is the scale height given by

$$H(r_o) = (\frac{r_o}{R_\odot})^2 H(R_\odot) = \frac{\mathrm{K}T}{\mu m_p g_\odot}(\frac{r_o}{R_\odot})^2 = 50\cdot 10^6(\frac{r_o}{R_\odot})^2\frac{T}{1\ \mathrm{MK}}\ [\mathrm{m}], \tag{2.34}$$

where K, μ, m_p and $g_\odot$ are the Boltzmann constant, the mean molecular weight, the proton mass and the gravity at 1 $R_\odot$ respectively.

Some models for the solar atmosphere have been inferred from observations of white-light emission during solar eclipses as well. They are also based on the decrease of

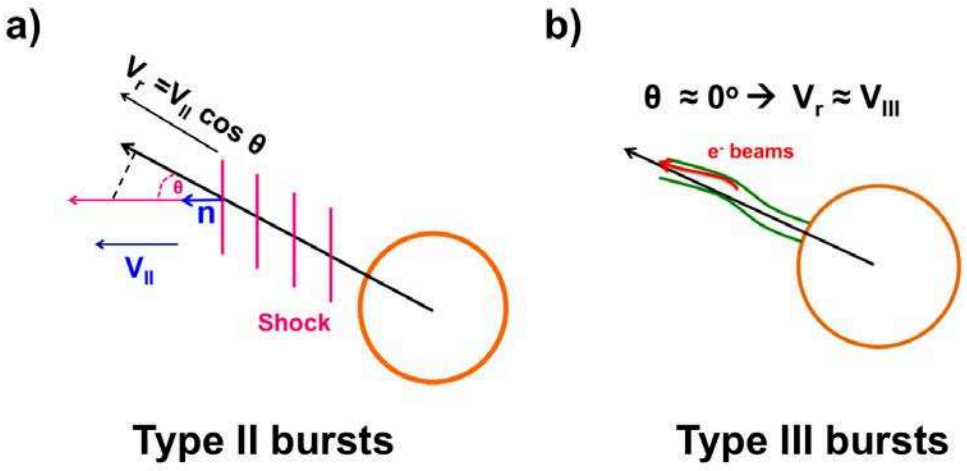

FIGURE 2.19: Schematic scenarios of a) a shock and b) electron beam propagation. The exciter travels at speed V_{II} along a direction that is inclined to the radial direction by an angle θ. For electron beams this θ is close to 0°.

electron density as the altitude increases. Among them, the most used are the models by Newkirk [1961] and Saito, Poland, and Munro [1977] which describe different types of solar atmospheres. The Newkirk [1961] model is an hydrostatic model which describes the density as a function of heliocentric distance by

$$N_e(r) = N_e(r_0) \times 10^{\frac{4.32}{R}}, \tag{2.35}$$

where R is the distance from the solar centre in units of solar radius and the temperature is found to be $1.4{\times}10^6$ K. This model is used to describe streamer regions and active regions while the model by Saito, Poland, and Munro [1977] is more used for equatorial regions in the corona.

2.4.2 Drift rate and exciter speed

The speed of the exciter associated with both type II and type III bursts can be estimated from the drift rate (Df=$\frac{\mathrm{d}}{\mathrm{dt}} \ln \nu$) of the emission in the spectrum. Since type II bursts are related with a shock moving outwards in a direction that is inclined to the radial direction by an angle θ as is shown in Figure 2.19.a, the exciter travels at speed V_{ex} along the same direction. Since the radiation is emitted at the plasma frequency and $\nu_{pe} \sim \sqrt{n_e}$, the Df can be expressed in terms of plasma density as

$$\mathrm{Df} = \frac{\mathrm{d}}{\mathrm{dt}} \ln \nu_{\mathrm{pe}} = \frac{\mathrm{d}}{\mathrm{dt}} \ln n_e^{\frac{1}{2}} = \frac{V_{rad}}{2} \frac{\mathrm{d}}{\mathrm{dr}} \ln n_e. \tag{2.36}$$

Using the electron density variation of Equation 2.33, we obtain

$$\frac{\mathrm{d}}{\mathrm{dr}} \ln(n_e(r_0)) = \frac{-1}{H(r_0)}, \tag{2.37}$$

and then, Equation 2.36 becomes

$$\mathrm{Df} = -\frac{V_{rad}}{2H(r_0)}, \tag{2.38}$$

where $V_{rad} = V_{\mathrm{ex}} \cos\theta$ is the speed of the exciter in the radial direction. So, the radial component of the excited speed at the height r_o inferred from the drift rate is

$$V_{rad} = V_{\mathrm{ex}} \cos\theta = -2H(r_0) \cdot \frac{d}{dt} \ln\nu. \tag{2.39}$$

On the other hand, since we cannot have an estimation of the θ in type III bursts, we do not obtain the real speed of the exciter but a lower limit of V_{rad} by applying the Equation 2.39 as

$$V_{\mathrm{rad}} = V_{\mathrm{III}} = -2H(r_0) \cdot \frac{\Delta \ln\nu}{\Delta t}. \tag{2.40}$$

Because of the calculation of the drift rate of type III bursts requires a higher cadence than the NDA instrument used in this work, the difference in time (Δt) cannot be measured but must be smaller than the integration time of the dynamic spectrum (2.5 sec in the NDA spectrum). Then, the radial speed of the type III burst exciter can be given by

$$V_{\mathrm{III}} = -2H(r_0) \cdot \frac{(\ln\nu_{\mathrm{end}} - \ln\nu_{\mathrm{st}})}{\Delta t}, \tag{2.41}$$

where ν_{end} and $\ln\nu_{\mathrm{st}}$ are the highest and the lowest frequencies of the type III burst in the dynamic spectrum.

2.4.3 Shock parameters

Shocks are large amplitude waves that propagate faster than the magneto-sonic speed (V_{ms}) of the ambient medium which is given by [e.g., Cravens, 1997]

$$V_{\mathrm{ms}} = (V_{\mathrm{A}}^2 + C_{\mathrm{S}}^2)^{1/2}\ , \tag{2.42}$$

where $V_{\rm A}$ and $C_{\rm S}$ are the Alfven and the sound speeds respectively. Since shocks are a type of MHD discontinuity, they must satisfy the Rankine-Hugoniot equations which are the fundamental MHD equations for the case of a plane surface of discontinuity across which there is a jump in the physical fields from both sides of the discontinuity [e.g., Burlaga, 1995]. Figure 2.12.a shows both sides of the discontinuity: upstream region (left, denoted by the subscript u) and downstream region (right, denoted by the subscript l). The dashed and solid lines in the downstream region refer to magnetic field associated with slow and fast shocks respectively. In this work we focus on fast shocks.

At the present, two kinds of shocks according to the driving agent associated with type II bursts are discussed: the shock is a *blast wave* or is a *piston-driven*. The *blast wave* is associated with a pressure pulse [Vršnak and Lulić, 2000] without mass motions driving the wave while the *piston-driven* shock implies mass motion (e.g. Vršnak and Cliver [2008]). The type II burst observe in the event studied in Salas-Matamoros, Klein, and Rouillard [2016] was interpreted as a shock on the expanding flank of the CME. This interpretation was developed based on its close timing respect to the type III burst. Because of both type II and type III bursts occur at the same time, we assume the location of the shock is close to the CME flank position which is near the type III burst source seen at 150.9 MHz. This inference is consistent with the speeds at the CME flank revealed by the modelling.

Also, in the study on 2008 April 26 event we assume the classical band-splitting interpretation for the upstream and downstream emissions to obtain the magnetic parameters of the associated shock. The frequency ratio of the split bands, $\chi = (\frac{\nu_{\rm u}}{\nu_{\rm l}})^2$, is related with the density compression ratio of the shock wave in the type II source by

$$\chi = \frac{n_{\rm u}}{n_{\rm l}}, \tag{2.43}$$

where 'u' and 'l' are the subscripts for the *upstream* and *downstream* shock regions respectively. Consequently, we can use the compression ratio to infer the Alfvénic and magneto sonic Mach numbers of the shock. Type II bursts are believed to be emitted at quasi-perpendicular shocks. We has shown that this is the case of the type II burst in Salas-Matamoros, Klein, and Rouillard [2016]. At the assumed location of the type II burst source on 2008 April 26 (the CME flank) the shock is found to be quasi-perpendicular. The general expression for the Alfvénic Mach number of a perpendicular shock can be obtained from Eq. 5.35 by [Priest, 1982]:

$$2(2-\gamma)\chi^2 + (2\beta + (\gamma-1)\beta M_A^2 + 2)\gamma\chi - \gamma(\gamma+1)\beta M_A^2 = 0. \tag{2.44}$$

If we assume a polytropic index $\gamma = \frac{5}{3}$, the Alfvénic Mach number can be obtained by

$$M_{\rm A} = (\frac{\chi}{2}\frac{5+5\beta+\chi}{4-\chi})^{1/2}. \tag{2.45}$$

Using the exciter speed $V_{\rm II}$, we can then calculate the Alfvén speed and the magnetic field strength upstream of the shock. The relationship between the plasma beta and the Alfvén and sound speeds is given by

$$\beta = \frac{2}{\gamma}(\frac{C_{\rm S}}{C_{\rm A_u}})^2, \tag{2.46}$$

where $C_{\rm A_u} = \frac{V_{\rm II}}{M_{\rm A}}$ is the upstream Alfvén speed. In addition, we can use the upstream Alfvén speed to infer the upstream magnetic field by applying

$$B_{\rm u} = (\mu_{\rm o}\rho_{\rm u}C_{\rm A_u})^{1/2}, \tag{2.47}$$

where $\mu_{\rm o}$ and $\rho_{\rm u}$ are the magnetic permeability and the volume density respectively.

During the STEREO era, multi-spacecraft and stereoscopic modelling have been developed to obtain the CME parameters. In Chapter 4 we describe the new technique developed by Rouillard *et al.* [2016] to derive the properties of the 3D expansion of pressure fronts forming in the corona during eruptive events. The 3D evolution of CMEs obtained by this technique can be used to infer parameters of shocks. The combination of this technique and parameters obtained from the dynamic spectrum was used for the event on 2008 April 26 which involves a type II and type III bursts occurred both after the flare peak.

We were able to obtain r_0 and θ from the comparison of the modelled pressure front with the spectral observations parameters, by assuming the location for both type II and type III burst sources at the same region at different altitudes. This implies two different regions of electron acceleration in the solar corona.

We were also able to obtain the M_A by using the values of r_0 and θ. The typical M_A of the type II shock as inferred from the hypothesis of simultaneous emission upstream and downstream of the shock front ranges between about 1.5 and 2.8 for a quasi-perpendicular shock [Kouloumvakos *et al.*, 2014, Mancuso and Garzelli, 2013, Mann, Classen, and Aurass, 1995, Vasanth *et al.*, 2014, Vršnak *et al.*, 2002, Zucca *et al.*, 2014]. Similar Mach numbers were derived from white-light observations [Bemporad and Mancuso, 2010, 2011]. From the combination of spectral observations and 3-D modelling, the

Mach number associated to the type II burst of the event on 2008 April 26 was found to be $M_A \approx 1.9$, which is comparable with these values found in the literature.

2.5 Study of CME-related particle acceleration regions during a simple eruptive event near solar minimum (paper)

A&A 590, A135 (2016)
DOI: 10.1051/0004-6361/201528015

Astronomy & Astrophysics

Coronal mass ejection-related particle acceleration regions during a simple eruptive event

Carolina Salas-Matamoros[1,5], Karl-Ludwig Klein[1,2], and Alexis P. Rouillard[3,4]

[1] LESIA-UMR 8109 – Observatoire de Paris, PSL Research. Univ., CNRS, Univ. P & M Curie and Paris-Diderot, 92190 Meudon, France
e-mail: carolina.salas@obspm.fr
[2] Station de radioastronomie – Observatoire de Paris, PSL Research Univ., CNRS, University Orléans, OSUC, 18330 Nançay, France
[3] Institut de Recherche en Astrophysique et Planétologie, Université de Toulouse (UPS), 31028 Toulouse Cedex 4, France
[4] Centre National de la Recherche Scientifique, UMR 5277, 31300 Toulouse, France
[5] Space Research Center, University of Costa Rica, 2060 San Jose, Costa Rica

Received 20 December 2015 / Accepted 23 March 2016

ABSTRACT

An intriguing feature of many solar energetic particle (SEP) events is the detection of particles over a very extended range of longitudes in the heliosphere. This may be due to peculiarities of the magnetic field in the corona, to a broad accelerator, to cross-field transport of the particles, or to a combination of these processes. The eruptive flare on 26 April 2008 provided an opportunity to study relevant processes under particularly favourable conditions since it occurred in a very quiet solar and interplanetary environment. This enabled us to investigate the physical link between a single well-identified coronal mass ejection (CME), electron acceleration as traced by radio emission, and the production of SEPs. We conduct a detailed analysis, which combines radio observations (Nançay Radio Heliograph and Nançay Decametre Array, Wind/Waves spectrograph) with remote-sensing observations of the corona in extreme ultraviolet (EUV) and white light, as well as in situ measurements of energetic particles near 1AU (SoHO and STEREO spacecraft). By combining images taken from multiple vantage points, we were able to derive the time-dependent evolution of the 3D pressure front that was developing around the erupting CME. Magnetic reconnection in the post-CME current sheet accelerated electrons, which remained confined in closed magnetic fields in the corona, while the acceleration of escaping particles can be attributed to the pressure front ahead of the expanding CME. The CME accelerated electrons remotely from the parent active region, owing to the interaction of its laterally expanding flank, which was traced by an EUV wave, with the ambient corona. SEPs detected at one STEREO spacecraft and SoHO were accelerated later, when the frontal shock of the CME intercepted the spacecraft-connected interplanetary magnetic field line. The injection regions into the heliosphere inferred from the radio and SEP observations are separated in longitude by about 140°. The observations for this event show that it is misleading to interpret multi-spacecraft SEP measurements in terms of one acceleration region in the corona. The different acceleration regions are linked to different vantage points in the interplanetary space.

Key words. acceleration of particles – Sun: coronal mass ejections (CMEs) – Sun: particle emission – Sun: radio radiation – solar-terrestrial relations – Sun: flares

1. Introduction

A correct theory of the acceleration and subsequent transport of solar energetic particles (SEPs) in the heliosphere must explain the wide range of heliolongitudes over which a given SEP event can be detected in the inner heliosphere. While this fact was known before (Wibberenz & Cane 2006), the comprehensive imaging and in situ measurements taken by the Solar Terrestrial Relations Observatory (STEREO) mission have demonstrated that the release of energetic particles over a very broad range of longitudes is neither an exceptional fact nor is it restricted to particularly strong events (Wiedenbeck et al. 2010; Dresing et al. 2012, 2014; Lario et al. 2013; Gómez-Herrero et al. 2015). Besides interplanetary transport across field lines (Dröge et al. 2014) or the expansion of open magnetic field lines in the corona (Klein et al. 2008), a spatially extended accelerator is often considered. For instance, the shock produced by the high-speed expansion of a fast coronal mass ejection (CME) can accelerate particles to high energies (Zank et al. 2000; Lee 2005; Afanasiev et al. 2015). The prime evidence of the existence of these shocks in the corona are type II radio bursts (Smerd et al. 1962; Nelson & Melrose 1985; Mann et al. 1995; Nindos et al. 2008). Extreme ultraviolet (EUV) and white-light imaging can be used to track the effect of the strong pressure fronts, which disrupt the low (e.g., EUV waves) and upper corona during the formation and eruption of CMEs (see, for example, the recent review by Warmuth 2015). The CME shock is a convenient explanation of why SEPs are detected at spacecraft that are poorly connected with the solar active region where the activity originates (Torsti et al. 1999; Krucker et al. 1999; Rouillard et al. 2012; Park et al. 2015). When EUV waves alone are considered, however, the onset time of SEPs measured near 1AU cannot always be explained by the spatio-temporal evolution of the wave (Miteva et al. 2014).

In this work, we use non-thermal radio emissions as tracers of electron acceleration and transport during the eruption of a CME on 26 April 2008, during otherwise very quiet solar conditions in the deep solar minimum between cycles 23 and 24. This enables a study that does not suffer from coincidental associations of phenomena related with different events that happen at

the same time. To map the plasma environment of the CME and its parent active region, we use EUV imaging and white-light coronagraphy from the STEREO and SoHO spacecraft, and advanced techniques of detailed modeling based on complementary sets of remote-sensing observations (Rouillard et al. 2016).

An overview of the event is given in Sect. 2, followed by a detailed description of the imaging and spectrographic observations of the radio emission (Sect. 3). The radio emission consisted of a broadband continuum from trapped electrons above the parent active region, and electron beams and a shock wave at remote locations. The connection between the regions is provided by an EUV wave. Its relation to the remote radio bursts is described in Sect. 4. SEPs were seen by one of the STEREO spacecraft and by SoHO (Sect. 5). The multi-spacecraft CME observations are modelled in Sect. 6, and used in a comparison with the radio imaging and spectrography to establish the relationship with the type III and type II bursts, and to derive parameters of the type II shock. A qualitative discussion of the most plausible mechanisms for particle acceleration during the development of this event is given in Sect. 7.

2. Overview of the event on 26 April 2008

On 26 April 2008, during the minimum of solar cycle 24, the Large Angle and Spectrometric Coronagraph experiment (LASCO; Brueckner et al., 1995) of the Solar and Heliospheric Observatory (SoHO) recorded a CME at 14:30 UT. This CME was associated with a weak B 3.8 soft X-ray (SXR) burst that occurred in an unnumbered spotless active region at N10°E10°. The STEREO spacecraft were located at 14° east (STEREO B – henceforth STB), and 35° west (STEREO A – STA), from the active region. The EUV imagers on board the SoHO (Delaboudinière et al. 1995) and STEREO (Wuelser et al. 2004) spacecraft observed the initial development of the event. The CME appeared some time later as a halo CME in coronagraphic images from STB and as an east limb event in STA images. Using a reconstruction technique, Wood & Howard (2009) interpreted the white-light images of the CME as a flux rope driving a bright shock.

The formation and evolution of the flux rope were studied by Huang et al. (2011), Temmer et al. (2011), and Cheng et al. (2012). Huang et al. (2011) argue that the formation of the flux rope could be traced by radio and EUV observations. The flux rope expanded and erupted leaving two footprints in the low corona imaged as two EUV dimmings on either side of the active region, where an arcade of loops formed. Temmer et al. (2011) describe in detail the propagation of the EUV waves away from the dimming.

The observations of the CME by the Sun-Earth Connection Coronal and Heliospheric Investigation (SECCHI) telescopes aboard STEREO permitted reconstructions of the CME structure and kinematics in and beyond the COR-2 field of view, above about 10 $R_\odot$ (Wood & Howard 2009; Thernisien et al. 2009; Temmer et al. 2011). From their 3D reconstruction, using the coronographs on board STEREO spacecraft, Wood & Howard (2009) find an average CME velocity of 676 km s^{-1}, while Thernisien et al. (2009) find 741 km $^{-1}$. The studies cited above make no attempt to reconstruct the morphology of the solar eruptive event in the EUV field of view. Such a reconstruction is presented in this paper, in combination with the coronographs.

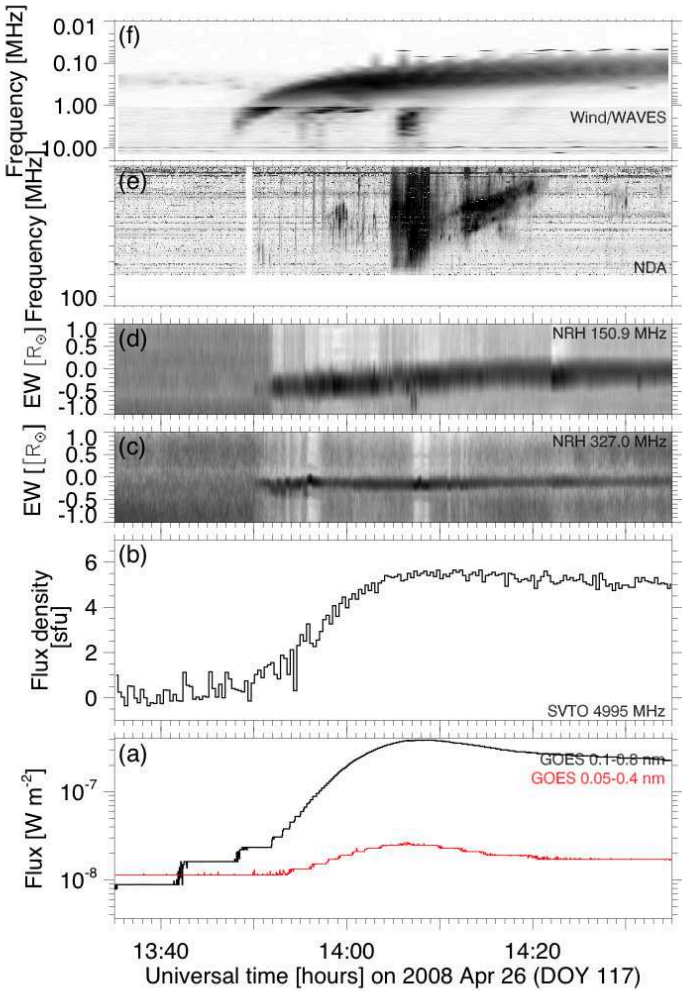

Fig. 1. Time series of the soft X-ray and radio emissions: **a)** soft X-ray profile; **b)** microwave profile at 5 GHz; **c)**, **d)** 1D images projected onto the solar east-west direction at 150 and 327 MHz (y axis graded in solar radii from the eastern to the western limb); **e)**, **f)** dynamic spectra between 70 MHz and 10 kHz.

3. Time evolution of the SXR and radio emission

3.1. Overview

The multifrequency plot in Fig. 1 provides a complete visualization of the event. The soft X-ray burst observed by the Geosynchronous Operational Environmental Satellites (GOES; NOAA) in the bottom panel starts at 13:50 UT and peaks at 14:08 UT. The smooth microwave profile at 5 GHz in Fig. 1b is similar to the soft X-rays. The usual gyrosynchrotron emission that reveals mildly relativistic electrons in the low corona during flares is lacking, which suggests that there was no substantial electron acceleration to energies above 100 keV in the flaring active region.

The two central panels, Figs. 1c and d, show the space-time imaging by the Nançay Radio Heliograph (NRH; Kerdraon & Delouis 1997) at 150.9 and 327 MHz, respectively. 1D brightness scans as a function of the east-west position on the Sun are calculated from images integrated over 10 s. The 1D scans are then scaled to show both weak and strong emissions. They are stacked and plotted as a grayscale image with time on the abscissa and the position on the solar east-west axis on the ordinate. The position is given in multiples of the solar radius, from the east limb (−1) to the west limb (+1). The gray surface before 13:50 UT shows the quiet corona. A broadband emission

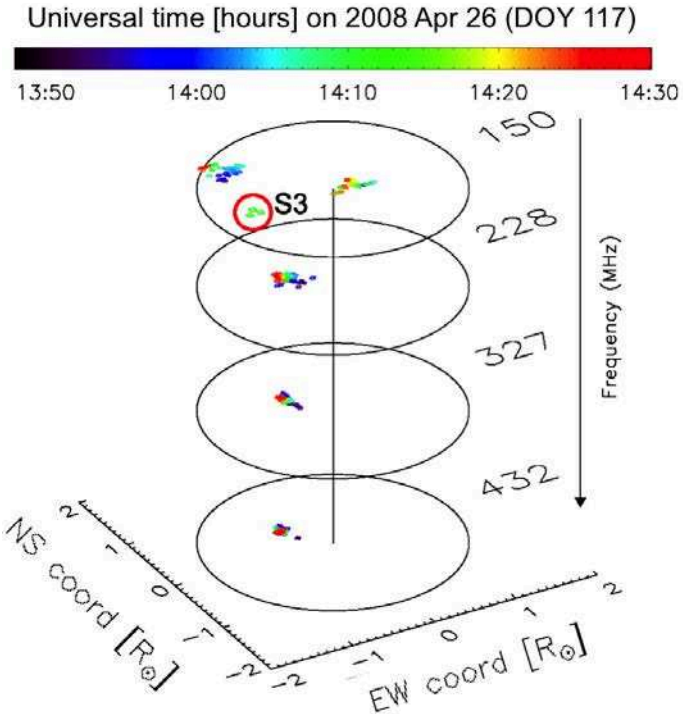

Fig. 2. 4D multifrequency plot showing the time evolution of the peak position in each image of the NRH at four frequencies. Time is represented by the color of the plot symbol, as indicated in the color bar at the top. The positions of the type III bursts (S3) near 14:07 UT at 150.9 MHz are enclosed in the red circle

(type IV burst) starts shortly after the SXR onset, and persists until the end of the observation (15:18 UT). This emission is detected at both frequencies. This source is located in the eastern hemisphere and presents an apparent movement westwards at 150.9 MHz until around 14:30 UT when it becomes more stationary, with only a slight movement at 327 MHz. A different source, located to the east of the type IV burst, appears around 14:06:30 UT at 150.9 MHz.

Figure 2 shows how the position of the brightest pixel evolves in the course of time at four frequencies. The color of the plotted points denotes the time as indicated in the color bar at the top. The figure shows that the type IV source at the higher frequencies (228, 327, 432 MHz) behaved differently from 150.9 MHz: at the higher frequencies the source appeared simple, with a slight north-eastward motion during the burst. At 150.9 MHz, three distinct sources were seen: two appeared throughout the burst, both north-eastwards and south-westwards of the source at higher frequencies. As discussed by Huang et al. (2011), the type IV sources outline the expansion of a flux rope at 150.9 MHz and emissions related to the current sheet below the flux rope at higher frequencies. Also, Fig. 2 shows the distinct locations of the bursts near 14:07 UT at 150.9 MHz (S3, enclosed in the red circle). The green diamonds mark the positions of three successive peaks in NRH data using a cadence of 1 s.

The dynamic spectrum observed by the Nançay Decametre Array (NDA; Lecacheux 2000) at long metre-waves (20−80 MHz) in Fig. 1e, shows few faint type III bursts that extend down to at least 20 MHz (13:50−13:58 UT) followed by bursts that show a clear low-frequency cut-of, which was observed between 13:58 and 14:02 UT. The most prominent features in the spectrum are a group of broadband bursts between 14:04 and 14:09 UT and a type II burst, which starts during or immediately after this group and lasts until 14:21 UT. These two radio features will be discussed in the following sections. The WIND/Waves instrument (Bougeret et al. 1995) detects three interplanetary type III burst groups at low frequencies (see Fig. 1f). The first starts before 13:50 UT, which is before the type IV burst, at the start of the SXR and microwave bursts. Subsequently, two weak bursts accompany the faint type III bursts observed by NDA. A strong type III burst is associated with the bright broadband emission (14:04−14:09 UT) in the 20−80 MHz range. Because of the similar timing, we assume that these spectral features are the low-frequency counterpart of the radio source S3 detected far from the eruptive active region in the NRH images.

The type IV emission suggests that electrons are accelerated in the post-CME current sheet up to some keV or some tens of keV. The exact energies of electrons producing the broadband plasma emission are not known. While some electrons escape to the high corona and the interplanetary space in the early phase of the type IV burst (faint type III bursts between 13:50 and 13:58 UT), others are injected into closed expanding magnetic structures, emitting the bursts with the drifting low-frequency cut-off between 13:58 and 14:02 UT. Unusual features are the broadband and type II bursts seen by NDA, because they occur late during the event, 15 min after the start of the type IV burst, and because the source of the broadband bursts seems to be far from the eruptive active region.

3.2. Remote type III burst

The differential spectrum of Fig. 3c reveals that the bright 20−80 MHz emission between 14:04 and 14:09 UT is a group of type III bursts. We can identify individual bursts that start at about 70 MHz and continue beyond 20 MHz. The burst group is time-related with the 150.9 MHz source S3 in Fig. 2. On the low frequency side the source is accompanied by type III bursts observed by WIND/Waves (Figs. 1e and f).

The spinning of the Wind spacecraft can, in principle, be used to infer the direction of radio emission arrival (Reiner 2001). This direction finding technique can be applied in the low-frequency channel RAD1, at frequencies below 1.075 MHz. Until 14:00 UT, the direction finding observations (courtesy S.Hoang) show an azimuth at 1.04 MHz slightly east of central meridian (fluctuating around 2°) and an elevation north of the ecliptic, with a broad scatter around an average of 4°. The type III burst, observed between about 14:06 and 14:12, is clearly seen above the decaying flux density at 1.04 MHz, but with less and less contrast as the frequency decreases. At 548 kHz it is hidden in the decaying flux of the previous bursts. This burst is the low-frequency counterpart of the strong type III group seen by NDA and of the burst at 150.9 MHz that was observed by NRH (S3, Fig. 2). At the time of this burst, the direction finding at 1.04 MHz shows a peak at about 6° azimuth, east of the previous type III bursts. As expected, no distinct position can be identified at lower frequencies, given the low contrast of the burst.

The direction finding observations by Wind/Waves are consistent with the location S3 of the bursts at 150.9 MHz: both show radio emissions from sources that are well to the east of the earlier emission, which is related to the flaring active region. The temporal association with the type III bursts observed by NDA thus suggests that the 150 MHz emission of source S3 is also produced by electron beams which propagate outward, or else by downward-propagating electron beams. A third possibility are metric spikes, which are often found near

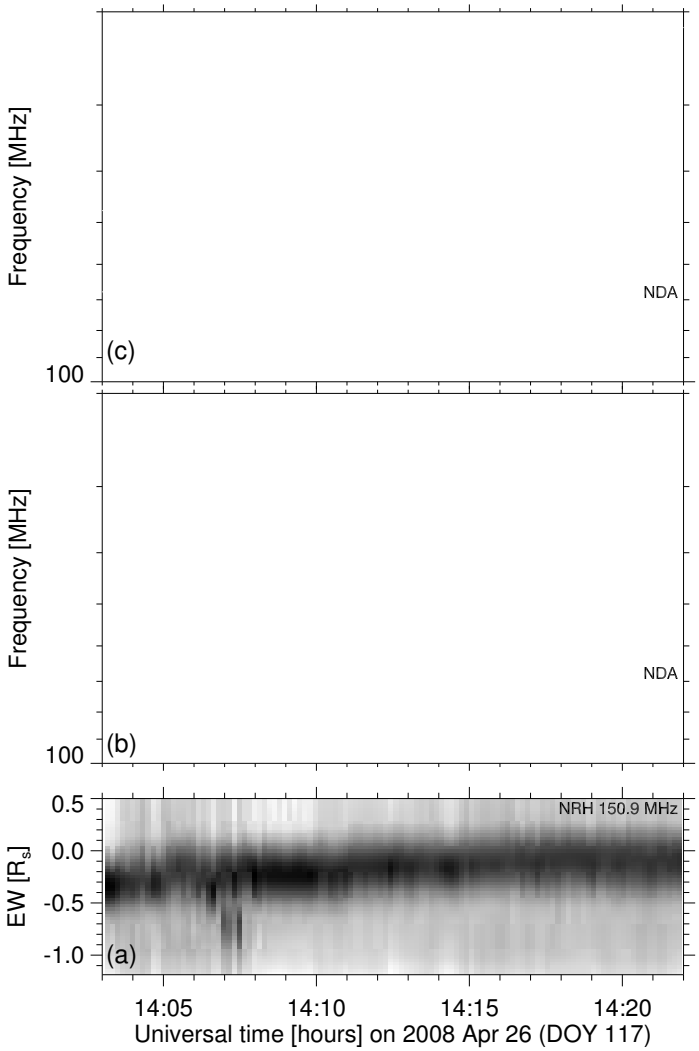

Fig. 3. Time history of the metre-wave radio emission during the late type III and type II bursts: **a)** 1D images projected onto the solar east-west direction at 150 MHz (y-axis graded in solar radii from the eastern to the western limb) showing a continuum emission and a sporadic source on its eastern side at around 14:07 UT, **b)** dynamic spectrum between 70 and 20 MHz and **c)** time-difference spectrum of **b)**. The dashed lines are fits of the upper and lower borders of the type II burst in **b)**.

the starting frequencies of type III bursts (Paesold et al. 2001). We cannot differentiate between these possibilities, because we have no detailed spectrum around 150 MHz. But in all cases the acceleration region in the corona is near S3. The relation between this electron acceleration and the eruptive activity will be discussed in the following sections.

3.3. Type II burst

The type II burst (14:10−14:21 UT) follows the group of type III bursts. The dynamic spectrum in Fig. 3b shows a regular drift, which suggests that the exciter travels along a smooth density gradient. The exciter of a type II burst is considered to be a region of a shock wave where electrons that are able to produce radio emission via plasma instabilities are accelerated (Holman & Pesses 1983). We determined the drift rate of the low-frequency ($\nu_{\rm LF}$) and high-frequency ($\nu_{\rm HF}$) borders by identifying ten points in each band with the cursor between 14:10 and 14:19 UT, and fit straight lines in the time-log(frequency) plane, minimizing the absolute deviation. The drift rate of the low-frequency band of the type II burst is $\frac{\rm d}{{\rm d}t}\ln\nu = -7.0\times10^{-4}$ s^{-1}, and of the high-frequency band -7.4×10^{-4} s^{-1}. The uncertainty of the drift rate is about 10%, if we assume an uncertainty of 5% of the cut-off frequencies inferred visually from the dynamic spectrogram. The dashed white lines overplotted on the differential dynamic spectrum in Fig. 3c are the fits in the time-log(frequency) plane.

To transform the frequency drift into the propagation speed of the exciter, we consider an isothermal hydrostatic density distribution with scale height $H(r_o)$ developed around the height r_o, which corresponds to the central frequency of the type II burst, $\nu_o = 30$ MHz. If the exciter travels at speed $V_{\rm II}$ along a direction that is inclined to the radial direction by an angle θ, the drift of the logarithm of the frequency ν is

$$\frac{\rm d}{{\rm d}t}\ln\nu = -\frac{V_{\rm II}\cos\theta}{2H(r_o)}. \quad (1)$$

In the isothermal hydrostatic model,

$$H(r_o) = \left(\frac{r_o}{R_\odot}\right)^2 H(R_\odot) = 50\times10^6\left(\frac{r_o}{R_\odot}\right)^2\frac{T}{1\ {\rm MK}}\ [{\rm m}]. \quad (2)$$

So, for a temperature $T = 1.5$ MK the radial speed of the exciter at the height r_o inferred from the drift of the low-frequency type II band is

$$V_{\rm rad} = V_{\rm II}\cdot\cos\theta = 105\cdot\left(\frac{r_o}{R_\odot}\right)^2\ [{\rm km\ s^{-1}}]. \quad (3)$$

The uncertainties from the fit of the type II drift rate formally carry over to an uncertainty of about 10% in all speed estimates. Using the fitted values of the upper and lower frequency limits of the type II burst, we find that the frequency ratio is on average 1.39, and that the relative bandwidth is on average 0.32 with a statistical uncertainty of ±0.01 of both values.

4. Magnetic configuration and EUV-wave observations

The PFSS extrapolation of Schrijver & De Rosa (2003) based on SoHO/MDI magnetic field measurements of the entire solar disk shows closed magnetic structures in a wide region around the flaring active region. Only the open field lines are plotted in Fig. 4a. The type III burst sources S3 at 150.9 MHz were found in the red square. They project onto open magnetic field lines at the south-eastern border of the large region with closed fields around the flare site. These open field lines correspond to a narrow coronal hole seen in EUV images (SoHO/EIT) and in NRH Earth-rotation synthesis images (C. Mercier, priv. comm.).

From the 3D coordinates of the open PFSS magnetic field lines through the square, the radial distance of the type III burst source at 150.9 MHz is found to be 1.7 $R_\odot$. This heliocentric distance is very high compared to usual estimates of type III burst source heights at 150 MHz (Saint-Hilaire et al. 2013), and appears especially high in the present event where the magnetic field configuration is far from the active region. A possible explanation is that the open magnetic field lines are affected by the impinging CME, as will be discussed below. The above value should not be considered as the real altitude of the source S3.

The two open PFSS lines through the type III source plotted in Fig. 4b are connected to the source surface at longitudes E69°

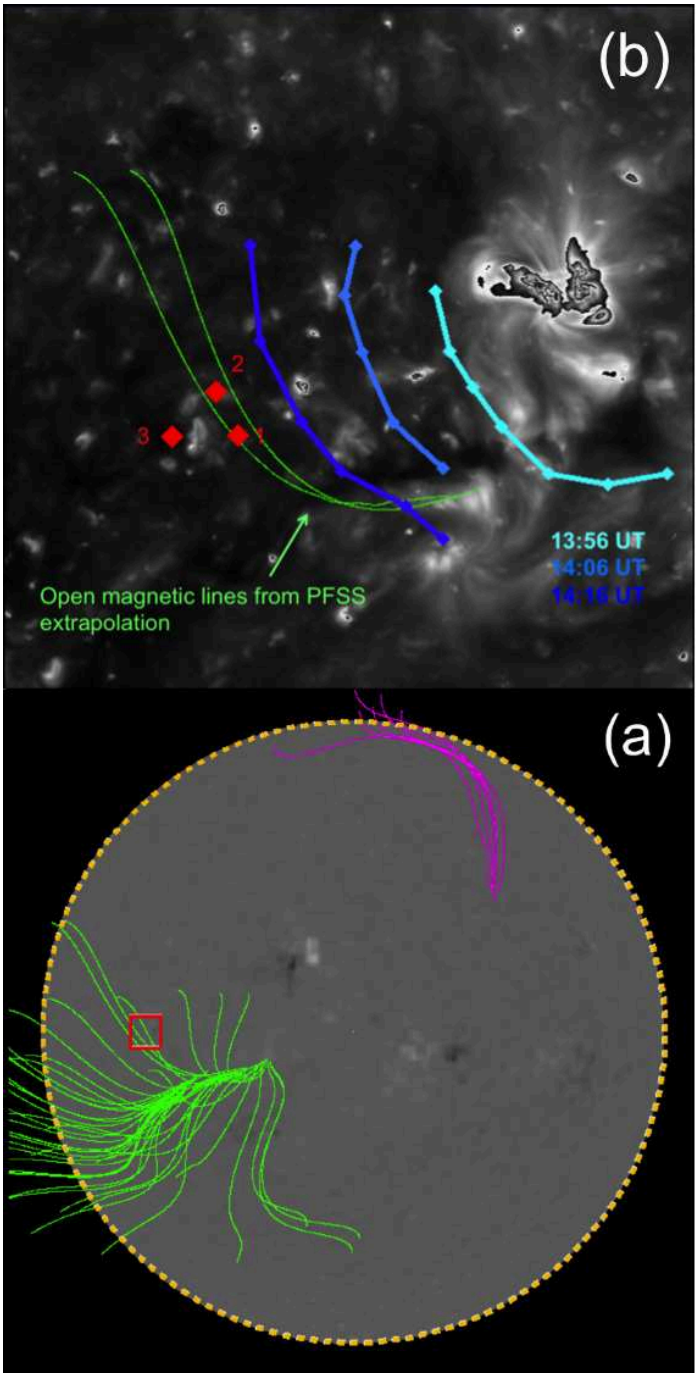

Fig. 4. a): Source region of the type III bursts (red square) over the open magnetic field lines (in green) inferred using the PFSS extrapolation model by Schrijver & De Rosa (2003). **b)**: Superposition of two open magnetic field lines (in green) close to the positions of three successive individual type III bursts (red diamonds) on the 19.5 nm EUVI synoptic map from STEREO B. The blue lines outline the EUVI wave front at different times: 13:56, 14:06 (near the time of the type III burst), and 14:16 UT.

and E77°. The interplanetary Parker spirals rooted there are plotted as dashed curves in Fig. 5. They were computed using a solar angular speed of 1.664×10^{-4} ° s^{-1} (rotation period 25.3 days) and an average solar wind speed of 420 km s^{-1}. The direction to the interplanetary type III burst measured by WIND/Waves is plotted by the solid line in Fig. 5. This line crosses the Parker spiral field lines at a heliocentric distance of around 19 $R_\odot$. The comparison with the locations of the STEREO, SoHO, and Wind

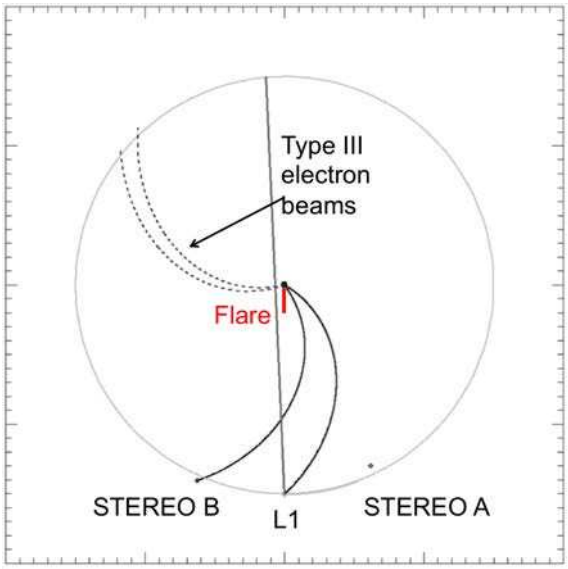

Fig. 5. Schematic configuration of the three spacecraft positions: L1 (SoHO and WIND), STEREO A, and STEREO B. The curved lines correspond to the Parker spiral connecting the source surface to STEREO B and to Earth. The dashed lines represent the Parker spirals connected at the source surface (2.5 $R_\odot$) to the open magnetic field lines through the type III source at 150 MHz. The solid line shows the line of sight from the Wind/Waves experiment to the type III burst source at 1.04 MHz.

spacecraft in Fig. 5 shows that the electron beams accelerated near source S3 are released onto interplanetary field lines, which are not connected to any spacecraft.

The acceleration of these electrons far from the active region requires an alternative accelerator to the flare process. An EUV wave observed by STEREO/EUVI is a possible candidate. The lateral expansion of the EUV wave was tracked. Its front is traced at three different times by light and dark blue lines in Fig. 4b. The propagation speed along the solar surface is found to be 207 km s^{-1}. The central (medium blue) line shows the wave front as measured at 14:06 UT. This observation implies that the CME flank reaches the footpoints of the open magnetic field lines through the radio source S3 near the time when the type III bursts appear. This is evidence that the interaction of the EUV wave with the open magnetic field lines triggered the acceleration of the electron beams that caused the type III bursts far from the flaring active region.

5. Solar energetic particles

The Solar Electron and Proton Telescope (SEPT; Müller-Mellin et al. 2008) aboard STB detected a tiny electron event in close time relationship with the eruption. Figure 6b shows that the intensity of electrons streaming away from the Sun starts to rise near 14:00 UT, peaks around 16:00 UT, and then decays until 18:00 UT, when a new rise starts. Even though this weak peak is time-related with the eruption, a similar peak was observed near 06:00 UT without an associated flare. This casts doubt on the association of the enhancement between 14 and 16 UT with the eruptive flare.

The radio observations suggest that some electrons might escape from the type IV source region. This is consistent with the weak electron event. The electrons from S3 have no magnetic connection through the nominal Parker spiral with STB (Fig. 5). An association between the electron intensity enhancement seen at STB with this type III burst is hence not plausible.

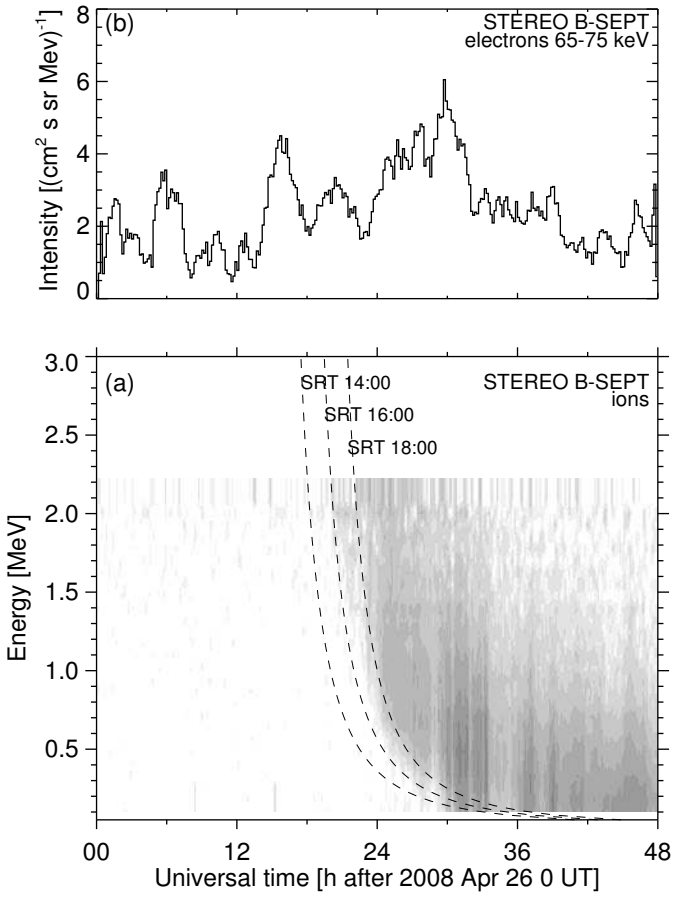

Fig. 6. Time evolution of solar energetic particle (SEP) intensities as seen by the sunward looking detectors of STEREO B/SEPT. **a)** Dynamic spectrum representing the 30 channels of the SEPT instrument. The dashed curves give the expected arrival time of protons at the spacecraft for three different solar release times (SRT) assuming an interplanetary path length of 2 AU. **b)** Electron intensity.

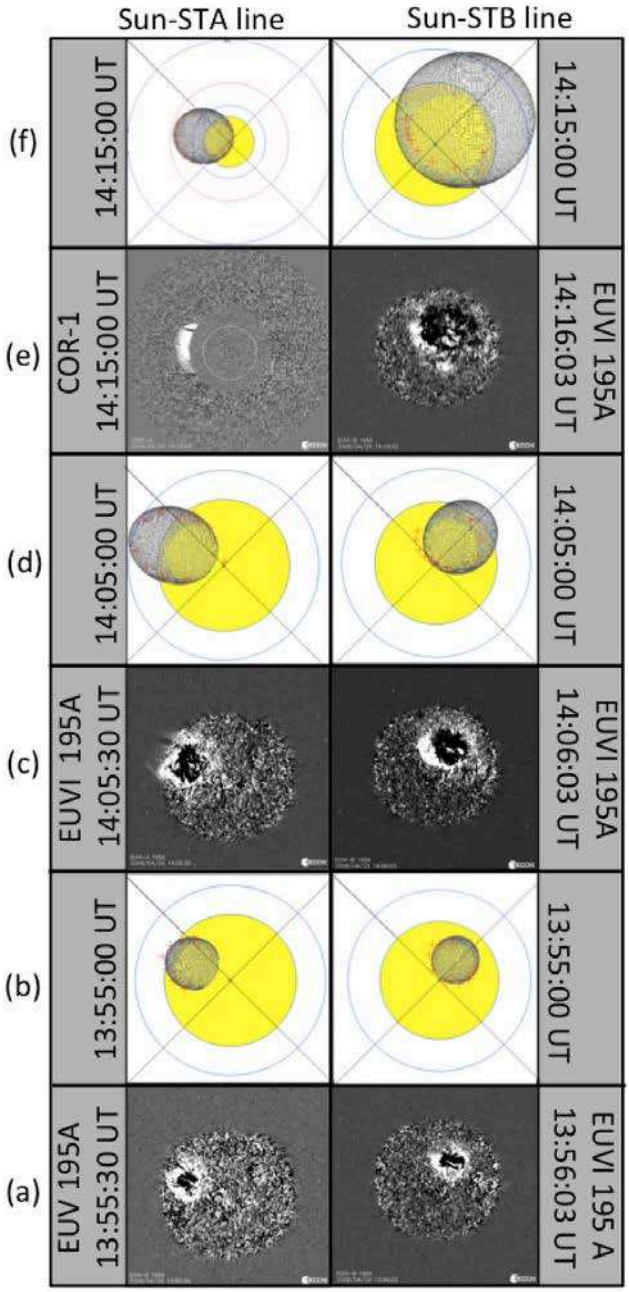

Fig. 7. Comparison of running-difference images (rows **a)**, **c)**, **e)**) of the eruptive event observed by STA (*left hand-column*) and STB (*right-hand column*) with the results of applying the fitting technique (rows **b)**, **d)**, **f)**) developed by Rouillard et al. (2016). The images are all from the EUVI instruments, except the left-hand image shown in row **f)** obtained by COR1-A. Red crosses superposed on the fitted ellipsoids show the contour of the propagating front observed in the running difference images and are used to constrain the extent and location of the ellipsoid at each time.

The electron enhancement could also be associated with the type II burst, but we argue below that the type II source is at a similar location as S3.

The STB/SEPT also observed an ion event. Figure 6a shows, in the form of a dynamical spectrum, the ion intensities normalized to their pre-event background. The ions detected by SEPT are considered to be mostly protons unless the proton spectrum is steep (Müller-Mellin et al. 2008), and protons are expected to arrive at the spacecraft before the heavy ions. Therefore, in the following, we consider that the first ions arriving at the detector are protons. A weaker, but significant SEP event was also observed in the (4−7) MeV channels of the Electron Proton Helium Instrument (EPHIN, Müller-Mellin et al. 1995) aboard SoHO.

The three dashed curves in Fig. 6a show the expected arrival times of protons at STB as a function of their energy, for three different solar release times. We assume that the protons travel a path of 2 AU. This is longer than the Parker spiral, but may account for a prolonged travel path owing to particle scattering by the turbulent interplanetary magnetic field (see Laitinen et al. 2015, and references therein). These curves suggest that a proton injection starting near 14:00 UT is not consistent with the data. A more plausible solar release time is 16:00 UT, but this value is of course only a rough estimate. The SXR and microwave profiles do not show any other burst on 26 April. Neither do the observations of WIND/Waves present any interplanetary type III burst that would reveal fresh particle injections after 14:10 UT. Therefore, the most plausible candidate for the ion acceleration and later electron acceleration is the CME high in the corona. The height-time trajectory of the CME front seen by STA, shown in Fig. 7 of Cheng et al. (2010) and also in Fig. 6 of Temmer et al. (2011), suggests a distance from the solar surface of 7 $R_\odot$ at 16:00 UT.

6. Comparison with 3D CME modeling

Rouillard et al. (2016) present a new technique to derive the properties of the 3D expansion of pressure fronts forming in the

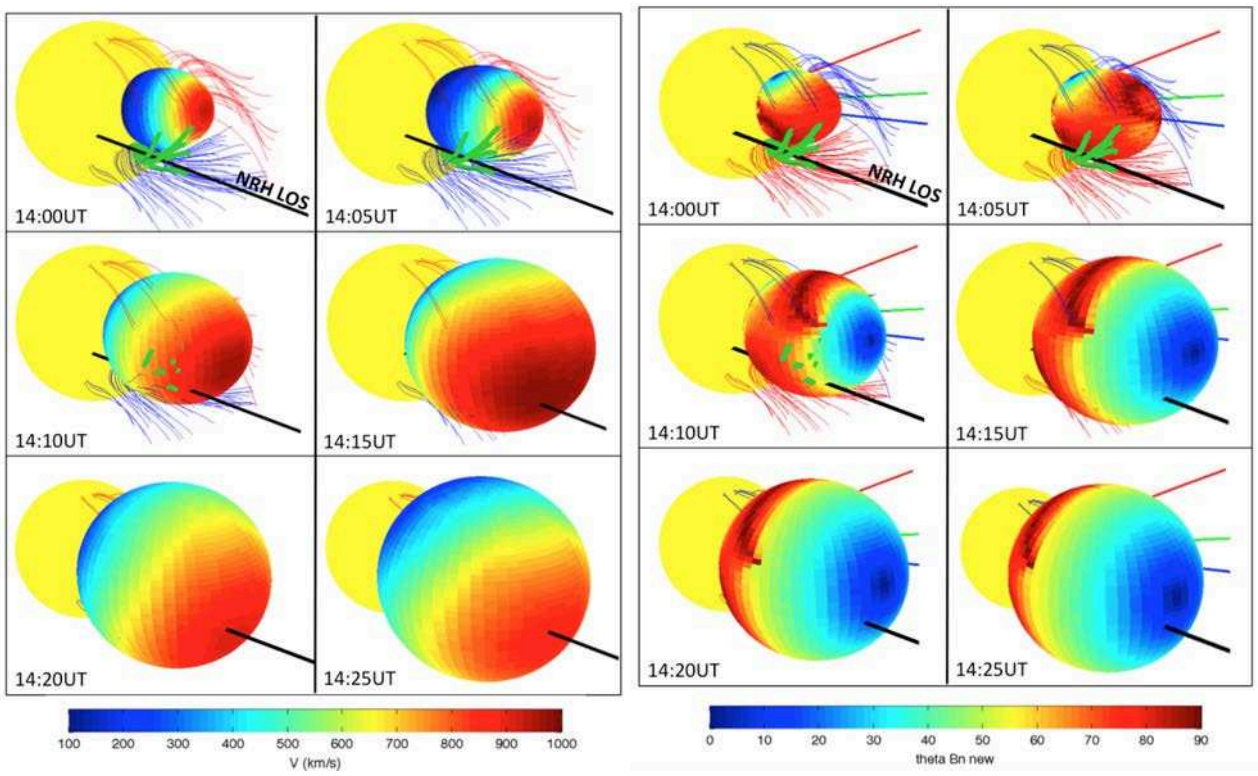

Fig. 8. 3D evolution of the CME at different times from 14:00 UT to 14:25 UT. The color code shows the distribution of the speed (*left panel*) and the angle between the normal on the front and the direction of the upstream magnetic field lines (*right panel*). The open magnetic field lines are plotted in red (positive polarity) and blue (negative polarity). The thick black line is the line of sight (LOS) from Earth to the type III source at 150 MHz. The green lines are the open field lines intercepted by the LOS.

corona during eruptive events. The technique uses a combination of EUV and white-light images and maps of the outermost extent of the coronal region perturbed by the CME as a function of time. In this respect, the technique is similar to the technique proposed by Lario et al. (2014). Rows a, c, and e of Fig. 7 present images covering the first 20 min of the CME eruption as viewed along the Sun-STA and Sun-STB lines. The surface of the pressure front generated around the expanding CME is visible in these EUV and white-light images, it is initially fairly regular and we found that an ellipsoid fits the outermost extent of this perturbed region very well. We manually extracted the location of the outermost extent of the pressure front formed around the CME for all cameras and at all available times. These points are plotted as red crosses in the images given in rows b, d, and f, and are used to outline the contour of the ellipsoids fitted in this study.

Just as for other CME events, we found that the ellipsoid that passes through the contour of the pressure front observed in coronagraphic images intersects the solar surface at the location of the EUV wave. The EUV wave is here considered the low-coronal counterpart of the expanding front surrounding the erupting flux rope.

Our technique goes beyond previous studies (e.g., Kwon et al. 2014) in the following manner: once the parameters of the successive ellipsoids are obtained, we interpolate these parameters at regular time steps of $\delta t = 300$ s to generate a sequence of regularly time-spaced ellipsoids. To compute the 3D expansion speed of the surface of the pressure wave, we find for a point P on the ellipsoid at time $t + \delta t$, the location of the closest point on the ellipsoid at previous time-step t. We then compute the distance travelled between these two points, which we divide by the time interval $\delta t = 300$ s to obtain an estimate of the speed of the disturbance at point P.

The left panel in Fig. 8 presents the results of extracting the normal speed of the pressure front at these six successive times displayed as a color-coded speed distribution over the front surface. In addition, we show the location of open magnetic field lines derived using the same PFSS model as in Fig. 4. In this computation, the source surface was set at 2.5 $R_\odot$.

Only open field lines derived from the PFSS extrapolation are shown in Fig. 8. They trace the location of the streamer out of which the CME emerges, with (in red/blue) inward/outward pointing field lines. Also shown, in green, are the open field lines that are located along the line of sight of the type III burst imaged by the NRH instrument. The line of sight from the Earth to the source S3 of type III bursts is shown as a black line labeled "NRH LOS" in these figures.

6.1. CME and type III bursts

It had been shown in Sect. 4 that the type III bursts occur far from the flaring active region, when the EUV wave impacts onto the open magnetic field lines shown by the PFSS extrapolation (see Fig. 4).

The triangulation at 14:00 UT in Fig. 8 shows that no magnetic field line open to the interplanetary medium is connected with the pressure front. At this time the CME presents an elongated shape, with a speed of just under 1000 km s^{-1} near its so-called nose. The speed decreases along the flank towards 200 km s^{-1} in the low corona near the location of the EUV wave. The CME is hence expected to drive a shock wave at and around its nose, but not at the lower parts of its flanks. At 14:05, near

the onset of the type III bursts in the NDA spectrum, and two minutes before the start at 150 MHz, the pressure front is just about to pass through the open field lines situated near the south-eastern flank. This confirms the idea that the type III bursts occur at the interface between the expanding CME and the open field lines of the coronal hole. At 14:10 UT, the speed of the front intersecting the green lines is greater than 700 km s^{-1} and the front has by then almost certainly steepened into a shock.

6.2. CME and type II burst

The type II burst starts at or immediately after the time of the type III emission, and is also observed much later than usual during the event. We therefore assume that the type III bursts and the type II burst are physically related, and the type II burst is another consequence of the interaction of the south-eastern CME flank with the open coronal magnetic field lines. Since the type II burst starts at lower frequency than the type III bursts, this interaction most likely takes place at a greater altitude than the type III source at 150 MHz. This is also consistent with the modeling result that the CME expansion is probably too slow to drive a shock wave at the low coronal altitude where the type III bursts originate, whereas speeds able to drive a shock are found at greater height (Fig. 8). The six right-hand panels in Fig. 8 present, in a similar format to the left-hand panels, the angle between the normal vector of the front and the direction of the ambient magnetic field lines derived from the PFSS model. Both open and closed magnetic field lines are considered for this derivation. The angle is close to 90 degrees, shown by red colors, over a large part of the south-eastern flank of the front at 14:10 UT. The quasi-perpendicular region rapidly shrinks, however, to the lower parts of the front as it proceeds to higher altitudes. We conclude that at 14:10 UT the shock surface is mostly quasi-perpendicular on the south-eastern flank of the CME.

Assuming the type II source is related to a shock wave at the south-eastern CME flank, we compared the height profiles of the radial component of its outward speed derived from the dynamic spectrum (Eq. (3)), plotted by the solid line in Fig. 9a, and of the radial component of the expansion speed on the south-eastern CME flank inferred from the 3D modeling, plotted by filled triangles and fitted by a parabola, as shown by the dashed curve. The gray band represents the ±10% uncertainty of the type II speed discussed above. The two curves intersect at heliocentric distance $r_o = 2.1 \pm 0.3\ R_\odot$. We recall that r_0 denotes the height where the central frequency of the type II burst (30 MHz) is emitted. At this distance, the angle between the CME surface and the radial direction, whose height profile is plotted in Fig. 9b, is 54° with a range of uncertainty (42°−63°) induced by the uncertainty of the height where the two parabolas intersect in Fig. 9a. These quantities are listed in Table 1, together with the parameters derived from the dynamic spectrum of the type II burst.

Table 2 summarizes the model-dependent derivation of further parameters of the shock wave. We do not include error estimates, since a considerable uncertainty comes from various model assumptions, such as a hydrostatic isothermal electron density at a temperature of 1.5 MK. The quantitative indications are meant to give an idea of how consistent the results are with respect to other work. Their relevance to coronal physics has to be discussed in the framework of the model assumptions. The start height of the type II source (line 1) is deduced from the hydrostatic density model. Since the low-frequency side of the type II spectrum is generally assumed to come from the upstream plasma, which has not yet been disturbed by the CME, the hydrostatic assumption is not unreasonable. The upstream

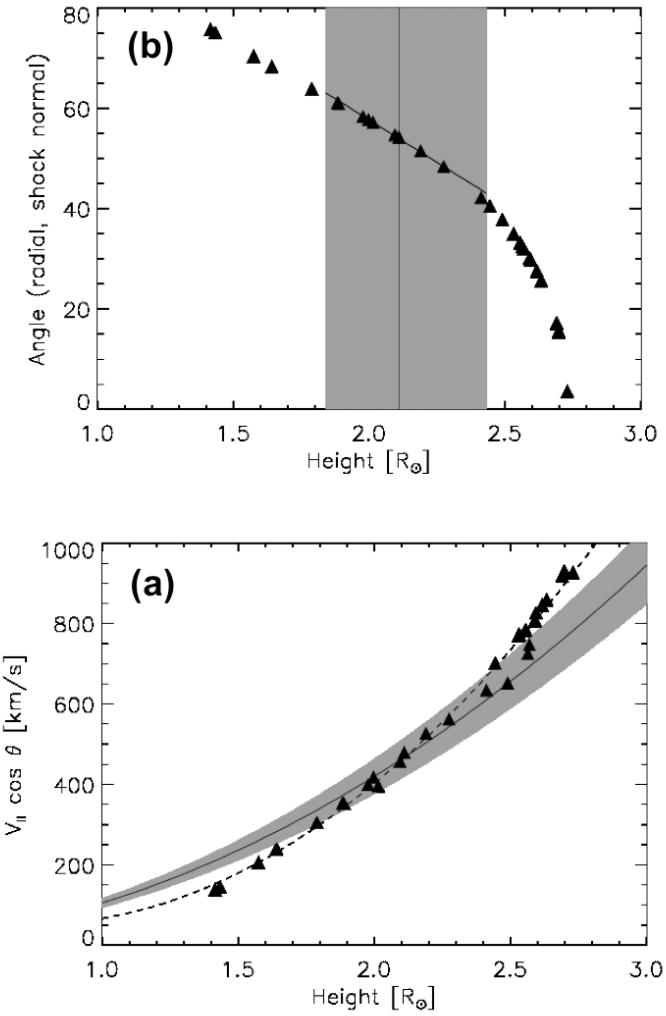

Fig. 9. **a)** Radial speed of the CME and the type II exciter. Solid line: type II exciter from Eq. (3). Symbols: radial component of the expansion CME speed on the south-eastern flank. The dashed line: quadratic fit of these points. The gray band shows the ±10% uncertainty of the type II exciter speed. **b)** Height profile of the angle between the normal to the CME front and the radial direction. Symbols: angles inferred from the CME modeling. Inclined solid line: linear fit of the points around the reference height r_o. Vertical solid line: corresponding angle at the reference height $r_o = 2.1\ R_\odot$. The gray band presents the uncertainty of the height owing to the type II exciter speed.

Table 1. Parameters of type II burst.

Type II burst spectrum	
Centre frequency ν_0	30 MHz
Start frequency ν_{st}	40 MHz
High-to-low frequency ratio	1.39
Frequency drift rate (log)	$(-7.0 \pm 0.7) \times 10^{-4}$ s^{-1}
CME modeling	
Central height r_0	$(2.1 \pm 0.3)\ R_\odot$
Angle (***n***, radial)	54° (42°−63°)

electron density and mass density (lines 4 and 5) are directly determined by the low-frequency limit of the type II burst. The values given in the table refer to the emission frequency of $\nu_0 = 30$ MHz, hence to a plasma frequency of 15 MHz in the

Table 2. Inferred parameters of the type II shock.

(1) Start height	$r_{\rm st} = r_0 \left(1 + \frac{2H(r_0)}{r_0} \ln \frac{\nu_{\rm st}}{\nu_0}\right)^{-1}$	1.9 $R_\odot$
(2) Height extent	$\Delta r \leq 2H(r_0) \ln \frac{\nu_{\rm HF}}{\nu_{\rm LF}}$	$\leq$0.32 $R_\odot$
(3) Exciter speed $V_{\rm II}$	$V_{\rm II} = -\frac{2H(r_0)}{\cos\theta} \frac{\rm d}{{\rm d}t} \ln \nu$	800 km s^{-1}
(4) Upstream electron density (r_0)	$n_{\rm eu} = \frac{4\pi^2 \epsilon_0 m_{\rm e}}{e^2} \left(\frac{\nu_0}{2}\right)^2$	2.8×10^{12} m^{-3}
(5) Upstream mass density (r_0)	$\rho_{\rm u} = 1.14 n_{\rm eu} m_{\rm p}$	5.3×10^{-15} kg m^{-3}
(6) Density compression	$X = \left(\frac{\nu_{\rm HF}}{\nu_{\rm LF}}\right)^2$	1.9
(7) Alfvén Mach number	$M_{\rm A} = \sqrt{\frac{X}{2} \frac{5+5\beta+X}{4-X}}$	1.9
(8) Upstream Alfvén speed (r_0)	$c_{\rm Au} = \frac{V_{\rm II}}{M_{\rm A}}$	400 km s^{-1}
(9) Upstream magnetic field (r_0)	$B_{\rm Au} = \sqrt{\mu_0 \rho_{\rm u}} c_{\rm Au}$	0.33 G
(10) Upstream plasma β (r_0)	$\frac{2}{\gamma} \left(\frac{c_{\rm s}}{c_{\rm Au}}\right)^2$	0.25

usual assumption that when a single type II band is seen, the emission is harmonic.

The instantaneous width of the type II burst spectrum can be used to estimate the height extent in the same hydrostatic model (line 2). This is an upper limit, where we assume that the entire type II burst emission comes from the upstream region. The estimate suggests that the type II source only occupies a fraction of the surface of the CME. This is consistent with the general assumption that type II emission comes from the quasi-perpendicular region of a shock. The right panel of Fig. 8 shows that in the snapshots during the type II burst (14:10–14:20 UT) the quasi-perpendicular region, shown by the red color, covers a substantial, but decreasing, part of the CME flank. It is tempting to relate the well-defined end of the type II burst near 14:21 UT to the development of an increasingly large quasi-parallel geometry on the CME front in regions of high expansion speed. At 14:25 UT the quasi-perpendicular part of the CME front is exclusively at low altitudes, where the expansion speed is probably too low to drive a shock wave. The exciter speed of the type II shock follows from Eq. (3) and the parameters in Table 1.

If we adopt the interpretation of band splitting in type II bursts as revealing simultaneous emission from the upstream and downstream plasma (Smerd et al. 1974; Vršnak et al. 2001), the frequency ratio of the split bands gives the density compression ratio at the shock (Table 2, line 6). This determines the Alfvénic Mach number (line 7), where the polytropic index γ and the β of the plasma are undetermined. We assume $\gamma = 5/3$ and leave β as an unknown. Using the exciter speed $V_{\rm II}$, we can then calculate the Alfvén speed and the magnetic field strength upstream of the shock, still with an unknown β. The relationship between the plasma beta and the Alfvén and sound speeds is given in the last line of the table. Since we know the sound speed, we can insert the upstream Alfvén speed into this expression, with β as an unknown, then determine β, and use its value to quantify the Alfvénic Mach number, the Alfvén speed, and the magnetic field strength. All these parameters refer to the height $r_o = 2.1 \pm 0.3\ R_\odot$.

6.3. CME shock and SEP acceleration

Particles accelerated in the quasi perpendicular shock (revealed by the type II burst) will not be observed by any spacecraft because of their location in the interplanetary space (Fig. 5). These particles reach 1 AU at a heliolongitude of around –137° relative to L1 and the Earth. All spacecraft are magnetically connected to the western regions of the flare-CME system.

We applied the same triangulation technique as used in Fig. 8 to locate the extent of the pressure front much higher in the solar atmosphere when the CME has sufficiently expanded to intersect the nominal Parker spiral connected with STB. The triangulation work was carried out by considering both the COR-2 coronagraph, as well as the inner heliospheric imager (HI-1).

To infer how STB connects with the low corona at the time of the event, we must verify that the solar wind situated between the corona and STB is not significantly disturbed. To do so, we considered the STEREO catalogs of CMEs and corotating interaction regions (CIRs), which were made available by the Heliospheric Cataloguing, Analysis and Techniques Service (HELCATS) FP7 project. Since STA was directly imaging the Sun-STB line (see Fig. 5), the catalogs are perfectly suited for this analysis. The analysis reveals that (1) the CME of interest to the present paper was the only one observed by STEREO for many days before and after the event; (2) a CIR was also passing in the field of view of HI at the same time and should have hit STB at roughly the same time as the CME shock. Comparison of the location of both structures during their propagation to 1 AU shows that the magnetic connectivity of STB to the western part of the shock (Fig. 5) could not have been altered by the formation of the CIR on 26 April 2008. The CIR was forming well upstream of the CME but was not present near the heights

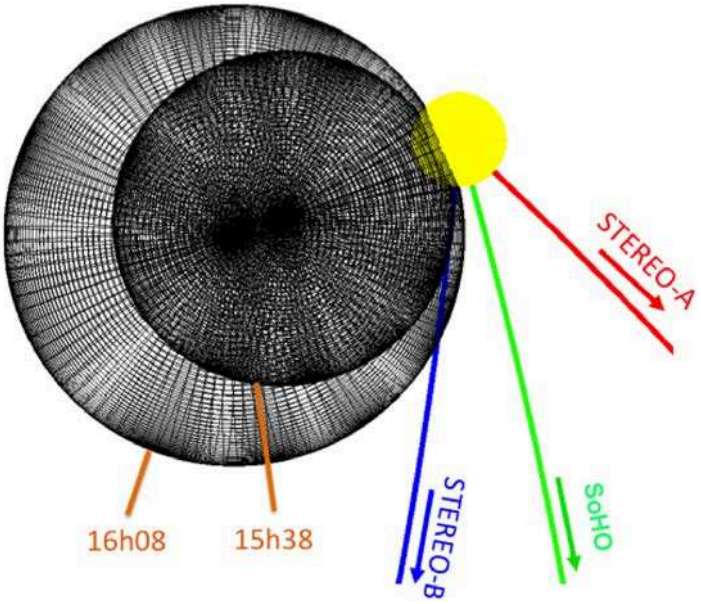

Fig. 10. Pressure wave triangulated from STEREO/COR2 observations at 15:38 UT and at 16:08 UT, as seen by an observer above the northern solar pole. The three labeled lines represent the Parker spiral field lines in the ecliptic plane that connect the parent active region to the spacecraft.

and longitudes of the shock at 15:38 UT and at 16:08 UT on 26 April 2008. For more details, see the analysis presented in Appendix A.

The triangulation work carried out high up in the corona using COR-2 and HI-1 confirms the gradual southward and eastward shift of the central axis of the pressure front that was already detected in EUVI and COR-1 (Sect. 6). The longitudinal shift goes from 216° at 13:55 UT to 200° at 16:08 UT.

The derived position of the propagating front at these later times reveals that the western CME flank intercepts the interplanetary field lines connected with the STB spacecraft after 15:38 UT (Fig. 10). This is consistent with the injection time, which was estimated by considering the measured ion time profile discussed in Sect. 5 (Fig. 6). A similar configuration between the CME shock and the Parker spiral has been analysed and modelled in Rouillard et al. (2011). Careful analysis of the magnetic connectivity of the shock with the particle detectors also showed a delayed onset of the SEP event (about 16 h), which was attributed to the time for the modelled shock to intersect the relevant magnetic field lines.

7. Discussion

The eruptive event on 26 April 2008 illustrates different energetic particle populations associated with different acceleration sites related to a CME. The observations are summarized as follows:

1. The event showed no evidence of electron acceleration to mildly relativistic energies in the low corona: the microwave emission had a purely thermal character.
2. Electron acceleration was first observed above the flaring active region, most likely related to the post-eruptive current sheet, through the type IV continuum seen over a broad range of dm-to-m-waves. Spectrography from longer metre-wavelengths to kilometre-wavelengths suggests that few electrons could escape. This is consistent with the large-scale closed magnetic configuration revealed by the PFSS extrapolation.
3. Type III bursts from electron beams and a type II burst from a coronal shock wave were observed unusually late, more than 15 min after the start of the eruptive event. The type III source could be imaged at 150 MHz, and was found to be located far south-eastward of the flaring active region, on open field lines revealed by the PFSS extrapolation and indirectly by a coronal hole in EUV and radio images. An EUV wave was found to arrive at the open field lines related to the type III bursts near the time of the bursts. The 3D modeling of the stereoscopic CME observations confirms the occurrence of the type III bursts, and therefore the acceleration of the electron beams, as the south-eastern flank of the laterally expanding CME impacted the open magnetic field lines of the coronal hole. At 1 AU the Parker spirals connected to those PFSS field lines which traverse the type III burst source are separated by ~110° in heliolongitude from the nearest spacecraft, STB.
4. Parameters of the shock wave were derived from the combination of the spectrographic observations and the CME modeling under the assumption that the type II burst also occurred on the south-eastern flank of the CME. This leads to a fairly complete, but model-dependent, description of the shock and the upstream plasma. The geometry of the CME flank at the presumed site of the type II burst is quasi-perpendicular.
5. The shock at the front of the CME is not observed directly, but its presence is strongly suggested by the high speed ~1000 km s^{-1}. Its geometry is quasi-perpendicular during the first 5−10 min of the CME rise. Thereafter it becomes quasi-parallel, and the quasi-parallel geometry occupies an increasing fraction of the CME surface as the event progresses.
6. SEPs up to several MeV are observed by the best-connected spacecraft, STB. Their intensity starts to rise nearly two hours after the start of the eruption. The Parker spiral through the spacecraft originates westward of the eruptive active region. The expanding CME reaches this field line near the time when the SEPs seen at the spacecraft were released at the Sun.
7. The radio observations of electron acceleration at the Sun and of SEPs near 1 AU reveal particle acceleration at different regions of an expanding CME. They cover a remarkably extended range of heliolongitudes of about 140°.

The high cadence of the data and the multiple view points during this event give us a unique opportunity to see different particle populations from different acceleration sites linked to the same CME. The observations allow us to discuss qualitatively different acceleration mechanisms involved.

7.1. Type III burst and particle acceleration during the interaction of the CME with the coronal hole

STEREO and SoHO images have shown an EUV wave reaching a coronal hole close to the type III burst source position at 150 MHz (S3). The observed speed of the EUV wave, 207 km s^{-1}, and the expansion of the CME front inferred from stereoscopic modeling at heliocentric distances of <1.5 $R_\odot$, are unlikely to be fast enough to reveal a shock. The shock traced by the type II burst likely occurred at a greater height than S3.

Thus, we can conclude that even though both sources, S3 and the type II burst, are most likely located in the coronal hole region and are linked to the expansion of the CME, they are independent manifestations of the CME impact on the coronal hole. Therefore, an alternative accelerator is needed to explain the electron acceleration near S3 taking into account the interaction of the EUV wave with its surroundings.

In solar plasmas, the magnetic reconnection process is normally related to the energy release in flares that can accelerate energetic particles (e.g., Aschwanden 2002). Nevertheless, the magnetic reconnection can also happen when the expanding magnetic structure of the CME that formed in the active region interacts with the surrounding field lines (Dasso et al. 2006). Magnetic reconnection can inject energetic electrons onto open magnetic field lines in two ways.

On the one hand, if the CME magnetic structure is filled with energetic electrons, the reconnection with the surroundings will give them access to open magnetic field lines. This was envisaged by Schatten & Mullan (1977) and modelled by Masson et al. (2013). Evidence of electrons confined in the flux rope was presented in Sect. 3. However, radio emission from these accelerated electrons was observed only north-eastward and south-westward of the active region (see Fig. 2), far from region S3. So the scenario is not supported by the observations, although we cannot exclude it definitely, because we do not fully understand the radiation process.

An alternative idea is that the particles are locally accelerated near the S3 location. In a magnetic reconnection scenario related to flares, pairs of oppositely drifting bursts (type III and reverse slope) are expected. These pairs of bursts that start simultaneously and at the same frequency reveal electrons that are accelerated upwards and downwards from the reconnection region (Aschwanden 2002). These pairs of bursts are not observed in the spectrum in Fig. 3, although we cannot exclude the idea that the bursts at 150 MHz are reverse slope bursts. In addition, downward-propagating electron beams may not be observed because the plasma is compressed, so that the enhanced collision rate or turbulence is able to isotropize the beams, while the enhanced magnetic field is able to reflect them.

Another process that must be considered because of the magnetic compression is betatron acceleration. Since the magnetic moment is conserved in a collisionless plasma, the particles gain perpendicular kinetic energy when the local magnetic field increases (e.g., Baumjohann & Treumann 1996). The increase in kinetic energy is equal to that of the magnetic field. If the plasma is slightly collisional or subjected to wave turbulence, the perpendicular momentum can be transferred to parallel momentum.

We examine if this process can be effective in accelerating the electrons through the compression of the open magnetic field in the coronal hole by the impact of the CME. If we use the reference height of the type II burst ($r_o = 2.1\ R_\odot$, Sect. 6), we find that the height of the S3 source at 150 MHz is $r = 1.2\ R_\odot$. At this altitude the magnetic field given by the PFSS extrapolation is $B \simeq 0.49$ G. To estimate the magnetic field compression, we compare this value with an upper limit reached during the compression, namely the magnetic field required to stop the CME expansion by the build-up of magnetic pressure at the interface of the CME and the coronal hole. The compressed magnetic field (B) was calculated from the condition of equilibrium between the dynamic pressure of the expanding CME and the magnetic pressure in the compressed open magnetic flux tube:

$$B = \sqrt{2 \cdot \mu_0 \rho} \cdot V \simeq 1.47\ [\mathrm{G}], \quad (4)$$

with $\rho = 1.14 n_e m_p$. The electronic density inside the CME (n_e) was taken 12% higher than the ambient density (Kozarev et al. 2011; Schrijver et al. 2011). The ambient electron density was found to be 6.9×10^7 cm^{-3}, assuming harmonic emission of the source at 150.9 MHz. The speed of the impact, V, is the velocity of the EUV wave.

Considering that electrons at speeds around three times the thermal speed in the ambient plasma can be accelerated by the magnetic field compression, we obtain an energy of about 3.5 keV. This is less than the energy usually associated with type III emitting electron beams in the corona (Alvarez & Haddock 1973; Lin 1974; Poquerusse 1994; Klassen et al. 2003). In the present case, we can estimate the exciter speed of the type III burst from the drift rate. In fact no drift is discernible in the type III bursts of the differential spectrum in Fig. 3 between 70 and 20 MHz. Given that the integration time is 2.5 s, this implies a lower limit of the absolute value of the logarithmic drift rate of 0.5 s^{-1} and a lower limit of the exciter speed of $0.4c$, which corresponds to a kinetic energy of about 45 keV. This value is higher than the one estimated from the compression ratio, which was already a generous estimate of an upper limit. Successive episodes of magnetic pumping might be more efficient, for instance if the CME expansion produced large-amplitude fast magnetosonic waves.

In conclusion, both magnetic reconnection and betatron acceleration can qualitatively account for the acceleration of type III emitting electron beams, but we have no definite observational evidence to distinguish between them.

7.2. CME shock

Because of its high speed, the CME is expected to drive a shock wave. This is consistent with the occurrence of a type II radio burst. Although only spectral observations of this burst were available, the combination with the CME modeling gave valuable, albeit model-dependent, insights into the type II burst and its role in the particle acceleration at the CME shock. The physical relationship between the metre-wave type II burst and the CME is strongly supported by the timing and the coincidence with the impact of the south-eastern flank of the CME on the coronal hole.

7.2.1. CME shock and type II radio burst

The emission of metre-wave type II bursts on the flank of a CME was reported in a number of recent studies (e.g., Magdalenić et al. 2014; Zucca et al. 2014a), although evidence on a location near the nose is also frequent, especially at altitudes within a solar radius above the photosphere (Dauphin et al. 2006; Zimovets et al. 2012; Zucca et al. 2014b). In the present case, no imaging observations of the type II burst are available, but the consistency between the type II spectrum and the height profile of the expansion velocity derived from the stereoscopic CME modeling strongly argues for a source location on the flank. Using this constraint, we infer that the shock geometry must be quasi-perpendicular. This again adds evidence to existing knowledge (Steinolfson 1984; Zimovets et al. 2012), using a new technique. The observations suggest that the type II emission ceases as the quasi-perpendicular part of the CME front shrinks to a small region of relatively low expansion speed in the low corona. This is a new possible interpretation of the finite duration of metre-wave type II bursts.

The Mach number of the type II shock, as inferred from the hypothesis of simultaneous emission upstream and downstream of the shock front, is moderate, $M_A = 1.9$. The value is consistent with previous work (Vršnak et al. 2002; Mancuso & Garzelli 2013; Kouloumvakos et al. 2014; Vasanth et al. 2014; Zucca et al. 2014b), but it is more closely constrained in the present event by the combination of the type II spectrum and the stereoscopic CME modeling. Similar Mach numbers were derived from white-light observations (Bemporad & Mancuso 2010, 2011).

The interpretation of band splitting in terms of simultaneous emission upstream and downstream of the shock was challenged on theoretical grounds (Cairns 2011), and alternative ideas were developed (McLean 1967; Treumann & LaBelle 1992; Sakai & Karlický 2008). Those which localize the split-band sources in different regions upstream of the shock front have not been confirmed by imaging observations. Zimovets et al. (2012) and Zucca et al. (2014b) present two case studies where multi-frequency imaging show the high-frequency split band to be slightly, but systematically, displaced inward with respect to the low-frequency split band, which is in agreement with the hypothesis of simultaneous emissions from the upstream and downstream region. Another major support to this interpretation is the finding that, in type II bursts where the feature was observed in interplanetary space, the in situ density measurements upstream and downstream of the shock wave near 1 AU were indeed consistent with the Earthward extrapolation of the type II split bands (Vršnak et al. 2001). Finally, numerical simulations also show that shock-accelerated electrons may penetrate into the downstream region (Savoini et al. 2005).

7.2.2. CME shock and SEP acceleration

CMEs are thought to accelerate particles over an extended spatial range. The Mach number found on the south-eastern flank of the 26 April 2008 CME corresponds to a subcritical shock in quasi-perpendicular geometry (see Fig. 5 of Mann et al. 1995). It is therefore not clear if this part of the CME shock was able to accelerate protons. Electrons that were accelerated at this shock would be expected to be seen about 120° eastward of the flaring active region.

The first protons observed in interplanetary space were accelerated when the part of the shock that was situated close to the western flank of the Sun was magnetically connected to the spacecraft. In the present event, this occurred only when the CME front was far from the Sun. The SEPs detected at STEREO B and SoHO complete the manifestations of particle acceleration at this particular CME, demonstrating that physically different accelerators are at work in different acceleration regions, so that the remotely observed particle signatures depend on the region of the CME front to which the observer is connected.

8. Summary and conclusions

The occurrence of an eruptive event on 26 April 2008 during very quiet coronal conditions gave us the opportunity to identify different energetic particle populations originating in different acceleration sites that were triggered by the evolution of the CME. In summary, we were able to determine the relationship between the CME expansion, the EUV wave, and the particle acceleration regions:

1. No non-thermal electrons are seen from the flaring active region itself. The acceleration occurs only higher in the corona as was revealed by decimetric and decametric radio emission.
2. Energetic electrons were accelerated, which produced type III burst emission at the interaction region between the south-eastern CME flank and the ambient corona, far from the active region. Candidate acceleration processes operating there are magnetic reconnection and compressional acceleration at the interface between the CME flank and the corona.
3. The shock revealed by the type II burst was most likely also located at the south-eastern CME flank, but at a slightly greater height (~1.9 $R_\odot$). The local geometry was found to be quasi-perpendicular. While the shock wave was clearly able to accelerate electrons, its inferred Mach number suggests that it was sub-critical and therefore not an efficient proton accelerator.
4. The late SEP event (MeV protons) observed at STEREO B and SoHO is associated with the shock-acceleration near the western CME flank, where the geometry was quasi-parallel. The late onset is consistent with the time when the pressure wave (CME border) higher in the corona became magnetically connected to the spacecraft.
5. The various acceleration regions identified during this event released electrons and/or protons over an extended range of heliolongitudes reaching nearly 140°.

The observations of this well-defined CME, which occurred in a rather simple environment that is typical of solar minimum, reveal the simultaneous or successive action of different acceleration regions. These acceleration regions are linked to different vantage points in the interplanetary space. While this example does show that a CME releases energetic particles into a broad range of heliolongitudes, it does demonstrate that multi-spacecraft SEP measurements may not probe one acceleration region in the corona.

Acknowledgements. The authors are indebted to Sang Hoang for providing the direction-finding analysis of the Wind/Waves observations. They acknowledge helpful discussions within the team The Connection Between Coronal Shock Wave Dynamics and Early SEP Production led by K. Kozarev and N. Nitta at the International Space Science Institute (ISSI) in Bern. C.S.-M. gratefully acknowledges the financial support of her doctorate studies by the University of Costa Rica and the Ministry of Science, Technology and Telecommunications of Costa Rica (MICITT) through the National Council of Scientific and Technological Research (CONICIT). This research was also supported by the Agence Nationale pour la Recherche (ANR/ASTRID, DGA) project Outils radioastronomiques pour la météorologie de l'espace (ORME, contract No. ANR-14-ASTR-0027) and by the French space agency (CNES). A.P.R. acknowledges use of the tools made available by the French plasma physics data centre (Centre de Données de la Physique des Plasmas; CDPP; http://cdpp.eu/), CNES and the space weather team in Toulouse (Solar-Terrestrial Observations and Modelling Service; STORMS). This includes the data-mining tools AMDA (http://amda.cdpp.eu/), the CLWEB tool (clweb.cesr.fr/) and the propagation tool (http://propagationtool.cdpp.eu). The catalogs used in the Appendix to track the location of the CME and CIRs in the interplanetary medium were created by the HELCATS project under the FP7 EU contract number 606692.

References

Afanasiev, A., Battarbee, M., & Vainio, R. 2015, A&A, 584, A81
Alvarez, H., & Haddock, F. T. 1973, Sol. Phys., 29, 197
Aschwanden, M. J. 2002, Space Sci. Rev., 101, 1
Baumjohann, W., & Treumann, R. A. 1996, Basic space plasma physics (London: Imperial College Press)
Bemporad, A., & Mancuso, S. 2010, ApJ, 720, 130
Bemporad, A., & Mancuso, S. 2011, ApJ, 739, L64
Bougeret, J.-L., Kaiser, M. L., Kellogg, P. J., et al. 1995, Space Sci. Rev., 71, 231
Brueckner, G. E., Howard, R. A., Koomen, M. J., et al. 1995, Sol. Phys., 162, 357

Cairns, I. H. 2011, in IAGA Special Sopron Book Series, Vol. 4, The Sun, the Solar Wind, and the Heliosphere, eds. M. P. Miralles, & J. Sánchez Almeida (Springer), 267
Cheng, X., Ding, M. D., & Zhang, J. 2010, ApJ, 712, 1302
Cheng, X., Zhang, J., Saar, S. H., & Ding, M. D. 2012, ApJ, 761, 62
Dasso, S., Mandrini, C. H., Démoulin, P., & Luoni, M. L. 2006, A&A, 455, 349
Dauphin, C., Vilmer, N., & Krucker, S. 2006, A&A, 455, 339
Delaboudinière, J.-P., Artzner, G. E., Brunaud, J., et al. 1995, Sol. Phys., 162, 291
Dresing, N., Gómez-Herrero, R., Klassen, A., et al. 2012, Sol. Phys., 281, 281
Dresing, N., Gómez-Herrero, R., Heber, B., et al. 2014, A&A, 567, A27
Dröge, W., Kartavykh, Y. Y., Dresing, N., Heber, B., & Klassen, A. 2014, J. Geophys. Res. (Space Phys.), 119, 6074
Gómez-Herrero, R., Dresing, N., Klassen, A., et al. 2015, ApJ, 799, 55
Holman, G. D., & Pesses, M. E. 1983, ApJ, 267, 837
Huang, J., Démoulin, P., Pick, M., et al. 2011, ApJ, 729, 107
Kerdraon, A., & Delouis, J.-M. 1997, in Coronal Physics from Radio and Space Observations, ed. G. Trottet (Berlin: Springer Verlag), Lect. Notes Phys., 483, 192
Klassen, A., Karlický, M., & Mann, G. 2003, A&A, 410, 307
Klein, K.-L., Krucker, S., Lointier, G., & Kerdraon, A. 2008, A&A, 486, 589
Kouloumvakos, A., Patsourakos, S., Hillaris, A., et al. 2014, Sol. Phys., 289, 2123
Kozarev, K. A., Korreck, K. E., Lobzin, V. V., Weber, M. A., & Schwadron, N. A. 2011, ApJ, 733, L25
Krucker, S., Larson, D. E., Lin, R. P., & Thompson, B. J. 1999, ApJ, 519, 864
Kwon, R.-Y., Zhang, J., & Olmedo, O. 2014, ApJ, 794, 148
Laitinen, T., Huttunen-Heikinmaa, K., Valtonen, E., & Dalla, S. 2015, ApJ, 806, 114
Lario, D., Aran, A., Gómez-Herrero, R., et al. 2013, ApJ, 767, 41
Lario, D., Raouafi, N. E., Kwon, R.-Y., et al. 2014, ApJ, 797, 8
Lecacheux, A. 2000, in Radio Astronomy at Long Wavelengths, eds. R. G. Stone, K. W. Weiler, M. L. Goldstein, & J.-L. Bougeret, AGU Geophys. Monogr. Ser., 119, 321
Lee, M. A. 2005, ApJS, 158, 38
Lin, R. P. 1974, Space Sci. Rev., 16, 189
Magdalenić, J., Marqué, C., Krupar, V., et al. 2014, ApJ, 791, 115
Mancuso, S., & Garzelli, M. V. 2013, A&A, 560, L1
Mann, G., Classen, T., & Aurass, H. 1995, A&A, 295, 775
Masson, S., Antiochos, S. K., & DeVore, C. R. 2013, ApJ, 771, 82
McLean, D. J. 1967, PASA, 1, 47
Miteva, R., Klein, K.-L., Kienreich, I., et al. 2014, Sol. Phys., 289, 2601
Müller-Mellin, R., Kunow, H., Fleissner, V., et al. 1995, Sol. Phys., 162, 483
Müller-Mellin, R., Böttcher, S., Falenski, J., et al. 2008, Space Sci. Rev., 136, 363
Nelson, G. J., & Melrose, D. B. 1985, in Solar Radiophysics: Studies of Emission from the Sun at Metre Wavelengths, eds. D. McLean, & N. Labrum (Cambridge, Great Britain: Cambridge University Press), 333
Nindos, A., Aurass, H., Klein, K.-L., & Trottet, G. 2008, Sol. Phys., 253, 3
Paesold, G., Benz, A. O., Klein, K.-L., & Vilmer, N. 2001, A&A, 371, 333
Park, J., Innes, D. E., Bucik, R., Moon, Y.-J., & Kahler, S. W. 2015, ApJ, 808, 3
Plotnikov, I., Rouillard, A. P., Davies, J. A., et al. 2016, Sol. Phys., submitted
Poquerusse, M. 1994, A&A, 286, 611
Reiner, M. J. 2001, Space Sci. Rev., 97, 126
Rouillard, A. P., Davies, J. A., Lavraud, B., et al. 2010a, J. Geophys. Res. (Space Phys.), 115, A04103
Rouillard, A. P., Lavraud, B., Davies, J. A., et al. 2010b, J. Geophys. Res. (Space Phys.), 115, A04104
Rouillard, A. P., Odstrčil, D., Sheeley, N. R., et al. 2011, ApJ, 735, 7
Rouillard, A. P., Sheeley, N. R., Tylka, A., et al. 2012, ApJ, 752, 44
Rouillard, A. P., Plotnikov, I., Pinto, R., et al. 2016, ApJ, submitted
Saint-Hilaire, P., Vilmer, N., & Kerdraon, A. 2013, ApJ, 762, 60
Sakai, J. I., & Karlický, M. 2008, A&A, 478, L15
Savoini, P., Lembège, B., Krasnosselskhik, V., & Kuramitsu, Y. 2005, Ann. Geophys., 23, 3685
Schatten, K. H., & Mullan, D. J. 1977, J. Geophys. Res., 82, 5609
Schrijver, C. J., & De Rosa, M. L. 2003, Sol. Phys., 212, 165
Schrijver, C. J., Aulanier, G., Title, A. M., Pariat, E., & Delannée, C. 2011, ApJ, 738, 167
Smerd, S. F., Wild, J. P., & Sheridan, K. V. 1962, Austr. J. Phys., 15, 180
Smerd, S. F., Sheridan, K. V., & Stewart, R. T. 1974, in Coronal Disturbances, ed. G. A. Newkirk, IAU Symp., 57, 389
Steinolfson, R. S. 1984, Sol. Phys., 94, 193
Temmer, M., Veronig, A. M., Gopalswamy, N., & Yashiro, S. 2011, Sol. Phys., 273, 421
Thernisien, A., Vourlidas, A., & Howard, R. A. 2009, Sol. Phys., 256, 111
Torsti, J., Kocharov, L., Teittinen, M., & Thompson, B. 1999, ApJ, 510, 460
Treumann, R. A., & LaBelle, J. 1992, ApJ, 399, L167
Vasanth, V., Umapathy, S., Vršnak, B., Žic, T., & Prakash, O. 2014, Sol. Phys., 289, 251
Vršnak, B., Aurass, H., Magdalenić, J., & Gopalswamy, N. 2001, A&A, 377, 321
Vršnak, B., Magdalenić, J., Aurass, H., & Mann, G. 2002, A&A, 396, 673
Warmuth, A. 2015, Liv. Rev. Sol. Phys., 12, 3
Wibberenz, G., & Cane, H. V. 2006, ApJ, 650, 1199
Wiedenbeck, M. E., Mason, G. M., Gómez-Herrero, R., et al. 2010, in Twelfth International Solar Wind Conference, AIP Conf. Proc., 1216, 621
Wood, B. E., & Howard, R. A. 2009, ApJ, 702, 901
Wuelser, J.-P., Lemen, J. R., Tarbell, T. D., et al. 2004, in Telescopes and Instrumentation for Solar Astrophysics, eds. S. Fineschi, & M. A. Gummin, SPIE Conf. Ser., 5171, 111
Zank, G. P., Rice, W. K. M., & Wu, C. C. 2000, J. Geophys. Res., 105, 25079
Zimovets, I., Vilmer, N., Chian, A. C.-L., Sharykin, I., & Struminsky, A. 2012, A&A, 547, A6
Zucca, P., Carley, E. P., Bloomfield, D. S., & Gallagher, P. T. 2014a, A&A, 564, A47
Zucca, P., Pick, M., Démoulin, P., et al. 2014b, ApJ, 795, 68

Appendix A: Analysis of interplanetary conditions between 20 and 30 April 2016

In this section, we evaluate whether the magnetic field line invoked in Sect. 6.3 (Fig. 5), which connects STEREO-B to the western flank of the shock is perturbed by heliospheric structures, such as CMEs and corotating interaction regions (CIRs). To do so, we employ the CME and CIR catalogs produced by the HELCATS[1] project using images from STEREO.

The catalog uses the fitting technique developed by Rouillard et al. (2010a,b), which is based on J-maps. Through a systematic analysis, Plotnikov et al. (2016) show that all CIRs measured in situ were also detected in white-light imagery between 2007 and 2009.

The range of elongation angles shown in the J-maps of Figs. A.1a and b (vertical axis), goes from 4° to 74°. This angular range that was imaged by the heliospheric imagers onboard STEREO-A includes the elongation of STEREO-B, shown by the dotted horizontal lines near elongation 70° in Figs. A.1a and b. Hence STEREO-A was at the time imaging plasma flowing between the Sun and STEREO-B (see Fig. A.1c). No large CME propagated outward in the heliospheric images of STEREO-A, other than the event of interest in this paper. The various trajectory estimates listed in the HELCATS Catalogue confirm that the CME studied in this paper propagated to within 20° of the longitude of STEREO-B at an estimated speed of around 550 km s^{-1}. This agrees with the speed of plasma located downstream of the shock, which was measured by STEREO-B at the impact time. We repeated the trajectory analysis by combining the fixed-phi model (Rouillard et al. 2008) with the results of the triangulation work given in Sect. 6.3. The latter gave a longitude of propagation of 200° along the central axis and a shock passage time at 10 $R_\odot$ of 16:00 UT on 26 April with a speed of 550 km s^{-1}. The time-elongation variation of this hypothetical CME produces the red track shown in Fig. A.1a. For an average transit speed of 550 km s^{-1}, the track very closely matches the leading edge of the CME track that was shown to be the time-varying location of the shock by Wood & Howard (2009). The derived location of the CME is shown on the view of the ecliptic in Fig. A.1c at 12:00 UT on 27 April 2008.

The J-map in Fig. A.1a also reveals the presence of a pattern of converging tracks that is typical of a CIR passing in the field of view (e.g., Rouillard et al. 2008). Each track corresponds to a density inhomogeneity (or so-called blob) that becomes compressed inside the CIR, acting as a tracer of the CIR progression along a specific longitude. The CIR corotates and density blobs are released periodically from the low corona, which produces this characteristic pattern of tracks in the J-map that acts as a tracer of the longitudinal and radial progression of the CIR (Rouillard et al. 2008). The HELCATS Catalogue confirms the presence of a CIR propagating towards STEREO-B at the time; the CIR pattern extracted from the J-map is shown as the family of black lines overlying the J-map shown in Fig. A.1b. In this calculation, a reference track (red line in Fig. A.1b) is usually assumed to reconstruct the pattern of a converging track. The position of the CIR in the ecliptic plane at 12:00 UT on 27 April 2008, as calculated by the propagation tool, is shown in Fig. A.1d. The CIR is approaching STEREO-B at the time and the tool computed an impact time based on radial propagation and corotation on 29 April 2008 at around 7 UT with a typical uncertainty of 8 h. The interplanetary CME (ICME) shock clearly identified by Wood & Howard (2009) in white-light images and tracked in Fig. A.1a arrives at STEREO-B near 13:00 UT, we conclude that the CME must have encountered the CIR during its radial propagation to STEREO-B.

The complex in situ signature downstream of the shock may result from the complex interaction that must have occurred between the CME and the CIR during the propagation of the CME to STEREO-B. According to Fig. A.1, this complex interaction should have occurred well after 12:00 UT on 27 April 2008. Therefore the magnetic connectivity of STEREO-B to the shock at the time of the early SEP signatures (Sect. 6.3) is not yet affected by that interaction. This is particularly true at the low heights at which the triangulation work was carried out (<15 $R_\odot$), where CIRs have not yet formed.

[1] http://www.helcats-fp7.eu/products.html

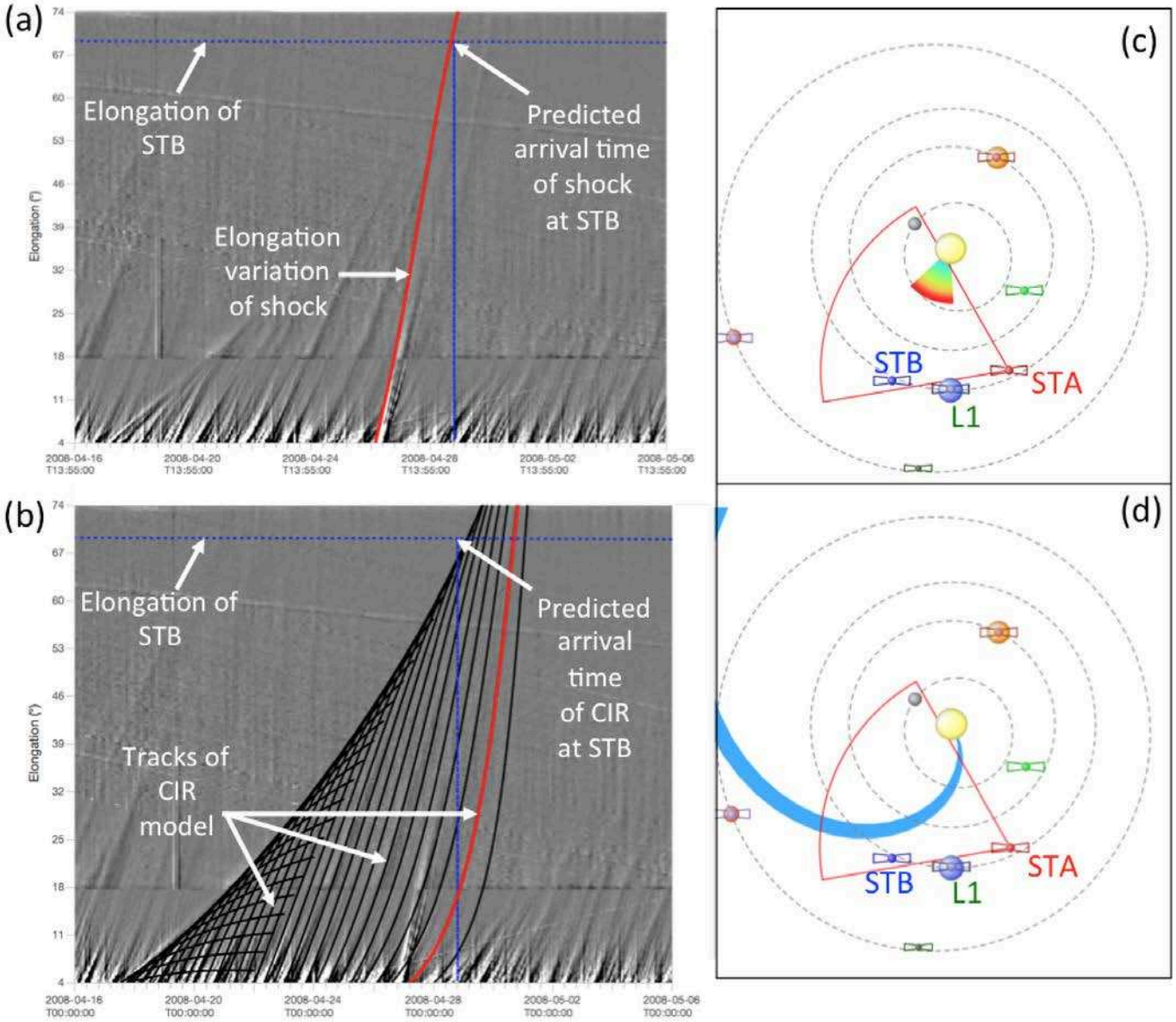

Fig. A.1. a), **b)**: J-maps derived from heliospheric imaging made by STEREO-A showing the state of the interplanetary medium between 16 April and 6 May 2008. Each track on these J-maps corresponds to a density structure moving radially outward from the Sun and leaving a strong signature in the white-light images. The horizontal dotted line near the top of the maps shows the elongation of STEREO-B (STB). The inclined red line in **a)** is the track of a hypothetical CME launched near the time of the 26 April 2008 event and propagating at constant speed 550 km s^{-1}. The vertical blue line marks its arrival at STB. **c)**, **d)**: view of the ecliptic plane from solar north with the respective locations of STEREO-A (STA), STB and L1 as well as other planets and probes that are not all labeled for clarity purposes. The angular extents of the J-maps shown in the *left-hand columns* are shown as red contour lines emanating from the STA. The locations of the CME (**c)** and CIR (**d)**; blue band) derived by the J-map analysis are shown at 12:00 UT on 27 April 2008. These four panels were produced using the IRAP propagation tool (`propagationtool.cdpp.eu`).

Chapter 3

Characterisation of Type IV Bursts: Localisation and Polarisation

As was discussed in Chapter 1, the magnetic structures associated with halo CMEs are the most probable disturbances that reach the Earth and cause geomagnetic storms. These magnetic storms occur when the Earth's magnetic field is weakened as a result of the enhancement of the ring current around the Earth. Some studies [e.g. Echer *et al.*, 2008, Gonzalez and Tsurutani, 1987] have revealed that the component B_z of the interplanetary magnetic field is correlated with geomagnetic storms since if B_z is southward, the reconnection with the dayside magnetopause occurs. Thus, the direction of the CME propagation and the orientation of its flux rope are relevant properties for space weather forecasting.

Since CMEs are closed structures composed by mass and magnetic field (flux rope) ejected from the Sun, they have been related to *moving* type IV radio bursts. Because type IV burst sources are produced by confined non-thermal electrons, their evolution could give a diagnostic of the CME development in the low corona.

Pick and Vilmer [2008] propose that radio images of type IV radio bursts at metric wavelengths can be used to track the early evolution and extension of CMEs in the low corona before they become visible in coronographic images. Likewise, since the sense of polarisation of type IV radio sources is directly related to the magnetic field configuration where the sources are located, the characterisation of the source polarisation could provide an idea about the magnetic field direction of the erupted flux rope.

N	Date	LASCO CME		Origin		
		t_0 [UT]	Width	Type	t_0 [UT]	Coordinate of the AR
(1)	(2)	(3)	(4)	(5)	(6)	(7)
1	26 April 2008	14:30	Partial Halo	Flare	13:50	N10°E10°
2	3 April 2010	10:33	Halo	Flare +Filament eruption	08:50	S22°W29°
3	4 March 2012	11:00	Halo	Flare	10:29	N16°E65°

TABLE 3.1: Table of events: event number (col. 1), date (col. 2), time (col. 3), width of the CME (col. 4), type of origin (col. 5); onset time (col. 6) and coordinates of the AR (col. 7).

As a first stage of a study about this subject, we select three CME events associated with type IV radio sources and examine if the direction of CME propagation and the CME extension can be anticipated by the evolution of associated type IV bursts observed with the NRH at 150.9 MHz.

Subsequently, we want to explore the possibility of predicting the orientation of B_z in the erupting flux rope from the characterisation of the polarisation of the associated type IV radio sources at the Sun. We also want to compare the direction of the flux rope inferred from the polarisation of type IV burst sources at the Sun with the orientation of the B_z of the associated ICME begin aware that CMEs can interact with previous CMEs and with the solar wind magnetic field during their travels to the Earth [Lavraud and Rouillard, 2014]. From this comparison one can investigate if the polarisation of type IV radio bursts can be used as a predictor of geomagnetic storms. In this chapter we present an introduction about radio source polarisation and an initial characterisation of the polarisation of three coronal type IV radio bursts with the aim to be extended in a future work.

3.1 Relationship between the CME Propagation and Extension and the Motion and Extension of Radio Sources

The events used in this section to illustrate the study of radio sources in terms of their spatial evolution and polarisation. These events were selected firstly by inspection based on their evolution in the 1D dynamic plots obtained from NRH data. The sample includes two Earth-directed CME events, one from Salas-Matamoros and Klein [2015] and the other (on 2008 April 26) from Salas-Matamoros, Klein, and Rouillard [2016], and a limb CME event from the ISEST CME catalog[1].

Table 3.1 contains the parameters of the selected CMEs (Cols. 3 and 4) as well as the parameters of the associated origin on the solar disc (Cols. 5-7). The initial times, t_0, in

[1] http://solar.gmu.edu/heliophysics/index.php/The_ISEST_Master_CME_List

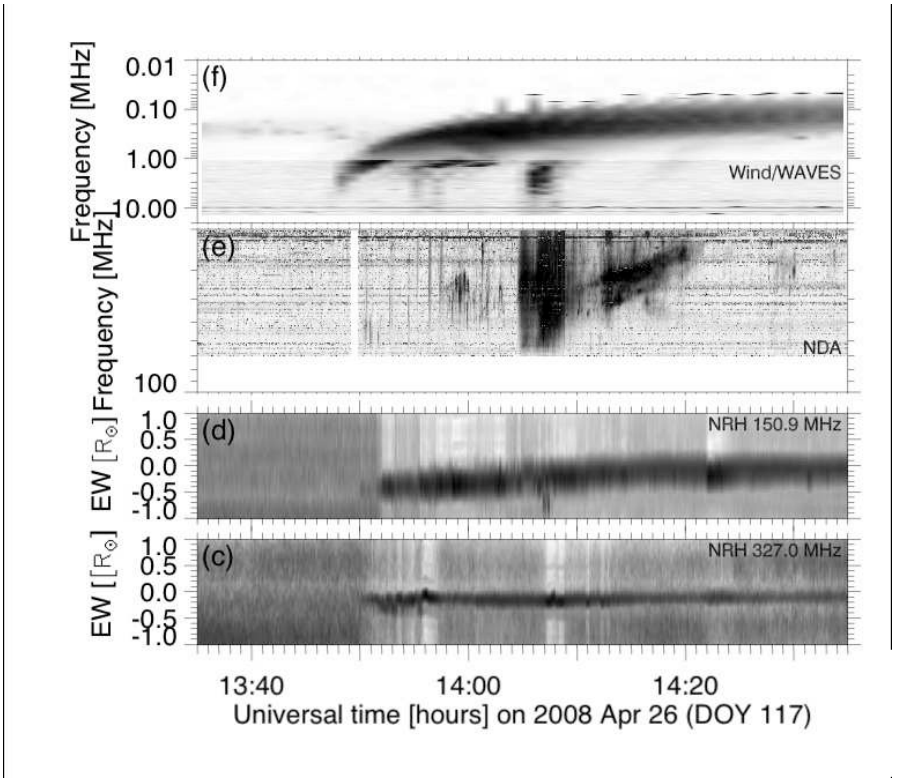

FIGURE 3.1: 1D images and dynamic spectra of the event on 2008 April 26. Two bottom panels: 1D images projected onto the solar east-west direction at 150 and 327 MHz (y axis graded in solar radii). Top panels: dynamic spectra between 70 MHz and 10 kHz.

columns 3 and 6 denote the CME first appearance in coronographs and the onset of the flare, respectively. The flares as origin related to the events were identified from EIT and SDO images and the locations were obtained from the Flare Locator Image in the SDO package archived in SolarMonitor data base[2]. The filament eruption associated with the event 2 was observed in STEREO B EUVI 304 images.

3.1.1 Identification of Type IV Radio Burst Sources

To identify the type IV sources associated to the CMEs in Table 3.1, we firstly analyse the 1D projection of the images onto the east-west (EW) direction as well as the dynamic spectra of each event.

The development of the CME associated with the event on 2008 April 26 has been studied in detail by Huang *et al.* [2011] and Salas-Matamoros, Klein, and Rouillard [2016]. Figure 3.1 shows the 1D images and dynamic spectra of the event. We observe a long lasting source at 327 MHz in the 1D images remaining almost at the same location (with the exception of some fluctuations between 13:50 UT and 13:57 UT) during the

[2] https://solarmonitor.org/

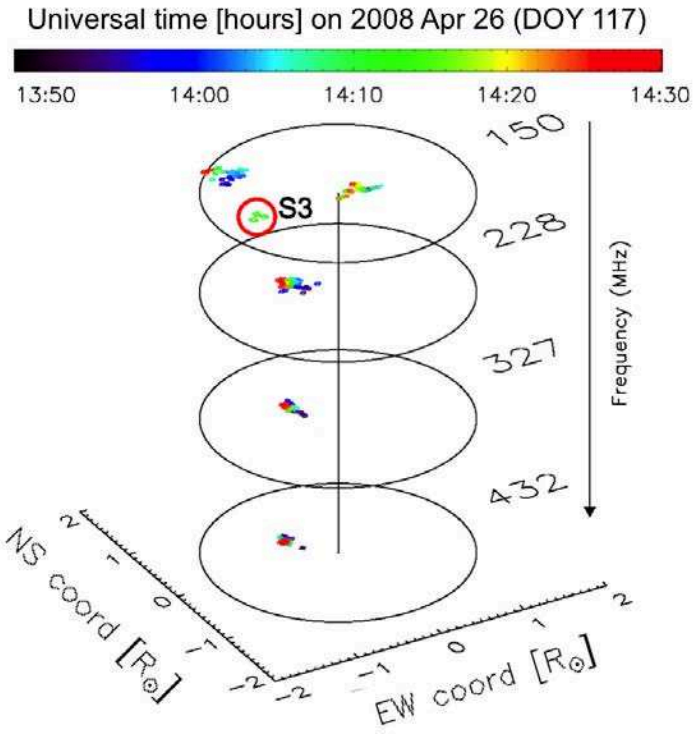

FIGURE 3.2: 4D multifrequency plot showing the time evolution of the peak position in each image of the NRH at four frequencies in the event on 2008 April 26. Time is represented by the colour of the plot symbol, as indicated in the colour bar at the top. Figure by Salas-Matamoros, Klein, and Rouillard [2016].

observation time. This emission starts at the flare onset (13:50 UT) as the source at 150.9 MHz which presents a slight motion to the eastern limb until 14:05 UT where the motion is towards the central meridian. The dynamic spectrum reveals no type IV bursts at frequencies between 20-80 MHz.

The motion of the source is confirmed by the evolution in time of the location of their maximum intensity at different frequencies presented in Figure 3.2. We observed that at higher frequencies the source remains at the place of the post-flare loops location. The motion of the source at 150.9 MHz is considered as evidence of the existence of a *moving* type IV burst that can be associated to the expansion of the magnetic structure.

On the other hand, the dynamic spectrum between 20-80 MHz of the event on 2010 April 3 in Figure 3.4 shows a type IV burst with a clear drift after ≈ 09:40 UT. This event also presents continuum sources at 150.9 MHz and 327 MHz which are time related to the flare onset (08:50 UT) as observed in the two bottom panels in Figure 3.4. Two sources are distinguished at 327 MHz between 09:10 and 09:50 UT while at ≈ 09:20 UT an increase of the source extension at 150.9 MHz is observed followed by a slight motion

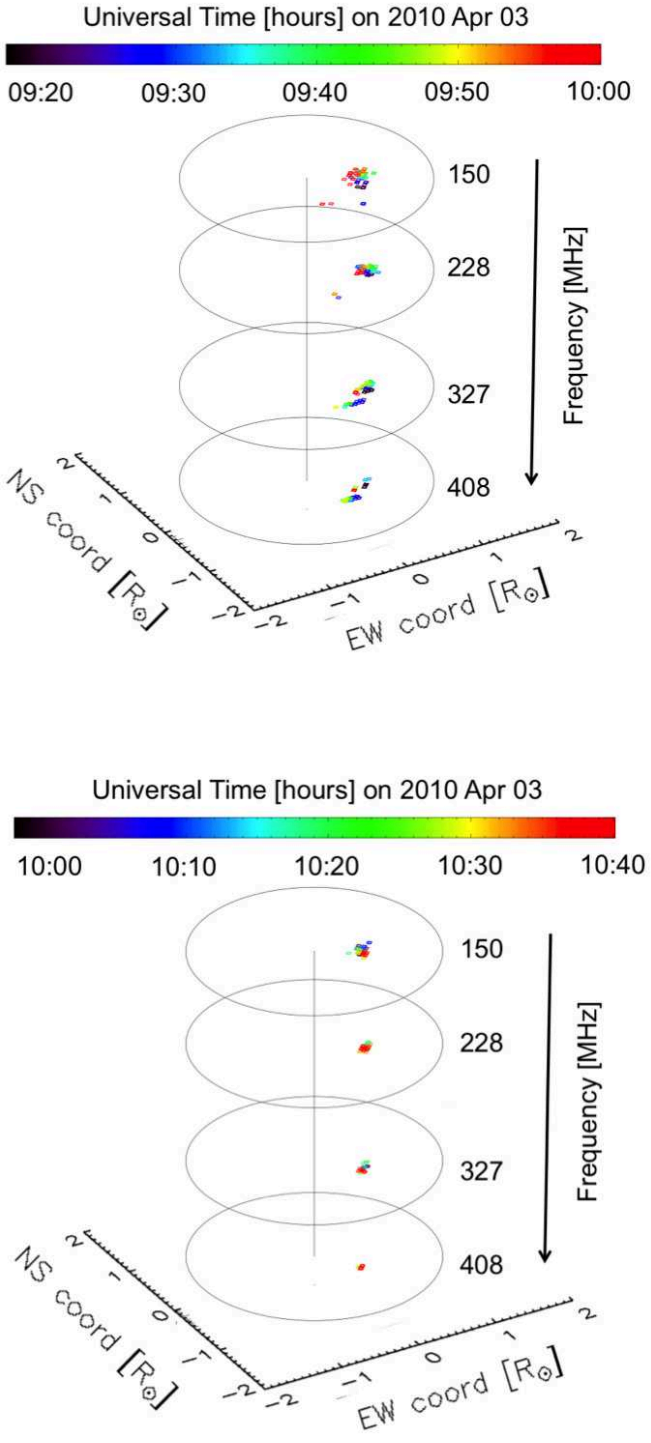

FIGURE 3.3: 4D multifrequency plot showing the time evolution of the peak position in each image of the NRH at four frequencies in the event on 2010 April 3. Time is represented by the colour of the plot symbol, as indicated in the colour bar at the top.

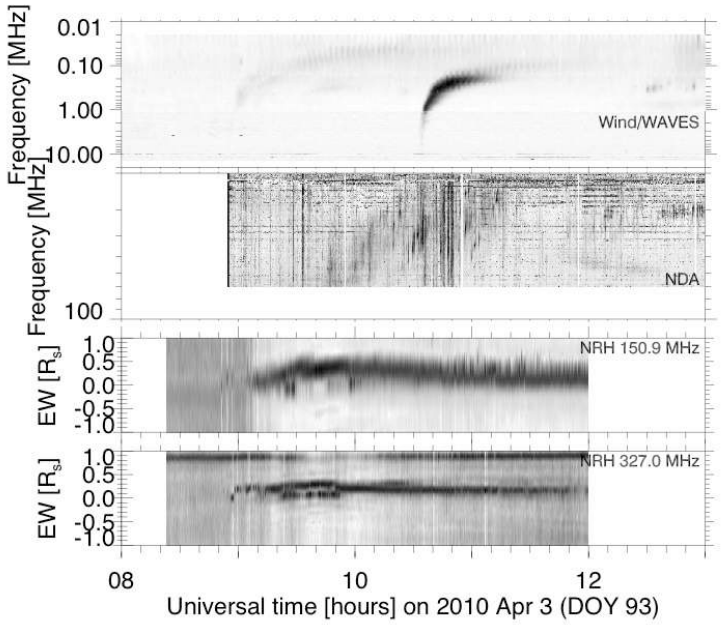

FIGURE 3.4: 1D images and dynamic spectra of the event on 2010 April 3. Two bottom panels: 1D images projected onto the solar east-west and north-south direction at 150 MHz (y axis graded in solar radii). Top panels: dynamic spectra between 70 MHz and 10 kHz.

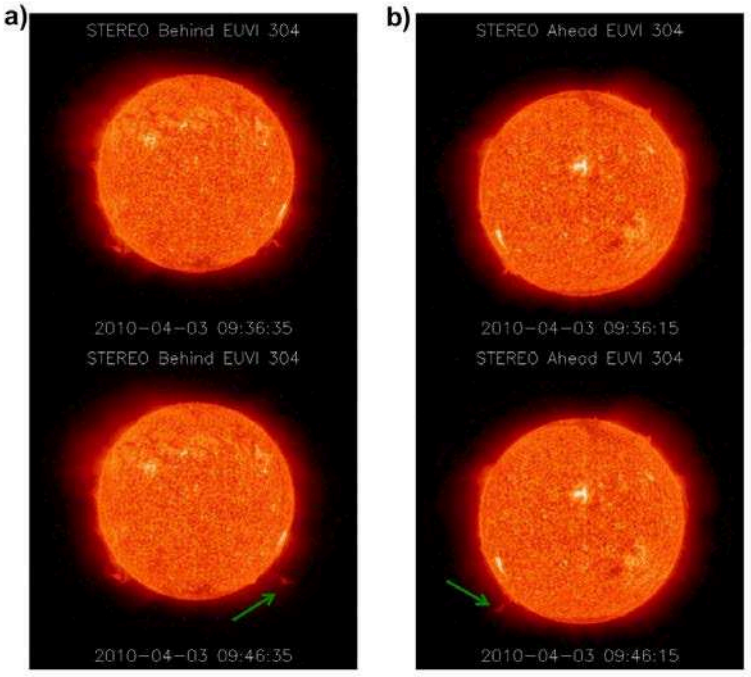

FIGURE 3.5: Compilation of EUVI 304 images by STB (a) and STA (b) from where the filament eruption associated to the event on 2010 April 3 was observed at the south hemisphere. The green arrows in a) and b) show the location of the filament.

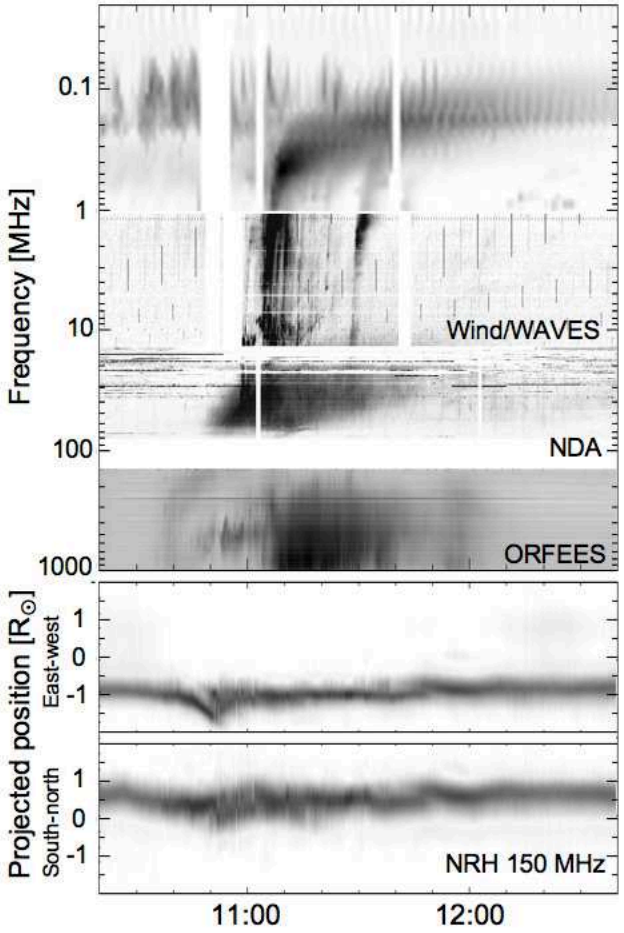

FIGURE 3.6: 1D images and dynamic spectra of the event on 2012 March 4. Two bottom panels: 1D images projected onto the solar east-west and north-south direction at 150 MHz (y axis graded in solar radii). Top panels: dynamic spectra between 70 MHz and 10 kHz.

until 09:40 UT. A new motion of this source starts at about 09:40 UT which coincides in time with the filament eruption observed by both STA and STB spacecraft (Figure 3.5).

After 10:00 UT the source at 150.9 MHz has a broader extension and its motion is now towards the central meridian. The evolution in time of the maximum intensity position of the sources at different frequencies is shown in Figure 3.3. The observed systematic motion of the source positions confirms that the CME of this event is associated with a *moving* type IV burst.

Finally, 1D images at 150.9 MHz of the event on 2012 March 4 in the two bottom panels of Figure 3.6 also show a long lasting emission at the place of the AR NOAA 11429 which could be identified as a noise storm. This noise storm is not related to the type IV bursts studied in this event which start at the onset of the flare (10:29 UT). After the flare onset a movement of the source (*moving* type IV burst) is detected towards the eastern limb while another source remains at the location of the AR. This movement is

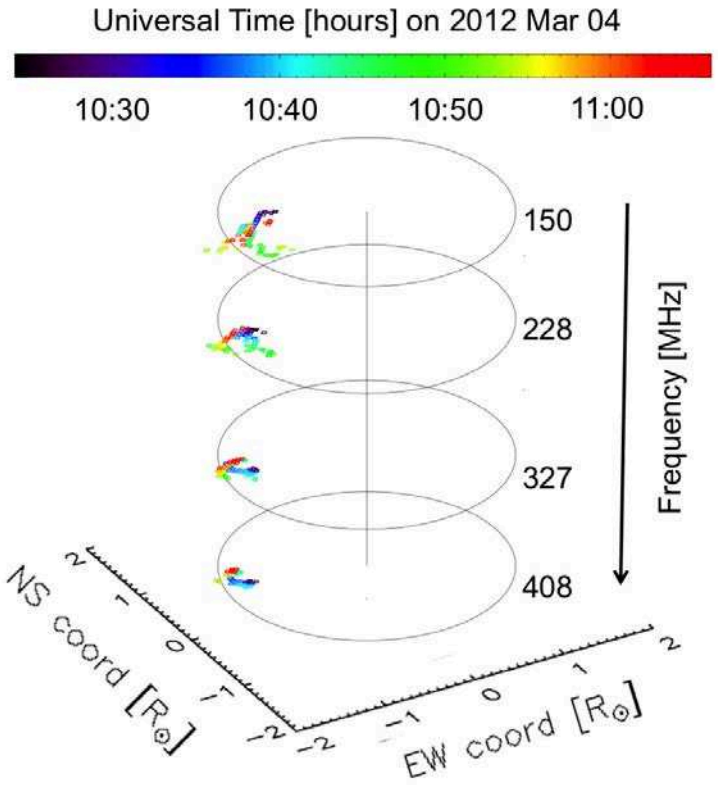

FIGURE 3.7: 4D multifrequency plot showing the time evolution of the peak position in each image of the NRH at four frequencies in the event on 2012 March 4. Time is represented by the colour of the plot symbol, as indicated in the colour bar at the top.

confirmed by the time evolution of the location of the maximum intensity of the sources at four frequencies shown in Figure 3.7. Besides, a faint drifting feature is also observed at ≈10:40 UT in the dynamic spectrum between 110 and 1000 MHz which can be the high frequency counterpart of the *moving* type IV burst observed at 150.9 MHz.

The dynamic spectrum between 20-80 MHz in Figure 3.6 (third panel from the bottom) presents a broadband emission with a drift that starts when the *moving* source at 150.9 MHz disappears at about 10:50 UT. This *moving* type IV burst at lower frequencies can be the continuation of the emission observed at 150.9 MHz and is accompanied by type III bursts which appear well after the flare onset. An additional broadband feature is also observed between 10:50 UT and 11:40 UT without any drift in the dynamic spectrum between 110-1000 MHz which coincides with the possible *stationary* type IV burst observed in the 1D NRH images in Figure 3.6.

From this observational analysis, we have identified *moving* type IV radio bursts associated to the three CMEs studied here. Since the events on 2008 April 26 and 2010 April 3 originated on the solar disc, the motion of the associated type IV sources was

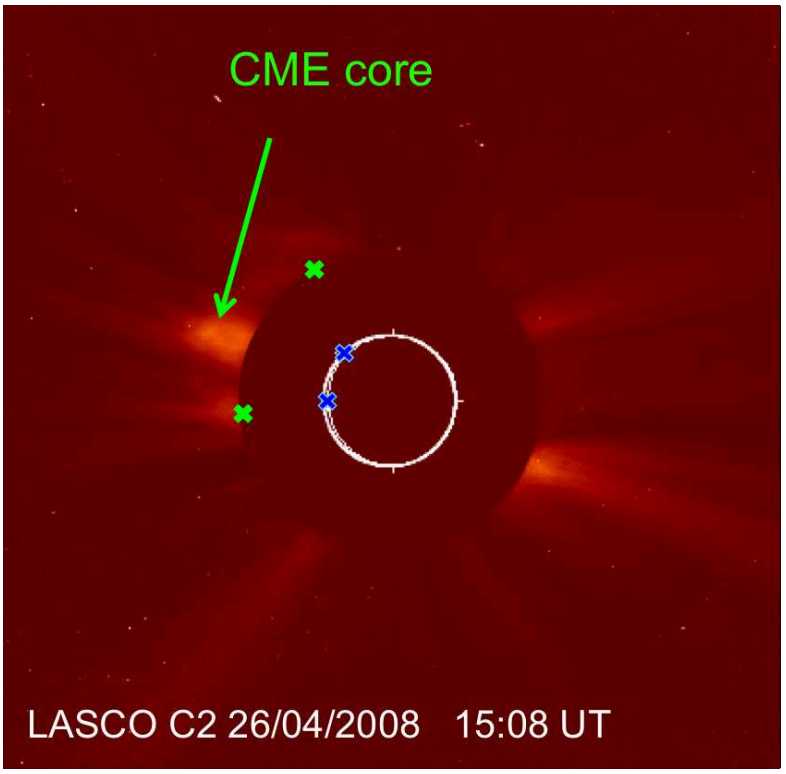

FIGURE 3.8: Superposition of the minimum angular width of the radio source at 150 MHz (marked by blue crosses) on white light image observed by STB COR2 showing the CME on 2008 April 26. The green arrow points the CME core while the green crosses mark the angular width of the CME.

inconspicuous while the clearest *moving* type IV burst was the one associated with the event on 2012 March 4 whose origin was localised close to the limb.

3.1.2 Comparison between the Extensions and Locations of CME and the Associated Type IV Radio Sources

In this section we compare the CME position angle and angular width with the extension and location of the associated type IV burst sources.

As was presented in last section, the event on 2008 April 26 was related to a *moving* and a *stationary* type IV bursts at 150.9 MHz. To compare the overall extension of the sources with the angular width of the CME, we identify the maximum separation of the source location at 150.9 MHz in the north-south direction as seen in Figure 3.2. This projection on the solar disc can be seen as a range of position angles of the source at the solar limb. Even though this procedure does not provide the real projection of the radio source, this estimation gives an idea of the maximum angular width of the source. Figure 3.8 shows the superposition of this equivalent source width (marked by blue crosses) on the LASCO C2 image. The CME width is marked by green crosses

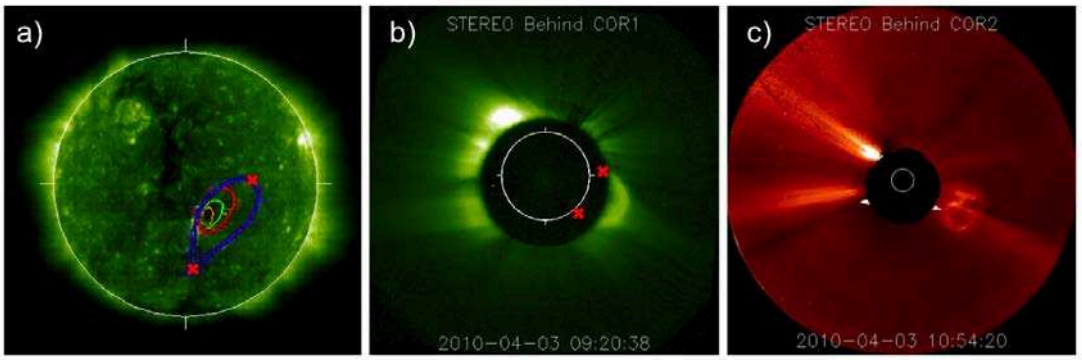

FIGURE 3.9: a) Superposition of the radio sources seen in Stokes parameter I on the EIT SoHO image. The contours of equal brightness temperature at 50 % of the maximum are plotted in colours to represent the different frequencies. Red crosses mark the maximum extension of the source at 150.9 MHz. b) Superposition of the maximum extension of the source in a) projected on the STB field of view on the STB COR1 image. c) STB COR2 image that shows the propagation direction of the CME with respect to the ecliptic plane.

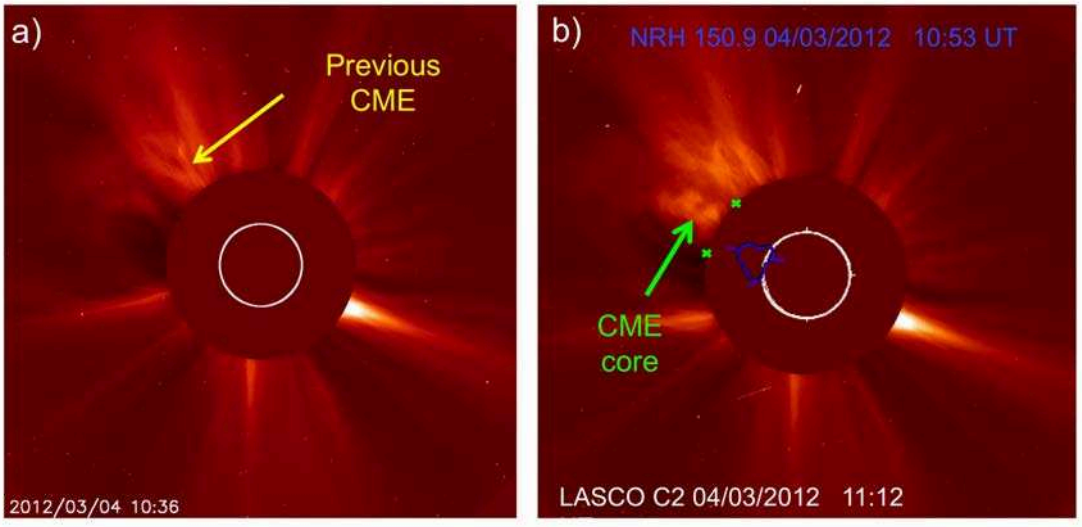

FIGURE 3.10: a) LASCO C2 image showing the previous CME observed at 10:36 UT. b) Superposition of the radio source as observed at 10:53 UT at 150.9 MHz on a white light image of the associated CME by LASCO C2. The core of the CME is pointed by the green arrow and the green crosses point the CME width.

in the LASCO C2 image. From this figure we notice that the CME width seems to correspond as well with the extension of the radio source at 150.9 MHz.

Figure 3.9.a shows the radio source at 150.9 MHz on 2010 April 3 which is located in the southern hemisphere. We identify two extreme points of the source contour (marked by red crosses) and we rotate the locations to obtain the position of these two points in the plane of the sky observed by the STB spacecraft (Fig.3.9.b). We superpose these two points on the STB COR1 image to compare the extension of the radio source with the CME extension. We observe that the two points are very close to the CME flanks.

The event on 2012 March 4 was preceded by a CME near the location of the CME related to the studied event as is shown in Figure 3.10.a. If we consider only the CME observed at 11:00 UT the extension of the source at 150.9 MHz on 2012 March 4 reflects very well the width of the CME (represented by the green crosses) observed by LASCO C2 as presented in Figure 3.10.b. We observed that the two sources close to the limb coincide with the CME flanks while the *moving* source concurs with the CME core.

Even though we have described only three events, the observations reveal that type IV bursts could be related not only with the propagation but also with the extension of CMEs in the low corona. These results support the idea of considering type IV bursts at 150.9 MHz as an indicator of the CME flux rope in the low corona. In the next section we investigate if we can obtain the magnetic field orientation of the flux rope based on the polarisation of these type IV sources.

3.2 Polarisation of Radio Sources

3.2.1 Polarisation of Electromagnetic Radiation

Plane electromagnetic waves are transverse in a dielectric medium and the x and y components of both electric and magnetic fields for a wave that propagates in the z direction obey the same wave equation whose solutions for the electric field ($\vec{E}$) of a monochromatic wave are

$$\begin{aligned} E_{\mathrm{x}} &= E_1 \cos(\mathrm{kz} - \omega \mathrm{t} + \delta_1) \\ E_{\mathrm{y}} &= E_2 \cos(\mathrm{kz} - \omega \mathrm{t} - \delta_2) \\ E_{\mathrm{z}} &= 0 \end{aligned} \tag{3.1}$$

here k=$\frac{2\pi}{\lambda}$, where λ is the wavelength and $\omega = 2\pi\nu$ where ν is the frequency. The tip of the electric field vector of the wave (Eq. 3.1) is an ellipse whose equation is given by

$$(\frac{E_{\mathrm{x}}}{E_1})^2 + (\frac{E_{\mathrm{y}}}{E_2})^2 - 2\ \frac{E_{\mathrm{x}}}{E_1}\ \frac{E_{\mathrm{y}}}{E_2}\ \cos\delta = \sin^2\delta, \qquad \text{with } \delta = \delta_1 - \delta_2 \tag{3.2}$$

Here δ is the phase angle and sinδ determines the sense of the polarisation. The total Poynting flux of the polarised wave is the sum of the fluxes of two orthogonal, but otherwise arbitrary directions as

$$S_0 \equiv E_1^2 + E_2^2. \tag{3.3}$$

Since sinδ determines the sense in which the wave vector is rotating:

If sin δ > 0 then the emission is right-handed polarised

If sin δ < 0 then the emission is left-handed polarised

Also, if $\delta = \mathrm{m}\pi;\ \mathrm{m} = 0, \pm1, \pm2, ...$ then $\vec{E}$ is linearly polarised while if sin $\delta = \frac{\pi}{2}(1 + \mathrm{m})$ with m=$0, 1, \pm2, \pm3, ...$ is circularly polarised and Equation 3.2 reduces to the equation of a circle because $E_1 = E_2 = E$.

3.2.2 Stokes Parameters

To describe the state of polarisation of a monochromatic wave three independent parameters are needed: the two amplitudes of $\vec{E}$ and the relative phase δ. To visualise the different states of polarisation of a wave, one can use the Poincaré sphere which relates the polarisation states and the points on the sphere. So, the equator represents linear polarisation, the north pole and south pole correspond to right-circular and left-circular polarisation respectively.

The points on the sphere in cartesian coordinates are the definition of Stokes parameters given by

$$\begin{aligned} S_0 = I &= E_1^2 + E_2^2 \\ S_1 = Q &= E_1^2 - E_2^2 \\ S_2 = U &= 2\ E_1\ E_2\ \cos\delta \\ S_3 = V &= 2E_1\ E_2\ \sin\delta \end{aligned} \tag{3.4}$$

As was described in Chapter 2, the NRH consists on two interferometers disposed in a T shape. Both branches, east-west and north-south, register two orthogonal linear polarisations corresponding to both components E_x and E_y in Equation 3.1. The signal from the orthogonal dipole is correlated under the assumption of not having linear polarisation to obtain the stokes parameter V. The hypothesis of no detection of linear polarisation is ascribed to the effects of the Faraday rotation in the corona. This effect describes as linearly polarised wave can be subjected to a rotation of the polarisation plane during its path through a magneto-ionic medium (e.g. Ramaty [1969], Wilson, Rohlfs, and Hüttemeister [2013]) which change of the position angle (Θ) of the wave is given by Alissandrakis and Chiuderi Drago [1995]

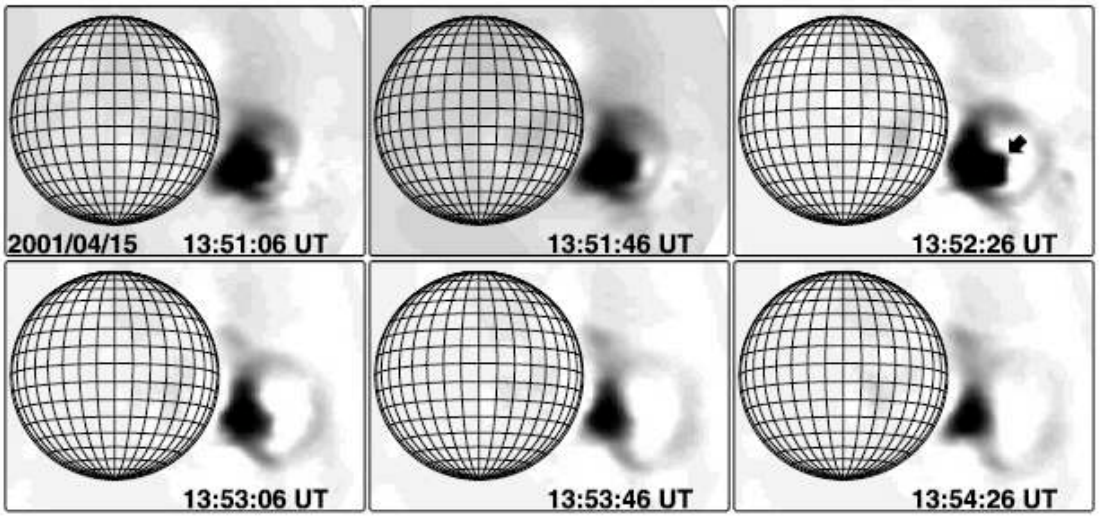

FIGURE 3.11: Series of NRH images at 410 MHz showing the evolution of the radio CME on 2001 April 15. Figure from Maia *et al.* [2007].

$$\Delta\Theta = 2.6 \times 10^{-17} \lambda^2 \int N \; B_L \; dr \; , \tag{3.5}$$

where λ, N, B_L are the wavelength, electron density and the longitudinal component of the magnetic field respectively. The c.g.s units are used and the integral is performed along the ray path (r). Introducing average values for N and B_L in Equation 3.5 we can calculate $\Delta\ \Theta$ for the observing frequencies of NRH including the bandwidth ($\pm$350 kHz). The high number of rotations indicates that the original linear polarisation is totally cancelled and can only be detected by a receiver with a very narrow bandwidth. Thus, the degree of polarisation can be described by

$$p = \frac{V}{I}. \tag{3.6}$$

3.2.3 How is the Polarisation of Radio Sources Related to the Emission Mechanism of Type IV bursts?

As was discussed in Chapter 2, type IV bursts can be explained in terms of two emission mechanisms: gyrosynchrotron and plasma emission. To distinguish between both, some attempts have been developed in the past. In the study of *moving* type IV bursts Boischot [1957] argue for gyrosynchrotron emission based on two arguments: 1) no observation of the typical dispersion of the source location as the frequency decreases for an expanding source emitting via plasma emission, and 2) the sources were observed at higher altitudes than expected for plasma level.

Expanding structures have been observed (few cases) by radio imaging at the limb [Bastian *et al.*, 2001, Démoulin *et al.*, 2012, Maia *et al.*, 2007]. Radio images in Figure 3.11 show a loop which extends radially from 1.4 $R_\odot$ to 2.1 $R_\odot$. These heliocentric distances are higher than the plasma level at the given frequency of 410 MHz. Thus, Maia *et al.* [2007] conclude that the radio loop results from gyrosynchrotron emission as was also described by Bastian *et al.* [2001]. Later, Bain *et al.* [2014] related, through radio observations, a *moving* type IV burst with the core of the CME and conclude that the type IV burst source emitted via gyrosynchrotron emission.

Nevertheless, if we consider a flux rope description for the erupting structure (in the case of *moving* type IV bursts), we have a core with very high magnetic field strength and high density plasma while the surroundings have less plasma density. So, we may observe plasma emission from the dense core even if the altitude does not correspond to the plasma level in the quiet corona. The usual drift observed in the dynamic spectrum of the *moving* type IV bursts can be then explained either by the expansion of the magnetic structure (a loop for instance) giving a decrease of the magnetic field strength and, as a consequence, the gyro-frequency associated to gyrosynchrotron emission mechanism or by the expansion of the structure resulting in a decrease of the ambient density. Thus, the distinction between the two emission mechanisms of the type IV bursts cannot be done from the classical arguments such as the frequency dispersion of the source positions [e.g. Boischot, 1957].

An important aspect to consider in order to distinguish the emission mechanism in type IV bursts is the polarisation of the source. Ramaty [1969] shows that, for homogeneous spatial electron distributions (transfer equations solved for large Faraday rotations), the gyrosynchrotron process produces moderate polarisation (less than 50 % of polarisation degree) where the polarisation in the extraordinary mode is observed in the optically thin regime while in the optically thick part of the spectrum the polarisation in the ordinary mode dominates. On the other hand, the fundamental plasma emission shows polarisation in the ordinary mode because the extraordinary mode cannot propagate in a narrow frequency range above the plasma frequency, while the harmonic plasma emission is expected to show weak polarisation or no polarisation at all.

Brightness temperature of the sources is also related to the emission mechanism. Higher brightness temperatures ($\geq 10^9$ K) cannot be explained by electrons emitting via gyrosynchrotron. As was discussed in Chapter 2, there is a limit to the brightness temperature that an incoherent emission process such as gyrosynchrotron cannot exceed. Thus, this high brightness temperature involves a very large number of energetic electrons not consistent with this mechanism. Since gyrosynchrotron and plasma emission present different polarisations and brightness temperature profiles, the diagnostic of the

polarisation and brightness temperature of the type IV burst sources can be used to distinguish the emission mechanism.

To establish the starting point of the study described at the beginning of this chapter, we explore for specific cases if we can constrain the orientation of the magnetic field in the corona based on the polarisation of type IV burst emission. In the next section we start the examination with a description of three events selected because of favourable observing conditions such as well-defined type IV bursts and no noise storms whose polarisation might disturb the determination of the type IV burst polarisation. We characterise the polarisation of each type IV burst associated with the CMEs and determine the emission mechanism based on the polarisation and brightness temperature criteria. Because we studied only few events, the results presented here are very preliminary and a systematic evaluation of the polarisation of type IV bursts is planed to be developed as part of the future work.

3.3 Characterisation of the Polarisation of Type IV Radio Bursts

The polarisation of the radio sources together with their brightness temperature profiles, have been examined in order to inspect the possible emission mechanism. Each event is described and characterised in detail in the following subsections.

3.3.1 Event on 2008 April 26

To study the polarisation of the sources associated with this event, we use the Stokes parameters I and V observed by NRH. Figure 3.12 presents the location of the sources seen in the Stokes I and Stokes V parameters (b and c respectively) as well as the MDI magnetogram (a). The contours of equal brightness temperature in Stokes parameters I and V are plotted in colours according to the frequency. In Figure 3.12.a the AR shows two polarities: the positive polarity is located north-west of the neutral line while the negative polarity is south-east of it.

Additionally, we obtain the Stokes I and V profiles along two lines across the sources at both frequencies. The two cuts are represented by the blue and orange lines in Figures 3.13.a and 3.14.a. Even though the blue (or the orange) cut lines in Stokes parameter I and in Stokes parameter V are not the same, each line crosses the sources seen in each Stokes parameter. We select different cuts in order to compared the location of the sources seen in both Stokes parameters, I and V.

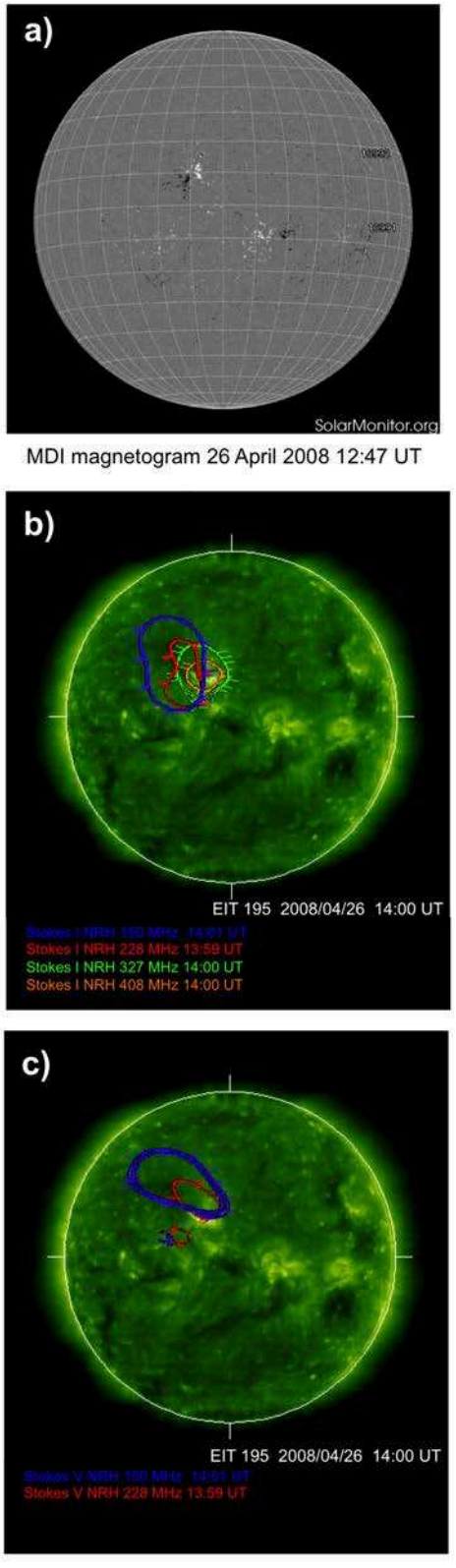

FIGURE 3.12: a) MDI magnetogram on 2008 April 26. b) Superposition of radio sources seen in Stokes parameter I on the EIT SoHO image at 14:00 UT. The contours of equal brightness temperature at 50 % of the maximum are plotted in colours to represent the different frequencies. c) Superposition of radio sources seen in Stokes parameter V at 50 % of the maximum on he EIT SoHO image at 14:00 UT.

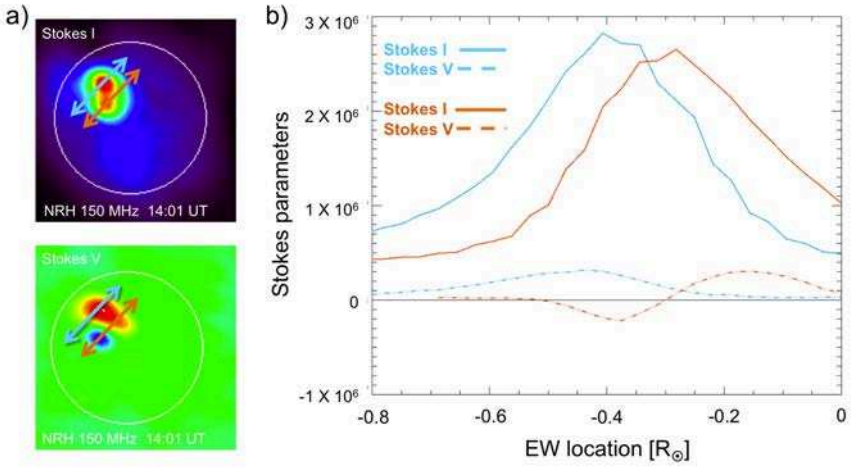

FIGURE 3.13: a) Cuts of the sources observed at 150.9 MHz by NRH. Blue and orange arrows represent the lines along which we obtain the Stokes parameter I profile as a function of EW location. b) Stokes parameters I and V profiles of the cuts as a function of the EW location. The profiles are plotted in the same colours as the cuts traced in a). Solid lines refers to Stokes parameter I while discontinuous line refers to Stokes parameter V.

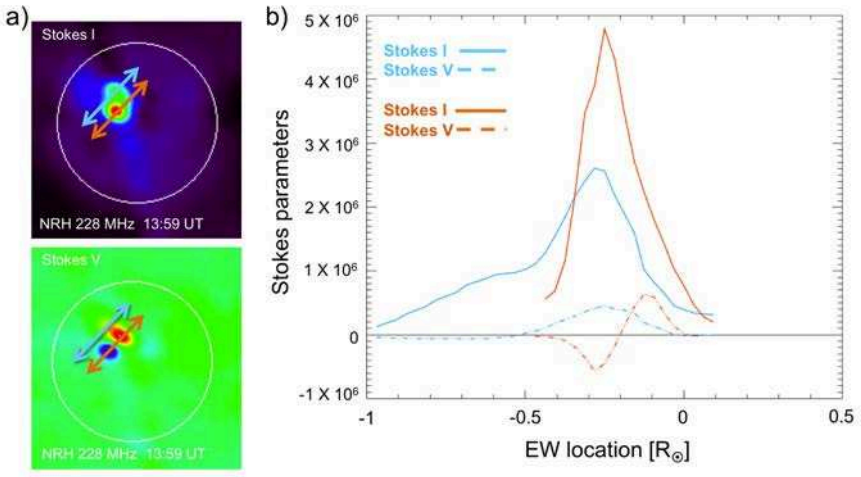

FIGURE 3.14: Cuts of the sources observed at 228 MHz by NRH. As in Figure 3.13.

The profiles in Figures 3.13.b and 3.14.b are the Stokes parameters I and V (solid and dashed lines respectively) plotted as a function of the east-west (EW) location. These profiles contain the closest values of Stokes parameters to each cut line. In this event, we notice that orange cuts cross only one source at each frequency which are related to two different polarisations while the blue cuts cross also only one source at each frequency but they are positively single polarised sources.

The location of the sources in Stokes I and V at 150.9 and 228 MHz implies one positive single polarisation associated to the expansion of the magnetic structure and the other bipolar source related to the *stationary* type IV bursts located over the post-flare loops. Unfortunately the data of Stokes parameter V at the higher frequencies (327 and

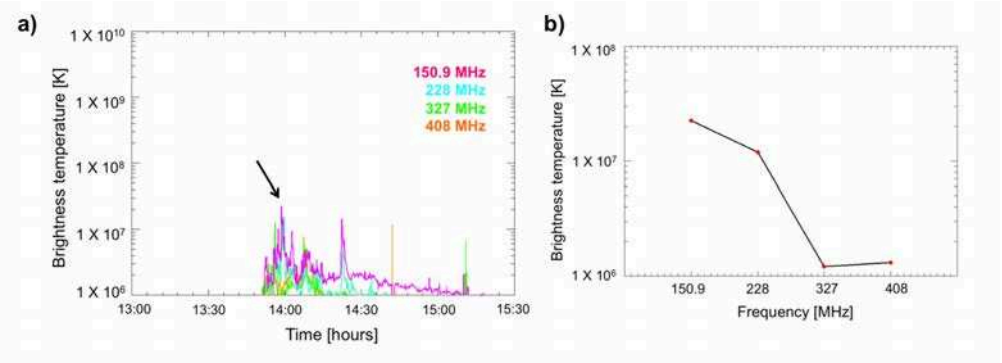

FIGURE 3.15: a) Brightness temperature profile as a function of time within the region where the radio sources were observed. The colours represent the different frequencies. b) Brightness temperature spectrum at the peak marked by the black arrow in a).

432 MHz) contain too much noise and the polarisation of the sources cannot be well identified.

From the comparison of source positions in Stokes parameters V with Figure 3.12, we notice that the positive sources in Stokes V are located above the positive polarity of the AR while the negative sources are above the negative polarity. Since a positive Stokes parameter V means a left hand polarised source, we find from the sense of polarisation and the direction of the magnetic field in the underlying photosphere (upward-directed field) that the all sources are polarised in the ordinary mode. Also, from the Stokes parameters I and V in Figures 3.13.b and 3.14.b, we obtain the polarisation degree from the Stokes parameters at the same location. We find maximum polarisation degree values of $< 40\%$ for both cuts at both frequencies.

On the other hand, the brightness temperature profile in Figure 3.15 shows moderate values of less than 10^8 K and a spectrum that would imply an optically thin gyrosynchrotron emission. Therefore, since all radio sources are polarised in the ordinary mode, we conclude that both *moving* and *stationary* type IV sources are plasma emission.

3.3.2 Event on 2010 April 3

In this event, the location and expansion of the sources seen in Stokes parameters I and V shown in Figures 3.16.a and 3.16.b suggest that the sources are emitting from the branch of the magnetic structure located westwards of the inversion line underneath the post-flare loops observed in the EIT image. The Stokes parameter V is positive as shown in the profiles at 150.9 and 228 MHz in Figures 3.17.b and 3.18.b. In this case, the cuts in both Stokes parameters I and V are the same because only one polarisation was observed.

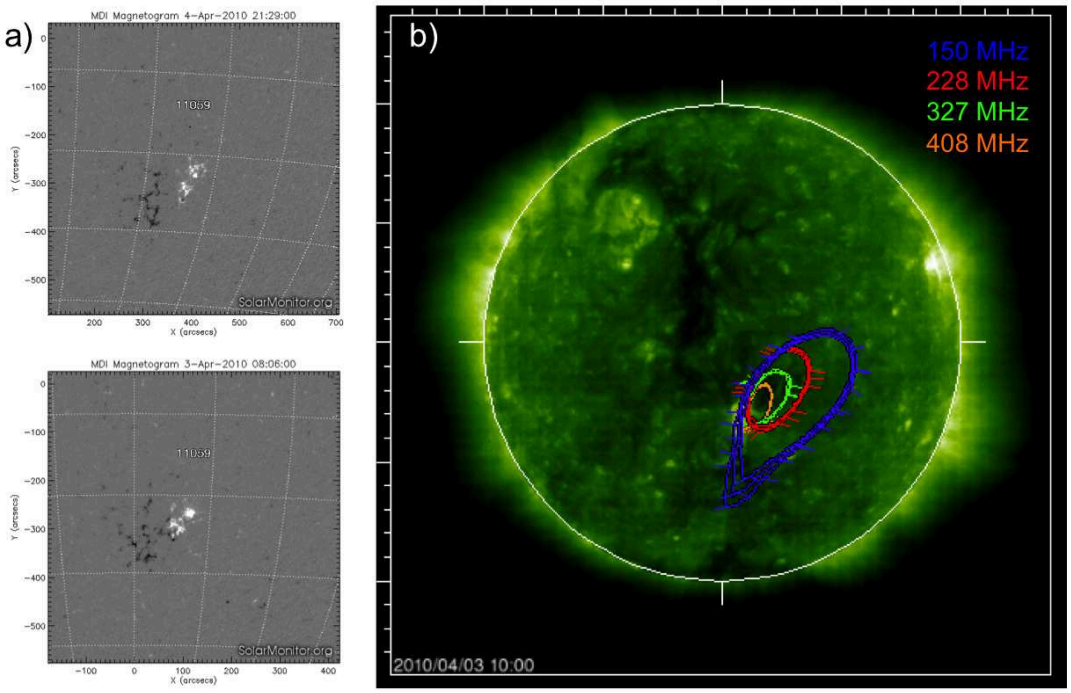

FIGURE 3.16: a) MDI magentograms on 2010 April 3 in the bottom panel and on 2010 April 4 in the top panel. b) Superposition of the sources at different frequencies on EIT image at 10:00 UT.

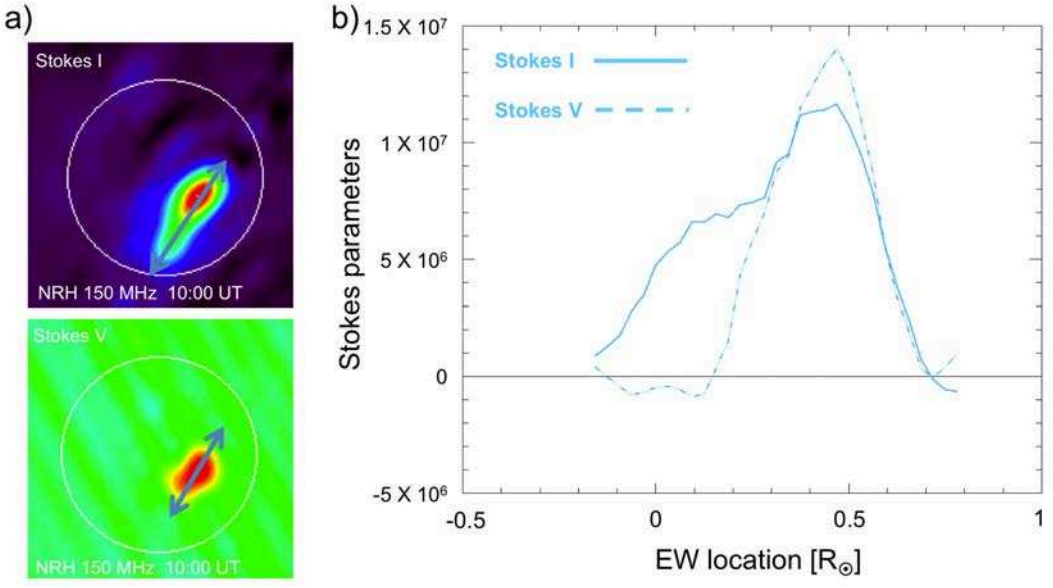

FIGURE 3.17: Cuts of the sources observed at 150.9 MHz by NRH. As in Figure 3.13.

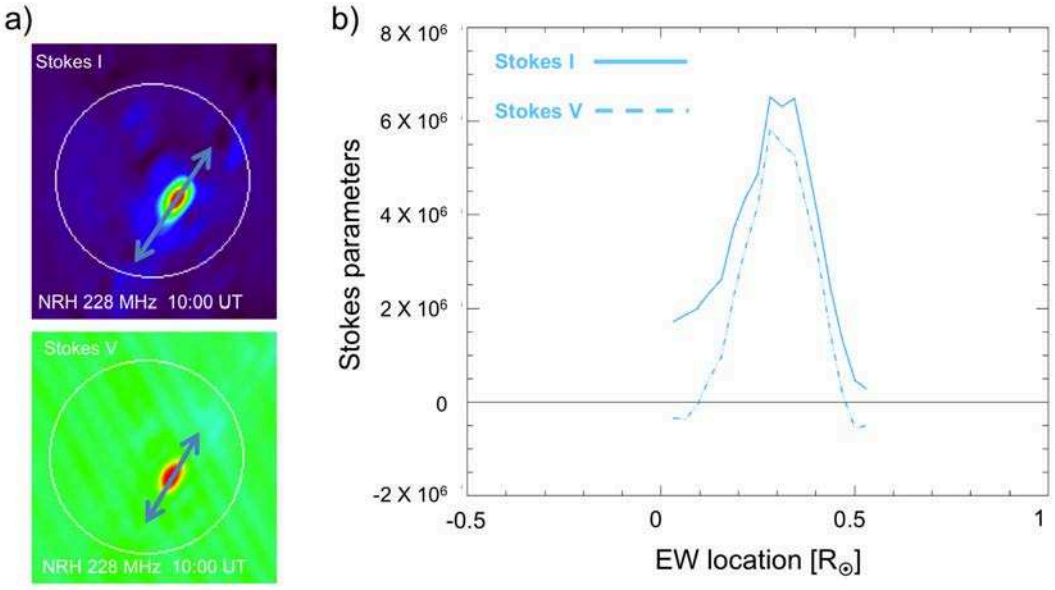

FIGURE 3.18: Cut of the sources observed at 228 MHz by NRH. As in Figure 3.13.

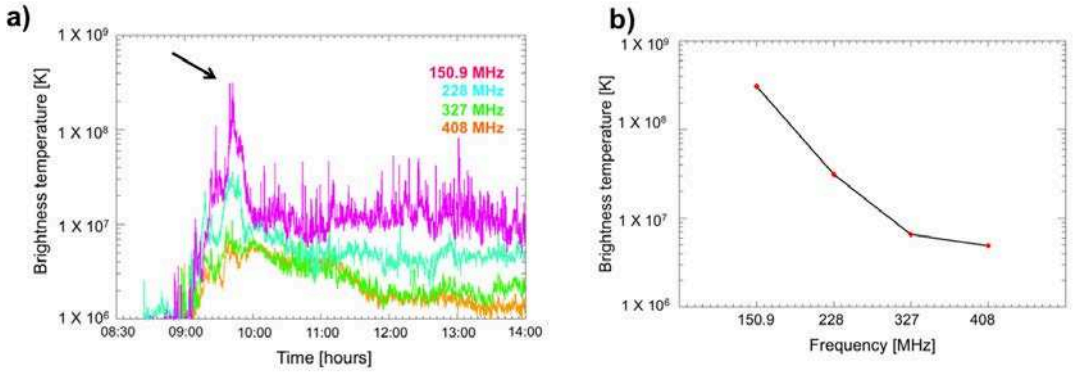

FIGURE 3.19: a) Brightness temperature profile as a function of time within the region where the radio sources were observed. The colours represent the different frequencies. b) Brightness temperature spectrum at the peak marked by the black arrow in a).

On the other hand, the MDI magnetogram in Figure 3.16.a reveals positive polarity of the magnetic field on the western side and negative polarity on the eastern side. Since the sources are located above the positive magnetic polarity and knowing that the sources are left hand polarised (V>0), the emissions are polarised in the ordinary mode. The polarisation degrees at both frequencies deduced from Figures 3.17.b and 3.18.b. are found to be very high (more than 90%). The curves in Figure 3.17 show higher values of Stokes parameter V compared to Stokes parameter I. This probably reveals a calibration problem that must be addressed in the future.

Regarding the brightness temperature profile in Figure 3.19 we observe a high value (more than 10^8 K) at 150.9 MHz and moderate values at higher frequencies (less than 5×10^7 K). Even though the spectrum shows a decrease of the brightness temperature

as frequency increases which could be interpreted as a gyrosynchrotron spectrum in the optically thin regime, we must discard gyrosynchrotron mechanism because of the polarisation degree. Then, based on the polarisation in the ordinary mode, likely a high degree of polarisation, we argue for plasma emission as emission mechanism of both *moving* and *stationary* type IV bursts.

3.3.3 Event on 2012 March 4

To analyse the polarisation of the sources associated with the event on 2012 March 4, we follow the same procedure as in the previous events. The Stokes I and V profiles at 150.9 and 228 MHz are shown in Figures 3.21.a and 3.22.a respectively. The first cut (in blue) reveals one source with negative polarisation while from the second cut (in orange) we distinguish two sources with opposite polarisations. The negative polarised source crossed by the blue cut corresponds to the *moving* type IV burst whose movement was observed in the NRH movies while the sources crossed by the orange cut could be associated with the *stationary* type IV bursts at both frequencies.

From the Stokes I and V profiles, we estimate the maximum polarisation degree related to the two cuts from the Stokes parameters at the same location. We find values of <60% and <80% for the orange cut and the blue cut respectively at 150.9 MHz. Likewise, we find a maximum polarisation degree related to the orange cut of <86% while the blue cut shows maximum value of < 40% at 228 MHz (Figure 3.22.b).

Unfortunately, since the AR is very close to the limb, the identification of the polarity in the region where the sources are located is very difficult and then we cannot give a statement about the polarisation mode of the emission.

Regarding the brightness temperature profile in Figure 3.23, we notice that the values are in general moderate (about 10^8 K) at 150.9 MHz. Nevertheless, even though the general spectrum in Figure 3.23.b seems to be an optically thin gyrosynchrotron spectrum, the brightness temperature is too high at higher frequencies (228-408 MHz) to be interpreted in terms of gyrosynchrotron mechanism. Thus, based on these profiles and on the the polarisation degree of the sources we could suggest plasma emission in the sources. The fact of having different brightness temperature profiles at 150,9 MHz and at higher frequencies supports the hypothesis of having two different electron populations associated to the observed radio sources at different frequencies.

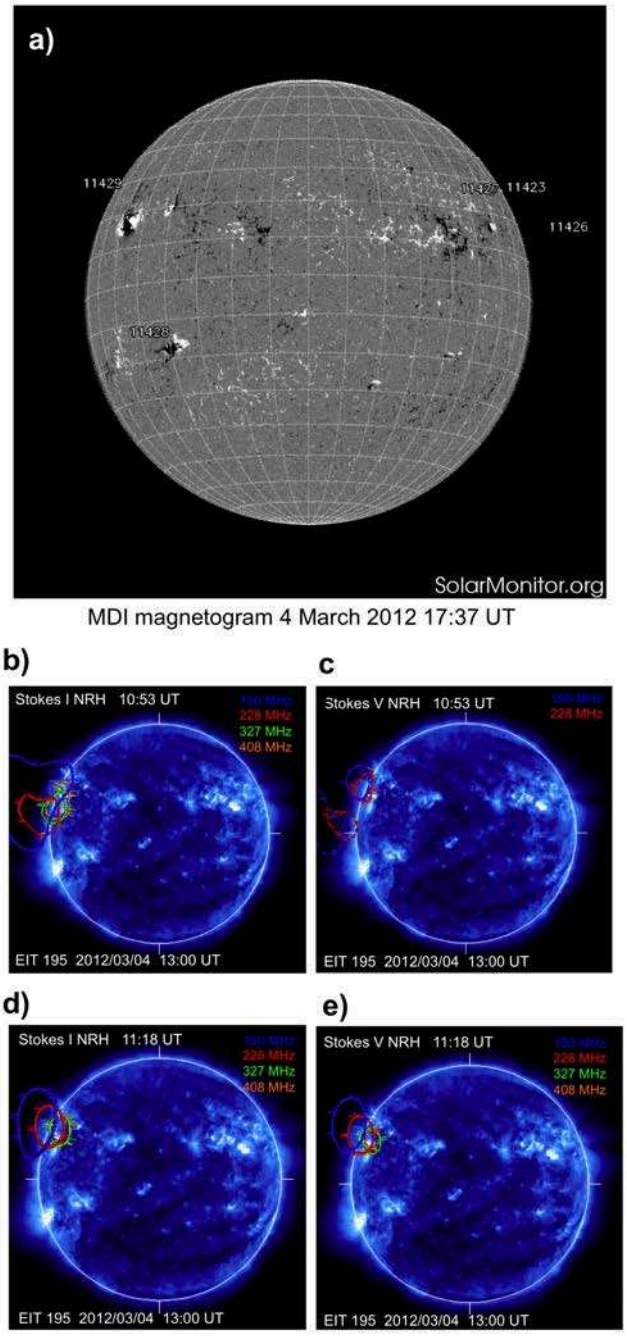

FIGURE 3.20: a) MDI magnetograms on 2012 March 4. b) and d) Superposition of the sources at different frequencies on EIT image at 10:53 UT. c) and e) Superposition of the polarisation location at 150.9 and 228 MHz on EIT image at 10:53 UT

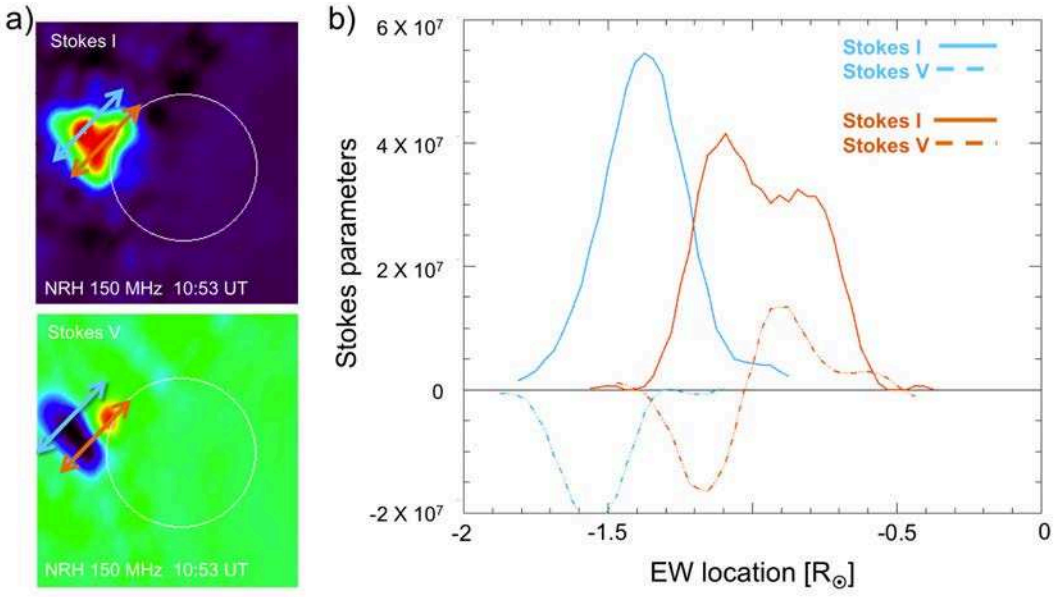

FIGURE 3.21: Cuts of the sources observed at 150.9 MHz by NRH. As in Figure 3.13.

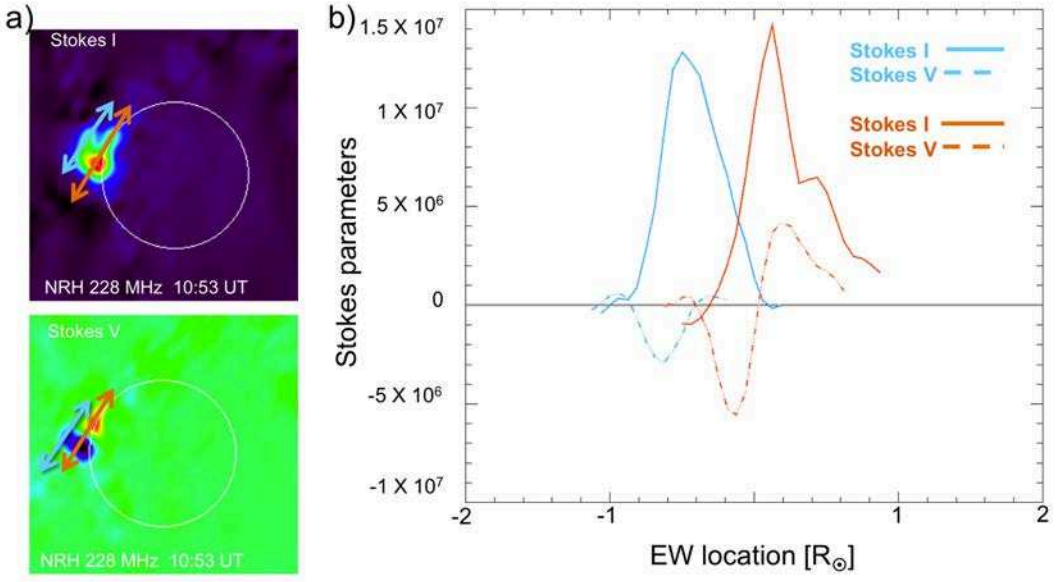

FIGURE 3.22: Cut of the sources observed at 228 MHz by NRH. As in Figure 3.13.

3.4 Preliminary Results

We have identified the type IV bursts associated to the three events. We also have studied the spatial extension and polarisation of the sources. This study reveals some preliminary results:

1. The extensions of the three radio sources at the lowest frequency coincide well with the CME widths. This confirms the statement provided by Pick and Vilmer [2008].

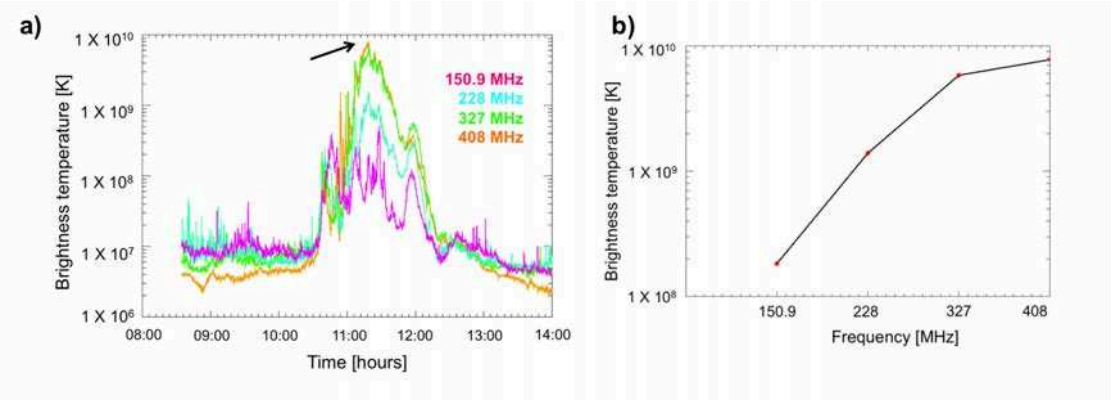

FIGURE 3.23: a) Brightness temperature profile as a function of time within the region where the radio sources were observed. The colours represent the different frequencies. b) Brightness temperature spectrum at the peak marked by the black arrow in a).

2. The location and evolution of the studied radio sources provide an idea about the direction of the CME propagation in the low corona which was confirmed by STEREO images.

3. We found that the identified bipolar sources were associated with *stationary* type IV bursts while the *moving* type IV bursts were identified as single polarised sources.

4. We have found for events on 2008 April 26 and on 2010 April 3 that the *stationary* sources were polarised in the ordinary mode which is consistent with what is expected for sources located at the base of expanding magnetic structures [e.g Wild, 1969]. We also find that the emission mechanism associated to all *moving* type IV sources in this study is plasma emission which supports previous studies [e.g Duncan, 1980, Kai, 1978].

5. With a statement on the emission mechanism of radio sources and the polarisation mode of the radio waves, we could be able to describe the magnetic field orientation of the CME flux rope.

Chapter 4

Radiative Proxies for CME Propagation Speed in ICME Arrival Time Predictions

As was discussed in Chapter 1, CMEs (especially Earth-directed CMEs) are one type of interplanetary structures that can affect the geomagnetic field. As a result, one of the principal aims of space weather forecasting is the prediction of the travel time of these magnetic structures from the Sun to the Earth.

The CMEs are detected remotely by coronagraphs while their interplanetary counterpart, the Interplanetary Coronal Mass Ejections (ICMEs), are detected *in situ*. These observations reveal that CMEs spend between 13 hours and several days on arriving at the Earth. In order to have an advance warning of these disturbances, prediction techniques have been developed based on remote observations and validated by measurements *in situ*. Most techniques to predict the arrival of ICMEs involve two factors which should be known: the radial propagation speed and the interplanetary propagation.

4.1 CME Radial Propagation Speed

Generally, estimations of radial propagation velocities of limb-CMEs are obtained from coronographic observations of the time-height evolution of the CME front projected on the plane of the sky. Figure 4.1 shows an example for the CME propagation speed estimation. Figure 4.1.a presents a compilation of differential images by LASCO/C2 of the CME front projected on the plane of the sky at different times. The height-time

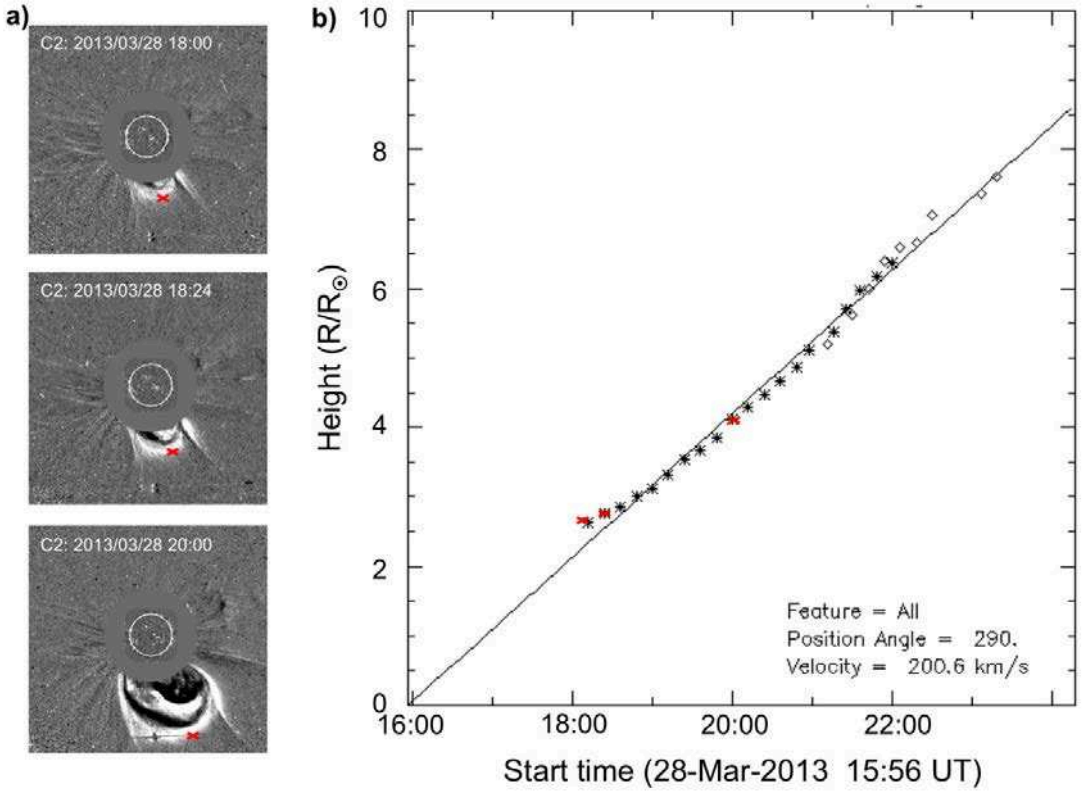

FIGURE 4.1: Evolution of the CME on 2013 March 28 projected in the plane-of-the-sky. a) Differential images by LASCO/C2 showing the radial position of CME front (marked by red cross) at three different times. b) Height-time plot of the CME front propagation where the red cross represent the measure of height and time in shown in coronographic images (a). Height-time plot from LASCO CME catalogue.

plot deduced from this kind of observations is shown in Figure 4.1.b where the points inferred from the images in Figure 4.1.a are shown by red crosses.

However, the apparent properties of the CME observed by coronographs (such as the size and the location) cannot be the true values of the properties for Earth-directed CMEs because they are affected by projection effects. These projection effects arise from the fact that coronographic images show the projection of the 3D CME on the plane of the sky [Burkepile *et al.*, 2004]. Figure 4.2 displays diagrams of different projections onto the plane of the sky of a CME at different longitude positions. For a CME observed at the limb, Figure 4.2.a, the properties as the radius (R), the position angle (λ), the width and the heliocentric distance are the real properties. However, as the CME is observed closer to the solar centre, its properties are distorted by projection effects as the projection on Figure 4.2.c which represents an Earth-directed CME (a halo CME seen by LASCO).

The most relevant property for our propose is the heliocentric distance from which one can obtain the propagation speed as was shown in Figure 4.1. The upward speed

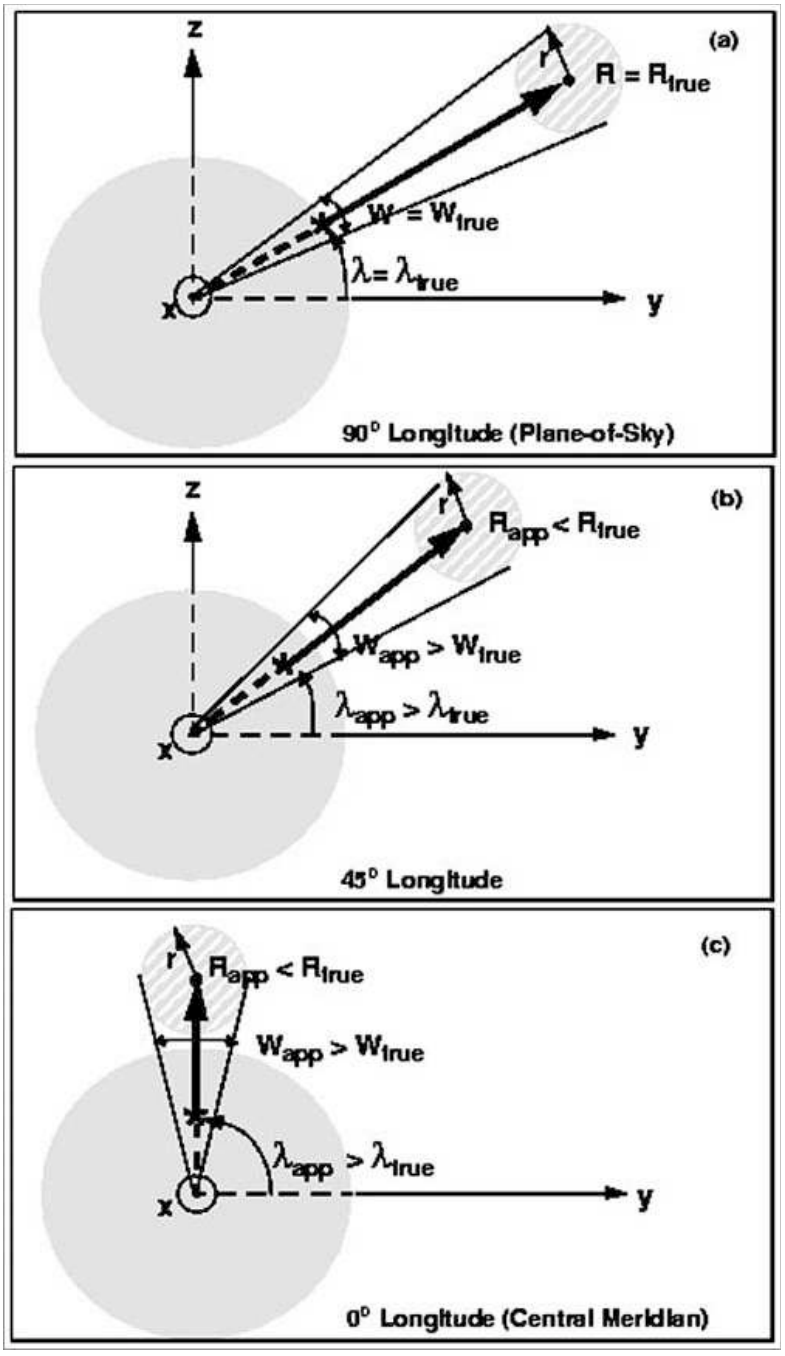

FIGURE 4.2: Schematic projections of CMEs on the plane-of-the-sky at different longitude positions: a) CME center is located in the plane-of-the-sky (above the solar limb) then the apparent properties of the CME, such as size and location, are equal to the true value of each property, b) and c) the distance of the CME to the plane-of-the-sky increases causing its apparent height to decrease and its apparent width and latitude to increase. Figure from Burkepile *et al.* [2004].

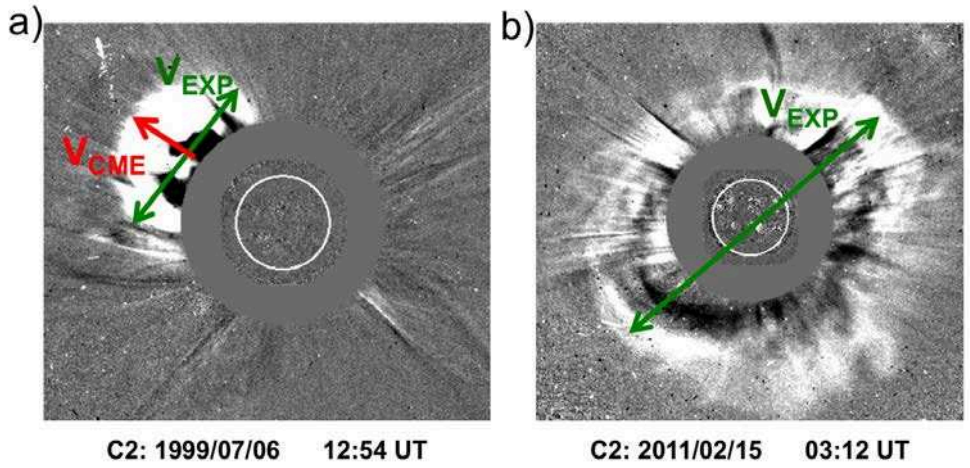

FIGURE 4.3: Two CMEs projected in the plane-of-the-sky observed with LASCO/C2 instrument. a) Propagation speed and expansion speed directions for a limb-CME shown in red and green respectively. b) Only the expansion speed direction (in green) can be observed for Halo CMEs.

(V_{CME}) in the direction of the propagation and the expansion speed (V_{EXP}) projected on the plane of the sky for limb-CMEs are shown in red and green respectively in Figure 4.3.a. The projection effect in the propagation speed increases as the propagation speed direction of CMEs approaches the line-of-sight of the spacecraft. In this way, the propagation speed is not measurable for Earth-directed CMEs by a coronograph on the Sun-Earth line, which sees only the expansion speed as is shown in Figure 4.3.b.

Since V_{CME} cannot be estimated directly from coronographic observations for Earth-directed CMEs, one proxy is needed. Schwenn *et al.* [2005] find a correlation between V_{CME} and V_{EXP} for limb-CMEs. They use this correlation as a proxy for the radial speed of Halo CMEs as

$$V_{CME} = 0.88 \cdot V_{EXP} \tag{4.1}$$

Michalek, Gopalswamy, and Yashiro [2009] find another correlation between V_{CME} and V_{EXP}, taking into account the width of the CMEs,

$$V_{CME} = 1.17 \cdot V_{EXP} \tag{4.2}$$

These estimations can be used for Earth-directed CMEs observed by LASCO coronagraph which was, for many years, the unique coronograph in Space. However, the difference between both correlations shows that different results can be obtained from

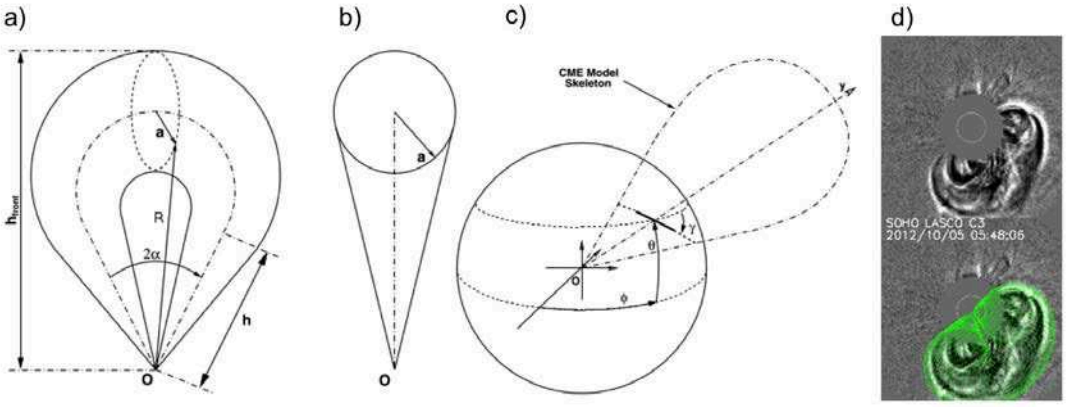

FIGURE 4.4: Graduated Cylindrical Shell modeling. Representations of the model: (a) face-on and (b) edge-on. The dash-dotted line is the axis through the centre of the shell. The solid line represents a planar cut through the cylindrical shell and the origin. O corresponds to the center of the Sun. (c) Positioning parameters. The loop represents the axis through the center of the shell. Figure adapted from Thernisien, Vourlidas, and Howard [2009]. d) Running difference images of the 2012 October 5 CME where in the bottom row, the fitted GCS model is overlaid as the green wire frame. Figure adapted from Shi *et al.* [2015].

different data and then, V_{EXP} as a proxy for V_{CME} is not conclusive. The Solar TErrestrial RElations Observatory (STEREO) was launched on October 2006. This mission has provided a novel view of the Sun-Earth System. The two identical observatories, one ahead of Earth in its orbit (STA), the other trailing behind (STB), have allowed to trace the flow of energy and matter from the Sun to Earth through observations of the solar activity from different angles.

Combination of both STEREO and SoHO missions provide us with an unique tool to observe and study the Sun with three eyes in different positions which allow us to develop techniques for 3D reconstruction and derive the CME properties based on coronographic observations by STEREO/COR2 and LASCO/SOHO C2 and C3 including imaging of the interplanetary space between the Sun and the Earth. Nowadays, the Graduated Cylindrical Shell model (GCS) is one of the most used models (e.g. Colaninno, Vourlidas, and Wu [2013], Möstl *et al.* [2014], Rouillard [2011]). GCS is meant to reproduce large scale structures of flux-rope like CMEs and consists of a tubular section forming the main body of the structure with two cones which correspond to the CME 'legs' as is shown in Figure 4.4 (a-c). Figure 4.4.d shows an example of a modelled CME using GCS. The green grid is the fit of the large structure of the CME on 2012 October 5 overploted on differential white-light coronographic images. The Epipolar Geometry and Tie-point (TP) reconstruction model is another very useful technique. This model is based on finding a correspondence between pixels of STA and STB images along the same epipolar line. The epipolar line is located in the plane which contains the positions of both STA and STB and any point in the solar corona to be triangulated (epipolar plane).

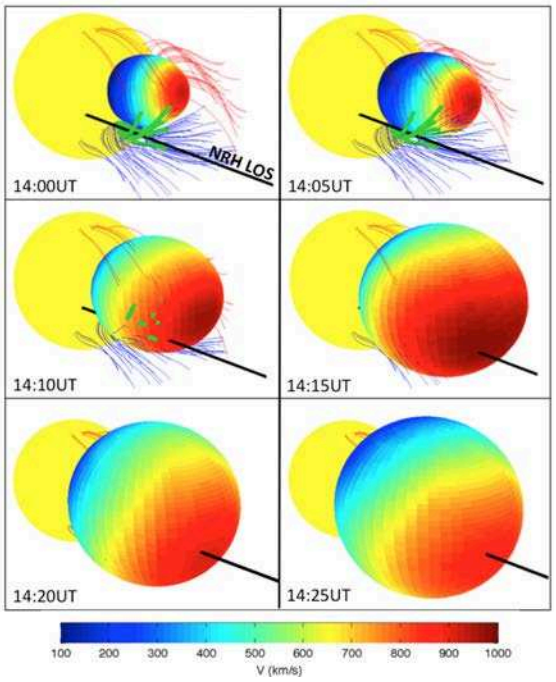

FIGURE 4.5: 3D evolution of the CME on 2008 April 26 using the technique by Rouillard *et al.* [2016] at different times from 14:00 UT to 14:25 UT. The colour code shows the distribution of the speed. Figure adapted from Salas-Matamoros, Klein, and Rouillard [2016].

Once the correspondence between images is done, the 3D reconstruction is achieved by calculating the lines of sight that belong to the respective pixels in the image and plot them onto 3D space. Since the lines of sight must lie in the same epipolar plane, their intersection is unambiguous. This procedure is called 'Tie-point' (e.g. review by Mierla *et al.* [2009]).

Additional models have been employed such as the Polarisation Ratio technique or he Solar Rotational Tomography technique. Polarisation Ratio technique applies the degree of polarisation of Thomson-scattered light by coronal electrons to obtain a 3D reconstruction of CMEs (e.g. Dere, Wang, and Howard [2005], Moran and Davila [2004]) while the Solar Rotational Tomography technique consists in using the rotation of the Sun and its corona to record projections of the corona over the course of a half rotation [Frazin, 2000].

Combinations of techniques and models have been also developed recently. Lario *et al.* [2014] combine two models of the CME structure to be fitted: the CME ejecta is described by the GCS model while an ellipsoid shape centred at a certain altitude is used to describe the outermost front driven by the CME as used by Kwon, Zhang, and Olmedo [2014]. A similar technique has been established by Rouillard *et al.* [2016]. With this technique one derives the properties of the 3D expansion of pressure fronts forming in

the corona during eruptive events by using a combination of EUV and white-light images and maps of the outermost extent of the coronal region perturbed by the CME as a function of time. Figure 4.5 presents the results of extracting the normal speed of the pressure front at six successive times displayed as a color-coded speed distribution over the front of the surface for the event on 2008 April 26 [Salas-Matamoros, Klein, and Rouillard, 2016]. In this case the surface of the pressure front generated around the expanding CME visible in EUV and white-light images could be fitted as an ellipsoid very well.

Nevertheless, even when in some events the shape of the CME front can be approximated very well, not all CMEs can be approximated by a simple shape and the estimation of 3D speed can be affected by this fact. The difficulty in this kind of speed estimation increases when several CMEs occur within a few hours of each other and overlap making difficult to distinguish the different parts of the CMEs.

Likewise, even when STEREO satellites allow to obtain speed measurements together with SOHO, STEREO spacecraft are not always positioned under an angle respect to Sun-Earth line suitable to provide observations of CMEs with minimum projection effects. This information is relevant for Space Weather and forecasting studies, so it is necessary to find an alternative method to estimate the propagation speed of Earth-directed CMEs by using the data continuously available.

4.2 Propagation of CMEs into the Interplanetary Space

The interplanetary medium refers the material which fills the Solar System. Interplanetary medium includes interplanetary dust, cosmic rays and hot plasma from the solar wind [e.g., Cravens, 1997]. The plasma in the interplanetary medium can be described through the single-fluid MHD equations and the magnetic field configuration models the trajectory of energetic particles throughout the interplanetary space.

4.2.1 Interplanetary Magnetic Field Configuration

The understanding of how the interplanetary plasma flow is able to control the field or vice versa, can be studied applying the MHD equations. The MHD momentum equation for the case where $\frac{\partial \vec{u}}{\partial t} = 0$ is given by

$$\underbrace{\rho \vec{u} \cdot \nabla \vec{u}}_{\text{C.1}} = \underbrace{-\nabla P}_{\text{C.2}} + \underbrace{\vec{j} \times \vec{B}}_{\text{C.3}} + \underbrace{\rho \vec{g}}_{\text{C.4}}, \tag{4.3}$$

where ρ, $\vec{u}$, and P are the density, the local flow velocity and the thermal pressure. The magnitudes of the terms C.1-C.4 in Equation 4.3 can be related as

$$\frac{C.1}{C.2} = M^2 \equiv \frac{u^2}{\gamma(P/\rho)} = \frac{u^2}{C_S} \quad \rightarrow \text{Mach Number}$$

$$\frac{C.2}{C.3} = \beta \quad \rightarrow \quad \beta \text{ plasma}$$

$$\frac{C.1}{C.3} = M_A^2 \equiv \frac{u^2}{B^2/(4\pi\rho)} = (\frac{u}{V_A})^2 \quad \rightarrow \text{Alfvenic Mach Number}$$

$$\frac{C.4}{C.2} = \frac{\rho g}{KT} \equiv H_p \quad \rightarrow \text{Pressure scale height}$$

Two physical quantities derived from MHD approximation, the Alfvenic Mach Number (M_A) and the plasma beta (β), can help us to understand the behaviour of the plasma in a magnetic configuration:

$$M_A = \frac{u}{V_A}, \tag{4.4}$$

and

$$\beta = \frac{\text{Kinetic plasma pressure}}{\text{Magnetic pressure}} = \frac{P_{\text{plasma}}}{P_{\text{mag}}}, \tag{4.5}$$

where V_A is the Alfven speed.

Since the solar wind flows outward supersonically, the M_A is found to be greater than 1 in that region. We can assume that solar wind becomes supersonic at a certain heliocentric distance where M_A changes from less than 1 to greater than 1. This heliocentric distance describes a surface from which the flow is supersonic. Likewise, if $\beta \gg 1$, the kinetic pressure, ρu^2, exceeds the magnetic pressure and becomes more important than the magnetic tension force, $\vec{j} \times \vec{B}$ and, as a consequence, the dynamic pressure determines the flow pattern. On the contrary, where $\beta \ll 1$, the magnetic field constrains the flow of the plasma.

According to the general values of these quantities at different altitudes above the photosphere, all the non-magnetic terms in the MHD approximation are less than the magnetic force in the region that comprises distances from $\approx$ 1.04-2.5 $R_\odot$ and become dominant again for higher radial distances. So, a surface can be defined at about 2.5 $R_\odot$ from which the solar wind flows out radially. This surface is called *source surface* [e.g., Cravens, 1997, Schulte in den Bäumen, Cairns, and Robinson, 2012] and is the source of the interplanetary magnetic field. Figure 4.6 was adapted from Cravens [1997] and

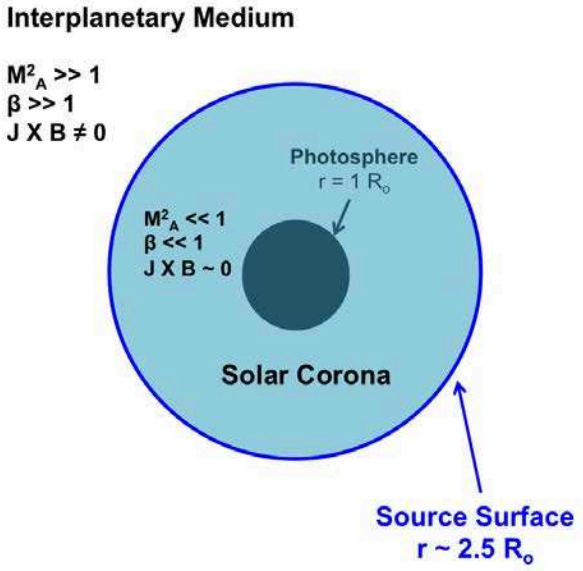

FIGURE 4.6: Schematic regions of the corona and the values of M_A and β in each region. The source surface is plotted as a contour in blue. Figure adapted from Cravens [1997].

shows schematically the different regions of the solar corona and the values of M_A and β in each region.

Outside the *source surface*, the solar wind plasma is assumed to flow radially from the Sun with an almost constant speed, $\mathbf{u}(r, \theta, \phi) = u_{\text{sw}}\mathbf{r}$. Besides, because the magnetic field is 'frozen' into the plasma and carried out with the flow, the interplanetary magnetic field is affected by the kinematic deformation because of the solar rotation (with a period of about 27 days).

Parker [1958, 1963] predicted the variation of the interplanetary magnetic field with distance (B_R) from the Sun and the heliographic latitude (θ) as [Burlaga, 1995]:

$$B_r(r, \theta, \phi) = B_s(\theta, \phi - \frac{r\Omega}{u_{\text{sw}}})(\frac{R_{\text{ref}}}{r})^2, \tag{4.6}$$

where R_{ref} is the reference distance which is usually chosen to be 1 AU and B_s is the magnetic field strength at R_{ref}. Likewise, the curve describing the magnetic field in the interplanetary space rooted in the solar surface can be described by:

$$\Phi(r) = \Phi_s - \frac{\Omega}{u_{\text{sw}}}(r - R_{\odot}). \tag{4.7}$$

The shape of the interplanetary magnetic field lines shown in Figure 4.7 which are described by Equation 4.7 is called *Parker Spiral*.

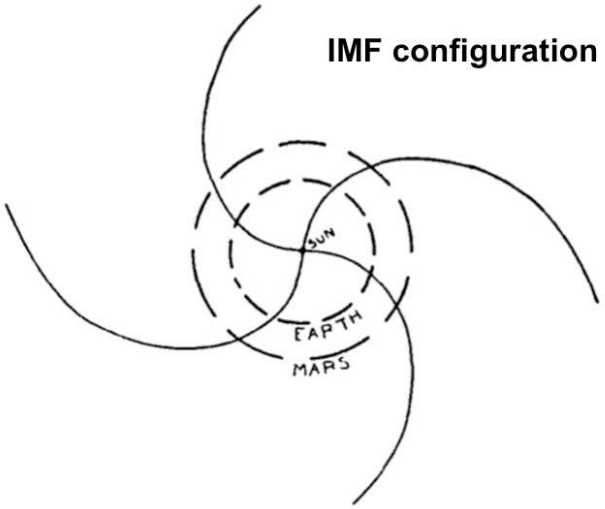

FIGURE 4.7: Schematic configuration of the interplanetary magnetic field which is projected onto the ecliptic plane. Figure from Parker [1958]

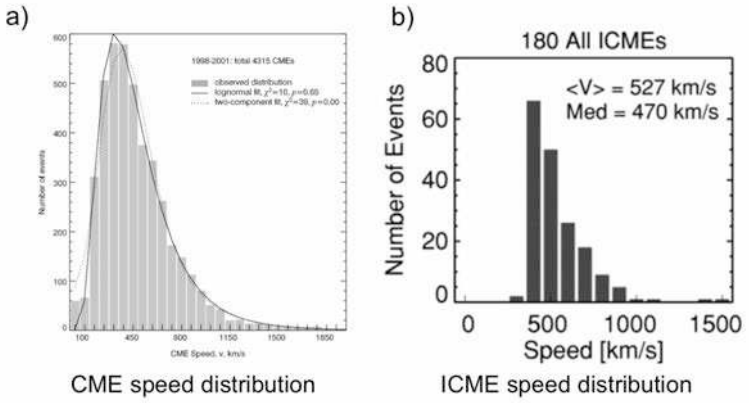

FIGURE 4.8: Distributions of CME speeds and ICME speeds. a) Distribution of the observed speeds of 4315 CMEs with a bin size of 70 km s^{-1}. Figure adapted from Yurchyshyn *et al.* [2005]. b) Distributions of 180 ICMEs with a bin size of 100 km s^{-1}. Figure adapted from Gopalswamy [2010].

4.2.2 Interplanetary Propagation of CMEs

Generally, observational studies show that CMEs associated with flares have higher speeds ($\geq$ 450 km s^{-1}) while CMEs associated with filament eruptions slower speeds ($\leq$ 400 km s^{-1}) [e.g., Moon *et al.*, 2002]. Figure 4.8.a shows this broad distribution in the CME speed. However, observations at 1 AU show that ICME speeds present a narrow distribution **about** the solar wind speed value as is shown in Figure 4.8.b. This result implies that fast CMEs in the interplanetary medium are decelerated while slow CMEs are accelerated.

This observational result has been confirmed by the Heliospheric Imager (HI) on board the STEREO spacecraft. Colaninno, Vourlidas, and Wu [2013] study the kinematics

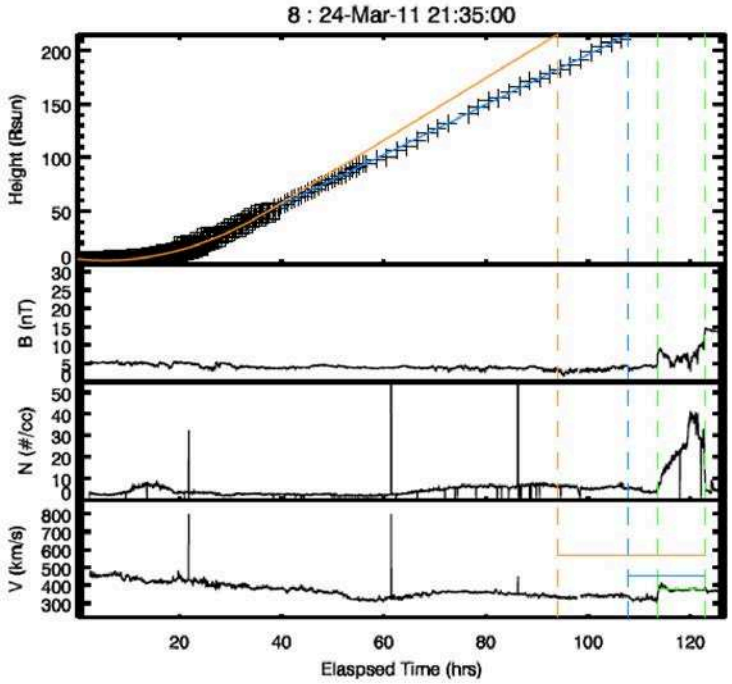

FIGURE 4.9: The height-time measurements and *in situ* data of the CME on 2011 March 24 plotted in the same temporal axis. The time axis rages between 0 and 120 hours from 00:00 UT on 2011 Mars 24. The top panel contais the height-time measurements while the bottom three panels show the magnetic field magnitude, proton density and proton velocity in situ data from the Wind spacecraft. Adapted from Colaninno, Vourlidas, and Wu [2013]

of nine Earth-impacting CMEs between May 2010 and June 2011. Figure 4.9 shows an example of height-time (H-T) CME evolution in the top panel. The second order fit (orange line) in the H-T plot represents very well the data at a certain distance ($R \approx$ 50-80 AU), but at higher distances the best fit is linear (blue line), which implies that the CME is accelerated until a distance R and after that, CME continues with a constant speed in the interplanetary medium close to the solar wind speed value. This is confirmed by *in situ* data from the Wind spacecraft in the bottom panel of Figure 4.9. Therefore, these observational results imply that ICMEs are accelerated/decelerated because of some forces acting in the interplanetary space.

The observational techniques using coronographs on board SoHO and both STEREO spacecraft have improved modelling of the heliospheric propagation of ICMEs and also provide a valuable testing of forecast methods. Firstly, there are the empirical models based on relationships between coronographic measurements and ICME parameters in the interplanetary space. On the other hand, there are the MHD-based models of the heliospheric ICME propagation which are completely numerical. And finally, the kinematical methods based on MHD or HD-based models developed analytically.

4.2.2.1 Empirical Interplanetary Propagation Models

Many attempts were undertaken in the literature to derive simple methods to forecast ICME arrival times at the Earth using CME observations at the Sun. For instance, Schwenn *et al.* [2005] find an empirical relationship between the propagation speed and the expansion speed of CMEs (Eq. 4.1) in order to obtain the propagation speed of Halo CMEs from coronographic observations. On the other hand, Manoharan and Mujiber Rahman [2011] provide an empirical relationship between the average acceleration of CMEs and their measured transit times.

Gopalswamy *et al.* [2001] and Gopalswamy [2009] find simple empirical relationships for the acceleration/deceleration of CMEs in the interplanetary space in first and second order of the velocity difference. These relationships were scaled using SoHO observations of CMEs and the arrival time of ICMEs at Wind and ACE spacecraft to obtain the CME acceleration. The empirical laws are

$$a\ [\mathrm{m\ s^{-2}}] = -0.0054(\mathrm{V_{CME}} - \mathrm{V_{01}}),\ \mathrm{V_{01}} = 406\ \mathrm{km\ s^{-1}}\ (1^\circ\ \text{order}) \tag{4.8}$$

$$a\ [\mathrm{m\ s^{-2}}] = -3.29{\cdot}10^{-6}(\mathrm{V_{CME}}-\mathrm{V_{02}})^2 - 3.64{\cdot}10^{-3}(\mathrm{V_{CME}}-\mathrm{V_{02}}),\ \mathrm{V_{02}} = 482\ \mathrm{km\ s^{-1}}\ (2^\circ\ \text{order}) \tag{4.9}$$

where $\mathrm{V_{01}}$ and $\mathrm{V_{02}}$ correspond to an equivalent ambient solar wind speed in the first and second order of the acceleration respectively. These speeds, are presented in this form to be compared with the drag force acting in the interplanetary space.

Then, using the simple kinematic motion the final CME speed is given by

$$V_\mathrm{f} = V_\mathrm{CME} + a \cdot t. \tag{4.10}$$

In this model the acceleration is assumed constant until a heliocentric distance of 0.76 AU from where the CME is assumed to have a constant speed. The duration of the acceleration (t) is calculated from

$$S = V_\mathrm{CME} \cdot t + \frac{1}{2} \cdot a \cdot t^2 \qquad (S\ =\ 0.76\ \mathrm{AU}) \tag{4.11}$$

Finally, the total transit time is obtained by addition of the time from Equation 4.11 and the time that the CME spends to travel from 0,76 to 1 AU (t_f) with V_f by

$$t_{\text{total}} = t + t_f \ = t + \frac{(1[\text{AU}] - S)}{V_f}. \tag{4.12}$$

Even when the ICME arrival time prediction is difficult because of different factors such as the irregular shape of the CME and the CME-CME interaction, this model provides a simple method of advance warning of ICME arrival at the Earth.

4.2.2.2 Numerical MHD-based Propagation Models

These models are MHD simulations of the heliosphere to describe the CME propagation through the interplanetary space [e.g., Cargill, 2002]. Nowadays a very sophisticated technique is the combination of near-Sun observations with MHD modelling to forecast ICME arrivals. Some authors [e.g., Mays *et al.*, 2015, Millward *et al.*, 2013, Vršnak *et al.*, 2014] utilise the cone model to obtain the CME parameters to be used as input in the WSA-ENLIL+Cone model which is one of the most used MHD models to forecast the arrivals.

ENLIL is a 3D MHD model code which calculates the time-dependent behaviour of an ideal fluid due to various initial and boundary conditions. ENLIL cone model forecasts CME propagation from the ENLIL inner radial boundary (beyond the sonic point, typically at 21.5 or 30 $R_\odot$) to the point of interest (outer radial boundary) to include planets and spacecraft. The cone model is based on the idea that close to the Sun CME propagates with constant angular and radial velocities, and so has the shape of a cone [Odstrcil *et al.*, 2004].

Another MHD model is the one used by Wu *et al.* [2011]. They combine a kinematic model (the HAFv.3 code) for simulating the solar corona in the range 2.5-18 $R_\odot$ with a 3D MHD code to model the heliosphere in the range of 18-285 $R_\odot$.

4.2.2.3 Analytical Interplanetary propagation Model: Drag-Based Model (DBM)

Most of the analytical models are based on the hypothesis that beyond a certain heliospheric distance the ICME dynamics becomes governed only by the interaction of the ICME with the ambient solar wind [e.g., Cargill, 2004, Owens and Cargill, 2004, Vršnak and Žic, 2007, Vršnak *et al.*, 2010].

Cargill *et al.* [1996] study the evolution of a flux tube accelerated through a magnetised plasma by magnetohydrodynamic simulations. Their study suggests that the acceleration of the flux tube came from the interaction between the external field and the

magnetic field of the flux tube. This interaction can be explained in terms of *Kelvin-Helmholtz instability* which has been applied to interactions between the magnetopause and the solar wind. The basic idea is that the shear in the flow across the magnetopause can produce surface waves because of its interaction with the solar wind, similar to waves observed in a lake when a strong wind is blowing. The waves in the solar wind can be convected through the bow shock and can introduce wave power into the magnetosphere [Kivelson and Russell, 1995]. Since the solar wind is considered as a colisionless plasma, the interaction of ICMEs (magnetic structures) with the solar wind plasma can be explain through the same scenario.

Vršnak and Žic [2007] propose that the observed acceleration/deceleration of ICME in the interplanetary space can be expressed in terms of the magnetohydrodynamical analogue of the aerodynamic drag. This model is called *Drag-Based Model* (DBM).

In this model, the drag acceleration is expressed as [Cargill, 2004]

$$a = -\gamma(V_{\mathrm{ICME}} - V_{\mathrm{SW}}) \mid V_{\mathrm{ICME}} - V_{\mathrm{SW}} \mid \ , \tag{4.13}$$

where γ is the drag parameter and is given by

$$\gamma = \frac{C_D \ A \ \rho_{\mathrm{SW}}}{M_{\mathrm{CME}}} \ , \tag{4.14}$$

where A is the cross-sectional area of the ICME, ρ_{SW} is the solar wind density, C_D is the drag coefficient and V_{ICME} and V_{SW} are the ICME velocity and the solar wind velocity respectively. Here M_{CME} is the ICME mass.

This model has been applied to describe ICME propagation in several studies [e.g., Temmer and Nitta, 2015, Temmer *et al.*, 2011, Žic, Vršnak, and Temmer, 2015]). Also, this model has been combined with other techniques as CME prediction tool such as Shi *et al.* [2015] who use a combination of GCS and DBM and Rollett *et al.* [2016] who use DBM combined with an analytical model that describes the shock as an ellipse in the ecliptic plane and is called Ellipse Evolution model (ElEvo) developed by Möstl *et al.* [2015].

4.2.3 CME-CME Interaction in the Interplanetary Space

Since in most cases CMEs are not launched in isolation, the CME-CME interaction may occur in the interplanetary space. In the studies developed in Salas-Matamoros and

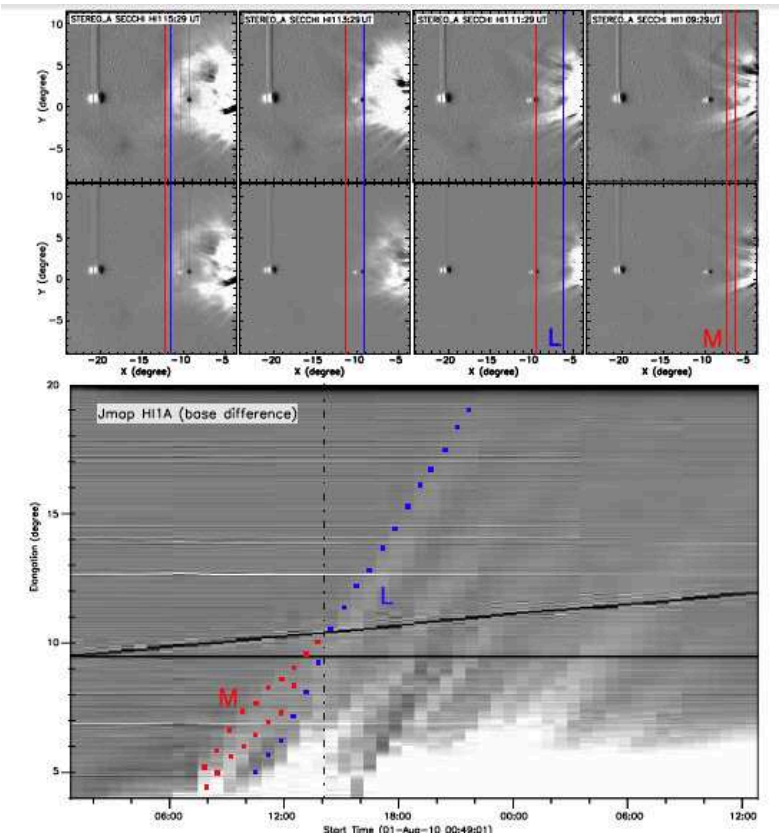

FIGURE 4.10: Top: base difference images from HI-A showing the evolution of two CMEs (denoted as M and L) in a distance range of 20-40 $R_{\odot}$. The fronts of M and L are indicated by red and blue lines respectively. Bottom: J-map constructed from base difference images and overplotted tracks of both CMEs (squares). Figure from Temmer *et al.* [2012].

Klein [2015] and Salas-Matamoros, Klein, and Trottet [2016] we examine most events occurred in isolation and we do not consider CME-CME interactions.

Historically, the studies of CME-CME interactions have been developed principally from *in situ* measurements [e.g., Wang, Ye, and Wang, 2003]. Since the launch of STEREO spacecraft, heliospheric observations can be used to study this phenomenon at few tens of $R_{\odot}$. Figure 4.10 shows the interaction between two successive CMEs in the J-maps in the bottom panel. This technique of creating elongation-time maps (J-maps) has been applied to track CMEs [Liu *et al.*, 2011, Möstl *et al.*, 2010, Rouillard *et al.*, 2008] and the CME-CME interaction can be followed and studied in the heliosphere [e.g., Lavraud and Rouillard, 2014, Mishra and Srivastava, 2014, Temmer *et al.*, 2012].

The CME-CME interaction is complex and can involve different physical process such as momentum transfer [e.g., Lugaz, Vourlidas, and Roussev, 2009] and magnetic reconnection of flux ropes [e.g., Wang, Ye, and Wang, 2003]. Even though sophisticated techniques have been developed, this interaction is not fully understood yet. The change in the mass of CMEs and the fact that the shape and orientation of the magnetic structures

play an important role in the interaction process, make the identification of interaction type more difficult [Lugaz and Kintner, 2013, Temmer *et al.*, 2014].

Studies of the interaction of CMEs observed in the interplanetary space reveal that the CME kinematics changes during the interaction [e.g., Démoulin, 2010, Forbes *et al.*, 2006]. Generally the slow CME can be accelerated by the encounter with a second faster CME, while the faster CME can be decelerated by the interaction with the slowest one [e.g., Temmer *et al.*, 2012]. But not only the kinematics of the CME can change because of interaction. Lugaz *et al.* [2012] find a change in the longitude direction of the CMEs during their interaction. These results implies that the CME-CME interaction can affect the predictions in arrival time of ICMEs.

4.3 Soft X-ray and Microwave Emissions and their Relationship with CMEs

The CMEs are often associated with Soft X-ray (SXR) bursts [Tandberg-Hanssen and Emslie, 1988], which are routinely observed by the GOES spacecraft. This association between SXR emission and CME is explained by the flare/CME scenario discussed on detail in Chapter 1.

Observational studies (e.g. Bein *et al.* [2012]) reveal that the acceleration phase of a CME is temporally associated with the rise phase of related flare when the energy is released [Zhang *et al.*, 2001]. Figure 4.11 shows the kinematics of a CME-flare event (from the top panel: the height-time, velocity and acceleration profiles) together with the SXR profile of the flare (bottom panel) studied by Bein *et al.* [2012]. From this study, they find evidence of the timing association based on the study of 57 flare events, between the flare energy release, during the impulsive phase, and the CME dynamics as is demostrated in the example in Figure 4.11. This result supports previous results from Zhang *et al.* [2004].

Based on these timing associations and in order to find if some correlation exists between the parameters of CMEs (as the linear velocity) and the associated SXR bursts, many statistical studies have been developed, with conflicting results. Aggarwal *et al.* [2008] find no significant correlation between the linear speed of the CMEs and peak SXR flux. Significant correlations with a broad scatter have been found between CME speed and SXR peak flux [Bein *et al.*, 2012, Moon *et al.*, 2003, Vršnak, Sudar, and Ruždjak, 2005] and between CME kinetic energy and SXR peak flux[Burkepile *et al.*, 2004, Hundhausen, 1997].

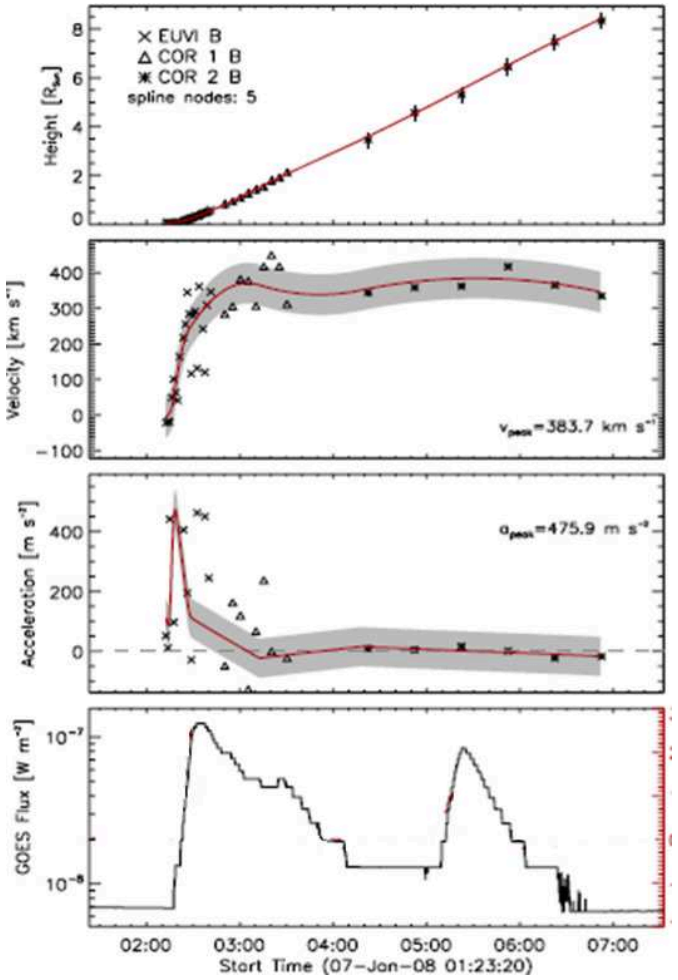

FIGURE 4.11: CME kinematics and GOES 1-8 A soft X-ray flux for the CME-flare event on 2008 January 7. Figure adapted from Bein *et al.* [2012].

One of the reasons for the low correlations found in these studies can be the projection effect in the speed of halo CMEs. This fact can affect the correlations if one considers CMEs irrespective of their location on the Sun. This idea has been adopted by Moon *et al.* [2003] who find a higher correlation, $r = 0.77$, from the eight flare-CME selected events near the limb. This correlation is very similar to the study by Burkepile *et al.* [2004], r =0.78, with a bigger sample of about 24 events whose flares occurred within 15° of the solar limb.

In addition, correlations between CME speed and total flux (fluence) of SXR have been found as well. Moon *et al.* [2002] find a correlation of 0.47 whereas Yashiro and Gopalswamy [2009] a little higher coefficient of 0.56.

Since the projections effects are significant in the speed measurements of Halo CMEs, the finding of an appropriate approximation for the radial speed of the CMEs could lead to a better prediction of the travel time of ICMEs. Because of the correlation with CME kinetics, SXR emission can be an alternative for this propose.

Likewise, observations show a relationship between microwave emission, flares and CME kinetics which can be explained in the flare/CME scenario.

Chertok, Gnezdilov, and Zaborova [1992a] analysed a sample of 30 flare events at the limb zone of heliolongitude $| l | \geq 45°$ and the associated microwave emission together with the CME parameters. They find a close relationship between the parameters of microwave and SXR bursts (intensity and duration) and the characteristics of the corresponding CMEs. They find that the intensity and duration of the SXR and microwave bursts can be directly related to the speed of the associated CME.

In their second paper, Chertok, Gnezdilov, and Zaborova [1992b] used a sample of 60 CMEs. These CMEs were associated with flares near the limb ($| l | \geq 45°$). They find the same correlations as the previous work. The prolonged energy release during the decay phase of the flare is very important and can give an additional contribution to the electromagnetic emission in the relationships with CME kinetics. They conclude that such close dependence between parameters of microwave (and SXR) bursts and CMEs can be used for the electromagnetic diagnostics of flares causing interplanetary disturbances and geomagnetic storms.

In 1964, Caroubalos [1964] studied the correlation between the travel time of CMEs and the radio importance (flux of the microwave bust times the duration). They calculate the linear dependence and find that the dispersion decreases as the events become strongest. This dependence can be used to obtain the arrival time of ICMEs based on radio emission. Recently, Tobiska *et al.* [2013] use the correlation between the SXR fluence and the CME speed (considered as the average speed between the coronal speed and the ICME speed *in situ*) to obtain an empirical deviated speed-fluence relationship.

Both relationships were obtained from the measured CME travel times which is a bit **uncertain** because the propagation of CMEs is complex and this can introduce additional errors in the correlations. To obtain a suitable method procedure for predicting travel time of CMEs, we address the CME initial speed and the CME propagation in the interplanetary space separately. Firstly, the possibility of using the electromagnetic emission (not only SXR but also microwave) as a proxy of CME speed of Earth-directed CMEs is explored in this work. The entire SOHO/LASCO data during the cycle 23 and early cycle 24 was investigated to know if a more significant correlation between CME speed, SXR busts and microwave burst is revealed when the sample is restricted to CMEs near the limbs (where the projection effects are minimised). Relationships are obtained between radiative fluences (SXR and microwave emission) and limb-CME speed which are applied to calculate the speed of Earth-directed CMEs. Since the empirical interplanetary acceleration model devised in Section 4.2.2.1 has V_{CME} as the only input parameter, the inferred halo CME speeds will be used as the input in the empirical

propagation model to predict the CME arrival time at Earth. Finally, the results will be compared with observations to examine how accurate they are.

4.3.1 On the statistical relationship between CME speed and soft X-Ray fux and fluence of the associated flare (paper)

Solar Phys (2015) 290:1337–1353
DOI 10.1007/s11207-015-0677-0

On the Statistical Relationship Between CME Speed and Soft X-Ray Flux and Fluence of the Associated Flare

C. Salas-Matamoros[1,2] · K.-L. Klein[1]

Received: 25 July 2014 / Accepted: 23 March 2015 / Published online: 10 April 2015

Abstract Observation and theory both reveal a close relationship between the kinematics of coronal mass ejections (CMEs) and the thermal energy release traced by the related soft X-ray (SXR) emission. A major problem of empirical studies of this relationship is the distortion of the CME speed by the projection effect in the coronagraphic measurements. We present a re-assessment of the statistical relationship between CME velocities and SXR parameters using the SOHO/LASCO catalog and GOES whole-Sun observations during the period 1996 to 2008. Forty-nine events were identified in which CMEs originated near the limb, at central meridian distances between 70° and 85°, and had a reliably identified SXR burst, the parameters of which – peak flux and fluence – could be determined with some confidence. We find similar correlations between the logarithms of CME speed and of SXR peak flux and fluence as several earlier studies, with correlation coefficients of 0.48 for the flux and 0.58 for the fluence. Correlations are slightly improved over an unrestricted CME sample when only limb events are used. However, a broad scatter persists. We derive the parameters of the CME–SXR relationship and use them to predict ICME arrival times at Earth. We show that the CME speed inferred from SXR fluence measurements tends to perform better than SoHO/LASCO measurements in predicting ICME arrival times near 1 AU. The estimation of the CME speed from SXR observations can therefore make a valuable contribution to space weather predictions.

Keywords Coronal mass ejections · Interplanetary coronal mass ejections · Flares · X-ray bursts

✉ C. Salas-Matamoros
carolina.salas@obspm.fr; carolina.salas@cinespa.ucr.ac.cr

K.-L. Klein
ludwig.klein@obspm.fr

1 LESIA-UMR 8109 – Observatoire de Paris, CNRS, Univ. Paris 6 & 7, 92190, Meudon, France

2 Space Research Center, University of Costa Rica, San Jose, Costa Rica

1. Introduction

Coronal mass ejections (CMEs) are expulsions of huge masses of plasma and magnetic field into the heliosphere. When intercepting the Earth, they can trigger geomagnetic storms, *i.e.* major disturbances of the terrestrial magnetic field (Gold, 1962; Gonzalez and Tsurutani, 1987; Gosling, 1993; Zhang *et al.*, 2007; Gopalswamy, 2010). CMEs are often associated with soft X-ray (SXR) bursts (Tandberg-Hanssen and Emslie, 1988), which are routinely observed by the *Geosynchronous Operational Environmental Satellites* (GOES) spacecraft. SXR bursts reveal the heating of plasma in a flaring active region. The mechanical energy release to CMEs and the thermal energy release are closely related in many models on the origin of large-scale instabilities in the corona (Forbes *et al.* (2006), and references therein). Observational studies confirm such a close relationship: they revealed that the acceleration phase of a CME is temporally associated with intense energy release during the rise of the associated SXR burst (Zhang *et al.*, 2001, 2004; Maričić *et al.*, 2007). Relationships between the speed or kinetic energy of CMEs on the one hand and the importance of the SXR burst, most often the peak flux, on the other hand have also been revealed by many statistical studies (Moon *et al.*, 2003; Burkepile *et al.*, 2004; Vršnak, Sudar, and Ruždjak, 2005; Maričić *et al.*, 2007; Yashiro and Gopalswamy, 2009; Bein *et al.*, 2012). Occasional negative reports (Aggarwal *et al.*, 2008) and the broad scatter in the statistical relationship show, however, that the quantitative relationship between CMEs and SXR bursts is complex.

The interest in clarifying the situation is twofold: on the one hand, such statistical relationships show to which extent different manifestations of magnetic energy release in solar eruptions are related. On the other hand, empirical relationships between different parameters of solar activity can assist space weather forecasting. This is especially interesting for Earth-directed CMEs whose velocity is not directly measurable by coronagraphs on the Sun–Earth line. Understanding how different quantities describing the output of eruptive solar activity are related is also essential if correlation analyses are to be used to derive physical relationships with a third quantity, for instance the intensity of solar energetic particle events (see, *e.g.*, Trottet *et al.* 2015).

A major source of errors in statistical studies involving CME speed comes from the uncertainly of the measurement in coronagraphic images by projection effects. Moon *et al.* (2003), Burkepile *et al.* (2004), and Yashiro and Gopalswamy (2009) investigated these correlations with event samples restricted to CMEs that originated near the solar limb, where projection effects are not expected to affect the CME speed. These authors suggested that the correlations are indeed improved. However, they did not consider the statistical uncertainties of the correlation coefficients. Yashiro and Gopalswamy (2009) also concluded that the CME speed is more strongly correlated with SXR fluence than with SXR peak flux, but again without addressing the uncertainties in their comparison.

In the present work we re-assess the correlation between CME speed and both SXR peak flux and SXR fluence, restricting ourselves to CMEs near the solar limb. The event selection based on CMEs between 1996 and 2008 from the LASCO CME catalog and the associated GOES SXR bursts is described in Section 2. In Section 3 the results of the statistical analysis are presented, and empirical relationships between CME speed and SXR parameters are derived. The empirical relationships are used in Section 4 in an attempt to predict the arrival times of interplanetary CMEs (ICMEs) at Earth. The results are compared with predictions using CME measurements from SOHO/LASCO and with the observations of ICME arrival near 1 AU.

2. Methodology and Data Selection

The data set we analyzed consists of parameters of CMEs originating near the solar limb and of the associated SXR bursts. CME parameters (position angles, widths, heights, and speeds) are provided in the catalog of CMEs[1] observed by the *Large Angle and Spectrometric Coronagraph* experiment (LASCO; Brueckner *et al.* 1995) of the *Solar and Heliospheric Observatory* (SOHO), during the period from 1996 until 2008. Time histories of SXR flux measured by the GOES satellites in the 0.1 – 0.8 nm range were retrieved through the database at NASA/GSFC using the IDL routine *goes.pro* in the *SolarSoft* package.

2.1. Selection of Limb CMEs

Limb CMEs were selected in two steps. We first excluded events whose central position angle (PA, measured counterclockwise from solar north) was within $\pm 60°$ of the projected solar north and south, because such CMEs can only be associated with activity at relatively small central meridian distances. To obtain only CMEs with a well-defined direction of propagation, we delimited also the CME width to between 60° and 120°, especially avoiding halo CMEs. We also excluded CMEs whose speed was ≤ 100 km s^{-1} to facilitate the flare association.

For the subsequent correlation studies, we checked the quality of the linear fits to the time-height trajectory and the representativity of the derived CME speed in the LASCO/CME catalog. We found some CMEs whose time-height diagram showed acceleration or deceleration phases in the LASCO field of view (FOV). We included events in which only few points at low altitudes were affected by this acceleration/deceleration, and the linear fit gave a satisfactory estimate of the final speed. In 11 events the acceleration/deceleration was pronounced in the LASCO/C2 FOV. In this case, we used the speed at a distance of 20 solar radii inferred from the constant acceleration fit as approximation of the final CME speed.

2.2. Identification of the Associated Flares

For the final determination of the CME origins, we identified CMEs associated with flares close to the limb. As a compromise between proximity to the limb and a significant number of events, we focused on flares located, according to *Solar Geophysical Data*,[2] at central meridian distance between 70° and 85°. The events too close to the limb were excluded to avoid a partial occultation of the SXR emission. The CME-associated flares were searched in a first step within a fixed time interval with respect to the CME origin. The CME speed (see Section 2.1) and the time and heliocentric distance when the CME was first detected were used to extrapolate its trajectory to the limb of the Sun. An automated procedure was used to identify SXR bursts that peaked between an hour before and an hour after the instant when the backward-extrapolated trajectory intersected the solar limb. This way, we identified 77 CMEs associated with flares near the limbs; 44 occurred in the eastern and 33 in the western solar hemisphere.

The time profile of each SXR burst of this sample was studied in detail to identify cases when the CME-flare association found by the automated search was ambiguous. We discarded weak bursts because they would not allow us to obtain reliable values of the fluence.

[1] http://cdaw.gsfc.nasa.gov/CME_list/.

[2] National Geophysical Data Center http://www.ngdc.noaa.gov.

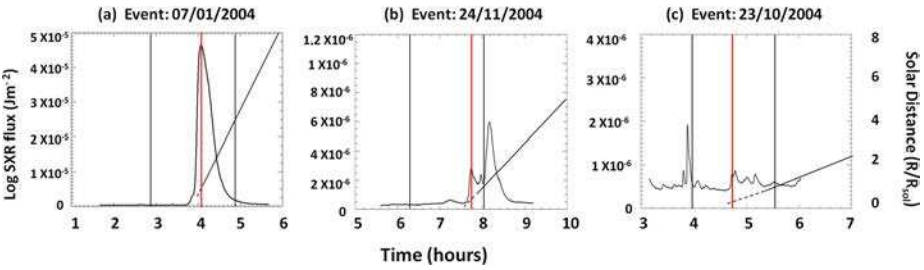

Figure 1 Time profiles of three different SXR bursts: (a) a well-defined burst with a single peak, (b) a superposition of two different soft X-ray bursts, and (c) a burst with a very complex time profile. Vertical black lines delimit the 2-h window centered on the time when the extrapolated CME trajectory intersected the solar limb. The vertical red line marks the peak of the SXR burst associated with the CME.

Three different types of time profiles were identified (see Figure 1): (a) a well-defined peak, (b) a burst with more than one peak, which may mean a superposition of different bursts, and (c) a very complex profile where no burst could be unambiguously associated with the CME. The events in the latter category were discarded. For the cases with several peaks, we verified the coordinates of the flare related to each peak in the time profile directly through the analysis of image sequences from SOHO/EIT 19.5 nm (Delaboudinière *et al.*, 1995) or *Yohkoh*/SXT (Tsuneta *et al.*, 1991). The events where images revealed flares in active regions within $\pm 70^\circ$ from the central meridian or at the opposite limb of the CME were eliminated, as well as events where several peaks were associated with the same active region without possibility of distinguishing whether one or several were actually associated with the CME. We also discarded cases when the CME reported in the catalog was not clearly recognizable in the LASCO daily movies. We eventually obtained a list of 49 events for which the correlation between CME speed and SXR peak flux and fluence could be studied. They are listed in Table 1. The fluence calculation is discussed in Section 3.

The CME speeds in the sample range from 154 to 1822 $\mathrm{km\,s^{-1}}$, with a median of 639 $\mathrm{km\,s^{-1}}$, the SXR peak fluxes from 6×10^{-7} to 1.6×10^{-3} $\mathrm{W\,m^{-2}}$, *i.e.* from GOES X-ray flare classes B6 to X16.

3. Correlation Between CME Speed and SXR Peak Flux and Fluence

Based on the new short list of 49 events (25 at the eastern and 24 at the western limb), we related the speeds of the CMEs with parameters of the associated SXR bursts as observed by GOES in the 0.1 – 0.8 nm channel. Figure 2 displays the scatter plot of the CME speed *vs* the SXR peak flux on a double-logarithmic scale. We found a positive correlation of $r = 0.48 \pm 0.12$ between the logarithms of the CME speed and of the SXR peak flux. Here and in the following, the errors were calculated using a bootstrap method (Wall and Jenkins, 2012, Chapter 6.6): the correlation coefficient was calculated repeatedly for a randomly selected sample of 49 out of the 49 observed data pairs, and the mean and standard deviation are quoted as the correlation coefficient and its statistical uncertainty.

In addition to the peak flux, we also considered the fluence. Two types of fluence were calculated in the 0.1 – 0.8 nm band for these events, namely start-to-peak fluence and total fluence. The background was determined as the average flux in a suitable time interval before the SXR burst. The start-to-peak fluence was calculated by integrating the background-subtracted flux from the start of the SXR burst until its maximum, including possible small

Table 1 Table of events: date (column 1), time (2), heliocentric distance (3) of the first detection of the CME in the SoHO/LASCO field of view, speed in the plane of the sky (4), time when the linear backward extrapolation of the time-height trajectory intersected the solar limb (5), times of onset (6), peak (7), peak flux (8), start-to-peak fluence (9) of the SXR bursts, quality flag of the fluence determination (10).

N Date	CME parameters				SXR parameters				
	t_0	$r(t_0)$ [$R_\odot$]	V_{CME} [$km\,s^{-1}$]	t_{limb}	t_0	t_p	F [Wm^{-2}] ($\times 10^5$)	Φ_{sp} [Jm^{-2}] ($\times 10^4$)	Qu
(1)	(2)	(3)	(4)	(5)	(6)	(7)	(8)	(9)	(10)
1996									
07 12	16:01	5.1	1085	15:17	14:59	15:32	0.49	22.80	2
1997									
06 30	00:30	2.9	346	23:25	23:35	23:53	0.11	4.20	1
1998									
03 13	21:30	2.7	409	20:40	20:51	21:10	0.56	27.70	1
04 25	15:11	2.9	349	14:09	14:02	14:37	0.36	31.30	1
1999									
04 03	23:47	5.5	923	22:50	22:50	23:10	4.46	137.60	1
05 08	14:50	3.8	641	13:59	14:21	14:40	4.87	256.05	1
05 11	22:26	4.3	735	21:34	21:25	22:05	0.40	47.80	2
09 13	17:31	3.3	444	16:30	17:17	17:31	0.13	5.70	2
11 08	07:26	3.5	154	04:18	05:55	06:01	0.53	7.20	1
2000									
06 17	03:28	4.8	857	02:36	02:19	02:37	0.38	119.30	1
06 23	14:54	4.7	847	14:03	14:18	14:32	3.22	120.30	1
2001									
02 03	00:30	4.0	639	23:36	23:47	24:06	2.45	122.10	1
04 15	14:06	4.3	1199	13:34	13:37	13:50	161.00	2708.80	1
08 10	02:06	2.5	376	01:18	01:27	01:36	0.75	15.30	1
10 29	08:26	2.6	617	07:56	08:00	08:13	1.08	17.96	1
11 01	14:30	2.7	1053	14:11	13:50	15:01	1.26	341.20	1
12 29	09:54	2.6	634	09:25	09:06	09:45	9.46	316.50	2
2002									
03 13	23:54	3.6	489	22:53	22:59	23:36	0.99	90.90	1
04 04	05:06	2.8	468	04:22	04:12	04:40	0.87	56.00	1
07 05	13:31	2.4	818	13:10	12:59	13:26	3.49	124.50	1
08 03	19:31	5.2	1150	18:49	19:00	19:07	11.80	137.50	1
08 16	06:06	2.5	1378	05:53	05:44	06:12	2.55	193.00	1
08 22	18:26	3.0	750	17:54	17:35	18:02	1.07	97.00	2
08 23	13:27	2.4	321	12:38	11:41	12:00	0.88	34.70	2
08 29	13:31	2.5	353	12:42	12:35	12:52	3.24	75.70	1
09 08	02:06	2.5	364	01:18	01:30	01:43	1.51	34.00	1
10 16	04:54	2.8	250	03:30	04:05	04:23	0.21	08.70	1

Table 1 (*Continued.*)

N Date	CME parameters				SXR parameters				
	t_0	$r(t_0)$ [$R_\odot$]	V_{CME} [km s^{-1}]	t_{limb}	t_0	t_p	F [Wm^{-2}] ($\times 10^5$)	Φ_{sp} [Jm^{-2}] ($\times 10^4$)	Qu
(1)	(2)	(3)	(4)	(5)	(6)	(7)	(8)	(9)	(10)
2003									
04 09	23:50	3.3	511	22:58	23:24	23:29	2.57	21.40	1
04 25	05:50	2.9	806	05:22	05:22	05:40	1.24	62.75	1
10 23	20:06	2.6	1136	19:49	19:50	20:03	11.20	383.70	1
10 24	02:54	2.7	1055	02:35	02:18	02:55	7.43	864.00	1
11 03	10:06	2.5	1420	09:53	09:44	09:56	43.50	1404.40	1
2004									
01 07	04:06	3.0	1581	03:51	03:42	04:03	4.65	170.00	1
01 07	10:30	3.5	1822	10:14	10:15	10:26	8.46	219.40	1
05 07	10:50	3.2	469	09:55	09:53	10:19	0.07	6.01	2
05 17	05:26	2.8	383	04:31	04:11	04:17	0.79	5.60	1
06 16	04:36	2.7	603	04:03	03:59	04:30	0.27	14.50	1
08 24	13:54	3.3	817	13:22	13:30	13:49	0.06	4.10	1
08 31	05:54	2.4	311	05:00	05:19	05:38	1.50	47.10	1
11 03	02:06	2.4	379	01:22	00:50	01:33	3.00	82.50	1
11 24	22:06	2.5	262	21:01	21:29	21:45	0.96	40.90	1
2005									
04 17	21:26	2.9	721	20:54	20:41	21:07	0.48	26.90	2
05 06	03:30	4.0	1120	02:59	03:06	03:13	0.88	19.20	1
05 06	11:54	5.8	1144	11:05	11:12	11:28	1.30	34.60	1
08 25	04:54	4.2	1327	04:26	04:33	04:40	6.63	93.10	1
09 04	14:48	2.5	1179	14:33	13:59	15:07	0.22	39.50	1
2006									
04 29	16:54	2.5	491	16:18	16:10	16:30	0.23	8.60	1
04 30	02:06	2.5	428	01:26	01:32	01:57	0.53	35.96	2
2008									
03 25	19:31	5.8	1103	18:40	18:39	18:56	1.72	74.20	1

earlier peaks that we considered as precursors. The existence of such precursor peaks and problems with background determination introduce uncertainties in the fluence calculation. The quality flag in column 10 of Table 1 is an assessment based on visible inspection. Qu = 1 means that the fluence is reliable, Qu = 2 labels less certain cases.

The total fluence is more difficult to calculate because the end of the SXR burst is generally poorly defined, and new events may be superposed on the decay phase of the burst of interest. Kahler, Sheeley, and Liggett (1989) defined the end of the burst as the time when the X-ray flux returns to the GOES C2 level, while Yashiro and Gopalswamy (2009) used the time when the soft X-ray flux decays to half of the peak value. We fitted the decay from the main peak by an exponential and calculated the fluence analytically until infinity. This avoids contamination by new SXR bursts during the decay phase as well as an arbitrary definition of the end time.

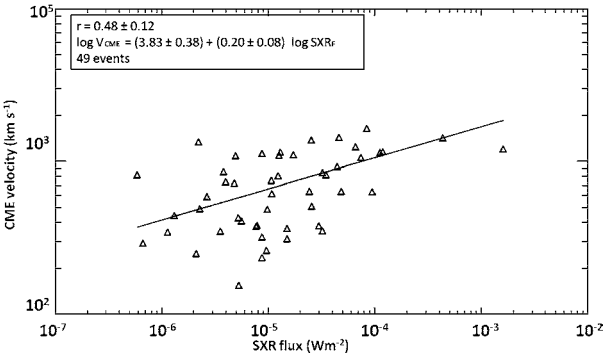

Figure 2 The logarithmic plot of the speed of CMEs near the solar limb during the period 1996 – 2008 versus the SXR peak F of the associated flares. The straight line is the result of a least-absolute deviation fit. The inset shows the correlation coefficient, the parameters of the straight line, and the number of events.

We obtained the same correlation between the CME speed and the SXR start-to-peak fluence and total fluence, $r = 0.58 \pm 0.09$. The probability of obtaining this or a higher correlation coefficient from an unrelated sample is 1.3×10^{-5}. The result is similar to those of Moon *et al.* (2002) and Yashiro and Gopalswamy (2009), who found correlations of 0.47 and 0.56, respectively.

The relationship between the logarithms of the CME speed $V_{\rm CME}$ and of the peak flux F and fluence (start-to-peak fluence $\phi_{\rm sp}$ and total fluence $\phi_{\rm p}$) of the associated SXR burst were inferred using linear fits minimizing least-squares deviation and least-absolute deviation. Differences between the resulting velocities amounted to some tens of $\mathrm{km\,s^{-1}}$ in extreme cases. Although these differences are small compared to the overall statistical uncertainty, in the following we use the result from the least-absolute deviation fit, which is less sensitive to outliers. This leads to the following empirical relationships:

$$\log V_{\rm CME} = (0.20 \pm 0.08) \log F + (3.83 \pm 0.38), \tag{1}$$

$$\log V_{\rm CME} = (0.24 \pm 0.05) \log \phi_{\rm sp} + (3.36 \pm 0.12), \tag{2}$$

$$\log V_{\rm CME} = (0.22 \pm 0.05) \log \phi_{\rm p} + (3.21 \pm 0.10). \tag{3}$$

These results are the same regardless of whether we use all events or only those with quality flag 1.

Our analysis is simplified in several respects. We used a standard minimization technique that is in principle only justified when all the measurement uncertainties are in the dependent variable, here the CME speed, whereas the independent variable is assumed to be exactly known. This is of course not the case, and we would have to apply a more general technique, such as total least-squares minimization. We checked this and found no significant difference with the results of the standard fits above.

A second problem is a bias in our statistics that is the result of rejecting CMEs that were accompanied by weak or undetected SXR bursts. The fitted straight line would be expected to have a steeper slope if these events, which are located in the lower left corner of Figures 2 and 3, had been considered. We found indeed that the straight line steepened when we gradually extended the minimum fluence considered from $10^{-2}\,\mathrm{J\,m^{-2}}$ to the lowest value detected, and it would likely steepen more than indicated by Equation (2) if weak SXR bursts were not hidden in the background. These relationships may hence overestimate the speeds of CMEs associated with weak SXR bursts and underestimate those of CMEs with intense SXR emission.

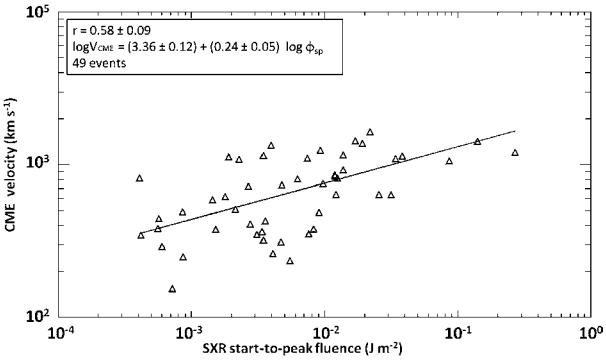

Figure 3 The logarithmic plot of the speed of CMEs near the solar limb during the period 1996 – 2008 versus the SXR start-to-peak fluence Φ_{sp} of the associated flares. See caption of Figure 2.

4. Application of the CME–SXR Relationship to ICME Propagation

In this section we test the relationship between CME speed and SXR fluence by applying it to the prediction of ICME arrival times at Earth.

The arrival of an ICME at Earth is one of the rare cases in space weather where the Sun leaves a substantial warning time. Yet predicting the arrival time is difficult: on the one hand, the speeds of Earth-directed CMEs cannot be directly measured by a coronagraph on the Earth-Sun line. On the other hand, the CME is not a rigid object, but changes during propagation in the interplanetary medium, where CMEs expand, change shape because of compression and reconnection, and are accelerated or decelerated. The relevant processes are reviewed, *e.g.*, in Forbes *et al.* (2006) and Démoulin (2010). Detailed analyses using heliospheric imaging from STEREO were reported by Colaninno, Vourlidas, and Wu (2013) and Möstl *et al.* (2014); see also the review of Rouillard (2011).

Many attempts were undertaken in the literature to derive simple methods to forecast ICME arrival times at Earth using CME observations at the Sun. These models must take account of the acceleration or deceleration of CMEs in the interplanetary medium (Gopalswamy *et al.*, 2001; Schwenn *et al.*, 2005; Vršnak *et al.*, 2010).

Gopalswamy *et al.* (2001) proposed a simple analytical treatment of the interplanetary propagation. It was based on an empirical relationship between the acceleration, which was assumed to be constant out to a limiting heliocentric distance, and the radial front speed of the CME in the corona. We applied the empirical relationship from their Equation (4), which can be formulated as

$$a\left[\mathrm{m\,s^{-2}}\right] = -0.0054\left(V_{\mathrm{CME}} - 406\left[\mathrm{km\,s^{-1}}\right]\right).$$

We assumed that the acceleration ceases either when the ICME attains a speed of 406 $\mathrm{km\,s^{-1}}$ or at the latest when it is at heliocentric distance 0.76 AU. This differs slightly from Gopalswamy *et al.* (2001), who considered that the acceleration or deceleration always continued out to 0.76 AU. For CME speeds below 800 $\mathrm{km\,s^{-1}}$ the travel times derived from the two methods differ by a few hours. We call this the empirical interplanetary propagation model in the following. We estimated the CME speed in the corona in two different ways: firstly, using the speed measurements from LASCO and secondly, using Equation (2) to infer the CME speed from the SXR fluence.

4.1. Results

We compared the predicted arrival time with observations at *Wind* and ACE for a list of selected ICMEs with well-observed arrival times at the spacecraft. We used 26 ICMEs listed

by Gopalswamy *et al.* (2001), in the online catalog of Richardson and Cane,[3] and by Möstl *et al.* (2014).

The predicted arrival times were compared with the observed arrival of both the shock and the driver. The driver is considered to be the ICME. While the shock arrival at the spacecraft was usually well determined by a sudden increase of the temperature, density, and magnetic field intensity, the arrival of the ICME was often ambiguous and may depend on the parameter used to identify it. We employed one or a combination of the following: the start of a magnetic field enhancement, of a depression of proton temperature or the proton plasma beta, of a gradually decreasing high solar wind speed, or of magnetic field rotation.

The 26 CME/ICME pairs displayed in Table 2 are those for which we could i) confirm the onset time identified in the published lists to within one or two hours, ii) clearly associate a SXR burst with the CME. ICMEs where such bursts could not be identified were discarded (*e.g.*, ICMEs on 10 January and 10 February 1997).

The first column of Table 2 shows the event number followed by the time of ICME arrivals identified from *Wind* and ACE measurements. In all cases but event 5, we used the ICME arrivals from *Wind*. In four cases (6, 20, 21, and 24) only the flank of the ICME passed over the spacecraft, making the determination of the arrival time uncertain. These events are identified with the label "f" in Table 2 after the date. The next three columns summarize the CME data from the LASCO catalog and the predicted arrival time of the ICME at the Earth using the LASCO speed as input to the empirical interplanetary propagation model, and taking as reference the heliocentric distance and the time of the first detection of the CME by LASCO as given in the catalog. The last columns give the start time and start-to-peak fluence of the related SXR bursts, the CME speed inferred from the fluence, and the arrival time of the ICMEs as calculated by the propagation model. The reference is the start time of the burst. Values within parentheses give the uncertainty interval of the expected ICME arrival due to the uncertainty of the coefficients of Equation (2).

A graphical comparison between the predicted and observed arrival times is given in Figure 4. The reference zero of the vertical axis is the time when the ICME, *i.e.* the driver, reached the *Wind* spacecraft. The vertical bars indicate the time interval between the arrival of the shock and the driver, that is, the size of the sheath region. The arrival time predicted using the LASCO CME speed is represented by an open square, the prediction using the propagation speed inferred from Equation (2) by a cross.

On average, we observe that the arrival times predicted using the SXR parameters are closer to the observed arrival times than those predicted using LASCO measurements. Figure 5 gives another comparison between the two predictions of the ICME arrival time and the observations in panels (b) and (d). The comparison with the observed shock arrival time is given in panels (a) and (c). Predictions using the LASCO observations are shown in the top row, those based on the SXR fluence in the bottom row. The events are grouped into 12 h intervals with respect to the arrival of the ICME shock (a, c) and the driver (b, d). The first bar hence gives the number of events where the absolute value of the delay between the predicted and observed arrival is greater or equal to 0 and less than 12 h, *etc*. The figure confirms the impression from Figure 4 that ICME travel times estimated from the SXR fluence tend to cluster more closely around the arrival times of both the shock and the driver than the travel times inferred from the LASCO measurements. In 15/26 events the SXR-inferred CME speed leads to an ICME arrival prediction within ± 12 h of the observed time. Only 9/26 cases where coronagraphic observations are used achieve this. The median error of the prediction is 11.5 h when SXR fluence is used and 14.5 h when LASCO measurements are used. Caution is of course necessary because of the small event sample.

[3] http://www.srl.caltech.edu/ACE/ASC/DATA/level3/icmetable2.htm.

Table 2 Comparison of the travel time of CMEs based on *Wind* and ACE measurements and based on inferred speeds using the empirical interplanetary propagation model. An asterisk (*) in column 1 indicates that the ICME arrival is uncertain. Suffix (f) in column 2 indicates that probably only the flank of the ICME passed over the spacecraft.

N	ICME onset		LASCO observations			SXR bursts			
	Wind ICME	ACE ICME	Date/Time	Speed [km s^{-1}]	Predicted arrival	Start	Φ_{sp} [J m^{-2}]	Speed [km s^{-1}]	Predicted arrival
	1997								
1	11 Apr 09:00	–	7 Apr 14:27	830	10 Apr 18:00	14:08	0.0036	592	11 Apr 09:08 (10 Apr 12:42 – 11 Apr 20:50)
2	15 May 10:30	–	12 May 06:30	306	16 May 19:30	04:55	0.0004	355	16 May 14:55 (16 May 01:08 – 16 May 23:13)
	1998								
3	24 Jun 18:00	24 Jun 17:00	21 Jun 05:35	307	25 Jun 18:25	05:18	0.0043	619	24 Jun 22:18 (24 Jun 01:00 – 25 Jun 10:43)
	1999								
4	16 Apr 19:00	16 Apr 18:00	13 Apr 03:30	282	17 Apr 18:00	02:14	0.0002	309	17 Apr 15:15 (17 Apr 03:04 – 17 Apr 22:58)
	2000								
5(*)	–	8 Jun 12:30	6 Jun 15:54	1098	8 Jun 22:05	15:26	0.2002	1557	8 Jun 02:26 (7 Jun 15:42 – 8 Jun 17:19)
6	24 Jun 07:00 (f)	24 Jun 03:00	20 Jun 09:10	471	24 Jun 11:40	08:27	0.0020	516	24 Jun 08:00 (23 Jun 15:00 – 24 Jun 18:57)
7	28 Jul 14:00	28 Jul 13:00	25 Jul 03:30	532	29 Jul 02:05	02:50	0.0077	712	28 Jul 13:50 (27 Jul 13:23 – 29 Jul 03:39)
8	31 Jul 23:00	31 Jul 22:00	28 Jul 18:30	832	31 Jul 21:50	17:16	0.0003	314	2 Aug 04:30 (1 Aug 15:29 – 2 Aug 12:38)
	2001								
9	21 Oct 20:00	–	19 Oct 16:50	901	22 Oct 13:50	16:15	0.0668	1197	21 Oct 16:45 (21 Oct 00:56 – 22 Oct 14:54)
10	6 Nov 12:00	–	4 Nov 16:35	1810	5 Nov 21:25	16:03	0.0460	1094	6 Nov 22:30 (6 Nov 04:14 – 7 Nov 21:35)
	2002								
11	8 Sep 04:00	8 Sep 04:00	5 Sep 16:54	1748	6 Sep 22:54	16:19	0.0073	704	9 Sep 04:00 (8 Sep 03:41 – 9 Sep 17:35)
	2003								
12	28 Oct 02:30	–	26 Oct 17:54	1537	28 Oct 05:10	17:15	0.2230	1598	28 Oct 02:45 (27 Oct 16:49 – 28 Oct 17:25)
	2004								
13	22 Jul 18:00	–	20 Jul 13:31	710	24 Jul 00:45	12:17	0.0190	885	23 Jul 10:45 (22 Jul 10:19 – 24 Jul 04:26)

Table 2 (*Continued.*)

N	ICME onset		LASCO observations			SXR bursts			
	Wind ICME	ACE ICME	Date/Time	Speed [km s^{-1}]	Predicted arrival	Start	Φ_{sp} [J m^{-2}]	Speed [km s^{-1}]	Predicted arrival
	2005								
14	21 Jan 19:00	21 Jan 19:00	20 Jan 06:54	882	23 Jan 05:45	06:32	0.5306	1968	21 Jan 08:30 (21 Jan 01:10 – 21 Jan 19:04)
15	15 May 06:00	15 May 06:00	13 May 17:12	1689	15 May 00:30	16:28	0.0615	1173	15 May 18:10 (15 May 01:54 – 16 May 16:50)
	2006								
16	14 Dec 22:00	14 Dec 22:00	13 Dec 02:54	1774	14 Dec 08:25	02:18	0.2243	1600	14 Dec 11:50 (14 Dec 01:50 – 15 Dec 02:23)
17	17 Dec 00:00	17 Dec 00:00	14 Dec 22:30	1042	17 Dec 08:30	22:00	0.0451	1089	17 Dec 04:50 (16 Dec 10:23 – 18 Dec 03:48)
	2010								
18	5 Apr 12:30	5 Apr 12:00	3 Apr 10:30	668	7 Apr 00:30	09:53	0.0012	453	7 Apr 13:20 (6 Apr 21:17 – 7 Apr 23:14)
	2011								
19	18 Feb 06:00	18 Feb 05:30	15 Feb 02:24	669	18 Feb 16:24	01:56	0.0570	1152	17 Feb 04:56 (16 Feb 12:04 – 18 Feb 03:52)
20	5 Aug 04:00 (f)	5 Aug 03:00	2 Aug 06:39	712	5 Aug 17:50	05:48	0.0118	790	5 Aug 12:05 (4 Aug 10:08 – 6 Aug 02:46)
21	10 Sep 03:30 (f)	10 Sep 05:00	6 Sep 22:30	575	10 Sep 18:30	22:02	0.0241	937	9 Sep 16:02 (8 Sep 17:11 – 10 Sep 11:33)
	2012								
22	23 Jan 00:30	22 Jan 23:30	19 Jan 15:09	1120	21 Jan 20:00	14:28	0.1002	1319	21 Jan 09:20 (20 Jan 19:45 – 22 Jan 04:52)
23	9 Mar 04:30	–	7 Mar 00:24	2684	7 Mar 18:24	00:00	0.2770	1683	8 Mar 07:30 (7 Mar 22:13 – 8 Mar 20:54)
24	12 Mar 22:00 (f)	–	10 Mar 17:54	491	14 Mar 19:05	17:15	0.0772	1239	12 Mar 15:45 (12 Mar 00:41 – 13 Mar 12:55)
25	16 Jun 23:00	16 Jun 22:30	14 Jun 14:09	987	17 Jun 04:10	12:50	0.0431	1077	16 Jun 20:20 (16 Jun 01:40 – 17 Jun 19:14)
26	15 Jul 07:00	15 Jul 06:30	12 Jul 16:54	885	15 Jul 15:25	15:42	0.1936	1545	14 Jul 02:40 (13 Jul 16:11 – 14 Jul 18:08)

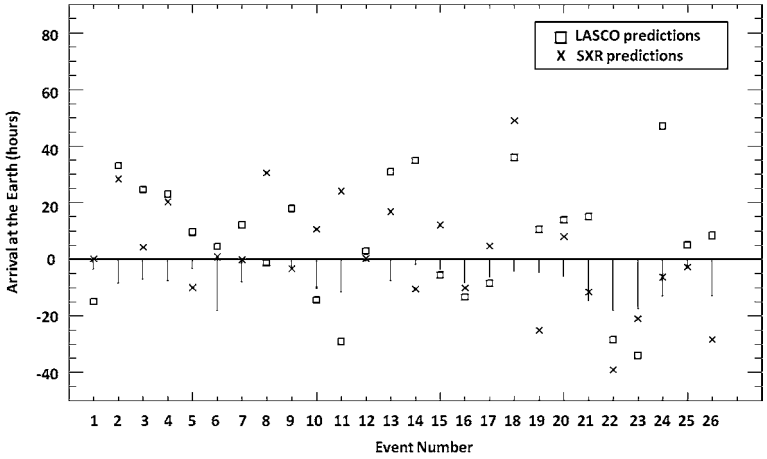

Figure 4 Representation of the predictions of arrival at Earth with reference to the observed ICME arrival (0 on the ordinate). The vertical lines indicate the time interval between the shock arrival and the ICME arrival at the *Wind* spacecraft.

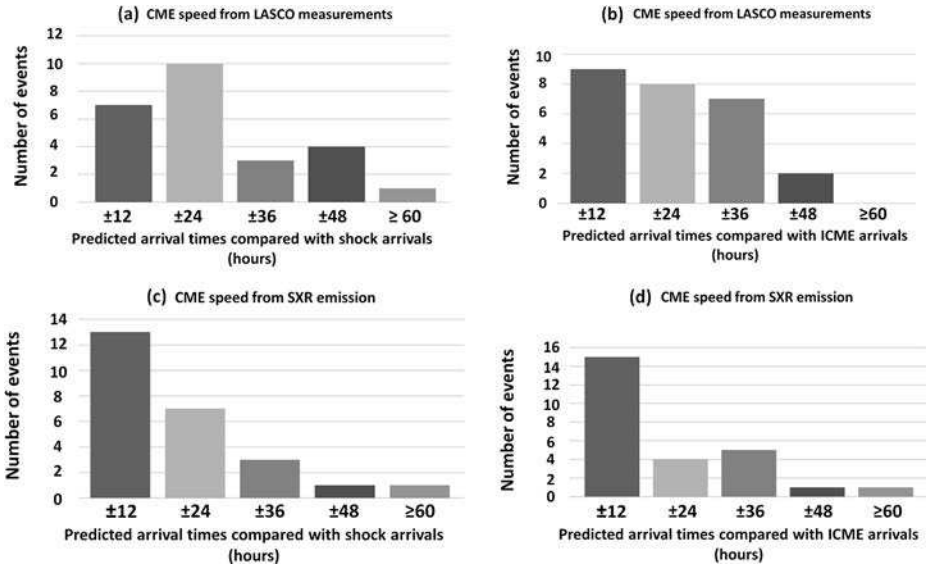

Figure 5 Comparison of predicted ICME arrival at 1 AU with the observed onset of the shock and ICME at the *Wind* spacecraft. The predictions are compared with the observed arrival of the shock in histograms (a) and (c), and of the ICME in histograms (b) and (d). Histograms in the top row show the predictions using LASCO measurements, those in the bottom row predictions using the propagation speed inferred from SXR fluence.

4.2. Assessment of Failed Predictions

In 8 of 26 events the observed arrival time of the ICME is outside the range of uncertainty of the SXR fluence prediction (events 2, 4, 8, 18, 19, 22, 23, and 26). This set includes the six events in the three highest bins of Figure 5(d) and two other events where the ICME arrival

prediction was incorrect by more than 20 h. Five of these events are also poorly predicted when the CME speed from LASCO is used, while in the three others (8, 19, and 26), the speeds from LASCO observations lead to a better estimate of the ICME arrival than the estimation based on the SXR fluence.

In some of the events we obtained an over- or underestimation of the speed that affected the predictions of ICME arrival. In events 2, 4, and 8, we found low speeds of 355, 309, and 314 $\mathrm{km\,s^{-1}}$, respectively, with a corresponding delay of the ICME arrival of 29, 20, and 29 h, respectively. The LASCO measurements were similarly slow for events 2 and 4, but not for event 8, where the observed speed was 832 $\mathrm{km\,s^{-1}}$, providing a prediction in advance by only 1 h of the observed ICME arrival.

In the remaining events we can use published observation from the *Solar Terrestial Relations Observatory* (STEREO) for a more detailed assessment of the failed predictions. For event 18 on 3 April 2010, the SXR prediction is late by 48 h, while LASCO is late by 36 h. The studied CME is moderately fast, with a higher speed observed by LASCO (668 $\mathrm{km\,s^{-1}}$) than inferred from the SXR fluence (456 $\mathrm{km\,s^{-1}}$). This event was observed by STEREO B at the limb with a speed of 833 $\mathrm{km\,s^{-1}}$ (Wood *et al.*, 2011). When this speed is used in the ICME propagation model, an interplanetary travel time of about 51 h and an ICME arrival at 1 AU near 12 UT on 5 April is predicted, which excellently agrees with the observations. This means that the failed ICME prediction based on the speeds from LASCO and from the SXR fluence is most likely due to the erroneous estimates of the Earth-directed CME speed.

The SXR prediction of the ICME arrival for event 19 on 15 February 2011 is early by 25 h, while the prediction from LASCO measurements is late by 10 h. The CME speed inferred from the SXR fluence is higher (1152 $\mathrm{km\,s^{-1}}$) than from LASCO observations (669 $\mathrm{km\,s^{-1}}$). An intermediate CME speed of 945 $\mathrm{km\,s^{-1}}$ was measured by STEREO A, where the event occurred near the limb (Schrijver *et al.*, 2011). The travel time to 1 AU is about 65 h, predicting the arrival of the ICME on 17 February near 19 UT, that is, about 6 h too early. On the other hand, the three-dimensional (3D) modeling by Temmer *et al.* (2014) and Mishra and Srivastava (2014) gave initial CME speeds of about 1000 – 1100 $\mathrm{km\,s^{-1}}$, in good agreement with the speed inferred from SXR fluence. Mishra and Srivastava (2014) reported a pronounced deceleration from 1100 $\mathrm{km\,s^{-1}}$ at 6 $\mathrm{R_\odot}$ to 580 $\mathrm{km\,s^{-1}}$ at 11 $\mathrm{R_\odot}$. This suggests that in this case the CME speed inferred from the SXR fluence was an adequate estimate, but the interplanetary transport was complex, probably due to the interaction with previous CMEs (Temmer *et al.*, 2014; Mishra and Srivastava, 2014).

For event 22 on 19 January 2012, the SXR fluence-based prediction is early by 39 h, LASCO by 28 h. The CME is fast, with a lower speed estimate from LASCO observations (1120 $\mathrm{km\,s^{-1}}$) than from the SXR fluence (1319 $\mathrm{km\,s^{-1}}$). A CME speed of 1335 $\mathrm{km\,s^{-1}}$ was inferred from 3D modeling (Möstl *et al.*, 2014), confirming our estimation from the SXR fluence. The failure of our arrival predictions is hence not likely to be due to erroneous estimate of the CME speed in the corona. The detailed analysis of the CME and its interplanetary propagation (Liu *et al.*, 2013) reveals a rapid deceleration of the CME down to 700 – 800 $\mathrm{km\,s^{-1}}$ within 35 $\mathrm{R_\odot}$ from the Sun and a subsequent propagation at roughly constant speed. The simple propagation model applied in the present study predicts such speeds only at the imposed terminal distance of 0.76 AU and therefore underestimates the interplanetary travel time.

The CME in event 23 on 7 March 2012 is very fast, with a higher speed observed by LASCO (2684 $\mathrm{km\,s^{-1}}$) than inferred from the SXR fluence (1683 $\mathrm{km\,s^{-1}}$). A similarly high speed as in the LASCO measurement (2585 $\mathrm{km\,s^{-1}}$) was found in the 3D modeling (Möstl *et al.*, 2014). But this CME has a complex propagation into the interplanetary medium (Rollett *et al.*, 2014). The speed inferred from SXR fluence underestimates the CME speed. On

the other hand, a deceleration of this ICME in the interplanetary space was observed by Liu *et al.* (2013), Davies *et al.* (2013), and Rollett *et al.* (2014). The analyses of Liu *et al.* (2013) and Rollett *et al.* (2014) suggest that the deceleration was enhanced by the interaction of the fast CME with previous ones. The interplanetary propagation cannot be described by a simple empirical propagation model in this case.

Finally, for event 26 (12 July 2012), the prediction of arrival time of the ICME based on the SXR fluence is early by 28 h and that based on LASCO observations is early by 8 h. The CME speed inferred from SXR fluence is high (1545 $\mathrm{km\,s^{-1}}$), while the LASCO measurement is 885 $\mathrm{km\,s^{-1}}$. From the analysis of STEREO observations with a drag model of interplanetary transport, Hess and Zhang (2014) derived an initial speed of 1316 $\mathrm{km\,s^{-1}}$. This speed would predict a travel time of about 43 h and an ICME arrival near 12 UT on 14 July, which is well in advance of the observed arrival. The issue is hence rather one of the interplanetary propagation of the CME than of the speed determination from the SXR fluence, which is closer to the result of the STEREO observations than the speed from LASCO.

5. Summary and Discussion

5.1. Summary of Observational Results

The re-assessment we conducted of the correlation between the speed of a CME near the limb and the parameters of the associated SXR burst, provided such a burst can be identified, is summarized as follows:

i) We confirm the frequently found correlation between CME speed and SXR peak flux.
ii) The correlation of the CME speed is slightly higher with SXR fluence ($r = 0.58 \pm 0.09$) than with SXR flux ($r = 0.48 \pm 0.12$).
iii) The SXR-inferred CME speed performed better than the speed measured by LASCO as an input to the arrival time prediction of ICMEs at Earth using a simple empirical interplanetary propagation model based on Gopalswamy *et al.* (2001).

5.2. Comparison with Earlier Work

Detailed comparisons of the kinematical evolution of CMEs in the low corona revealed a close relationship with energy release to the thermal plasma observed in SXR (Zhang *et al.*, 2001, 2004). The statistical studies of Maričić *et al.* (2007) and Bein *et al.* (2012) demonstrated that the CME acceleration is usually pronounced between the start and peak of the SXR burst, with a maximum near the time of the steepest rise of the time profile. After the SXR peak, the CME propagates at roughly constant speed in the corona. This relationship suggests a correlation between the terminal speed of the CME and parameters of the SXR burst, although exceptions from the general trend do exist (Maričić *et al.*, 2007) and are expected to blur the correlation.

The correlation coefficient between the logarithms of CME speed and of SXR peak flux we derived, $r = 0.48 \pm 0.12$, is similar to values reported by others: $r = 0.47$ (Moon *et al.*, 2002), $r = 0.35$ (Vršnak, Sudar, and Ruždjak, 2005), $r = 0.50$ (Yashiro and Gopalswamy, 2009), and $r = 0.32 \pm 0.13$ (Bein *et al.*, 2012). A distinctly higher correlation, $r = 0.93$, was found by Moon *et al.* (2003) in a carefully selected small sample of eight flare-CME events, where for four of them that were located on the solar disk, the CME speed was corrected for projection effects.

Moon *et al.* (2002), Yashiro and Gopalswamy (2009), and the present study were restricted to limb CMEs, where projection effects on the CME speed measurements are expected to be minimized. While the correlation coefficients in these limb-event studies are higher, the increase is not significant when compared with the statistical uncertainties derived in the present study and Bein *et al.* (2012). We note, however, that the coefficient of the logarithm of SXR peak flux F in the linear relationship $\log V_{\mathrm{CME}} = a \log F + b$ is higher in our study of limb events ($a = 0.20 \pm 0.08$) than in the unrestricted sample of Bein *et al.* (2012) ($a = 0.08 \pm 0.03$).

The correlation is only slightly increased when the SXR fluence is used ($r = 0.58 \pm 0.09$) instead of the SXR peak flux. Yashiro and Gopalswamy (2009) found $r = 0.56$ for a larger sample, but without error estimate. The use of fluence does not significantly improve the correlation between SXRs and CME speed. Burkepile *et al.* (2004) considered the correlation of the kinetic energy of the CME, instead of the speed, with SXR peak flux of limb events. They reported a high correlation ($r = 0.74$ for 24 events), well above the $r = 0.48$ of Yashiro and Gopalswamy (2009). The absence of an error estimate precludes a comparison of the two values, but the scatter plot in Figure 6 of Burkepile *et al.* (2004) suggests that the high correlation coefficient is favored by the two extreme events of their sample and that a lower value might be obtained from a larger sample.

We conclude that the focus on the limb events did provide an improved determination of the relationship between the logarithms of CME speed and of SXR fluence and peak flux. But a considerable scatter remains, probably due to physical differences between individual events. In their analysis of a 2D model of a flux rope eruption, Reeves and Moats (2010) found a power-law relationship between the peak acceleration and the peak SXR flux for a given reconnection rate, measured by the Alfvén Mach number of the plasma inflow into the current sheet. The authors showed that for a given CME peak acceleration the peak GOES flux is expected to increase with decreasing reconnection rate and concluded that different reconnection rates may contribute to explaining the broad scatter in the observed relationships between CME kinematics and SXR emission.

5.3. SXR Observations and the Prediction of ICME Arrival at Earth

We tested the performance of the SXR fluence as a proxy of the CME speed by applying it to the prediction of the ICME arrival near Earth, using an empirical interplanetary acceleration model based on Gopalswamy *et al.* (2001). For a set of 26 well-defined CME–ICME pairs with associated SXR bursts, we found that the SXR-inferred speed tended to perform better than the plane-of-the sky expansion speed measured by a coronagraph on the Earth-Sun line. This suggests that SXR observations can serve as an input to ICME prediction schemes, provided the existence of a CME is ascertained by coronagraphic observations. Problems arise with particularly slow and particularly fast CMEs, where our empirical relationship seems to be a poor predictor. This is probably at least partly due to an inadequate treatment of the bias of the CME–SXR relationship, which in turn is a result of the incomplete detection of slow CMEs and faint SXR bursts. Comparisons of selected events with CME speed from STEREO measurements and 3D modeling confirm the performance of the SXR fluence as a proxy of CME speed.

Recent work using STEREO emphasizes the importance of the interplanetary dynamics of the CME (Kilpua *et al.*, 2012; Colaninno, Vourlidas, and Wu, 2013; Möstl *et al.*, 2014) in arrival time predictions, which cannot be captured by a simple empirical model. But when sophisticated tools such as heliospheric imaging of the Sun–Earth system from a viewpoint away from the Sun–Earth line are not available, the SXR emission can provide valuable constraints for the ICME arrival prediction.

Acknowledgements This study made extensive use of the CME catalog, generated and maintained at the CDAW Data Center by NASA and The Catholic University of America in cooperation with the Naval Research Laboratory. SOHO is a project of international cooperation between ESA and NASA. GOES data were provided by NOAA and the Solar Data Analysis Center (SDAC) at NASA Goddard Space Flight Center. The data bases of ACE and omniweb (Wind) were also used. The authors thank P. Démoulin for his help with the identification of ICMEs, and G. Trottet for providing software for the SXR data analysis. The referee is thanked for the detailed reading of the manuscript and comments. C. S-M gratefully acknowledges the financial support of her doctorate studies given by the University of Costa Rica and the Ministry of Science, Technology and Telecommunications of Costa Rica (MICITT) through the National Council of Scientific and Technological Research (CONICIT). This work was partly supported by Centre National d'Etudes Spatiales (CNES).

References

Aggarwal, M., Jain, R., Mishra, A.P., Kulkarni, P.G., Vyas, C., Sharma, R., Gupta, M.: 2008, X-ray emission characteristics of flares associated with CMEs. *J. Astrophys. Astron.* **29**, 195. DOI.

Bein, B.M., Berkebile-Stoiser, S., Veronig, A.M., Temmer, M., Vršnak, B.: 2012, Impulsive acceleration of coronal mass ejections. II. Relation to soft X-ray flares and filament eruptions. *Astrophys. J.* **755**, 44. DOI.

Brueckner, G.E., Howard, R.A., Koomen, M.J., Korendyke, C.M., Michels, D.J., Moses, J.D., Socker, D.G., Dere, K.P., Lamy, P.L., Llebaria, A., Bout, M.V., Schwenn, R., Simnett, G.M., Bedford, D.K., Eyles, C.J.: 1995, The Large Angle Spectroscopic Coronagraph (LASCO). *Solar Phys.* **162**, 357. DOI.

Burkepile, J.T., Hundhausen, A.J., Stanger, A.L., St. Cyr, O.C., Seiden, J.A.: 2004, Role of projection effects on solar coronal mass ejection properties: 1. A study of CMEs associated with limb activity. *J. Geophys. Res.* **109**, 3103. DOI.

Colaninno, R.C., Vourlidas, A., Wu, C.C.: 2013, Quantitative comparison of methods for predicting the arrival of coronal mass ejections at Earth based on multiview imaging. *J. Geophys. Res.* **118**, 6866. DOI.

Davies, J.A., Perry, C.H., Trines, R.M.G.M., Harrison, R.A., Lugaz, N., Möstl, C., Liu, Y.D., Steed, K.: 2013, Establishing a stereoscopic technique for determining the kinematic properties of solar wind transients based on a generalized self-similarly expanding circular geometry. *Astrophys. J.* **777**, 167. DOI.

Delaboudinière, J.-P., Artzner, G.E., Brunaud, J., Gabriel, A.H., Hochedez, J.F., Millier, F., Song, X.Y., Au, B., Dere, K.P., Howard, R.A., Kreplin, R., Michels, D.J., Moses, J.D., Defise, J.M., Jamar, C., Rochus, P., Chauvineau, J.P., Marioge, J.P., Catura, R.C., Lemen, J.R., Shing, L., Stern, R.A., Gurman, J.B., Neupert, W.M., Maucherat, A., Clette, F., Cugnon, P., van Dessel, E.L.: 1995, EIT: Extreme-Ultraviolet Imaging Telescope for the SOHO mission. *Solar Phys.* **162**, 291. DOI.

Démoulin, P.: 2010, Interaction of ICMEs with the solar wind. In: Maksimovic, M., Issautier, K., Meyer-Vernet, N., Moncuquet, M., Pantellini, F. (eds.) *Twelfth International Solar Wind Conference*, *AIP Conf. Proc.* **1216**, 329. DOI.

Forbes, T.G., Linker, J.A., Chen, J., Cid, C., Kóta, J., Lee, M.A., Mann, G., Mikić, Z., Potgieter, M.S., Schmidt, J.M., Siscoe, G.L., Vainio, R., Antiochos, S.K., Riley, P.: 2006, CME theory and models. *Space Sci. Rev.* **123**, 251. DOI.

Gold, T.: 1962, Magnetic storms. *Space Sci. Rev.* **1**, 100. DOI.

Gonzalez, W.D., Tsurutani, B.T.: 1987, Criteria of interplanetary parameters causing intense magnetic storms (Dst of less than −100 nT). *Planet. Space Sci.* **35**, 1101. DOI.

Gopalswamy, N.: 2010, The CME link to geomagnetic storms. In: Kosovichev, A.G., Andrei, A.H., Rozelot, J.-P. (eds.) *Solar and Stellar Variability: Impact on Earth and Planets*, *IAU Symp.* **264**, 326. DOI.

Gopalswamy, N., Lara, A., Yashiro, S., Kaiser, M.L., Howard, R.A.: 2001, Predicting the 1-AU arrival times of coronal mass ejections. *J. Geophys. Res.* **106**, 29207. DOI.

Gosling, J.T.: 1993, The solar flare myth. *J. Geophys. Res.* **98**, 18937. DOI.

Hess, P., Zhang, J.: 2014, Stereoscopic study of the kinematic evolution of a coronal mass ejection and its driven shock from the Sun to the Earth and the prediction of their arrival Times. *Astrophys. J.* **792**, 49. DOI.

Kahler, S.W., Sheeley, N.R., Jr., Liggett, M.: 1989, Coronal mass ejections and associated X-ray flare durations. *Astrophys. J.* **344**, 1026. DOI.

Kilpua, E.K.J., Mierla, M., Rodriguez, L., Zhukov, A.N., Srivastava, N., West, M.J.: 2012, Estimating travel times of coronal mass ejections to 1 AU using multi-spacecraft coronagraph data. *Solar Phys.* **279**, 477. DOI.

Liu, Y.D., Luhmann, J.G., Lugaz, N., Möstl, C., Davies, J.A., Bale, S.D., Lin, R.P.: 2013, On Sun-to-Earth propagation of coronal mass ejections. *Astrophys. J.* **769**, 45. DOI.

Maričić, D., Vršnak, B., Stanger, A.L., Veronig, A.M., Temmer, M., Roša, D.: 2007, Acceleration phase of coronal mass ejections: II. Synchronization of the energy release in the associated flare. *Solar Phys.* **241**, 99. DOI.

Mishra, W., Srivastava, N.: 2014, Morphological and kinematic evolution of three interacting coronal mass ejections of 2011 February 13 – 15. *Astrophys. J.* **794**, 64. DOI.

Moon, Y.-J., Choe, G.S., Wang, H., Park, Y.D., Gopalswamy, N., Yang, G., Yashiro, S.: 2002, A statistical study of two classes of coronal mass ejections. *Astrophys. J.* **581**, 694. DOI.

Moon, Y.-J., Choe, G.S., Wang, H., Park, Y.D., Cheng, C.Z.: 2003, Relationship between CME kinematics and flare strength. *J. Korean Astron. Soc.* **36**, 61. DOI.

Möstl, C., Amla, K., Hall, J.R., Liewer, P.C., De Jong, E.M., Colaninno, R.C., Veronig, A.M., Rollett, T., Temmer, M., Peinhart, V., Davies, J.A., Lugaz, N., Liu, Y.D., Farrugia, C.J., Luhmann, J.G., Vršnak, B., Harrison, R.A., Galvin, A.B.: 2014, Connecting speeds, directions and arrival times of 22 coronal mass ejections from the Sun to 1 AU. *Astrophys. J.* **787**, 119. DOI.

Reeves, K.K., Moats, S.J.: 2010, Relating coronal mass ejection kinematics and thermal energy release to flare emissions using a model of solar eruptions. *Astrophys. J.* **712**, 429. DOI.

Rollett, T., Möstl, C., Temmer, M., Frahm, R.A., Davies, J.A., Veronig, A.M., Vršnak, B., Amerstorfer, U.V., Farrugia, C.J., Žic, T., Zhang, T.L.: 2014, Combined multipoint remote and in situ observations of the asymmetric evolution of a fast solar coronal mass ejection. *Astrophys. J. Lett.* **790**, L6. DOI.

Rouillard, A.P.: 2011, Relating white light and in situ observations of coronal mass ejections: A review. *J. Atmos. Solar-Terr. Phys.* **73**, 1201. DOI.

Schrijver, C.J., Aulanier, G., Title, A.M., Pariat, E., Delannée, C.: 2011, The 2011 February 15 X2 flare, ribbons, coronal front, and mass ejection: Interpreting the three-dimensional views from the Solar Dynamics Observatory and STEREO guided by magnetohydrodynamic flux-rope modeling. *Astrophys. J.* **738**, 167. DOI.

Schwenn, R., dal Lago, A., Huttunen, E., Gonzalez, W.D.: 2005, The association of coronal mass ejections with their effects near the Earth. *Ann. Geophys.* **23**, 1033. DOI.

Tandberg-Hanssen, E., Emslie, A.G.: 1988, *The Physics of Solar Flares*, Cambridge University Press, Cambridge/New York. Chapter 9.

Temmer, M., Veronig, A.M., Peinhart, V., Vršnak, B.: 2014, Asymmetry in the CME–CME interaction process for the events from 2011 February 14 – 15. *Astrophys. J.* **785**, 85. DOI.

Trottet, G., Samwel, S., Klein, K.-L., Dudok de Wit, T., Miteva, R.: 2015, Statistical evidence for contributions of flares and coronal mass ejections to major solar energetic particle events. *Solar Phys.* **290**, 819. DOI.

Tsuneta, S., Acton, L., Bruner, M., Lemen, J., Brown, W., Caravalho, R., Catura, R., Freeland, S., Jurcevich, B., Morrison, M., Ogawara, Y., Hirayama, T., Owens, J.: 1991, The Soft X-ray Telescope for the SOLAR-A mission. *Solar Phys.* **136**, 37. DOI.

Vršnak, B., Sudar, D., Ruždjak, D.: 2005, The CME-flare relationship: Are there really two types of CMEs? *Astron. Astrophys.* **435**, 1149. DOI.

Vršnak, B., Žic, T., Falkenberg, T.V., Möstl, C., Vennerstrom, S., Vrbanec, D.: 2010, The role of aerodynamic drag in propagation of interplanetary coronal mass ejections. *Astron. Astrophys.* **512**, A43. DOI.

Wall, J.V., Jenkins, C.R.: 2012, *Practical Statistics for Astronomers*, Cambridge University Press, Cambridge/New York. Chapter 6.6.

Wood, B.E., Wu, C.-C., Howard, R.A., Socker, D.G., Rouillard, A.P.: 2011, Empirical reconstruction and numerical modeling of the first geoeffective coronal mass ejection of solar cycle 24. *Astrophys. J.* **729**, 70. DOI.

Yashiro, S., Gopalswamy, N.: 2009, Statistical relationship between solar flares and coronal mass ejections. In: Gopalswamy, N., Webb, D.F. (eds.) *Universal Heliophysical Processes*, *IAU Symp.* **257**, 233. DOI.

Zhang, J., Dere, K.P., Howard, R.A., Kundu, M.R., White, S.M.: 2001, On the temporal relationship between coronal mass ejections and flares. *Astrophys. J.* **559**, 452. DOI.

Zhang, J., Dere, K.P., Howard, R.A., Vourlidas, A.: 2004, A study of the kinematic evolution of coronal mass ejections. *Astrophys. J.* **604**, 420. DOI.

Zhang, J., Richardson, I.G., Webb, D.F., Gopalswamy, N., Huttunen, E., Kasper, J.C., Nitta, N.V., Poomvises, W., Thompson, B.J., Wu, C.-C., Yashiro, S., Zhukov, A.N.: 2007, Solar and interplanetary sources of major geomagnetic storms (Dst $= -100$ nT) during 1996 – 2005. *J. Geophys. Res.* **112**, 10102. DOI.

4.3.2 Microwave radio emission as a proxy of CME speed in ICME arrival predictions at 1 AU (paper)

submitted to **Journal of Space Weather and Space Climate**

Microwave radio emission as a proxy of CME speed in ICME arrival predictions at 1 AU

C. Salas-Matamoros[1,2], K-L. Klein[1], and G. Trottet[1]

[1] LESIA-UMR 8109 - Observatoire de Paris, PSL Res. Univ., CNRS, Univ. P & M Curie and Paris-Diderot, 92190 Meudon, France
e-mail: carolina.salas@obspm.fr
e-mail: ludwig.klein@obspm.fr
e-mail: gerard.trottet@obspm.fr
[2] Space Research Center, University of Costa Rica, San Jose, Costa Rica
e-mail: carolina.salas@cinespa.ucr.ac.cr

ABSTRACT

The propagation of a coronal mass ejection (CME) to the Earth takes between about 15 hours and several days. We explore whether observations of non-thermal microwave bursts, produced by near-relativistic electons via the gyrosynchrotron process, can be used to predict travel times of interplanetary coronal mass ejections (ICMEs) from the Sun to the Earth. In a first step, a relationship is established between the CME speed measured by SoHO/LASCO near the solar limb and the fluence of the microwave burst. This relationship is then employed to estimate speeds in the corona of earthward-propagating CMEs. These speeds are fed to a simple empirical interplanetary acceleration model to predict the speed and arrival time of the ICMEs at Earth. The predictions are compared with observed arrival times and with the predictions based on other proxies, including soft X-rays (SXR) and coronographic measurements. We find that CME speeds estimated from microwaves and SXR predict the ICME arrival at the Earth with absolute errors of 11±7 and 9±7 hours, respectively. A trend to underestimate the interplanetary travel times of ICMEs is noticed for both techniques. This is consistent with the fact that in most cases of our test sample ICMEs are detected on their flanks. Although this preliminary validation was carried out on a rather small sample of events (11), we conclude that microwave proxies can provide early estimates of ICME arrivals and ICME speeds in the interplanetary space. This method is limited by the fact that not all CMEs are accompanied by non-thermal microwave bursts. But its usefulness is enhanced by the relatively simple observational setup and the observation from ground, which makes the instrumentation less vulnerable to space weather hazards.

Key words. Coronal mass ejections; Interplanetary coronal mass ejections; Flares; radio bursts

1. Introduction

Coronal Mass Ejections (CMEs) are a major space weather hazard because they disturb the Earth's magnetosphere and may induce strong electric currents in the ionosphere and in the crust (e.g. Zhang et al., 2007). For this reason one of the principal aims of space weather forecasting is the prediction of the travel time of these magnetic structures from the Sun until the Earth. CMEs take between about 15 hours (Cliver et al., 1990) and a few days to reach the Earth. Prediction techniques have been developed based on remote observations and validated by *in situ* measurements. Most of these techniques involve two essential elements: the radial propagation speed of the CME in the corona and the interplanetary acceleration or deceleration.

CME velocities are usually obtained from coronographic observations of the time-height evolution of the front of the CME projected in the plane of the sky. But when the CME travels earthward, only the expansion speed perpendicular to the direction of propagation can be measured from the Sun-Earth line. Combined coronographic observations by the STEREO and SoHO spacecraft were a great step forward by enabling observations of the Sun with three eyes in different positions. 3D reconstruction techniques describe the propagation of CMEs in the corona (e.g., Thernisien et al., 2009). The combination with heliospheric imaging makes it possible to track CMEs from the Sun to the Earth (e.g., Rouillard, 2011; Colaninno et al., 2013; Möstl et al., 2014) and, as a consequence, to develop and validate new prediction techniques (e.g Gopalswamy et al., 2013).

Different models were developed to describe the interplanetary propagation of ICMEs. Empirical models of interplanetary propagation are based on relationships between coronographic measurements and ICME parameters in the interplanetary space (e.g. Gopalswamy et al., 2001; Schwenn et al., 2005). More sophisticated techniques include MHD modelling of the ICME propagation in the heliosphere. Models such as H3DMHD (Wu et al., 2011) and WSA-ENLIL+Cone (Odstrcil et al., 2004) use the coronal and *in situ* observations as input to simulate the propagation of disturbances into the heliosphere and predict their arrivals. Kinematic methods based on MHD or HD models have been also developed analytically (Cargill, 2004; Vršnak and Žic, 2007).

The unique capabilities of the combined STEREO and SoHO missions will only exist for a limited time. Space weather monitoring, which relies on the continuous availability of data, will need alternative methods to estimate the propagation speed of CMEs. X-ray and radio emissions might serve this purpose. A direct empirical relationship was established between a proxy of the 3 GHz fluence and the travel time of interplanetary shock waves between the Sun and the Earth by Caroubalos (1964), well before the actual discovery of CMEs themselves. Tobiska et al. (2013) developed a similar technique using soft X-ray fluence. The present study follows a different line of reasoning. It investigates whether gyrosynchrotron emission from non-thermal electrons at GHz frequencies (microwaves) can be used to infer the speed of Earth-directed CMEs in the corona, which can then be fed into an interplanetary acceleration model. The approach is identical to work by Salas-Matamoros and Klein (2015), which uses soft X-rays (SXR). In Section 2 empirical relationships are established between the speed of limb-CMEs and microwave fluence. In Section 3 we use these relationships in a sample containing 11 Earth-directed CMEs to estimate their outward propagation speeds without resorting to coronographic measurements. These speeds, together with a simple analytical formula for the interplanetary acceleration or deceleration, are used to estimate the arrival times and speeds of the interplanetary coronal mass ejections (ICMEs) near 1 AU. The predictions are compared with *in situ* observations to evaluate their quality. The possible influence

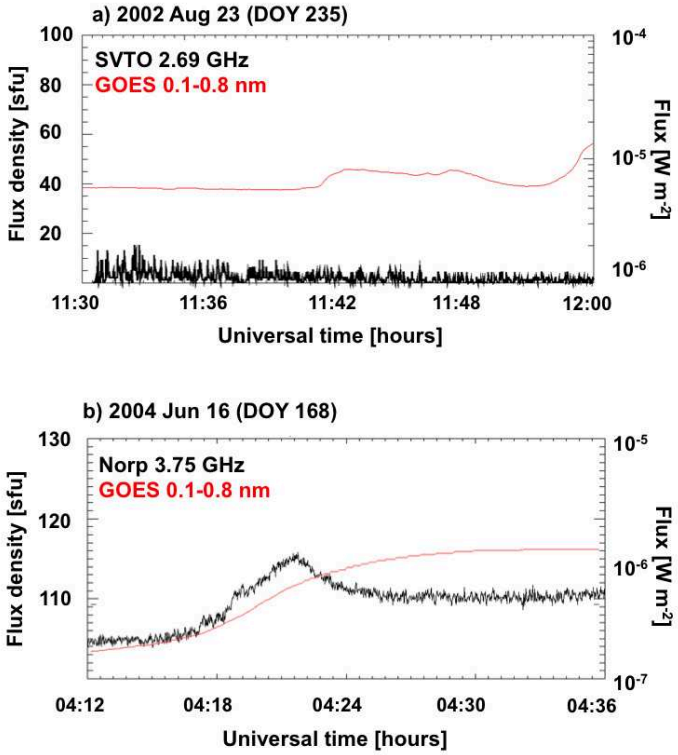

Fig. 1. Flux density profiles of discarded events. a) No microwave emission associated with the SXR burst. b) Thermal microwave emission.

of the geometry of the ICME on the estimation of arrival time is explored. The results are discussed with respect to other efforts of arrival time prediction in Section 4.

2. An empirical relationship between CME speed and microwave emission in limb events

2.1. Selection of the events

The data set that we use in this study is based on the 49 events listed in Table 1 in Salas-Matamoros and Klein (2015). Additionally, we incorporated events that occurred between 2009 and 2014. These CME events (with speeds more than 100 km s^{-1}) were carefully selected for their association with flares near the limb, at a central meridian distance between 70° and 85°, and with soft X-ray (SXR) bursts. The SXR burst must be unambiguous: cases where bursts from different active regions could be associated with one given CME, and cases where the SXR burst occurred far away from the CME were discarded. For this sample we analysed the microwave data provided by the US Air Force Radio Solar Telescope Network (RSTN)[1] at 1.41, 2.69, 4.99, 8.80 and 15.40 GHz and by the

[1] ftp://ftp.ngdc.noaa.gov/STP/space-weather/solar-data/solar-features/solar-radio/rstn-1-second/

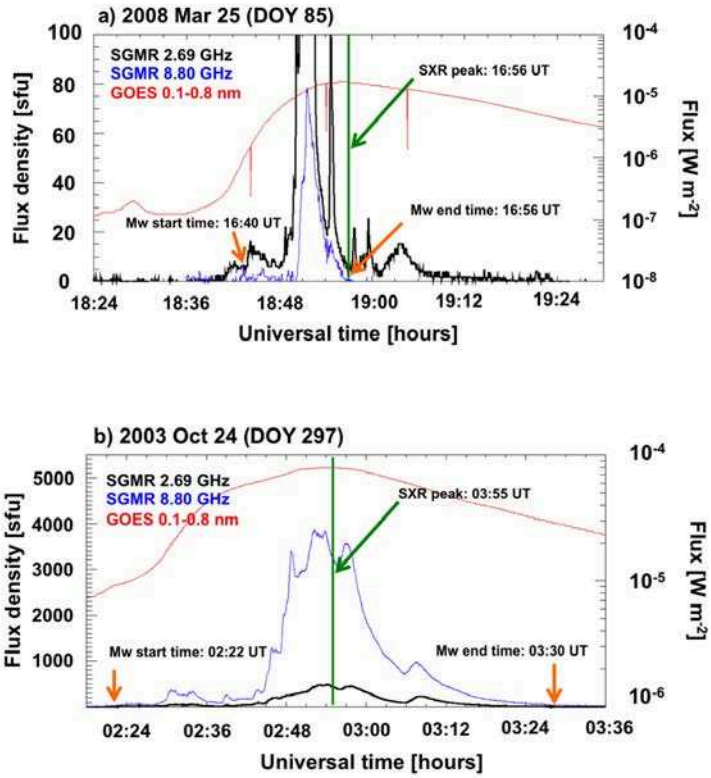

Fig. 2. Examples of time range selection for the fluence calculation. Black and blue curves are the microwave emissions at 2.69 and 8.8 GHz, respectively, while the SXR burst is plotted in red. The orange arrows show the start and the end of the time interval for the fluence calculation. a) End of the interval matches the peak of the SXR counterpart (green line). b) The microwave fluence calculation is extended until the end of the non-thermal microwave burst profile.

Nobeyama Radio Polarimeters (NoRP)[2] at 1, 2, 3.75, 9.40, 17 and 35 GHz (Nakajima et al., 1985). We searched for microwave emission that can be attributed to the gyrosynchrotron mechanism of mildly relativistic electrons (energy range ~100 keV-several MeV).

Whenever possible, microwave time profiles observed by different instruments were compared, and time profiles without data gap were selected. We discarded 19 events where the data were not available or incomplete, 7 events where no microwave emission was seen in relationship with the SXR burst (Figure 1.a) and the event on 16 June 2004, where the smooth profile with time scales similar to the one observed for SXR emission was identified as thermal emission (Figure 1.b). The final CME/microwave burst sample contains 41 events which are listed in Table 1.

[2] ftp://solar-pub.nao.ac.jp/pub/nsro/norp/xdr/

N	Date	CME parameters		SXR	Microwave parameters				
		t_0	V_{CME} [km s^{-1}]	t_p	t_0	t_f	Φ_{3GHz} [sfu ·s]	Φ_{9GHz} [sfu ·s]	Φ_{max} [sfu ·s]
(1)	(2)	(3)	(4)	(5)	(6)	(7)	(8)	(9)	(10)
1	1998 04 25	15:11	349	14:37	15:11	14:50	$2.3{\cdot}10^4$	-	$\geq 3.1{\cdot}10^4$
2	1999 04 03	23:47	923	23:10	23:00	23:17	$1.7{\cdot}10^4$	$1.6{\cdot}10^4$	$3.2{\cdot}10^4$
3	1999 11 08	07:26	154	06:01	05:55	06:01	$\leq 1.4{\cdot}10^2$	$\leq 2.8{\cdot}10^2$	$\leq 3.6{\cdot}10^2$
4	2000 06 17	03:28	857	02:37	02:30	02:40	$9.3{\cdot}10^3$	$1.1{\cdot}10^4$	$1.1{\cdot}10^4$
5	2000 06 23	14:54	847	14:32	14:20	14:37	$4.8{\cdot}10^4$	$2.2{\cdot}10^5$	$2.2{\cdot}10^5$
6	2001 04 15	14:06	1199	13:50	13:43	13:58	$4.0{\cdot}10^5$	$5.3{\cdot}10^5$	$\geq 1.2{\cdot}10^6$
7	2001 08 10	02:06	376	01:36	01:30	01:39	$3.9{\cdot}10^3$	$3.8{\cdot}10^3$	$\geq 7.2{\cdot}10^3$
8	2001 11 01	14:30	1053	15:01	14:15	16:00	$6.5{\cdot}10^5$	$4.8{\cdot}10^5$	$6.5{\cdot}10^5$
9	2001 12 29	09:54	634	09:45	09:39	09:45	$1.1{\cdot}10^4$	$1.7{\cdot}10^4$	$1.7{\cdot}10^4$
10	2002 03 13	23:54	489	23:36	23:09	23:36	$1.7{\cdot}10^4$	$2.0{\cdot}10^4$	$2.5{\cdot}10^4$
11	2002 04 04	05:06	468	04:40	04:25	04:42	$9.6{\cdot}10^3$	$7.4{\cdot}10^3$	$\geq 9.6{\cdot}10^3$
12	2002 07 05	13:31	818	13:26	13:12	13:26	$2.2{\cdot}10^4$	$1.5{\cdot}10^4$	$\geq 2.2{\cdot}10^4$
13	2002 08 03	19:31	1150	19:07	19:02	19:13	$1.3{\cdot}10^4$	$3.0{\cdot}10^4$	$\geq 3.0{\cdot}10^4$
14	2002 08 16	06:06	1378	06:12	05:43	07:18	$1.1{\cdot}10^5$	$3.4{\cdot}10^5$	$\geq 1.1{\cdot}10^7$
15	2002 08 22	18:26	750	18:02	17:35	18:08	$1.8{\cdot}10^4$	$6.8{\cdot}10^3$	$\geq 3.3{\cdot}10^4$
16	2002 09 08	02:06	364	01:43	01:36	01:45-01:53	$(1.6\text{-}2.2){\cdot}10^4$	$(2.9\text{-}4.7){\cdot}10^4$	$\geq 2.9{\cdot}10^4$
17	2003 04 09	23:50	511	23:29	23:26	23:33	-	$8.1{\cdot}10^3$	$\geq 8.1{\cdot}10^3$
18	2003 04 25	05:50	806	05:40	05:22	05:58	$2.1{\cdot}10^4$	$3.6{\cdot}10^3$	$\geq 3.6{\cdot}10^3$
19	2003 10 23	20:06	1136	20:03	19:52	20:04-20:36	$(2.7\text{-}9.8){\cdot}10^4$	$7.3{\cdot}10^4\text{-}1.2{\cdot}10^5$	$\geq 1.9{\cdot}10^5$
20	2003 10 24	02:54	1055	02:55	02:22	03:30	$5.1{\cdot}10^5$	$3.6{\cdot}10^6$	$\geq 3.9{\cdot}10^6$
21	2003 11 03	10:06	1420	09:56	09:48	09:57	$7.4{\cdot}10^5$	$9.4{\cdot}10^5$	$\geq 1.2{\cdot}10^6$
22	2004 01 07	04:06	1581	04:03	03:50	04:19	$2.7{\cdot}10^4$	$4.0{\cdot}10^5$	$\geq 5.7{\cdot}10^5$
23	2004 01 07	10:30	1822	10:26	10:15	10:34	$1.9{\cdot}10^5$	$2.6{\cdot}10^5$	$3.1{\cdot}10^5$
24	2004 05 17	05:26	383	04:17	04:13	04:19	$1.7{\cdot}10^3$	$2.5{\cdot}10^3$	$\geq 2.5{\cdot}10^3$
25	2004 08 31	05:54	311	05:38	05:31	05:38	$5.9{\cdot}10^3$	$5.1{\cdot}10^3$	$5.9{\cdot}10^3$
26	2005 04 17	21:26	721	21:07	21:00	21:10	$6.9{\cdot}10^3$	$6.6{\cdot}10^3$	$\geq 1.1{\cdot}10^4$
27	2005 05 06	03:30	1120	03:13	03:07	03:19	$1.8{\cdot}10^3$	$3.1{\cdot}10^4$	$\geq 3.3{\cdot}10^4$
28	2005 05 06	11:54	1144	11:28	11:21	11:28	$6.9{\cdot}10^3$	$2.3{\cdot}10^4$	$2.3{\cdot}10^4$
29	2005 08 25	04:54	1327	04:40	04:35	04:50	$3.7{\cdot}10^4$	$3.9{\cdot}10^5$	$\geq 6.4{\cdot}10^5$
30	2006 04 29	16:54	491	16:30	16:21	16:35	$1.4{\cdot}10^4$	$3.5{\cdot}10^3$	$1.4{\cdot}10^4$
31	2006 04 30	02:06	428	01:57	01:39	01:59-02:11	$(2.6\text{-}3.6){\cdot}10^4$	$(2.3\text{-}8.7){\cdot}10^4$	$\geq 1.0{\cdot}10^5$
32	2008 03 25	19:31	1103	18:56	18:40	18:57	$3.9{\cdot}10^4$	$1.1{\cdot}10^4$	$3.9{\cdot}10^4$
33	2010 06 14	01:31	343	00:51	00:47	00:51	$6.7{\cdot}10^2$	$5.4{\cdot}10^2$	$7.0{\cdot}10^2$
34	2011 08 09	14:00	428	13:45	13:29	13:45	$\leq 1.6{\cdot}10^3$	$\leq 5.2{\cdot}10^2$	$\leq 5.2{\cdot}10^2$
35	2011 11 14	20:24	383	20:13	19:42	20:13	$\leq 8.8{\cdot}10^2$	$\leq 7.8{\cdot}10^2$	$\leq 1.9{\cdot}10^3$
36	2011 11 16	02:12	456	03:01	02:55	03:01	$\leq 1.8{\cdot}10^2$	$\leq 4.6{\cdot}10^2$	$\leq 2.0{\cdot}10^3$
37	2012 06 06	03:12	375	02:19	02:12	02:19	$\leq 1.2{\cdot}10^2$	$\leq 4.6{\cdot}10^2$	$\leq 1.6{\cdot}10^3$
38	2012 07 08	10:48	662	09:53	09:44	09:53	$\leq 6.2{\cdot}10^2$	$\leq 3.5{\cdot}10^2$	$\leq 6.2{\cdot}10^2$
39	2013 07 17	09:48	355	09:16	09:12	09:16	$\leq 2.8{\cdot}10^2$	$\leq 1.8{\cdot}10^2$	$\leq 2.8{\cdot}10^2$
40	2014 02 14	17:24	283	16:52	16:33	16:47	$2.1{\cdot}10^4$	$1.4{\cdot}10^4$	$\geq 4.1{\cdot}10^4$
41	2014 07 12	14:24	479	14:08	14:02	14:13	$7.5{\cdot}10^1$	$2.1{\cdot}10^3$	$2.7{\cdot}10^3$

Table 1. Table of events: event number (col. 1), date (col. 2), time of the first appearance of the CME in LASCO/C2 coronograph (col. 3), CME speed in the plane of the sky reported in LASCO-CME (col. 4), SXR peak time (col. 5); times of onset (col. 6), end (col. 7), fluences at 3 GHz (col. 8), 9 GHz (col. 9), maximum (col. 10) of microwave bursts. Lower limits of the maximum fluence mean that the real maximum was outside the observed frequency range.

2.2. Fluence calculation

For all microwave bursts a background flux density[3] was determined as the average in a suitable time interval before the microwave burst, and was subtracted. The fluence (ϕ) was calculated by integrating the flux density during a user-defined time interval. Figure 2 shows two examples. The time interval for the fluence calculation depends on the event under consideration. In impulsive bursts the microwave emission occurs mainly during the rise phase of the SXR burst in the GOES 0.1-0.8 nm channel, as illustrated by the flux density profile at 8.8 GHz (blue curve) in Figure 2.a. In those cases the fluence was calculated until the end of the broad band microwave burst as observed at frequencies >5 GHz. The same end time was taken at all frequencies. This caused parts of the low-frequency microwave emission to be cut off when it had no counterpart at higher frequencies, such as the 2.69 GHz burst after 19:00 UT in Figure 2.a (black curve). Fluence was also calculated until the end of the microwave burst when a weak level of emission persisted in the early decay phase of the SXR burst, as illustrated in Figure 2.b. The fluences at 3 and 9 GHz, and the maximum fluence observed, are listed in cols. 8-10 in Table 1. In three cases (events 16, 19 and 31) the microwave bursts presented a new rise after the SXR peak. The microwave fluences with and without the late emission were computed and we found substantial changes in the fluence calculation for those events. Nevertheless, since those are only three events they do not affect the statistical relationships and they were not taken into account in the following where we consider that the CME acceleration is most pronounced during the rise phase of the SXR burst (e.g., Zhang et al., 2001; Maričić et al., 2007; Bein et al., 2012).

We use the fluence at 3 GHz ($\phi_{3\mathrm{GHz}}$), 9 GHz ($\phi_{9\mathrm{GHz}}$) and the maximum fluence (ϕ_{max}) when it could be identified. The synchrotron spectrum rises with increasing frequency in its optically thick part and decreases at higher frequencies, where the emission is optically thin. The spectral maximum was within the range of observed frequencies in only 13 cases. A lower limit of the maximum fluence is listed in the last column of Table 1 when the highest fluence is found at the highest observed frequency. In event 1 the emission at 9 GHz was of thermal origin. In event 17 the 3 GHz emission had a different time profile than the higher frequencies, suggesting it was due to collective plasma emission. In both cases the fluence is not listed in Table 1. In the seven cases (events 3, 34-39) where no microwave burst could be identified, upper limits of the fluence are given. The upper limits were calculated as the product of the background standard deviation of the flux densityand the duration of the rise phase of the SXR burst.

2.3. Relationships between CME speed and microwave fluence

Figure 3 shows the scatter plots between the logarithm of the limb-CME propagation speed (V_{CME}) and the logarithm of the fluence of the associated microwave bursts produced by gyrosynchrotron emission. The red arrows mark the upper limits of the fluence in the seven events where no microwave burst was seen. Lower limits of ϕ_{max} are shown by blue arrows in Figure 3.c. Even though some scatter remains in Figure 3 a clear relationship between CME speed and microwave fluence is obtained. Ignoring the upper and lower limits, we found significant correlations in all three cases:

- at 3 GHz: r=0.56 ± 0.14 for 33 events and p= 0.07%

[3] Flux density is given in solar flux units (sfu): 1 sfu = 10^{-22} W m^{-2} Hz^{-1}

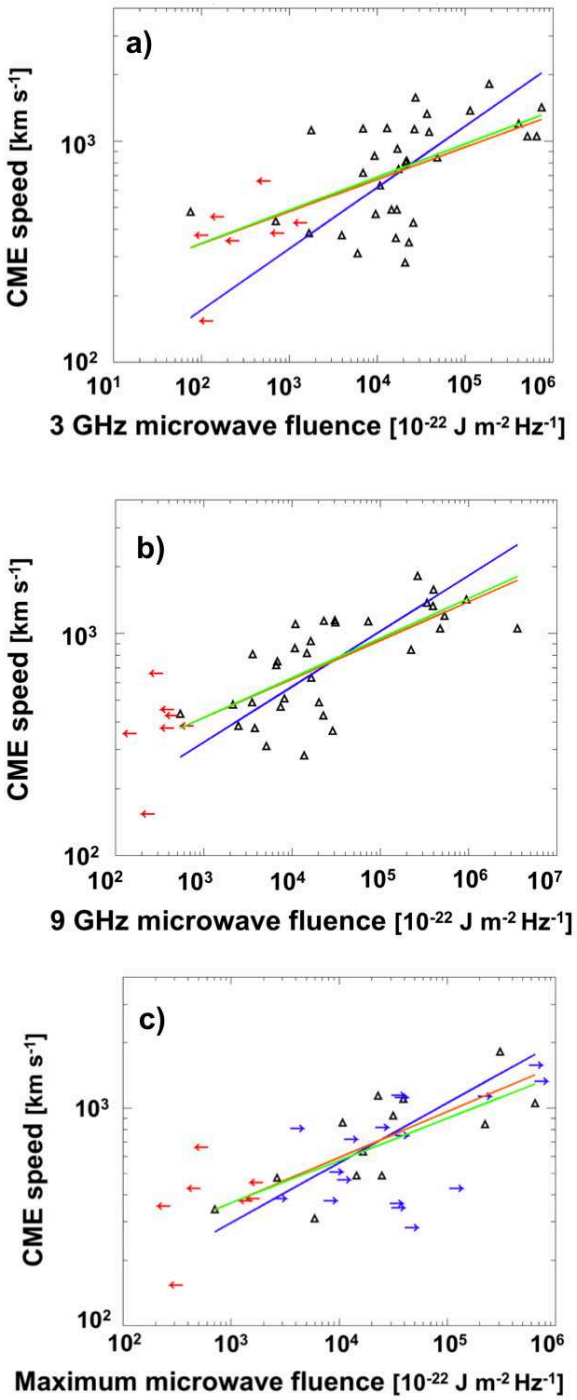

Fig. 3. Scatter plots for limb-CME speed during the period 1998-2014 versus the microwave fluences: a) $\phi_{3\mathrm{GHz}}$, b) $\phi_{9\mathrm{GHz}}$ and c) ϕ_{max}. The solid coloured lines represent the linear fits obtained by different methods: least absolute deviation (green), least squares (orange), and total least squares (blue). Red arrows show upper limits of the fluences, blue arrows the lower limits of ϕ_{max}.

Frequency	Least squares	Least absolute deviation	Total least squares
3 GHz	A=2.25±0.29	A=2.24±0.29	A=1.68±0.41
	B=0.14±0.06	B=0.15±0.06	B=0.28±0.10
9 GHz	A=2.10±0.23	A=2.09±0.23	A=1.76±0.36
	B=0.17±0.05	B=0.18±0.05	B=0.25±0.07
Maximum	A=1.93±0.70	A=1.98±0.70	A=1.65±0.57
	B=0.20±0.15	B=0.19±0.15	B=0.28±0.13

Table 2. Parameters of Equation 1 using three different methods of linear fit.

– at 9 GHz: r=0.72 ± 0.08 for 33 events and p= 0.0002%

– maximum fluence: r=0.75 ± 0.15 for 13 events and p= 0.3% ,

where p is the probability of obtaining this or a higher correlation coefficient from a random sample of uncorrelated events. The errors were calculated using a bootstrap method, where the correlation coefficient was calculated repeatedly a 1000 times for a randomly selected sample of 33 or 13 from the observed data pairs, and the mean and standard deviation are quoted as the correlation coefficient and its statistical uncertainty. The correlations are slightly higher at 9 GHz than at 3 GHz. That is expected, since the 3 GHz gyrosynchrotron emission is optically thick, and hence only weakly related to the energy released to non-thermal electrons.

To find the statistical relationships between $V_{\rm CME}$ and ϕ, we use three different linear fit methods to determine a straight line of the form

$$\log V_{\rm CME} = A \ + \ B \ \log \phi \ , \tag{1}$$

namely least squares (LS), least absolute deviation (LAD), and total least squares (TLS). Figure 2 shows the regression lines for the different methods. Table 2 contains the linear fit parameters of Eq. 1. The plots show that the methods of least absolute deviation (green line) and least squares (orange line) visually describe well the sample, including those observations where only upper limits were available. The TLS method (blue line), although it is formally more satisfying, since it assumes that both variables have uncertainties, provides a less convincing result, judging from visual inspection, when one includes the upper and lower limits of the microwave fluence: the straight line appears too steep, leading to an overestimation of CME speeds for high microwave fluences, and an underestimation for low fluences. LS and LAD methods provide comparable results when the statistical uncertainties are considered: the CME speeds calculated with the two methods at the extremes of the 9 GHz fluence differ by less than the statistical uncertainty calculated with the values of Table 2.

In the next Section we apply the correlations between $V_{\rm CME}$ and $\phi_{\rm 9GHz}$ obtained by the LS method to infer the speed of Earthward-directed CMEs, leaving aside $\phi_{\rm 3GHz}$, because it is optically thick. While the coefficients A and B in Table 2 are comparable, the dispersion is higher at 3 GHz. We did not use $\phi_{\rm max}$ either, because it could only be determined in few events.

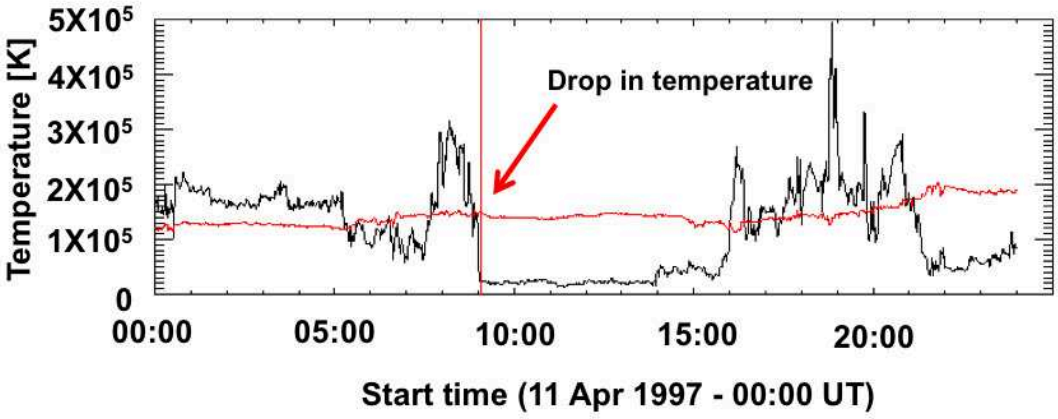

Fig. 4. Temperature profiles around and during the passage of an ICME at the Wind spacecraft. The black curve is the measured proton temperature. The red profile is the expected temperature (Eq. 2) for the observed solar wind speed as a function of time. The red arrow marks the ICME arrival time.

3. Application to ICME Arrival Time Predictions

3.1. Event selection, fluence calculation, empirical identification of ICME arrival

We collected a sample of Earth-directed CME events from the literature, which were related with flares located between ±40° from central meridian. We started with 26 events listed in Table 2 in Salas-Matamoros and Klein (2015), which were used in this publication to infer the speed of CMEs from SXR emission. We discarded events where microwave data were either unavailable or of bad quality (events on 12 May 1997, 21 June 1998, 13 April 1999, 5 September 2002, 3 April 2010, 6 September 2011, 19 January 2012 and 10 March 2012), or where no microwave emission was associated to the SXR burst (events on 20 June 2000 and 28 July 2000). The 12 July 2012 event was also discarded because we could not affirm from the microwave profile at 9 GHz that this was gyrosynchrotron emission. We selected twelve more ICME events to increase our sample: six (between 2011 and 2012) from the ISEST catalog[4], one from Table 1 in Shi et al. (2015), five (in years 2013 and 2014) from Table 1 in Mays et al. (2015).

Besides, 20 events listed in Table 1 in Gopalswamy et al. (2013) were also considered. Eight events in this list were already in our original sample. Other events were discarded because of the location of the source (one event), the absence of clear non-thermal microwave emission (three events), the unavailability of radio observations (one event), or because more than one CME was observed with few hours difference.

For the total compiled sample of 26 CME-ICME pairs we compared the arrival times found in the literature with the data obtained by the Wind spacecraft. Gosling et al. (1973) find that the ICME plasma is characterised by low proton temperature due to the expansion of the magnetic structure. Then, we can expect a drop in the observed proton temperature, when the ICME arrives at the

[4] http://solar.gmu.edu/heliophysics/index.php/The_ISEST_Master_CME_List

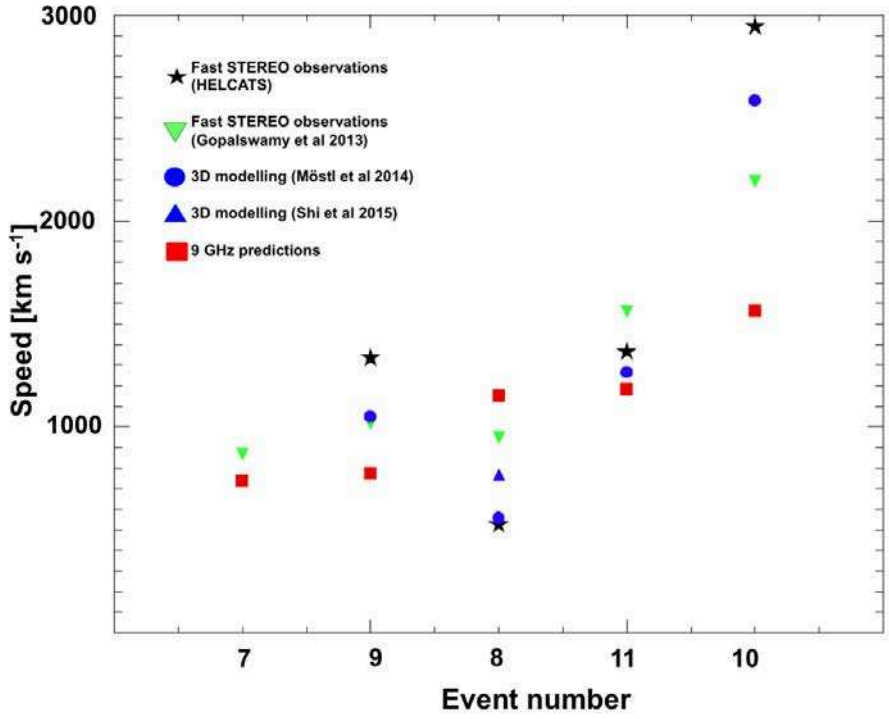

Fig. 5. Observed and predicted CME speeds. The black stars represent the higher of the two CME speeds derived from a geometric fit of observations from each of the two STEREO spacecraft (HELCATS catalogue). The green inverted triangles show the higher of the two CME speeds measured in the STEREO/COR2 images by Gopalswamy et al. (2013). The blue circles and blue triangles are the speeds resulting from multi-spacecraft modeling by Möstl et al. (2014) and Shi et al. (2015). The red filled squares denote the speeds found from the microwave fluence by using least squares (LS) fitting.

spacecraft, below the expected temperature ($T_{\rm exp}$) of the standard solar wind at the same speed, given by Elliott et al. (2005) as

$$T_{\rm exp}\ [\rm K] = 640 \cdot V\ [\rm km\ s^{-1}] - 1.56 \cdot 10^5\ [\rm K]\ . \quad (2)$$

For each ICME we overplotted $T_{\rm exp}$ on the observed temperature profile as is shown in Figure 4, and searched for a decrease in the proton temperature near the ICME arrival time reported in the literature. In most events the difference between the arrival time in the literature and the value determined using the drop in the proton temperature is less than 3 hours. In two events the difference was bigger: the ICME on 23 June 2013 was reported to arrive at 03:51 UT, but the very clear drop in temperature occurred at 16:13 UT. The strongest discrepancy was found for the ICME on 12 Mars 2012 (arrival reported at 08:30 UT but with a clear drop in temperature at 21:44 UT).

ICMEs with ambiguous observed arrival times, including events with multiple drops in the temperature that could not be uniquely related to the ICME arrival time, were discarded. The final sample contains 11 well-identified CME-ICME pairs whose origins were associated with non-thermal microwave emission. We calculated the 9 GHz fluence as in the previous section, and determined

the CME speed using Eq. 1 with the coefficients of Table 2 obtained through least squares minimisation. For comparison, we calculated also the CME speeds estimated from coronographic observations and from the SXR fluence, as described in Salas-Matamoros and Klein (2015).

3.2. CME speed determination

Before discussing the propagation of the 11 ICMEs to the Earth, we check the CME speed estimate from the microwave fluence with coronographic measurements using STEREO and SoHO. The five events where such observations are available are plotted in Figure 5. The events are ordered by increasing predicted CME speed using the microwave fluence (red squares). The black stars represent the CME speeds found through a single spacecraft geometric fitting technique used in the HELCATS catalogue[5]. This catalogue presents the fits to the observations of both STEREO spacecraft. Only the higher of the two speeds is plotted in Figure 5 because we assume that the higher speed is closer to the outward speed. The inverted green triangles are the speed measurements in that STEREO/COR2 FOV in which the CME was closest to the limb (Table 1 in Gopalswamy et al., 2013). The speeds resulting from multi-spacecraft modeling by Möstl et al. (2014) or Shi et al. (2015) are represented by filled blue circles and triangles, respectively.

The comparison between predictions, observations and modeling in Figure 5 reveals a large spread of CME speeds derived by different techniques. The predictions from the 9 GHz fluence (filled red squares) tend to give lower CME speeds than the other estimations (4/5 cases). In the special case of the event 8 the predicted speed was found to be higher. However the modeling of the speed at low altitudes ($\approx 2\ R_\odot$) reveals a value of about 1100 km s^{-1} (Temmer et al., 2014), which is closer to the speed predicted from radiative proxies. This event also presented a CME-CME interaction studied by Temmer et al. (2014), which apparently affected the estimation of the speed. CME-CME interactions were also observed for the events 9 and 10. CME interactions in the corona and in the interplanetary space can result in errors in both the speed estimations and the travel time predictions.

Overall Figure 5 shows that the discrepancy between microwave-inferred CME speeds and those derived from coronographic observations is not larger than the difference between different coronographic speed determinations themselves. Event 8 illustrates that even when 3D modelling is used, the speeds derived by different authors for the same even may differ substantially.

3.3. Prediction of ICME arrival times

CMEs undergo acceleration or deceleration in the corona (Vršnak et al., 2004) and interplanetary space (Gopalswamy et al., 2001). The latter was inferred from the observation that the range of ICME speeds near 1 AU is smaller than the range of CME speeds in the corona (Gopalswamy et al., 2000). The CME acceleration/deceleration is directly observed in heliospheric images from the STEREO mission (e.g. Colaninno et al., 2013).

Interplanetary propagation of ICMEs is generally discussed in terms of aerodynamic drag, i.e a friction-like effect, between the outward propagating ICME and the ambient plasma (Vršnak et al., 2014, and references therein). Interplanetary deceleration is also expected when plasma is piled up in front of the ICME. Both processes are treated by the so-called 'drag-based' model, where

[5] http://www.helcats-fp7.eu/catalogues/wp3_cat.html

the force acting on the ICME is proportional to the square of the difference between the speeds of the ICME and the ambient solar wind, with a coefficient that may be determined empirically. Gopalswamy et al. (2001) and Gopalswamy (2009) proposed simple empirical relationships in first and second order of the velocity difference, and scaled them using observations of CMEs and the leading edge of ICMEs. The empirical laws are

$$a\ [\mathrm{m\ s^{-2}}] = -0.0054(\mathrm{V_{CME}} - \mathrm{V_{01}}), \tag{3}$$

$$a\ [\mathrm{m\ s^{-2}}] = -3.29 \cdot 10^{-6}(\mathrm{V_{CME}} - \mathrm{V_{02}})^2 - 3.64 \cdot 10^{-3}(\mathrm{V_{CME}} - \mathrm{V_{02}}), \tag{4}$$

where $\mathrm{V_{CME}}$ is the propagation speed of the CME in the corona, $\mathrm{V_{01}} = 406$ km s^{-1} and $\mathrm{V_{02}} = 482$ km s^{-1}. These speeds have no specific physical meaning. In a model related to frictional drag, they could be considered as the equivalent ambient solar wind speed in the two acceleration models, respectively. We infer $\mathrm{V_{CME}}$ from the 9 GHz fluence. The ICME acceleration or deceleration is assumed to occur within a maximum range out to 0.76 AU. It stops earlier if the ICME has reached the speed V_{01} or $\mathrm{V_{02}}$. With this event-dependent, but otherwise constant acceleration, the determination of the speed and arrival time of the ICME at 1 AU is a matter of simple arithmetics. The results presented in the following were found using Eq. 3.

Table 3 summarises the ICME arrival time measurements and predictions. The event numbers are shown in col 1. Cols 2 and 3 contain, respectively, the shock arrivals and the arrival times of the magnetic obstacle identified by the temperature drop at the Wind spacecraft. Col. 4 presents the first time that the CME was observed by LASCO. Col. 5 lists the longitudes of the associated flares. Cols. 6 and 7 present the start and end times of microwave bursts, Col. 8 the 9 GHz fluence. The predictions for the CME speed and arrival using microwave fluence are listed in Cols. 9 and 10 respectively. Cols. 11 and 12 contain the differences between the predicted arrival time and the arrival times of the ICME and the shock, respectively.

The procedure employed here, as well as in published studies, predicts the arrival time of the top (or nose) of the ICME at 1 AU. The CME propagation speed measured in the corona, which we used as input for the empirical relationship with the microwave fluence, is the speed of the highest part of the CME in the coronagraphic images. But the first arrival of an ICME at 1 AU is not necessarily at the position of the Earth. One must therefore characterise which part of the ICME the spacecraft intercepts, the nose or the flank. If it intercepts the flank, we expect that the arrival time estimated from the speed of the top of the CME in the corona is earlier than the first detection of the ICME.

Jian et al. (2006) use the profile of the sum of kinetic and magnetic pressure, P_t, as a criterion to identify which part of an ICME sweeps over a given spacecraft. They distinguish three groups (their Fig. 5):

G1: The spacecraft encounters the ICME in the vicinity of its centre *i.e.* near its nose, seeing an increasing P_t profile up to a maximum near the centre of the flux rope, and a subsequent decrease.

G3: The spacecraft encounters the border of the ICME, but not the magnetic obstacle; the P_t profile is characterised by a rapid rise after the shock, followed by a gradual decay.

G2: The spacecraft encounters the ICME on its flank, seeing first an extended sheath region and then the outer regions of the magnetic obstacle: the P_t evolution is a mixture of G1 and G3.

	Shock onset	ICME onset	CME onset	Flare	Microwave burst observations			9GHz Predictions			
N	*Wind*	*Wind*	LASCO	longitude	Start	End	Φ_{9GHz} [sfu·s]	V_{CME} [km s^{-1}]	Arrival	ΔT_{ICME} [hours]	ΔT_{Sheath} [hours]
(1)	(2)	(3)	(4)	(5)	(6)	(7)	(8)	(9)	(10)	(11)	(12)
	1997										
1	11 Apr 05:00	11 Apr 09:07	07 Apr 14:27	E11°	13:54	14:20	$6.4 \cdot 10^4$	824	10 Apr 18:05	-15	-11
	2000										
2(*)	08 Jun 09:12	08 Jun 13:07	06 Jun 15:54	E10°	15:05	16:00	$2.0 \cdot 10^6$	1481	08 Jun 04:05	-9	-5
3	28 Jul 06:00	28 Jul 13:04	25 Jul 03:30	W08°	02:46	02:51	$1.5 \cdot 10^5$	950	27 Jul 19:40	-17	-10
	2003										
4	28 Oct 02:06	28 Oct 03:20	26 Oct 17:54	W38°	17:20	18:14	$2.6 \cdot 10^6$	1554	28 Oct 04:10	1	2
	2005										
5	15 May 02:38	15 May 09:15	13 May 17:12	E11°	16:32	17:18	$5.5 \cdot 10^5$	1190	15 May 17:25	9	16
	2006										
6	14 Dec 14:14	14 Dec 20:25	13 Dec 02:54	W23°	02:18	02:41	$3.2 \cdot 10^6$	1607	14 Dec 11:30	-9	-3
	2010										
7	15 Feb 17:28	16 Feb 04:53	12 Feb 13:42	E11°	11:22	11:38	$3.24 \cdot 10^4$	737	15 Feb 20:58	-8	3
	2011										
8	18 Feb 01:30	18 Feb 04:55	15 Feb 02:24	W10°	01:48	02:14	$4.4 \cdot 10^5$	1148	17 Feb 05:00	-24	-20
9	04 Aug 22:00	05 Aug 03:20	02 Aug 06:39	W10°	05:48	06:23	$4.4 \cdot 10^4$	774	5 Aug 13:05	10	15
	2012										
10	08 Mar 11:00	09 Mar 02:40	07 Mar 00:24	E26°	00:10	00:20	$2.7 \cdot 10^6$	1562	08 Mar 10:45	-16	0
11	12 Mar 08:30	12 Mar 21:44	10 Mar 18:00	W26°	17:10	18:27	$5.2 \cdot 10^5$	1180	12 Mar 18:30	-3	10

Table 3. Comparison between ICME arrival times measured at Wind spacecraft and predicted based on 9 GHz fluence: event number (Col. 1), shock arrival (Col. 2), ICME arrival (Col. 3), CME onset (Col. 4), flare longitude location (Col. 5), microwave observations (Cols. 6-8) and predictions based on the 9 GHz fluence (Cols. 9-12). (*) The ICME arrival of the event 2 was measured by ACE because no Wind data was available.

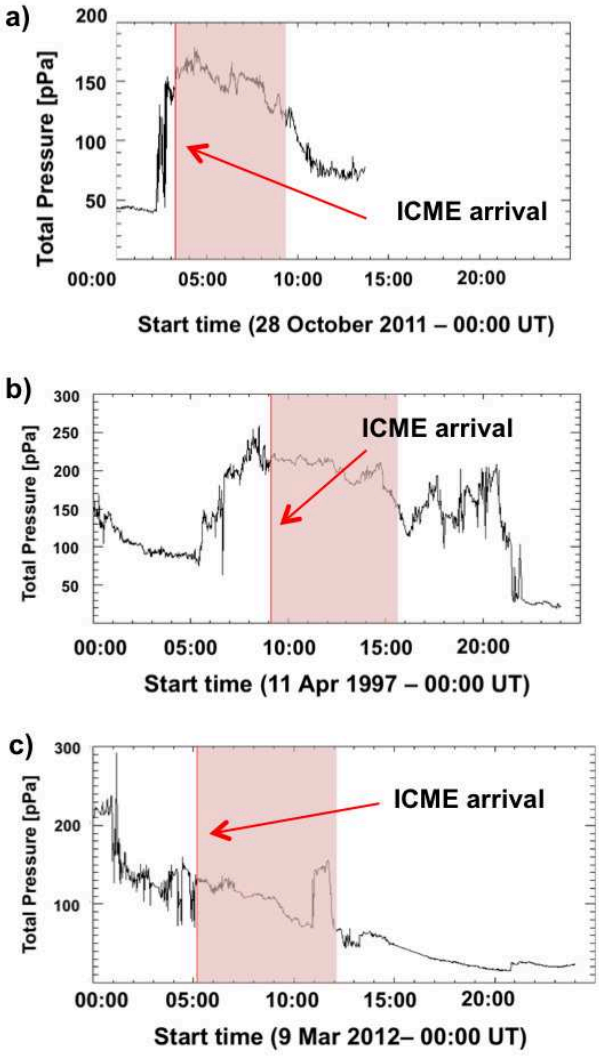

Fig. 6. Examples of total pressure profiles during ICME passages. The red arrow marks the ICME arrival time based on the criterion of temperature drop compared to the expected temperature at the same solar wind speed. The area with a constant low temperature profile is coloured in red. Interpretation of the total pressure profile from the criterion by Jian et al. (2006): a) G1, spacecraft encounters the ICME near its nose, b) G2, and c) G3, spacecraft encounters the ICME flank.

We calculated the total pressure profile for all events as the sum of magnetic pressure and plasma thermal pressure:

$$P_t = \frac{B^2}{2\mu_0} + \sum_j n_j k T_j \,, \tag{5}$$

where μ_0 is the permeability of the medium, and k the Boltzmann constant. The magnetic field (B) as well as the density (n_p) and temperature of protons (T_P) are measured aboard Wind. Plasma pressure is calculated using the abundances for the solar wind of protons (H^+), α particles (He^{2+})

and electrons. We use the parameters of Jian et al. (2006), i.e. the particle densities are such that 95% are protons, 4% He^{2+}, the temperature of He is four times the proton temperature, and the electron temperature is 130,000 K. The electron density is taken to be 1.03 times the proton density.

Figure 6 shows examples of total pressure profiles. The vertical red line indicates the ICME arrival based on the drop in the temperature with respect to the expected one for the given solar wind speed. The shaded area represents the region with an almost constant low temperature *i.e.* the magnetic obstacle of the ICME. The top panel shows a well-defined rise of the pressure after the entry into the ICME, with a clear maximum and subsequent somewhat irregular decay. The bottom panel shows a continuous decay of the pressure throughout the passage of the ICME, and the middle panel shows a mixed behaviour, without a peak. We found that 4/11 events show the well-defined maximum of total pressure within the ICME. This means that in most cases the Wind spacecraft intercepted the flank of the ICME.

3.4. Comparison between predicted and observed arrival times

The errors of the prediction, that is the difference between predicted and observed arrival times, are shown in Figure 7.a. The zero of the ordinate is the observed arrival time of the magnetic driver of the ICME which has been identified by the drop of the proton temperature. The vertical black lines related to each event show the extent of the sheath region. The labels F and N refer to the spacecraft encounter with the ICME: the flank and the nose, respectively. The events are ordered by increasing heliographic longitude of the related flare. Red squares represent the prediction errors using $\phi_{9\mathrm{GHz}}$. For comparison, the prediction errors achieved with two other methods are also shown: when the coronal speed of the CME is inferred from the SXR fluence (green asterisks) and from coronographic observations of the expansion speed in the plane of the sky (V_{EXP}) converted to outward propagation speed using the empirical relationship $V_{\mathrm{CME}} = 0.88 V_{\mathrm{EXP}}$ (blue filled circles, Schwenn et al., 2005). We assume a perfect halo CME where V_{EXP} is twice the speed reported in the LASCO CME catalogue[6] ($\mathrm{V_{CAT}}$). This probably overestimates the expansion speeds. Therefore we also quote the errors for the assumption $\mathrm{V_{EXP}}$=1.5$\mathrm{V_{CAT}}$. Table 4 contains the mean differences and the mean absolute differences between the predicted and observed arrival times and their standard deviations.

The following conclusions can be drawn from Figure 7 and Table 4:

- The predicted arrival times using the CME speed estimated from SXR and microwave fluences scatter in a broad range between 24 hours before and 10 hours after the observed arrival of the magnetic structure.

- On average, all approximations: the SXR fluence, the 9 GHz fluence and the estimate from the coronographic expansion speed, tend to underestimate the interplanetary travel time of ICMEs.

- The best performance is achieved when the CME speed is derived from the SXR fluence or from $\phi_{9\mathrm{GHz}}$. The arrival time predictions from SXR fluence and from 9 GHz fluence are usually similar. Both radiative proxies perform better than the coronographic expansion speed. This is confirmed by the high correlations between the observed and predicted arrival times shown in Figure 7.b.

[6] http://cdaw.gsfc.nasa.gov/CME_list/index.html

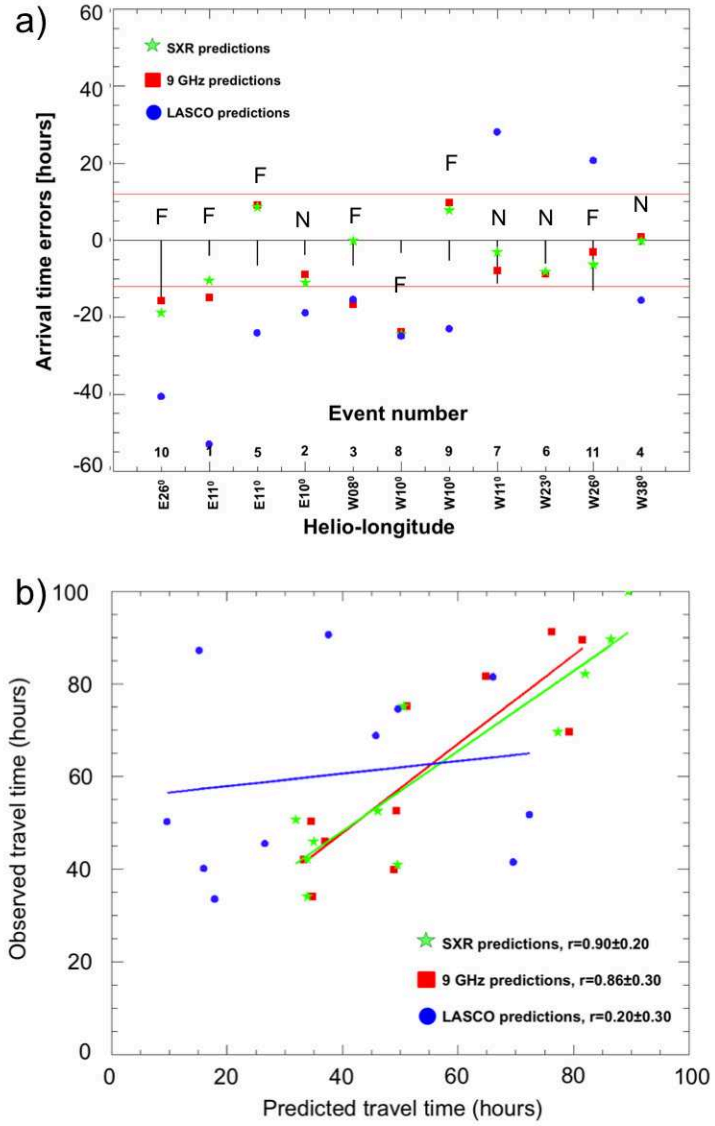

Fig. 7. Errors in arrival time predictions. a) Travel time errors (predicted - observed arrival times) ordered by increasing longitude. The numbers on the abscissa are the event numbers in Table 3. Green stars: SXR proxy. Red squares: $\phi_{9\mathrm{GHz}}$. Blue circles: LASCO coronographic observations (V_{EXP}=2 V_{CAT}). The red lines mark the ±12 h error window while the black vertical lines, the interval between the shock and ICME arrivals. b) Correlations between observed and predicted travel times.

– The arrival time predictions of the four ICMEs which are intercepted near the nose range between 12 hours before and one hour after the arrival of the magnetic obstacle. In two of the four cases the arrival predicted from microwaves or SXR emission occurs during the observed passage of the sheath, in one event it occurs within one hour after the observed arrival of the magnetic obstacle.

Proxies	Errors with respect to ICME arrival		Errors with respect to sheath arrival	
	Mean error [h]	Mean absolute error [h]	Mean error [h]	Mean absolute error [h]
(1)	(2)	(3)	(4)	(5)
Acceleration: Eq. 3				
Fluence at 9 GHz	-7.3±11	10.8±7	-0.2±11	8.7±7
SXR fluence	-6±10	9±7	1±11	8±6
Coronographic speed (V_{EXP}=2 V_{CAT})	-22±29	30.6±18	-14.6±30	28±17
Coronographic speed (V_{EXP}=1.5 V_{CAT})	-9±31	24±21	-2±33	23±22

Table 4. Average differences between the predicted and observed ICME arrival time (see Table 3): col. 1 contains the proxy used to infer the CME propagation speed. Cols. 2 and 3: the mean error and the mean absolute error (negative when the predicted arrival precedes the observed ICME arrival) and their standard deviations, respectively. Cols. 4 and 5: the mean error and the mean absolute error and their standard deviations with respect to the sheath arrival.

Proxies	Errors with respect to ICME speed	
	ΔV [km s^{-1}]	$\mid \Delta V \mid$ [km s^{-1}]
(1)	(2)	(3)
Acceleration: Eq. 3		
Fluence at 9 GHz	196±243	250±181
SXR fluence	202±236	264±155
Coronographic speed	870±1049	878±1041

Table 5. ICME speeds at 1 AU: (col. 1) proxy used to infer the ICME speed, (col. 2) mean error value and its standard deviation, and (col. 3) mean absolute error value and its standard deviation.

In the fourth case the arrival is predicted five hours before the observed arrival of the leading edge of the ICME.

– The largest errors of arrival time prediction from the two proxies are obtained in ICMEs where the flank is intercepted by the spacecraft.

In the previous section, we found that the spacecraft encountered the CME front in the events 2, 4, 6 and 7. Although the results in Figure 7 support the simple expectation that the CME arrival time depends on where the spacecraft encounters the ICME, the predictions of the events 5, 9 and 11, which are detected on the flanks, are also rather successful.

3.5. Prediction of ICME speeds at 1 AU

A straightforward further prediction using the CME speed in the corona and the interplanetary transport model is the speed of the ICME near 1 AU. Figure 8 shows the comparison between the ICME speeds predicted at 1 AU and measured at the Wind spacecraft within the ICME, i.e. the speeds determined when the temperature had dropped. We did not find any speed variation that

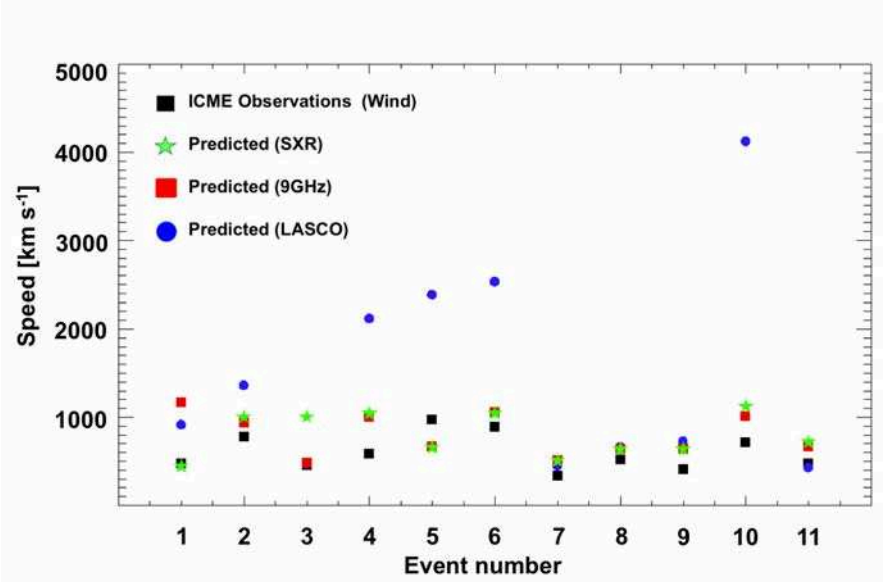

Fig. 8. Comparison between the observed and predicted ICME speeds at 1 AU. The black squares represent the speeds measured by Wind. The red filled squares show the predicted speeds from 9 GHz fluence. The green stars mark the predicted speeds from SXR fluence, while the blue circles represent the predicted speeds using coronographic observations. The abscissa shows the event number listed in Table 3.

could be related to the expansion to the ICME. Therefore, we consider the measured radial speed as the outward propagation speed of the ICME.

The Figure shows that the coronographic proxy predicts in general (5/11) the highest ICME speed, well above the observed value. The general overestimation of the ICME speed is in line with the prediction of early arrival times. The microwave fluence predicts speeds much closer to the observations. The mean errors ΔV and the mean absolute errors $\mid \Delta V \mid$ between the predicted and observed speeds are listed in Table 5. The results show comparable errors to the values found by Möstl et al. (2014) ($\Delta V = 284 \pm 288$ [km s^{-1}] and $\mid \Delta V \mid = 275 \pm 297$ [km s^{-1}]) from geometric modeling.

4. Summary and Discussion

In the present work an empirical relationship is inferred between the speeds of CMEs at the solar limb, which are supposed to show the outward propagation speeds of the CMEs without distortion by projection effects, and the fluence of the associated microwave bursts.

This relationship is then employed to infer the speeds of Earth-directed CMEs, which are fed into a simple analytical model of interplanetary acceleration or deceleration to predict the arrival times and speeds of the ICMEs at 1 AU. The predictions are compared with observations at the Wind spacecraft. Even though our samples are small, they have been carefully characterised such as to avoid spurious associations between limb CMEs and flares on the one hand, and uncertain ICME arrival times on the other hand. We provide furthermore a characterisation of the way in which the

spacecraft traverses the ICME whose arrival time is determined. This is necessary for comparing the predicted arrival times with observations.

4.1. Radiative proxies of CME speed in the corona

The search for microwave counterparts of limb CMEs was not always successful. Non thermal microwave signatures may be absent even in some CMEs where a SXR counterpart was clearly identified. This was especially the case in relatively slow CMEs, at speeds below 600 km s^{-1}. But even fast CMEs may have no non-thermal microwave signatures. This is the case of CMEs associated with filament eruptions outside active regions. The four CME events listed in Table 1 in Gopalswamy et al. (2015) have speeds between about 950 and 1550 km s^{-1}, but have either no detectable microwave burst or a purely thermal one.

When non-thermal microwave bursts are identified, their fluence does show a correlation, with a broad scatter, with the CME speed. Since the sample used to establish the relationship was restricted to CMEs observed near the solar limbs, the scatter can hardly be produced by projection effects on the CME speed measurement. The correlations are similar to what Trottet et al. (2015) found between the CME propagation speed and microwave fluence ($r = 0.65 \pm 0.09$) for events without any restriction in the location of the CME. The scatter must hence be intrinsic to the relationship between the CME speed and the importance of the radiative signatures. It most likely reveals differences from event to event of the energy partitioning between plasma heating, electron acceleration and mass motion. The event-dependence of this partitioning was discussed by Reeves and Moats (2010) in a 2D model of a standard flare-CME scenario, and by Chen and Kunkel (2010) in a model of flux rope destabilisation.

The empirical relationship can provide an estimation of CME speed in the corona from the SXR or microwave observation. A coronographic observation is needed to decide whether a CME exists or not. Yet, a first prediction of the arrival time and speed of the ICME at 1 AU can be issued since the end of the impulsive microwave burst, when the CME is only at a few solar radii from the Sun. We have shown that the method has the potential of a better prediction than a speed measurement with a coronagraph on the Sun-Earth line.

4.2. Comparison of radiative proxies with other tools of ICME arrival prediction

Proxies of CME speeds based on SXR or radio observations have so far not been used in the prediction of ICME arrivals at 1 AU. As shown in Section 3.4, they predict the arrival times of ICMEs at 1 AU with mean absolute errors of 9 to 11 hours. The error of the eight best predictions (about 73% of the sample of 11 events) is about ±15 h for the 9 GHz proxy and ±9 h for the SXR proxy, using the linear model of interplanetary deceleration of Gopalswamy et al. (2001). There is a clear trend to underestimate the ICME travel time, *i.e.* to predict too early an arrival of the ICME.

While the only relevant observations were for a long time the CME observations in the corona and *in situ* measurements at 1 AU, the advent of heliospheric imaging with the STEREO mission enabled researchers in recent years to track CMEs from the Sun to the Earth (see the early review by Rouillard, 2011). Heliospheric imaging is used by Colaninno et al. (2013) to predict the arrival time of nine CMEs, using the graduated cylindrical shell model to remove projection effects. They employ different extrapolations of the height-time trajectory of the CME front beyond a heliocentric distance of 50 $R_\odot$, and achieve a prediction of the shock arrival time near 1 AU within ±13 h for

the entire event set, and within ±6 h for the seven (78%) best predictions. Along the same lines Möstl et al. (2014) extrapolate the height-time trajectories of 22 CME-ICME fronts in heliospheric images. They obtain a prediction error of ICME speeds of about 250-300 km s^{-1}, a prediction error of ICME arrival time of 1-7 hours, and an absolute prediction error of 7-8 hours, depending on the method used. These studies show that heliospheric imaging is an efficient way to track ICMEs through the interplanetary space. It is able to identify nonstandard interplanetary acceleration due to interaction of CMEs. Since the prediction relies on the extrapolation beyond some distance from the Sun, about 0.25 AU, the advance warning time is reduced to about one day. The Drag Based Model reveals comparable results. Vršnak et al. (2013) calculate the mean error between the predicted arrival time and observed arrivals of 121 CMEs. They obtain a mean error of about 12 h. Núñez et al. (2016) report a lower error of about 7-9 hours for the shock arrival time prediction from another empirical drag-based model.

A very sophisticated technique is the combination of near-Sun observations with MHD modeling. Millward et al. (2013) utilise the cone model to obtain the CME parameters to be used as input in the WSA-ENLIL+Cone model to forecast the arrivals. They apply their numerical model to a sample of 25 CMEs and find a mean error of around 7.5 hours. Similar results are obtained by Vršnak et al. (2014) with the WSA-ENLIL+Cone model and the analytical drag-based model. The same numerical model is applied by Mays et al. (2015) to a sample of 17 events, where a mean error of about 12 hours is found. Again the prediction errors evaluated by Núñez et al. (2016) are smaller, about 5 hours. There is clearly a discrepancy between different evaluations of prediction errors in different publications for the same class of models.

4.3. The observational identification of an ICME: a limit to the comparison with predictions

The evaluation of a successful arrival prediction needs an observational determination of the ICME arrival time at a given spacecraft. This is often ambiguous, depending on the criterion to identify an ICME. Especially the time of first detection of the magnetic obstacle within the ICME, which often arrives after a very perturbed shock and sheath region, may be difficult. In the present work we use the temperature drop with respect to the standard solar wind at comparable speed. It is, however, clear that different criteria commonly used to identify ICME arrivals may on occasion lead to arrival times that differ by several hours. Another problem is the interaction of CMEs, which may significantly alter their interplanetary propagation (e.g., Forbes et al., 2006; Démoulin, 2010). Some of the ICMEs in our list are known to undergo interactions (at least events number 8, 9 and 10). This may partly explain why different evaluations of similar methods lead to different results in the published literature.

The success of a prediction is also expected to depend on which part of the ICME is intercepted by a spacecraft, the region around the nose or the flank. The mere comparison of predicted ICME arrival times at 1 AU and the observed arrival times at a given spacecraft like Wind is only conclusive if the spacecraft intercepts the nose of the ICME. Most comparisons between predictions and observations suppose tacitly that the nose of the ICME is intercepted. But this is most often not the case: in our sample 7/11 ICMEs originating within ±40° from the central meridian were seen on the flanks. The flank of the ICME arrives at the spacecraft when the nose is already beyond 1 AU, so that one should indeed expect that many prediction schemes underestimate the travel time. Owens and Cargill (2004) discuss this effect, and show that the arrival at Earth of ICMEs with thick sheath

regions is predicted too early. Since the sheath thickness of an ICME with a given speed increases with increasing distance from the nose, they ascribe part of the prediction error to the curvature of the ICME front. These authors use the same set of CME-ICME pairs to determine the interplanetary deceleration and to predict the ICME arrival time. The prediction errors therefore are by construction symmetrically distributed around zero. Our analysis is in remarkable agreement with the expectations, since 9/11 ICME arrivals are predicted about correctly or too early by the SXR and 9 GHz proxy. All predictions that are more than 12 hours ahead of the observed arrival refer to the flanks of ICMEs.

Two alternative interpretations of the early arrival time predictions are the overestimation of the initial CME speed and the uncertainty of the structure whose arrival is predicted, the leading edge or the magnetic obstacle of the ICME. The CME speed is unlikely to be the cause, because the estimates from the microwave fluence tend to be lower than speeds inferred from multi-spacecraft coronographic determinations. The uncertainty of the ICME region may play a role, because the errors in the arrival time prediction are more symmetric with respect to the leading edge of the ICME than with respect to the magnetic obstacle (see Figure 7). But the difference between arrival times of the nose and the flank discussed above is inevitable, and must be taken into account when evaluating the predictions. The importance is highlighted by the fact that this difference brings some order into the prediction errors of our test sample.

4.4. Concluding Remarks

The present work shows that even though many sophisticated numerical and analytical techniques have been developed to forecast ICME arrivals based on coronographic observations, the thermal and non-thermal flare-related SXR and microwave emissions are valuable contributions and can provide very early warnings, starting at the time when the CME is first seen in the field of view of a coronagraph on the Sun-Earth line. Although a full validation has not been achieved in the present article, given the small event sample, non-thermal microwave emission can play a major role, because non-thermal microwave bursts accompany many, though not all, fast CMEs.

The radio observations exploited in the present work are carried out with rather simple patrol instruments, which monitor the whole Sun flux density using parabolic antennae with a typical size of 1 metre. Although the RSTN and Nobeyama patrol instruments do not provide data in real time, there is no technical obstacle to do so. The major issues are a reliable calibration and stable and reliable antenna operations. Because these radio observations are carried out from ground, they have the additional advantage of being less vulnerable to space weather hazards than space assets.

Acknowledgements. The work presented in this article is based on radio data from the RSTN network (provided through NGDC) and the Nobeyama Radio Polarimeters. The Nobeyama Radio Polarimeters are operated by Nobeyama Radio Observatory, a branch of National Astronomical Observatory of Japan. Extensive use was made of the CME catalogue, which is generated and maintained at the CDAW Data Center by NASA and The Catholic University of America in cooperation with the Naval Research Laboratory. SOHO is a project of international cooperation between ESA and NASA. Plasma data from the Wind and ACE missions were used through the OMNIweb and CDAWeb servers at NASA GSFC, respectively. Supporting information was provided by the *Radio Monitoring* web site maintaiend at Paris Observatory with support by CNES. C.S.-M. gratefully acknowledges the financial support of her doctorate studies by the University of Costa Rica and the Ministry of Science, Technology and Telecommunications of Costa Rica (MICITT)

through the National Council of Scientific and Technological Research (CONICIT). This research was supported by the Agence Nationale pour la Recherche (ANR/ASTRID, DGA) project Outils radioastronomiques pour la mtorologie de l'espace (ORME, contract No. ANR-14-ASTR-0027) and by the French space agency (CNES). The authors thank P. Démoulin for his help with the identification of ICMEs and many other discussions, A. Isavnin for providing the STEREO solar wind data from the HELCATS project under the FP7 EU contract number 606692, and the referees for very constructive comments.

References

Bein, B. M., S. Berkebile-Stoiser, A. M. Veronig, M. Temmer, and B. Vršnak. Impulsive acceleration of coronal mass ejections. II. Relation to soft X-ray flares and filament eruptions. *Astrophys. J.*, **755**, 44, 2012. 10.1088/0004-637X/755/1/44. 2.2

Cargill, P. J. On the Aerodynamic Drag Force Acting on Interplanetary Coronal Mass Ejections. *Sol. Phys.*, **221**, 135–149, 2004. 10.1023/B:SOLA.0000033366.10725.a2. 1

Caroubalos, C. Contribution à l'étude de l'activité solaire en relation avec ses effects géophysiques. *Annales d'Astrophysique*, **27**, 333, 1964. 1

Chen, J., and V. Kunkel. Temporal and physical connection between coronal mass ejections and flares. *ApJ*, **717**, 1105–1122, 2010. 10.1088/0004-637X/717/2/1105. 4.1

Cliver, E. W., J. Feynman, and H. B. Garrett. An estimate of the maximum speed of the solar wind, 1938-1989. *J. Geophys. Res.*, **95**, 17,103–17,112, 1990. 10.1029/JA095iA10p17103. 1

Colaninno, R. C., A. Vourlidas, and C. C. Wu. Quantitative comparison of methods for predicting the arrival of coronal mass ejections at Earth based on multiview imaging. *Journal of Geophysical Research (Space Physics)*, **118**, 6866–6879, 2013. 10.1002/2013JA019205, 1310.6680. 1, 3.3, 4.2

Démoulin, P. Interaction of ICMEs with the Solar Wind. In M. Maksimovic, K. Issautier, N. Meyer-Vernet, M. Moncuquet, and F. Pantellini, eds., Twelfth International Solar Wind Conference, vol. 1216 of *AIP Conf. Proc.*, 329–334, 2010. 10.1063/1.3395866. 4.3

Elliott, H. A., D. J. McComas, N. A. Schwadron, J. T. Gosling, R. M. Skoug, G. Gloeckler, and T. H. Zurbuchen. An improved expected temperature formula for identifying interplanetary coronal mass ejections. *J. Geophys. Res.*, **110**, A04103, 2005. 10.1029/2004JA010794. 3.1

Forbes, T. G., J. A. Linker, J. Chen, C. Cid, J. Kóta, et al. CME theory and models. *Space Sci. Rev.*, **123**, 251–302, 2006. 10.1007/s11214-006-9019-8. 4.3

Gopalswamy, N. Coronal mass ejections and space weather. In T. Tsuda, R. Fujii, K. Shibata, and M. A. Geller, eds., Climate and Weather of the Sun-Earth System (CAWSES) Selected Papers from the 2007 Kyoto Symposium. Edited by T. Tsuda, R. Fujii, K. Shibata, and M.A. Geller. Tokyo: TERRAPUB, 2009, p.77-120, 77–120, 2009. 3.3

Gopalswamy, N., A. Lara, R. P. Lepping, M. L. Kaiser, D. Berdichevsky, and O. C. St. Cyr. Interplanetary acceleration of coronal mass ejections. *Geophys. Res. Lett.*, **27**, 145–148, 2000. 10.1029/1999GL003639. 3.3

518 Gopalswamy, N., A. Lara, S. Yashiro, M. L. Kaiser, and R. A. Howard. Predicting the 1-AU ar-
519 rival times of coronal mass ejections. *J. Geophys. Res. (Space Phys.)*, **106**, 29,207–29,218, 2001.
520 10.1029/2001JA000177. 1, 3.3, 4.2

521 Gopalswamy, N., P. Mäkelä, S. Akiyama, S. Yashiro, H. Xie, N. Thakur, and S. W. Kahler. Large Solar
522 Energetic Particle Events Associated with Filament Eruptions Outside of Active Regions. *ApJ*, **806**, 8,
523 2015. 10.1088/0004-637X/806/1/8, 1504.00709. 4.1

524 Gopalswamy, N., P. Mäkelä, H. Xie, and S. Yashiro. Testing the empirical shock arrival model using quadra-
525 ture observations. *Space Weather*, **11**, 661–669, 2013. 10.1002/2013SW000945, 1310.8510. 1, 3.1, 5,
526 3.2

527 Gosling, J. T., V. Pizzo, and S. J. Bame. Anomalously low proton temperatures in the solar wind following
528 interplanetary shock waves - evidence for magnetic bottles? *J. Geophys. Res. (Space Phys.)*, **78**, 2001,
529 1973. 10.1029/JA078i013p02001. 3.1

530 Jian, L., C. T. Russell, J. G. Luhmann, and R. M. Skoug. Properties of interplanetary coronal mass ejections
531 at one AU during 1995 - 2004. *Solar Phys.*, **239**, 393–436, 2006. 10.1007/s11207-006-0133-2. 3.3, 6, 3.3

532 Maričić, D., B. Vršnak, A. L. Stanger, A. M. Veronig, M. Temmer, and D. Roša. Acceleration Phase of
533 Coronal Mass Ejections: II. Synchronization of the Energy Release in the Associated Flare. *Sol. Phys.*,
534 **241**, 99–112, 2007. 10.1007/s11207-007-0291-x. 2.2

535 Mays, M. L., A. Taktakishvili, A. Pulkkinen, P. J. MacNeice, L. Rastätter, et al. Ensemble modeling of CMEs
536 using the WSA-ENLIL+cone model. *Solar Phys.*, **290**, 1775–1814, 2015. 10.1007/s11207-015-0692-1,
537 1504.04402. 3.1, 4.2

538 Millward, G., D. Biesecker, V. Pizzo, and C. A. Koning. An operational software tool for the analysis
539 of coronagraph images: Determining CME parameters for input into the WSA-Enlil heliospheric model.
540 *Space Weather*, **11**, 57–68, 2013. 10.1002/swe.20024. 4.2

541 Möstl, C., K. Amla, J. R. Hall, P. C. Liewer, E. M. De Jong, et al. Connecting speeds, directions and arrival
542 times of 22 coronal mass ejections from the Sun to 1 AU. *Astrophys. J.*, **787**, 119, 2014. 10.1088/0004-
543 637X/787/2/119, 1404.3579. 1, 5, 3.2, 3.5, 4.2

544 Nakajima, H., H. Sekiguchi, M. Sawa, K. Kai, and S. Kawashima. The radiometer and polarimeters at 80,
545 35, and 17 GHz for solar observations at Nobeyama. *PASJ*, **37**, 163–170, 1985. 2.1

546 Núñez, M., T. Nieves-Chinchilla, and A. Pulkkinen. Prediction of shock arrival times from CME and flare
547 data. *Space Weather*, in press, 2016. 4.2

548 Odstrcil, D., V. J. Pizzo, J. A. Linker, P. Riley, R. Lionello, and Z. Mikic. Initial coupling of coronal and he-
549 liospheric numerical magnetohydrodynamic codes. *Journal of Atmospheric and Solar-Terrestrial Physics*,
550 **66**, 1311–1320, 2004. 10.1016/j.jastp.2004.04.007. 1

551 Owens, M., and P. Cargill. Predictions of the arrival time of coronal mass ejections at 1AU: an analysis of
552 the causes of errors. *Annales Geophysicae*, **22**, 661–671, 2004. 10.5194/angeo-22-661-2004. 4.3

553 Reeves, K. K., and S. J. Moats. Relating coronal mass ejection kinematics and thermal energy release to
554 flare emissions using a model of solar eruptions. *Astrophys. J.*, **712**, 429–434, 2010. 10.1088/0004-
555 637X/712/1/429. 4.1

Rouillard, A. P. Relating white light and in situ observations of coronal mass ejections: A review. *Journal of Atmospheric and Solar-Terrestrial Physics*, **73**, 1201–1213, 2011. 10.1016/j.jastp.2010.08.015. 1, 4.2

Salas-Matamoros, C., and K.-L. Klein. On the statistical relationship between CME speed and soft X-ray flux and fluence of the associated flare. *Solar Phys.*, **290**, 1337–1353, 2015. 10.1007/s11207-015-0677-0, 1503.08613. 1, 2.1, 3.1, 3.1

Schwenn, R., A. dal Lago, E. Huttunen, and W. D. Gonzalez. The association of coronal mass ejections with their effects near the Earth. *Annales Geophysicae*, **23**, 1033–1059, 2005. 10.5194/angeo-23-1033-2005. 1, 3.4

Shi, T., Y. Wang, L. Wan, X. Cheng, M. Ding, and J. Zhang. Predicting the arrival time of coronal mass ejections with the graduated cylindrical shell and drag force model. *Astrophys. J.*, **806**, 271, 2015. 10.1088/0004-637X/806/2/271, 1505.00884. 3.1, 5, 3.2

Temmer, M., A. M. Veronig, V. Peinhart, and B. Vršnak. Asymmetry in the CME-CME interaction process for the events from 2011 February 14-15. *Astrophys. J.*, **785**, 85, 2014. 10.1088/0004-637X/785/2/85, 1402.6891. 3.2

Thernisien, A., A. Vourlidas, and R. A. Howard. Forward modeling of coronal mass ejections using STEREO/SECCHI data. *Sol. Phys.*, **256**, 111–130, 2009. 10.1007/s11207-009-9346-5. 1

Tobiska, W. K., D. Knipp, W. J. Burke, D. Bouwer, J. Bailey, D. Odstrcil, M. P. Hagan, J. Gannon, and B. R. Bowman. The Anemomilos prediction methodology for Dst. *Space Weather*, **11**, 490–508, 2013. 10.1002/swe.20094. 1

Trottet, G., S. Samwel, K.-L. Klein, T. Dudok de Wit, and R. Miteva. Statistical evidence for contributions of flares and coronal mass ejections to major solar energetic particle events. *Solar Phys.*, **290**, 819–839, 2015. 10.1007/s11207-014-0628-1, 1411.4133. 4.1

Vršnak, B., D. Ruždjak, D. Sudar, and N. Gopalswamy. Kinematics of coronal mass ejections between 2 and 30 solar radii. What can be learned about forces governing the eruption? *A&A*, **423**, 717–728, 2004. 10.1051/0004-6361:20047169. 3.3

Vršnak, B., M. Temmer, T. Žic, A. Taktakishvili, M. Dumbović, C. Möstl, A. M. Veronig, M. L. Mays, and D. Odstrčil. Heliospheric propagation of coronal mass ejections: comparison of numerical WSA-ENLIL+cone model and analytical drag-based model. *ApJS*, **213**, 21, 2014. 10.1088/0067-0049/213/2/21. 3.3, 4.2

Vršnak, B., and T. Žic. Transit times of interplanetary coronal mass ejections and the solar wind speed. *A&A*, **472**, 937–943, 2007. 10.1051/0004-6361:20077499. 1

Vršnak, B., T. Žic, D. Vrbanec, M. Temmer, T. Rollett, et al. Propagation of Interplanetary Coronal Mass Ejections: The Drag-Based Model. *Sol. Phys.*, **285**, 295–315, 2013. 10.1007/s11207-012-0035-4. 4.2

Wu, C.-C., M. Dryer, S. T. Wu, B. E. Wood, C. D. Fry, K. Liou, and S. Plunkett. Global three-dimensional simulation of the interplanetary evolution of the observed geoeffective coronal mass ejection during the epoch 1-4 August 2010. *Journal of Geophysical Research (Space Physics)*, **116**, A12103, 2011. 10.1029/2011JA016947. 1

593 Zhang, J., K. Dere, and R. A. Howard. Relationship Between Coronal Mass Ejections and Flares. *AGU Fall*
594 *Meeting Abstracts*, 2001. 2.2

595 Zhang, J., I. G. Richardson, D. F. Webb, N. Gopalswamy, E. Huttunen, et al. Solar and interplanetary sources
596 of major geomagnetic storms (Dst = -100 nT) during 1996-2005. *J. Geophys. Res.*, **112**, 10,102, 2007.
597 10.1029/2007JA012321. 1

4.3.3 Radiative proxies for CME speed in arrival predictions: final remarks

The success rate of the radiative relationships in Salas-Matamoros and Klein [2015] and Salas-Matamoros, Klein, and Trottet [2016] in ICME arrival predictions was found to be higher compared with coronographic measurements by LASCO. Also, the **accuracy** was comparable to the results from more sophisticated tools of ICME arrival prediction such as the combination of heliospheric imaging and analytical modelling [Colaninno, Vourlidas, and Wu, 2013, Möstl *et al.*, 2014] and the combination of MHD modelling with observations [Mays *et al.*, 2015, Millward *et al.*, 2013, Vršnak *et al.*, 2014]. Even though many sophisticated numerical and analytical techniques have been developed to forecast ICME arrivals based on coronographic observations, the thermal and non-thermal flare-related SXR and microwave emissions are valuable contributions and can provide very early warnings.

Radio observations exploited in Salas-Matamoros, Klein, and Trottet [2016] are carried out with rather simple patrol instruments, which monitor the whole Sun flux density using parabolic antennae with a typical size of 1 metre. Although the RSTN and Nobeyama patrol instruments do not provide data in real time, there is no technical obstacle to do so. The major issues are a reliable calibration and stable and reliable antenna operations. Because these radio observations are carried out from ground, they have the additional advantage of being less vulnerable to space weather hazards than space assets.

Chapter 5

Summary and Perspectives

The study of coronal mass ejections has been one of the principal objectives of space weather research. Since CMEs are directly linked with geomagnetic storms at the Earth and also with SEP events, the understanding of the phenomena involved in their evolution is relevant to develop prediction techniques in space weather forecasting. Nowadays, 3D reconstruction of CMEs as well as CME tracking in the interplanetary space have been developed due to multi-spacecraft observations in space and have contributed to a better appreciation of the solar activity. Nevertheless, the spacecraft located at positions suitable for 3D CME reconstruction CME tracking are not always available.

CMEs are observed and studied by coronographic observations. The fact that coronographs show the corona only in the plane of the sky and block the view of the solar disk is a basic limitation of coronographs, especially for the Earth-directed CMEs. However, this limitation can be compensated to some extent by applying other radiative diagnostics such as radio emission.

The studies developed in this thesis show that radio observations can be potentially used for space weather research and applications. Firstly, we have used radio and X-ray emissions to study the particle acceleration sites associated with the CME evolution in the low corona. We were able to identify not only different acceleration regions but also different acceleration processes related to one single CME. In general, multi-spacecraft observations of SEPs has been interpreted by the injection of particles from one broad acceleration region which could be the shock front. Nevertheless, the results presented here have shown that the multi-spacecraft SEP measurements over a broad range of heliolongitudes may not probe one acceleration region in the corona, on the contrary, different processes of particle acceleration may be associated with SEPs detected by different spacecraft.

We have also developed a promising alternative to estimate the speed of Earth-directed CMEs using radiative proxies (SXR and microwave emissions). This speed is used in an empirical propagation model to estimate the CME arrival times at 1 AU. The two proxies were tested by comparing with other propagation models and with *in situ* data. The results were found to be satisfactory because the accuracy in travel time was found to be comparable or better compared with other estimations, especially from coronographic observations. As one of the principal results from the study, we found that CME arrival times depend on which part of the ICME intercepts the spacecraft. Thus, if we could estimate the geometry of CMEs from early coronographic observations, we could give a statement about the region that will attain the Earth and improve the prediction. This hypothesis needs a further study.

But also, if microwave patrol observations were available in real time, we could test the estimations of CME arrival times using radiative proxies in order to examine if they can be a potential tool for real time space weather forecasting. A new prediction tool using microwave emission can contribute to the development of the global prediction techniques, where its usefulness is enhanced by the relatively simple observational setup and the observation from ground, which is a significant protection against space weather hazards.

Nowadays, different techniques have been developed to predict the space weather conditions. Most of these techniques are based on 3D models which use observations from different points of view, such as STEREO and SoHO observations. However, this study demonstrates that radio emission is a powerful tool for the CME diagnostics that can be used to develop techniques for space weather forecasting especially when multi-spacecraft observations are not available.

The estimation of ICME arrival is an important element in the prediction of geomagnetic storms. Another one is the prediction of the orientation of the ICME magnetic field. Since geomagnetic storms are directly linked with the magnetic field orientation of ICMEs, the orientation of the magnetic field in the erupting flux rope could be an important parameter to predict geomagnetic storms and radio emission could be used for this end if the polarisation of the radio source could be related to the magnetic field orientation.

In this thesis, we have presented the preliminary results on the characterisation of the polarisation of three type IV bursts associated with CME events. These results suggest that mapping the polarisation of type IV radio sources as a tool to obtain the orientation of the flux rope magnetic field is promising. We have also confirmed for the three events that the location and evolution of the radio sources can provide an idea about the direction of the CME propagation with respect of the ecliptic plane and also about

the extension of the CME in the low corona. These observational results support the hypothesis that radio emission is closely related to the erupting magnetic structure. This is a motivation for a deeper study of using the polarisation of radio sources to describe the magnetic field of the CME flux rope.

In general, the results presented in this thesis demonstrate that radio emission is a powerful tool for complementary diagnostics of CMEs which can also contribute on space weather forecasting.

To continue the study of radio emission as a tool for CME diagnostics, the University of Costa Rica, through the Space Research Center (CINESPA), is developing a project to construct a new radio observatory in Costa Rica where one antenna will be dedicated to solar radio spectroscopy. Since Costa Rica is located at GMT-6 hours longitude, this instrument can be an element of an earth wide network of solar radio observatories.

Considering that radio astronomy is a new field in Costa Rica and there is not an adequate infrastructure to develop it, this plan is projected in the long term. The solar radio spectroscopy in the metric range can be done with the antenna of 9 meters located in Santa Cruz, Guanacaste where a small station will be built to contain all the electronic equipment for radio observations. We expect that this project can contribute not only to the development of the radio astronomy and the science in general in Costa Rica but also to new studies of the international solar scientific community.

Bibliography

Aggarwal, M., Jain, R., Mishra, A.P., Kulkarni, P.G., Vyas, C., Sharma, R., Gupta, M.: 2008, X-ray emission characteristics of flares associated with CMEs. *Journal of Astrophysics and Astronomy* **29**, 195 – 205. DOI. ADS.

Alissandrakis, C.A., Chiuderi Drago, F.: 1995, Coronal magnetic fields from faraday rotation observations. *Solar Phys.* **160**, 171 – 179. DOI. ADS.

Antiochos, S.K., DeVore, C.R., Klimchuk, J.A.: 1999, A model for solar coronal mass ejections. *Astrophys. J.* **510**, 485 – 493. DOI. ADS.

Antonucci, E., Gabriel, A.H., Acton, L.W., Leibacher, J.W., Culhane, J.L., Rapley, C.G., Doyle, J.G., Machado, M.E., Orwig, L.E.: 1982, Impulsive phase of flares in soft X-ray emission. *Solar Phys.* **78**, 107 – 123. DOI. ADS.

Aschwanden, M.J.: 2002, Particle acceleration and kinematics in solar flares - a synthesis of recent observations and theoretical concepts (Invited Review). *Space Sci. Rev.* **101**, 1 – 227. DOI. ADS.

Aschwanden, M.J.: 2004, *Physics of the solar corona. an introduction*, Praxis Publishing Ltd, ??? ADS.

Aschwanden, M.J.: 2012, GeV Particle Acceleration in Solar Flares and Ground Level Enhancement (GLE) Events. *Space Sci. Rev.* **171**, 3 – 21. DOI. ADS.

Aulanier, G., Török, T., Démoulin, P., DeLuca, E.E.: 2010, Formation of torus-unstable flux ropes and electric currents in erupting sigmoids. *Astrophys. J.* **708**, 314 – 333. DOI. ADS.

Aurass, H., Klein, K.-L., Zlotnik, E.Y., Zaitsev, V.V.: 2003, Solar type IV burst spectral fine structures . I. Observations. *Astron. Astrophys.* **410**, 1001 – 1010. DOI. ADS.

Bain, H.M., Krucker, S., Saint-Hilaire, P., Raftery, C.L.: 2014, Radio imaging of a type IVM radio burst on the 14th of August 2010. *Astrophys. J.* **782**, 43. DOI. ADS.

Bastian, T.S., Pick, M., Kerdraon, A., Maia, D., Vourlidas, A.: 2001, The coronal mass ejection of 1998 April 20: direct imaging at radio wavelengths. *Astrophys. J. Lett.* **558**, L65 – L69. DOI. ADS.

Bein, B.M., Berkebile-Stoiser, S., Veronig, A.M., Temmer, M., Vršnak, B.: 2012, Impulsive acceleration of coronal mass ejections. II. Relation to soft X-ray flares and filament eruptions. *Astrophys. J.* **755**, 44. DOI. ADS.

Bemporad, A., Mancuso, S.: 2010, First complete determination of plasma physical parameters across a coronal mass ejection-driven shock. *Astrophys. J.* **720**, 130 – 143. DOI. ADS.

Bemporad, A., Mancuso, S.: 2011, Identification of super- and subcritical regions in shocks driven by coronal mass ejections. *Astrophys. J. Lett.* **739**, L64. DOI. ADS.

Bentley, R.D., Klein, K.-L., van Driel-Gesztelyi, L., Démoulin, P., Trottet, G., Tassetto, P., Marty, G.: 2000, Magnetic activity associated with radio noise storms. *Solar Phys.* **193**, 227 – 245. DOI. ADS.

Benz, A.O.: 1987, Acceleration and energization by currents and electric fields. *Solar Phys.* **111**, 1 – 18. DOI. ADS.

Benz, A.O., Thejappa, G.: 1988, Radio emission of coronal shock waves. *Astron. Astrophys.* **202**, 267 – 274. ADS.

Boischot, A.: 1957, Caractères d'un type d'émission hertzienne associé à certaines éruptions chromosphériques. *Academie des Sciences Paris Comptes Rendus* **244**, 1326 – 1329. ADS.

Burkepile, J.T., Hundhausen, A.J., Stanger, A.L., St. Cyr, O.C., Seiden, J.A.: 2004, Role of projection effects on solar coronal mass ejection properties: 1. A study of CMEs associated with limb activity. *Journal of Geophysical Research (Space Physics)* **109**, A03103. DOI. ADS.

Burlaga, L.F.: 1995, Interplanetary magnetohydrodynamics. *International Series in Astronomy and Astrophysics, Vol. 3, Oxford University Press. 1995. 272 pages; ISBN13: 978-0-19-508472-6* **3**. ADS.

Cairns, I.H.: 2011, Coherent radio emissions associated with solar system shocks. In: Miralles, M. P. & Sánchez Almeida, J. (ed.) *The Sun, the solar wind, and the heliosphere*, *IAGA Special Sopron Book Series* **4**, Springer, ???, 267 – 338. ADS.

Cairns, I.H., Robinson, R.D.: 1987, Herringbone bursts associated with type II solar radio emission. *Solar Phys.* **111**, 365 – 383. DOI. ADS.

Cairns, I.H., Knock, S.A., Robinson, P.A., Kuncic, Z.: 2003, Type II solar radio bursts: theory and space weather implications. *Space Sci. Rev.* **107**, 27 – 34. DOI. ADS.

Cane, H.V., White, S.M.: 1989, On the source conditions for herringbone structure in type II solar radio bursts. *Solar Phys.* **120**, 137 – 144. DOI. ADS.

Cane, H.V., Richardson, I.G., St. Cyr, O.C.: 2000, Coronal mass ejections, interplanetary ejecta and geomagnetic storms. *Geophys. Res. Lett.* **27**, 3591 – 3594. DOI. ADS.

Cargill, P.J.: 2002, Coupling models of disparate physical processes in the solar corona: the case of fragmented energy release. In: Sawaya-Lacoste, H. (ed.) *SOLMAG 2002. Proceedings of the magnetic coupling of the solar atmosphere euroconference*, *ESA Special Publication* **505**, 245 – 251. ADS.

Cargill, P.J.: 2004, On the aerodynamic drag force acting on interplanetary coronal mass ejections. *Solar Phys.* **221**, 135 – 149. DOI. ADS.

Cargill, P.J., Chen, J., Spicer, D.S., Zalesak, S.T.: 1996, Magnetohydrodynamic simulations of the motion of magnetic flux tubes through a magnetized plasma. *J. Geophys. Res. (Space Phys.)* **101**, 4855 – 4870. DOI. ADS.

Carley, E.P., Reid, H., Vilmer, N., Gallagher, P.T.: 2015, Low frequency radio observations of bi-directional electron beams in the solar corona. *Astron. Astrophys.* **581**, A100. DOI. ADS.

Carmichael, H.: 1964, A process for flares. *NASA Special Publication* **50**, 451. ADS.

Caroubalos, C.: 1964, Contribution à l'étude de l'activité solaire en relation avec ses effects géophysiques. *Annales d'Astrophysique* **27**, 333. ADS.

Chen, H., Zhang, J., Ma, S., Yang, S., Li, L., Huang, X., Xiao, J.: 2015, Confined flares in solar active region 12192 from 2014 October 18 to 29. *Astrophys. J. Lett.* **808**, L24. DOI. ADS.

Chen, P.F.: 2011, Coronal mass ejections: models and their observational basis. *Living Reviews in Solar Physics* **8**. DOI. ADS.

Chertok, I.M., Gnezdilov, A.A., Zaborova, E.P.: 1992a, Microwave and soft X-ray emission from solar flare events associated with coronal transients. *Soviet Astron.* **36**, 301. ADS.

Chertok, I.M., Gnezdilov, A.A., Zaborova, E.P.: 1992b, Relations between parameters of coronal mass ejections and solar flare microwave and soft X-ray bursts. In: Marsch, E., Schwenn, R. (eds.) *Solar wind seven colloquium*, 607 – 610. ADS.

Colaninno, R.C., Vourlidas, A., Wu, C.C.: 2013, Quantitative comparison of methods for predicting the arrival of coronal mass ejections at Earth based on multiview imaging. *Journal of Geophysical Research (Space Physics)* **118**, 6866 – 6879. DOI. ADS.

Cravens, T.E. (ed.): 1997, *Physics of solar system plasmas /Thomas E. Cravens. Cambridge : Cambridge*. ADS.

Dasso, S., Mandrini, C.H., Démoulin, P., Luoni, M.L.: 2006, A new model-independent method to compute magnetic helicity in magnetic CLOUDS. *Astron. Astrophys.* **455**, 349 – 359. DOI. ADS.

Del Zanna, G., Aulanier, G., Klein, K.-L., Török, T.: 2011, A single picture for solar coronal outflows and radio noise storms. *Astron. Astrophys.* **526**, A137. DOI. ADS.

Démoulin, P.: 2010, Interaction of ICMEs with the solar wind. *Twelfth International Solar Wind Conference* **1216**, 329 – 334. DOI. ADS.

Démoulin, P., Vourlidas, A., Pick, M., Bouteille, A.: 2012, Initiation and development of the white-light and radio coronal mass ejection on 2001 April 15. *Astrophys. J.* **750**, 147. DOI. ADS.

Dere, K.P., Wang, D., Howard, R.: 2005, Three-dimensional structure of coronal mass ejections from LASCO polarization measurements. *Astrophys. J. Lett.* **620**, L119 – L122. DOI. ADS.

Dulk, G.A., Leblanc, Y., Bastian, T.S., Bougeret, J.-L.: 2000, Acceleration of electrons at type II shock fronts and production of shock-accelerated type III bursts. *J. Geophys. Res. (Space Phys.)* **105**, 27343 – 27352. DOI. ADS.

Duncan, R.A.: 1980, The emission mechanism of solar moving type IV metre-wave radio sources. *Proceedings of the Astronomical Society of Australia* **4**, 67 – 70. ADS.

Echer, E., Gonzalez, W.D., Tsurutani, B.T., Gonzalez, A.L.C.: 2008, Interplanetary conditions causing intense geomagnetic storms (Dst <-100 nT) during solar cycle 23 (1996-2006). *Journal of Geophysical Research (Space Physics)* **113**, A05221. DOI. ADS.

Forbes, T.: 2010, Models of coronal mass ejections and flares. In: Schrijver, C.J., Siscoe, G.L. (eds.) *Heliophysics: space storms and radiation: causes and effects*, Cambridge University Press, Cambridge, UK, 159. ADS.

Forbes, T.G.: 2000, A review on the genesis of coronal mass ejections. *J. Geophys. Res. (Space Phys.)* **105**, 23153 – 23166. DOI. ADS.

Forbes, T.G., Acton, L.W.: 1996, Reconnection and field line shrinkage in solar flares. *Astrophys. J.* **459**, 330. DOI. ADS.

Forbes, T.G., Linker, J.A., Chen, J., Cid, C., Kóta, J., Lee, M.A., Mann, G., Mikić, Z., Potgieter, M.S., Schmidt, J.M., Siscoe, G.L., Vainio, R., Antiochos, S.K., Riley, P.: 2006, CME theory and models. *Space Sci. Rev.* **123**, 251 – 302. DOI. ADS.

Frazin, R.A.: 2000, Tomography of the solar corona. I. A robust, regularized, positive estimation method. *Astrophys. J.* **530**, 1026 – 1035. DOI. ADS.

Gary, D.E., Dulk, G.A., House, L.L., Illing, R., Wagner, W.J.: 1985, The type IV burst of 1980 June 29, 0233 UT - Harmonic plasma emission? *Astron. Astrophys.* **152**, 42 – 50. ADS.

Gonzalez, W., Parker, E. (eds.): 2016, *Magnetic reconnection*, *Astrophysics and Space Science Library* **427**. DOI. ADS.

Gonzalez, W.D., Tsurutani, B.T.: 1987, Criteria of interplanetary parameters causing intense magnetic storms (Dst of less than -100 nT). *Planet. Space Sci.* **35**, 1101 – 1109. DOI. ADS.

Gonzalez, W.D., Joselyn, J.A., Kamide, Y., Kroehl, H.W., Rostoker, G., Tsurutani, B.T., Vasyliunas, V.M.: 1994, What is a geomagnetic storm? *J. Geophys. Res. (Space Phys.)* **99**, 5771 – 5792. DOI. ADS.

Gopalswamy, N.: 2009, Coronal mass ejections and space weather. In: Tsuda, T., Fujii, R., Shibata, K., Geller, M.A. (eds.) *Climate and weather of the Sun-Earth system (CAWSES) selected papers from the 2007 Kyoto symposium. Edited by T. Tsuda, R. Fujii, K. Shibata, and M.A. Geller. Tokyo: TERRAPUB, 2009, p.77-120*, 77 – 120. ADS.

Gopalswamy, N.: 2010, Coronal mass ejections: a summary of recent results. In: Dorotovic, I. (ed.) *20th National solar physics meeting, Papradno, Slovakia*, 108 – 130. ADS.

Gopalswamy, N., Yashiro, S., Akiyama, S.: 2007, Geoeffectiveness of halo coronal mass ejections. *Journal of Geophysical Research (Space Physics)* **112**, A06112. DOI. ADS.

Gopalswamy, N., Lara, A., Yashiro, S., Kaiser, M.L., Howard, R.A.: 2001, Predicting the 1-AU arrival times of coronal mass ejections. *J. Geophys. Res. (Space Phys.)* **106**, 29207 – 29218. DOI. ADS.

Gosling, J.T.: 1993, The solar flare myth. *J. Geophys. Res. (Space Phys.)* **98**, 18937 – 18950. DOI. ADS.

Harrison, R.A.: 1986, Solar coronal mass ejections and flares. *Astron. Astrophys.* **162**, 283 – 291. ADS.

Hewish, A., Scott, P.F., Wills, D.: 1964, Interplanetary scintillation of small diameter radio sources. *Nature* **203**, 1214 – 1217. DOI. ADS.

Hirayama, T.: 1974, Theoretical model of flares and prominences. I: evaporating flare model. *Solar Phys.* **34**, 323 – 338. DOI. ADS.

Holman, G.D., Pesses, M.E.: 1983, Solar type II radio emission and the shock drift acceleration of electrons. *Astrophys. J.* **267**, 837 – 843. DOI. ADS.

Huang, J., Démoulin, P., Pick, M., Auchère, F., Yan, Y.H., Bouteille, A.: 2011, Initiation and early development of the 2008 April 26 coronal mass ejection. *Astrophys. J.* **729**, 107. DOI. ADS.

Hundhausen, A.J.: 1997, Coronal mass ejections. In: Jokipii, J.R., Sonett, C.P., Giampapa, M.S. (eds.) *Cosmic winds and the heliosphere*, 259. ADS.

Hundhausen, A.J., Sawyer, C.B., House, L., Illing, R.M.E., Wagner, W.J.: 1984, Coronal mass ejections observed during the solar maximum mission - Latitude distribution and rate of occurrence. *J. Geophys. Res. (Space Phys.)* **89**, 2639 – 2646. DOI. ADS.

Illing, R.M.E., Hundhausen, A.J.: 1985, Observation of a coronal transient from 1.2 to 6 solar radii. *J. Geophys. Res. (Space Phys.)* **90**, 275 – 282. DOI. ADS.

Kahler, S.W., Reames, D.V., Sheeley, N.R. Jr.: 2001, Coronal mass ejections associated with impulsive solar energetic particle events. *Astrophys. J.* **562**, 558 – 565. DOI. ADS.

Kai, K.: 1962, Some characteristics of type I bursts. *Pub. Astron. Soc. Japan* **14**, 1. ADS.

Kai, K.: 1978, Relation between circular polarization of moving Type IV bursts and polarity of photospheric magnetic fields. *Solar Phys.* **56**, 417 – 427. DOI. ADS.

Kerdraon, A., Delouis, J.-M.: 1997, The Nançay Radioheliograph. In: Trottet, G. (ed.) *Coronal physics from radio and space observations, Lecture Notes in Physics, Berlin Springer Verlag* **483**, 192. DOI. ADS.

Kerdraon, A., Mercier, C.: 1983, Brightness temperature of solar radio noise storm continua. *Astron. Astrophys.* **127**, 132 – 134. ADS.

Kivelson, M.G., Russell, C.T.: 1995, *Introduction to Space Physics*, 586. ADS.

Klein, K.-L., Mouradian, Z.: 2002, The dynamics of an erupting prominence. *Astron. Astrophys.* **381**, 683 – 693. DOI. ADS.

Klein, K.-L., Chupp, E.L., Trottet, G., Magun, A., Dunphy, P.P., Rieger, E., Urpo, S.: 1999, Flare-associated energetic particles in the corona and at 1 AU. *Astron. Astrophys.* **348**, 271 – 285. ADS.

Kopp, R.A., Pneuman, G.W.: 1976, Magnetic reconnection in the corona and the loop prominence phenomenon. *Solar Phys.* **50**, 85 – 98. DOI. ADS.

Kouloumvakos, A., Patsourakos, S., Hillaris, A., Vourlidas, A., Preka-Papadema, P., Moussas, X., Caroubalos, C., Tsitsipis, P., Kontogeorgos, A.: 2014, CME expansion as the driver of metric type II shock emission as revealed by self-consistent analysis of high-cadence EUV images and radio spectrograms. *Solar Phys.* **289**, 2123 – 2139. DOI. ADS.

Kundu, M.R.: 1965, *Solar radio astronomy*. ADS.

Kwon, R.-Y., Zhang, J., Olmedo, O.: 2014, New insights into the physical nature of coronal mass ejections and associated shock waves within the framework of the three-dimensional structure. *Astrophys. J.* **794**, 148. DOI. ADS.

Lario, D., Raouafi, N.E., Kwon, R.-Y., Zhang, J., Gómez-Herrero, R., Dresing, N., Riley, P.: 2014, The solar energetic particle event on 2013 April 11: an investigation of its solar origin and longitudinal spread. *Astrophys. J.* **797**, 8. DOI. ADS.

Lavraud, B., Rouillard, A.: 2014, Properties and processes that influence CME geo-effectiveness. In: Schmieder, B., Malherbe, J.-M., Wu, S.T. (eds.) *Nature of prominences and their role in space weather*, *IAU Symposium* **300**, 273 – 284. DOI. ADS.

Lecacheux, A.: 2014, The Nançay Decameter Array: a useful step towards giant, new generation radio telescopes for long wavelength radio astronomy. In: Stone, R.G., Weiler, K.W., Goldstein, M.L., Bougerot, J.-L. (eds.) *Radio astronomy at long wavelengths, tutorials and reviews*, *Geophysical monograph* **119**, 321. ADS.

Lin, J.: 2004, CME-flare association deduced from catastrophic model of CMEs. *Solar Phys.* **219**, 169 – 196. DOI. ADS.

Lin, J., Forbes, T.G.: 2000, Effects of reconnection on the coronal mass ejection process. *J. Geophys. Res. (Space Phys.)* **105**, 2375 – 2392. DOI. ADS.

Liu, Y., Luhmann, J.G., Bale, S.D., Lin, R.P.: 2011, Solar source and heliospheric consequences of the 2010 April 3 coronal mass ejection: a comprehensive view. *Astrophys. J.* **734**, 84. DOI. ADS.

Loewe, C.A., Prölss, G.W.: 1997, Classification and mean behavior of magnetic storms. *J. Geophys. Res. (Space Phys.)* **102**, 14209 – 14214. DOI. ADS.

Lugaz, N., Kintner, P.: 2013, effect of solar wind drag on the determination of the properties of coronal mass ejections from heliospheric images. *Solar Phys.* **285**, 281 – 294. DOI. ADS.

Lugaz, N., Vourlidas, A., Roussev, I.I.: 2009, Deriving the radial distances of wide coronal mass ejections from elongation measurements in the heliosphere - application to CME-CME interaction. *Annales Geophysicae* **27**, 3479 – 3488. DOI. ADS.

Lugaz, N., Farrugia, C.J., Davies, J.A., Möstl, C., Davis, C.J., Roussev, I.I., Temmer, M.: 2012, The deflection of the two interacting coronal mass ejections of 2010 may 23-24 as revealed by combined in situ measurements and heliospheric imaging. *Astrophys. J.* **759**, 68. DOI. ADS.

Maia, D.J.F., Gama, R., Mercier, C., Pick, M., Kerdraon, A., Karlický, M.: 2007, The radio-coronal mass ejection event on 2001 April 15. *Astrophys. J.* **660**, 874 – 881. DOI. ADS.

Malik, R.K., Mercier, C.: 1996, Motions, relative positions, and sizes of continua and bursts in solar noise storms. *Solar Phys.* **165**, 347 – 375. DOI. ADS.

Mancuso, S., Garzelli, M.V.: 2013, Coronal magnetic field strength from type II radio emission: complementarity with Faraday rotation measurements. *Astron. Astrophys.* **560**, L1. DOI. ADS.

Mann, G., Classen, H.-T., Motschmann, U.: 2001, Generation of highly energetic electrons by shock waves in the solar corona. *J. Geophys. Res. (Space Phys.)* **106**, 25323 – 25332. DOI. ADS.

Mann, G., Classen, T., Aurass, H.: 1995, Characteristics of coronal shock waves and solar type II radio bursts. *Astron. Astrophys.* **295**, 775. ADS.

Mann, G., Klassen, A., Aurass, H., Classen, H.-T.: 2003, Formation and development of shock waves in the solar corona and the near-Sun interplanetary space. *Astron. Astrophys.* **400**, 329 – 336. DOI. ADS.

Manoharan, P.K., Mujiber Rahman, A.: 2011, Coronal mass ejections: propagation time and associated internal energy. *Journal of Atmospheric and Solar-Terrestrial Physics* **73**, 671 – 677. DOI. ADS.

Masson, S., Antiochos, S.K., DeVore, C.R.: 2013, A model for the escape of solar-flare-accelerated particles. *Astrophys. J.* **771**, 82. DOI. ADS.

Mays, M.L., Taktakishvili, A., Pulkkinen, A., MacNeice, P.J., Rastätter, L., Odstrcil, D., Jian, L.K., Richardson, I.G., LaSota, J.A., Zheng, Y., Kuznetsova, M.M.: 2015, Ensemble modeling of CMEs using the WSA-ENLIL+Cone model. *Solar Phys.* **290**, 1775 – 1814. DOI. ADS.

McLean, D.J.: 1967, Band splitting in type II solar radio bursts. *Proceedings of the Astronomical Society of Australia* **1**, 47 – 49. ADS.

McLean, D.J., Labrum, N.R.: 1985, *Solar radiophysics: studies of emission from the sun at metre wavelengths*. ADS.

Melrose, D.B.: 1980, The emission mechanisms for solar radio bursts. *Space Sci. Rev.* **26**, 3 – 38. DOI. ADS.

Melrose, D.B.: 1987, Plasma emission - A review. *Solar Phys.* **111**, 89 – 101. DOI. ADS.

Melrose, D.B.: 1994, Turbulent acceleration in solar flares. *Astrophys. J. Supp.* **90**, 623 – 630. DOI. ADS.

Mercier, C., Chambe, G.: 2015, Electron density and temperature in the solar corona from multifrequency radio imaging. *Astron. Astrophys.* **583**, A101. DOI. ADS.

Mercier, C., Elgaroy, O., Tlamicha, A., Zlobec, P.: 1984, Solar noise storms coordinated observations - May 16-24, 1981. *Solar Phys.* **92**, 375 – 381. DOI. ADS.

Michalek, G., Gopalswamy, N., Yashiro, S.: 2009, Expansion speed of coronal mass ejections. *Solar Phys.* **260**, 401 – 406. DOI. ADS.

Mierla, M., Inhester, B., Marqué, C., Rodriguez, L., Gissot, S., Zhukov, A.N., Berghmans, D., Davila, J.: 2009, On 3D reconstruction of coronal mass ejections: I. Method description and application to SECCHI-COR data. *Solar Phys.* **259**, 123 – 141. DOI. ADS.

Millward, G., Biesecker, D., Pizzo, V., Koning, C.A.: 2013, An operational software tool for the analysis of coronagraph images: determining CME parameters for input into the WSA-Enlil heliospheric model. *Space Weather* **11**, 57 – 68. DOI. ADS.

Mishra, W., Srivastava, N.: 2014, Morphological and kinematic evolution of three interacting coronal mass ejections of 2011 February 13-15. *Astrophys. J.* **794**, 64. DOI. ADS.

Moon, Y.-J., Choe, G.S., Wang, H., Park, Y.D., Gopalswamy, N., Yang, G., Yashiro, S.: 2002, A statistical study of two classes of coronal mass ejections. *Astrophys. J.* **581**, 694 – 702. DOI. ADS.

Moon, Y.-J., Choe, G.S., Wang, H., Park, Y.D., Cheng, C.Z.: 2003, Relationship between CME kinematics and flare strength. *J. Korean Astron. Soc.* **36**, 61 – 66. DOI. ADS.

Moran, T.G., Davila, J.M.: 2004, Three-dimensional polarimetric imaging of coronal mass ejections. *Science* **305**, 66 – 71. DOI. ADS.

Möstl, C., Temmer, M., Rollett, T., Farrugia, C.J., Liu, Y., Veronig, A.M., Leitner, M., Galvin, A.B., Biernat, H.K.: 2010, STEREO and Wind observations of a fast ICME flank triggering a prolonged geomagnetic storm on 5-7 April 2010. *Geophys. Res. Lett.* **37**, L24103. DOI. ADS.

Möstl, C., Amla, K., Hall, J.R., Liewer, P.C., De Jong, E.M., Colaninno, R.C., Veronig, A.M., Rollett, T., Temmer, M., Peinhart, V., Davies, J.A., Lugaz, N., Liu, Y.D., Farrugia, C.J., Luhmann, J.G., Vršnak, B., Harrison, R.A., Galvin, A.B.: 2014, Connecting speeds, directions and arrival times of 22 coronal mass ejections from the Sun to 1 AU. *Astrophys. J.* **787**, 119. DOI. ADS.

Möstl, C., Rollett, T., Frahm, R.A., Liu, Y.D., Long, D.M., Colaninno, R.C., Reiss, M.A., Temmer, M., Farrugia, C.J., Posner, A., Dumbovic, M., Janvier, M., Demoulin, P., Boakes, P., Devos, A., Kraaikamp, E., Mays, M.L., Vrsnak, B.: 2015, Strong coronal channelling and interplanetary evolution of a solar storm up to Earth and Mars. In: *???* **6**, 7135. DOI. ADS.

Newkirk, G. Jr.: 1961, The solar corona in active regions and the thermal origin of the slowly varying component of solar radio radiation. *Astrophys. J.* **133**, 983. DOI. ADS.

Nindos, A., Aurass, H., Klein, K.-L., Trottet, G.: 2008, Radio emission of flares and coronal mass ejections. Invited review. *Solar Phys.* **253**, 3 – 41. DOI. ADS.

Nita, G.M., Gary, D.E., Lee, J.: 2004, Statistical study of two years of solar flare radio spectra obtained with the Owens Valley Solar Array. *Astrophys. J.* **605**, 528 – 545. DOI. ADS.

Odstrcil, D., Pizzo, V.J., Linker, J.A., Riley, P., Lionello, R., Mikic, Z.: 2004, Initial coupling of coronal and heliospheric numerical magnetohydrodynamic codes. *Journal of Atmospheric and Solar-Terrestrial Physics* **66**, 1311 – 1320. DOI. ADS.

Owens, M., Cargill, P.: 2004, Predictions of the arrival time of coronal mass ejections at 1AU: an analysis of the causes of errors. *Annales Geophysicae* **22**, 661 – 671. DOI. ADS.

Parker, E.N.: 1958, Dynamics of the interplanetary gas and magnetic fields. *Astrophys. J.* **128**, 664. DOI. ADS.

Parker, E.N.: 1963, *Interplanetary dynamical processes*. ADS.

Pick, M.: 1986, Observations of radio continua and terminology. *Solar Phys.* **104**, 19 – 32. DOI. ADS.

Pick, M., Vilmer, N.: 2008, Sixty-five years of solar radioastronomy: flares, coronal mass ejections and Sun Earth connection. *Astron. Astrophys. Rev.* **16**, 1 – 153. DOI. ADS.

Pinto, R.F., Vilmer, N., Brun, A.S.: 2015, Soft X-ray emission in kink-unstable coronal loops. *Astron. Astrophys.* **576**, A37. DOI. ADS.

Poquérusse, M., Hoang, S., Bougeret, J.-L., Moncuquet, M.: 1996, Ulysses-ARTEMIS radio observation of energetic flare electrons. In: Winterhalter, D., Gosling, J.T., Habbal, S.R., Kurth, W.S., Neugebauer, M. (eds.) *American institute of physics conference series, American Institute of Physics Conference Series* **382**, 62 – 65. DOI. ADS.

Priest, E.R.: 1982, *Solar magneto-hydrodynamics*. ADS.

Rachmeler, L.A., DeForest, C.E., Kankelborg, C.C.: 2009, Reconnectionless CME eruption: putting the Aly-Sturrock conjecture to rest. *Astrophys. J.* **693**, 1431 – 1436. DOI. ADS.

Ramaty, R.: 1969, Gyrosynchrotron emission and absorption in a magnetoactive plasma. *Astrophys. J.* **158**, 753. DOI. ADS.

Reeves, K.K., Moats, S.J.: 2010, Relating coronal mass ejection kinematics and thermal energy release to flare emissions using a model of solar eruptions. *Astrophys. J.* **712**, 429 – 434. DOI. ADS.

Roberts, J.A.: 1959, Solar radio bursts of spectral type II. *Australian Journal of Physics* **12**, 327. DOI. ADS.

Robinson, R.D.: 1978, Observations and interpretation of moving type IV solar radio bursts. *Solar Phys.* **60**, 383 – 398. DOI. ADS.

Rollett, T., Möstl, C., Isavnin, A., Davies, J.A., Kubicka, M., Amerstorfer, U.V., Harrison, R.A.: 2016, ElEvoHI: a novel CME prediction tool for heliospheric imaging combining an elliptical front with drag-based model fitting. *ArXiv e-prints*. ADS.

Rouillard, A.P.: 2011, Relating white light and in situ observations of coronal mass ejections: a review. *Journal of Atmospheric and Solar-Terrestrial Physics* **73**, 1201 – 1213. DOI. ADS.

Rouillard, A.P., Davies, J.A., Forsyth, R.J., Rees, A., Davis, C.J., Harrison, R.A., Lockwood, M., Bewsher, D., Crothers, S.R., Eyles, C.J., Hapgood, M., Perry, C.H.: 2008, First imaging of corotating interaction regions using the STEREO spacecraft. *Geophys. Res. Lett.* **35**, L10110. DOI. ADS.

Rouillard, A.P., Plotnikov, I., Pinto, R., Tirole, M., Linker, J., De Rosa, M., Vainio, R., Vourlidas, A., Warmuth, A., Mann, G.: 2016, Deriving the properties of coronal pressure fronts in 3-D: application to the 17 May 2012 ground level enhancement. *Astrophys. J.*, to be submitted.

Saint-Hilaire, P., Vilmer, N., Kerdraon, A.: 2013, A decade of solar type III radio bursts observed by the Nançay Radioheliograph 1998-2008. *Astrophys. J.* **762**, 60. DOI. ADS.

Saito, K., Poland, A.I., Munro, R.H.: 1977, A study of the background corona near solar minimum. *Solar Phys.* **55**, 121 – 134. DOI. ADS.

Sakai, J.I., Karlický, M.: 2008, Particle-in-cell simulations of shocks and band splitting of type II solar radio bursts. *Astron. Astrophys.* **478**, L15 – L18. DOI. ADS.

Salas-Matamoros, C., Klein, K.-L.: 2015, On the statistical relationship between CME speed and soft X-ray flux and fluence of the associated flare. *Solar Phys.* **290**, 1337 – 1353. DOI. ADS.

Salas-Matamoros, C., Klein, K.-L., Rouillard, A.P.: 2016, Coronal mass ejection-related particle acceleration regions during a simple eruptive event. *Astron. Astrophys.* **590**, A135. DOI. ADS.

Salas-Matamoros, C., Klein, K.-L., Trottet, G.: 2016, Microwave radio emission as a proxy of CME speed in ICME arrival predictions at 1 AU. *Journal of Space Weather and Space Climate.*, submitted.

Savoini, P., Lembège, B., Krasnosselskhik, V., Kuramitsu, Y.: 2005, Under and over-adiabatic electrons through a perpendicular collisionless shock: theory versus simulations. *Ann. Geophys.* **23**, 3685 – 3698. DOI. ADS.

Schatten, K.H., Mullan, D.J.: 1977, Fast azimuthal transport of solar cosmic rays via a coronal magnetic bottle. *J. Geophys. Res. (Space Phys.)* **82**, 5609 – 5620. DOI. ADS.

Schmidt, J.M., Cairns, I.H.: 2014, Type II solar radio bursts predicted by 3-D MHD CME and kinetic radio emission simulations. *Journal of Geophysical Research (Space Physics)* **119**, 69 – 87. DOI. ADS.

Schmieder, B., Démoulin, P., Aulanier, G.: 2013, Solar filament eruptions and their physical role in triggering coronal mass ejections. *Advances in Space Research* **51**, 1967 – 1980. DOI. ADS.

Schulte in den Bäumen, H., Cairns, I.H., Robinson, P.A.: 2012, Nonzero azimuthal magnetic fields at the solar source surface: extraction, model, and implications. *Journal of Geophysical Research (Space Physics)* **117**, A10104. DOI. ADS.

Schwenn, R., dal Lago, A., Huttunen, E., Gonzalez, W.D.: 2005, The association of coronal mass ejections with their effects near the Earth. *Ann. Geophys.* **23**, 1033 – 1059. DOI. ADS.

Schwenn, R., Raymond, J.C., Alexander, D., Ciaravella, A., Gopalswamy, N., Howard, R., Hudson, H., Kaufmann, P., Klassen, A., Maia, D., Munoz-Martinez, G., Pick, M., Reiner, M., Srivastava, N., Tripathi, D., Vourlidas, A., Wang, Y.-M., Zhang, J.: 2006, Coronal observations of CMEs. Report of working group A. *Space Sci. Rev.* **123**, 127 – 176. DOI. ADS.

Shi, T., Wang, Y., Wan, L., Cheng, X., Ding, M., Zhang, J.: 2015, Predicting the arrival time of coronal mass ejections with the graduated cylindrical shell and drag force model. *Astrophys. J.* **806**, 271. DOI. ADS.

Smerd, S.F., Sheridan, K.V., Stewart, R.T.: 1974, On split-band structure in type II radio bursts from the Sun (presented by S.F. Smerd). In: Newkirk, G.A. (ed.) *Coronal disturbances*, *IAU Symposium* **57**, 389. ADS.

St. Cyr, O.C., Plunkett, S.P., Michels, D.J., Paswaters, S.E., Koomen, M.J., Simnett, G.M., Thompson, B.J., Gurman, J.B., Schwenn, R., Webb, D.F., Hildner, E., Lamy, P.L.: 2000, Properties of coronal mass ejections: SOHO LASCO observations from January 1996 to June 1998. *J. Geophys. Res. (Space Phys.)* **105**, 18169 – 18186. DOI. ADS.

Stahli, M., Gary, D.E., Hurford, G.J.: 1989, High-resolution microwave spectra of solar bursts. *Solar Phys.* **120**, 351 – 368. DOI. ADS.

Stepanov, A.V.: 1974, A mechanism for generating type IV solar radio bursts. *Soviet Astron.* **17**, 781. ADS.

Sturrock, P.A.: 1966, Model of the high-energy phase of solar flares. *Nature* **211**, 695 – 697. DOI. ADS.

Sturrock, P.A. (ed.): 1980, *Solar flares: a monograph from SKYLAB solar workshop II.* ADS.

Svestka, Z., Cliver, E.W.: 1992, History and basic characteristics of eruptive flares. In: Svestka, Z., Jackson, B.V., Machado, M.E. (eds.) *IAU Colloq. 133: eruptive solar flares, Lecture Notes in Physics, Berlin Springer Verlag* **399**, 1. DOI. ADS.

Tandberg-Hanssen, E., Emslie, A.G.: 1988, *The physics of solar flares*. ADS.

Temmer, M., Nitta, N.V.: 2015, Interplanetary propagation behavior of the fast coronal mass ejection on 23 July 2012. *Solar Phys.* **290**, 919 – 932. DOI. ADS.

Temmer, M., Rollett, T., Möstl, C., Veronig, A.M., Vršnak, B., Odstrčil, D.: 2011, Influence of the ambient solar wind flow on the propagation behavior of interplanetary coronal mass ejections. *Astrophys. J.* **743**, 101. DOI. ADS.

Temmer, M., Vršnak, B., Rollett, T., Bein, B., de Koning, C.A., Liu, Y., Bosman, E., Davies, J.A., Möstl, C., Žic, T., Veronig, A.M., Bothmer, V., Harrison, R., Nitta, N., Bisi, M., Flor, O., Eastwood, J., Odstrcil, D., Forsyth, R.: 2012, Characteristics of kinematics of a coronal mass ejection during the 2010 August 1 CME-CME interaction event. *Astrophys. J.* **749**, 57. DOI. ADS.

Temmer, M., Veronig, A.M., Peinhart, V., Vršnak, B.: 2014, Asymmetry in the CME-CME interaction process for the events from 2011 February 14-15. *Astrophys. J.* **785**, 85. DOI. ADS.

Thalmann, J.K., Su, Y., Temmer, M., Veronig, A.M.: 2015, The confined X-class flares of solar active region 2192. *Astrophys. J. Lett.* **801**, L23. DOI. ADS.

Thernisien, A., Vourlidas, A., Howard, R.A.: 2009, Forward modeling of coronal mass ejections using STEREO/SECCHI data. *Solar Phys.* **256**, 111 – 130. DOI. ADS.

Tobiska, W.K., Knipp, D., Burke, W.J., Bouwer, D., Bailey, J., Odstrcil, D., Hagan, M.P., Gannon, J., Bowman, B.R.: 2013, The Anemomilos prediction methodology for Dst. *Space Weather* **11**, 490 – 508. DOI. ADS.

Török, T., Kliem, B.: 2005, Confined and ejective eruptions of kink-unstable flux ropes. *Astrophys. J. Lett.* **630**, L97 – L100. DOI. ADS.

Török, T., Kliem, B., Titov, V.S.: 2004, Ideal kink instability of a magnetic loop equilibrium. *Astron. Astrophys.* **413**, L27 – L30. DOI. ADS.

Treumann, R.A., LaBelle, J.: 1992, Band splitting in solar type II radio bursts. *Astrophys. J. Lett.* **399**, L167 – L170. DOI. ADS.

Trottet, G., Kerdraon, A., Benz, A.O., Treumann, R.: 1981, Quasi-periodic short-term modulations during a moving type IV burst. *Astron. Astrophys.* **93**, 129 – 135. ADS.

Tsurutani, B.T., Gonzalez, W.D.: 1998, Magnetic storms. In: Suess, S.T., Tsurutani, B.T. (eds.) *From the Sun, auroras, magnetic storms, solar flares, cosmic rays*, *American Geophysical Union, Washington, DC*, 57. ADS.

Žic, T., Vršnak, B., Temmer, M.: 2015, Heliospheric propagation of coronal mass ejections: drag-based model fitting. *Astrophys. J. Supp.* **218**, 32. DOI. ADS.

Vasanth, V., Umapathy, S., Vršnak, B., Žic, T., Prakash, O.: 2014, Investigation of the coronal magnetic field using a type II solar radio burst. *Solar Phys.* **289**, 251 – 261. DOI. ADS.

Vlasov, V.I.: 1981, Interplanetary shock waves from observations of scintillations of radio sources. *Geomagnetism and Aeronomy* **21**, 927 – 929. ADS.

Vršnak, B.: 2001, Solar flares and coronal shock waves. *J. Geophys. Res. (Space Phys.)* **106**, 25291 – 25300. DOI. ADS.

Vršnak, B., Cliver, E.W.: 2008, Origin of coronal shock waves. Invited review. *Solar Phys.* **253**, 215 – 235. DOI. ADS.

Vršnak, B., Lulić, S.: 2000, Formation of coronal MHD shock waves - II. The pressure pulse mechanism. *Solar Phys.* **196**, 181 – 197. DOI. ADS.

Vršnak, B., Žic, T.: 2007, Transit times of interplanetary coronal mass ejections and the solar wind speed. *Astron. Astrophys.* **472**, 937 – 943. DOI. ADS.

Vršnak, B., Sudar, D., Ruždjak, D.: 2005, The CME-flare relationship: Are there really two types of CMEs? *Astron. Astrophys.* **435**, 1149 – 1157. DOI. ADS.

Vršnak, B., Aurass, H., Magdalenić, J., Gopalswamy, N.: 2001, Band-splitting of coronal and interplanetary type II bursts. I. Basic properties. *Astron. Astrophys.* **377**, 321 – 329. DOI. ADS.

Vršnak, B., Magdalenić, J., Aurass, H., Mann, G.: 2002, Band-splitting of coronal and interplanetary type II bursts. II. Coronal magnetic field and Alfvén velocity. *Astron. Astrophys.* **396**, 673 – 682. DOI. ADS.

Vršnak, B., Žic, T., Falkenberg, T.V., Möstl, C., Vennerstrom, S., Vrbanec, D.: 2010, The role of aerodynamic drag in propagation of interplanetary coronal mass ejections. *Astron. Astrophys.* **512**, A43. DOI. ADS.

Vršnak, B., Temmer, M., Žic, T., Taktakishvili, A., Dumbović, M., Möstl, C., Veronig, A.M., Mays, M.L., Odstrčil, D.: 2014, Heliospheric propagation of coronal mass ejections: comparison of numerical WSA-ENLIL+Cone model and analytical drag-based model. *Astrophys. J. Supp.* **213**, 21. DOI. ADS.

Wang, Y.M., Ye, P.Z., Wang, S.: 2003, Multiple magnetic clouds: several examples during March-April 2001. *Journal of Geophysical Research (Space Physics)* **108**, 1370. DOI. ADS.

Webb, D.F., Howard, T.A.: 2012, Coronal mass ejections: observations. *Living Reviews in Solar Physics* **9**. DOI. ADS.

Weiss, A.A.: 1963, The type IV solar radio burst at metre wavelengths. *Australian Journal of Physics* **16**, 526. DOI. ADS.

Wild, J.P.: 1969, Observation of the magnetic structure of a type IV solar radio outburst. *Solar Phys.* **9**, 260 – 264. DOI. ADS.

Wild, J.P., Smerd, S.F., Weiss, A.A.: 1963, Solar bursts. *Annual Review of Astronomy and Astrophysics* **1**, 291. DOI. ADS.

Wilson, T.L., Rohlfs, K., Hüttemeister, S.: 2009, *Tools of radio astronomy*, Springer-Verlag, ??? DOI. ADS.

Wilson, T.L., Rohlfs, K., Hüttemeister, S.: 2013, *Tools of radio astronomy*, Springer, Heidelberg, New York, Dordrecht, London. DOI. ADS.

Wolfson, R., Dlamini, B.: 1997, Cross-field currents: an energy source for coronal mass ejections? *Astrophys. J.* **483**, 961 – 971. ADS.

Wu, C.-C., Dryer, M., Wu, S.T., Wood, B.E., Fry, C.D., Liou, K., Plunkett, S.: 2011, Global three-dimensional simulation of the interplanetary evolution of the observed geoeffective coronal mass ejection during the epoch 1-4 August 2010. *Journal of Geophysical Research (Space Physics)* **116**, A12103. DOI. ADS.

Yashiro, S., Gopalswamy, N.: 2009, Statistical relationship between solar flares and coronal mass ejections. In: Gopalswamy, N., Webb, D.F. (eds.) *Universal heliophysical processes*, *IAU Symposium* **257**, 233 – 243. DOI. ADS.

Yurchyshyn, V., Yashiro, S., Abramenko, V., Wang, H., Gopalswamy, N.: 2005, Statistical distributions of speeds of coronal mass ejections. *Astrophys. J.* **619**, 599 – 603. DOI. ADS.

Zank, G.P., Rice, W.K.M., Wu, C.C.: 2000, Particle acceleration and coronal mass ejection driven shocks: a theoretical model. *J. Geophys. Res. (Space Phys.)* **105**, 25079 – 25096. DOI. ADS.

Zhang, J., Dere, K.P., Howard, R.A., Kundu, M.R., White, S.M.: 2001, On the temporal relationship between coronal mass ejections and flares. *Astrophys. J.* **559**, 452 – 462. DOI. ADS.

Zhang, J., Dere, K.P., Howard, R.A., Vourlidas, A.: 2004, A study of the kinematic evolution of coronal mass ejections. *Astrophys. J.* **604**, 420 – 432. DOI. ADS.

Zhang, J., Richardson, I.G., Webb, D.F., Gopalswamy, N., Huttunen, E., Kasper, J.C., Nitta, N.V., Poomvises, W., Thompson, B.J., Wu, C.-C., Yashiro, S., Zhukov, A.N.: 2007, Solar and interplanetary sources of major geomagnetic storms (Dst = -100 nT) during 1996-2005. *J. Geophys. Res. (Space Phys.)* **112**, 10102. DOI. ADS.

Zimovets, I., Vilmer, N., Chian, A.C.-L., Sharykin, I., Struminsky, A.: 2012, Spatially resolved observations of a split-band coronal type II radio burst. *Astron. Astrophys.* **547**, A6. DOI. ADS.

Zucca, P., Pick, M., Démoulin, P., Kerdraon, A., Lecacheux, A., Gallagher, P.T.: 2014, Understanding coronal mass ejections and associated shocks in the solar corona by merging multiwavelength observations. *Astrophys. J.* **795**, 68. DOI. ADS.

Zuccarello, F.P., Meliani, Z., Poedts, S.: 2012, Numerical modeling of the initiation of coronal mass ejections in active region NOAA 9415. *Astrophys. J.* **758**, 117. DOI. ADS.

Zuccarello, F.P., Soenen, A., Poedts, S., Zuccarello, F., Jacobs, C.: 2008, Initiation of coronal mass ejections by magnetic flux emergence in the framework of the breakout model. *Astrophys. J. Lett.* **689**, L157. DOI. ADS.

Zuccarello, F.P., Romano, P., Zuccarello, F., Poedts, S.: 2014, Shearing motions and torus instability in the 2010 April 3 filament eruption. In: Schmieder, B., Malherbe, J.-M., Wu, S.T. (eds.) *Nature of Prominences and their Role in Space Weather*, *IAU Symposium* **300**, 475 – 476. DOI. ADS.

Zuccarello, F., Balmaceda, L., Cessateur, G., Cremades, H., Guglielmino, S.L., Lilensten, J., Dudok de Wit, T., Kretzschmar, M., Lopez, F.M., Mierla, M., Parenti, S., Pomoell, J., Romano, P., Rodriguez, L., Srivastava, N., Vainio, R., West, M., Zuccarello, F.P.: 2013, Solar activity and its evolution across the corona: recent advances. *Journal of Space Weather and Space Climate* **3**(27), A18. DOI. ADS.